ulm university universität ulm

Stability and Electrocatalytical Properties of Nanostructured Pt/Glassy Carbon Model Electrodes

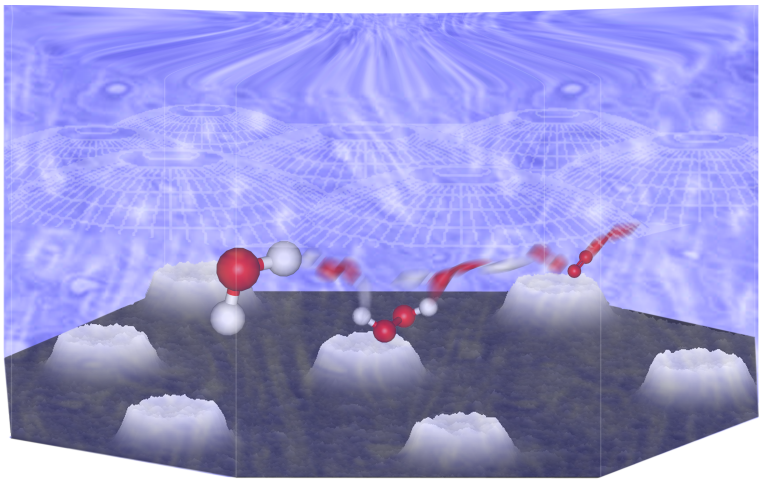

Dissertation
zur Erlangung des Doktorgrades Dr. rer. nat.
der Fakultät für Naturwissenschaften
am Institut für Oberflächenchemie und Katalyse
der Universität Ulm

vorgelegt von

Yvonne Eva Seidel
(geb. Soppa)
aus Heidenheim a.d. Brenz

Ulm, im Mai 2010

Dissertation eingereicht am 10. Mai 2010

Amtierender Dekan: Prof. Dr. Axel Groß
1. Gutachter: Prof. Dr. R. Jürgen Behm
2. Gutachter: Prof. Dr. Werner Tillmetz
3. Gutachter: Prof. Dr. Juan M. Feliu

Tag der Promotion: 21. Oktober 2010

Für Philipp,
Santina und Rasmus

Preface

In recent years, planar model catalysts have been increasingly employed for detailed mechanistic studies of catalytic and electrocatalytic processes, exploiting the well-defined structure as well as electronic and chemical properties of these model systems. Recent developments in *Nanotechnology* have provided new opportunities for the fabrication of, e.g., well-defined nanostructured planar Pt/glassy carbon (GC) model electrodes with essentially monodisperse particle sizes and/or regular particle separations. Model catalysts have so far mainly been employed in studies of heterogeneously catalyzed reactions at the solid-gas interface, whereas studies of electrocatalytic reactions are sparse. Therefore, the aim of this work was to learn more about the influence of transport processes on overall reaction processes, which can, via desorption and re-adsorption of volatile reaction intermediates, affect the product distribution in more complex electrocatalytic reaction processes with different main and side products and can be studied by evaluating the influence of the particle separation on the product distribution.

Within this thesis the stability and electrocatalytic properties of nanostructured Pt/GC surfaces, which represent simplified, but well-defined model versions of commonly used realistic carbon-supported Pt/C catalysts, e.g., in PEM fuel cells, were investigated.

The presented work is organized in eight chapters. In *chapter* 1 the application of model electrodes and their outstanding possibilities of studying mass transport effects in electrocatalytic reactions are described and motivated. *Chapter* 2 addresses fabrication procedures of nanostructured Pt/GC model electrodes, the in this study applied physical characterization techniques such as SEM, EDX, TEM, XPS and AFM and the employed electrochemical instrumentation.

The results presented in *chapters* 3 – 7 were already published in various journals. Each chapter represents a publication with its individual abstract, introduction, results and discussion part and summary. Whereas *chapters* 3 – 5 focus on different fabrication techniques, physical characterization methods and stability-tests of the nanostructured Pt/GC model electrodes, the influence of transport effects in electrocatalytic reactions such as oxygen reduction (*chapter* 6) or methanol oxidation (*chapter* 7), in particular their selectivity and hence the resulting product distribution is presented and discussed.

The preparation of nanostructured Pt/GC electrodes via lithographic techniques (*chapters* 3 – 7) and via deposition of Pt-salt loaded micelles (*chapter* 5) results from excellent collaborations with the groups of Prof. Dr. B. Kasemo (Department of

Applied Physics, Chalmers University, Gothenburg, Sweden) and Prof. Dr. P. Ziemann (Institute of Solid State Physics, Ulm University), respectively. The physical characterization was performed in cooperation with the group of Prof. Dr. H.-J. Fecht (SEM/EDX-Analysis, Institute of Micro- and Nanomaterials) and the group of Prof. Dr. U. Kaiser (TEM, Central Facility for Electron Microscopy) both located at Ulm University. XPS studies were operated in the Institute of Surface Chemistry and Catalysis at Ulm University.

In *chapter* 3 (*J. of Electrochem. Soc.* **155**(3) K50–K58, 2008) the preparation procedure of nanostructured Pt/GC electrodes via Colloidal Lithography is described in detail. The stability of these model catalysts upon exposure to a realistic electrocatalytic reaction environment was studied.

Chapter 4 (*J. of Electrochem. Soc.* **155**(10) K171–K179, 2008) verifies the presence of a dilute layer of secondary Pt nanoparticles in addition to the intended Pt nanodisks on Pt/GC electrodes prepared via Colloidal Lithography. It is further demonstrated that by using the related method of Hole-mask Colloidal Lithography nanostructured Pt/GC electrodes can be prepared which are free from these Pt nanoparticles.

Novel, nanostructured Pt/GC electrodes with homogeneously distributed Pt nanoparticles of uniform and more realistic particle diameters (3–8 nm) fabricated by deposition of Pt-salt loaded micelles and specific after treatment procedure are the topic of *chapter* 5 (*Langmuir* **23**(10) 5795–5801, 2007).

The influence of mesoscopic mass transport effects on the activity and selectivity of the oxygen reduction reaction over nanostructured Pt/GC electrodes prepared by Hole-mask Colloidal Lithography is presented in *chapter* 6 (*Faraday Discuss.* **140** 167–184, 2008). Based on these findings the „desorption–re-adsorption–reaction“ concept is introduced.

In *chapter* 7 (*Langmuir* **26**(5) 3569–3578, 2010) transport effects on the methanol oxidation reaction (MOR) product distribution over nanostructured Pt/GC electrodes fabricated by Hole-mask Colloidal Lithography are the main focus. The measurements reveal a distinct variation in the MOR selectivity, which is explained in terms of the „desorption–re-adsorption–reaction“ concept and verifies its validity.

The achieved results of the forth going *chapters* 3 – 7 are subsumed in English and additionally in German language in *chapter* 8.

May 2010 *Yvonne E. Seidel*

Contents

1 Introduction **1**

1.1 Departure to a new „Energy Age“ 2
1.2 Fuel Cells – Alternative Energy Sources 3
1.3 From Real Catalysts to Model Electrodes 6
1.4 Transport and Re-Adsorption Effects in Electrocatalytic Reactions . . 8
1.5 Outline of the Thesis 16

2 Experimental **19**

2.1 Preparation Methods of Nanostructured Pt/Glassy Carbon Electrodes 20
2.1.1 Colloidal Lithography – *CL* 21
2.1.2 Hole-mask Colloidal Lithography – *HCL* 24
2.1.3 Deposition of Pt-salt loaded Micelles and After-Treatment Procedure 26
2.2 Physical Characterization Methods 27
2.2.1 Scanning Electron Microscopy – *SEM* 28
2.2.2 Energy Dispersive X-Ray Spectroscopy – *EDX* 29
2.2.3 Transmission Electron Microscopy – *TEM* 31
2.2.4 X-Ray Photoelectron Spectroscopy – *XPS* 32
2.2.5 Atomic Force Microscopy – *AFM* 34
2.3 Electrochemical Principles and Instrumentation 35
2.3.1 General Electrochemical Principles 35
2.3.2 Differential Electrochemical Mass Spectroscopy – *DEMS* . . . 39
2.3.3 Thin-Layer Flow Cells 41
2.4 Electrochemical / Electrocatalytical Measurements and their Evaluation 44
2.4.1 Active Surface Area Determination 44
2.4.2 Quantitative Evaluation of DEMS Measurements 46
2.4.3 Measurements with a Double Disk Dual Thin-Layer Flow Cell 48
2.5 Chemicals 50

3 Stability of Nanostructured Pt/GC Electrodes **51**

3.1 Introduction 53

3.2 Results and Discussion . . . 55
3.2.1 Characterization of the GC Substrate Surface and of the Pt/GC Model Catalysts . . . 55
3.2.2 Electrochemical Properties of the Nanostructured Pt/GC Model Electrodes . . . 58
3.2.3 Stability of the Pt/GC Model Electrodes . . . 62
3.3 Conclusion . . . 69

4 Nanostructured Pt/GC Electrodes and Pt Nanoparticles 71
4.1 Introduction . . . 73
4.2 Results and Discussion . . . 74
4.2.1 Surface Characterization . . . 75
4.2.2 Electrochemical Characteristics . . . 81
4.3 Conclusion . . . 88

5 Nanostructured Pt/GC Electrodes Prepared by Micelles 91
5.1 Introduction . . . 93
5.2 Results and Discussion . . . 94
5.2.1 Surface Characterization . . . 94
5.2.2 Electrochemical Characterization . . . 98
5.3 Conclusion . . . 106

6 Mass Transport Effects in Electrocatalytic Processes 109
6.1 Introduction . . . 111
6.2 Results and Discussion . . . 115
6.3 Outlook . . . 125
6.4 Conclusion . . . 127

7 Transport Effects in the Electro-Oxidation of Methanol 131
7.1 Introduction . . . 133
7.2 Results and Discussion . . . 135
7.2.1 Characterization of the Nanostructured Electrodes . . . 135
7.2.2 Electrocatalytic Measurements . . . 137
7.3 Summary and Conclusions . . . 152

8 Summary / Zusammenfassung 155
8.1 Summary . . . 156
8.2 Zusammenfassung . . . 160

Bibliography 164

Appendix **185**
Publications 186
Conference Contributions 188
Acknowledgement 191

List of Figures

1.1 Principle scheme of a PEM fuel cell 4
1.2 Schematic illustration of a real catalyst and a Pt/glassy carbon (GC) model electrode 7
1.3 Simplified motion of a molecule in (a) *Heterogeneous Catalysis* and (b) *Electrocatalysis* 9
1.4 Reaction steps of an electrocatalytic reaction 10
1.5 Simplified reaction scheme for the oxygen reduction reaction (ORR) on a Pt electrode after Damjanovic et al. [1] 11
1.6 Reaction scheme for the methanol oxidation reaction (MOR) on a Pt electrode after Bagotzky et al. [2] 12
1.7 Schematic description of the diffusion front of a mass transport limited reaction 14
1.8 Schematic description of the „desorption – re-adsorption – reaction“ processes on (a) a continuous Pt electrode and nanostructured Pt/GC model electrodes with (b) high Pt surface coverage and (c) low Pt surface coverage 15

2.1 Scheme of the *Collodial Lithography* (CL) procedure 23
2.2 Scheme of the *Hole-mask Colloidal Lithography* (HCL) procedure . . 25
2.3 Schematic description of the preparation procedure by deposition of Pt-salt loaded micelles 27
2.4 Schematic description of (a) a scanning electron microscope (SEM) set-up and (b) the origin of secondary electrons, backscattered electrons and X-ray quanta due to excitation by primary electrons presented as depth profile 29
2.5 Principle scheme of energy dispersive X-Ray (EDX) analysis 30
2.6 Schematic description of (a) a transmission electron microscope (TEM) set-up and (b) the origin of diffracted and transmitted electrons due to excitation by a primary electron beam 31
2.7 (a) Photoemission and (b) the Auger process 33
2.8 Schematic description of an atomic force microscope (AFM). 35

2.9 Scheme of a standard differential electrochemical mass spectrometer (DEMS) set-up 40
2.10 Scheme of a dual thin-layer flow cell developed by Jusys et al. [3] . . 43
2.11 Scheme of a double disk dual thin-layer flow cell developed by Jusys et al. [4] 43

3.1 SEM images of a nanostructured Pt/GC electrode prepared by CL . . 56
3.2 XP spectra of GC substrates (C(1s) peak) 58
3.3 AFM images and line scans of GC substrate surfaces pre-treated in different ways prior to Pt deposition 59
3.4 CO electro-oxidation experiments on nanostructured Pt/GC electrodes prepared by CL and different Pt deposition techniques 61
3.5 SEM images and BCVs of nanostructured Pt/GC electrodes prepared by CL (Pt deposition: evaporation) on a GC substrate with and without Ar-plasma pretreatment 63
3.6 SEM images and BCVs of nanostructured Pt/GC electrodes prepared by CL (Pt deposition: sputter deposition) on a GC substrate pretreated in Ar-plasma and oxygen-plasma followed by Ar-plasma pretreatment 65
3.7 SEM images and BCVs of nanostructured Pt/GC electrodes prepared by CL (Pt sputter deposition in comparison to Pt evaporation) on a GC substrate illustrating effects evoked by different measurement methods such as repetitive cycling to higher potentials or after exposure to pressure-enhanced electrolyte flow 67
3.8 TEM cross-section micrographs of nanostructured Pt/GC electrodes prepared via CL (Pt sputter deposition in comparison to Pt evaporation) on GC substrates 69

4.1 Representative large-scale and high-resolution SEM images of nanostructured Pt/GC electrodes with different Pt surface coverages . . . 76
4.2 EDX spectra of the CL- and HCL-prepared nanostructured Pt/GC electrodes 78
4.3 TEM cross-section micrographs of the Pt/GC interface region on Pt/GC electrodes prepared via CL and HCL 80
4.4 BCVs recorded on different samples prepared via CL or HCL 82
4.5 CO_{ad} monolayer oxidation experiments recorded on nanostructured Pt/GC electrodes prepared via CL or HCL 85

4.6 Deconvolution of m/z = 44 mass spectrometric current signals recorded on CL-prepared, nanostructured Pt/GC electrodes during CO_{ad} monolayer oxidation 86

5.1 Large-scale and high-resolution SEM images of nanostructured Pt/GC model electrodes prepared by deposition of Pt-salt loaded micelles after different after-treatments 96

5.2 XP spectra of nanostructured Pt/GC model electrodes prepared by deposition of Pt-salt loaded micelles showing a survey and a detailed spectra of the Pt(4f) signal 97

5.3 BCVs of nanostructured Pt/GC model electrodes prepared by deposition of Pt-salt loaded micelles before and after electrochemical oxidation measurements 99

5.4 CO_{ad} monolayer oxidation current traces and subsequent BCVs on a micelle-based Pt/GC model catalyst, a CL-prepared nanostructured Pt/GC model catalyst and a polycrystalline Pt electrode 101

5.5 Potentiodynamic CO bulk electro-oxidation on a micelle-based Pt/GC model catalyst, a CL-prepared nanostructured Pt/GC model catalyst and a polycrystalline Pt electrode 103

5.6 Potentiostatic electro-oxidation of CO on a micelle-based Pt/GC model catalyst, a CL-prepared nanostructured Pt/GC model catalyst and a polycrystalline Pt electrode 105

6.1 Schematic description of the „desorption – re-adsorption – reaction“ process on (a) a polycrystalline Pt electrode and (b) a nanostructured Pt/GC model electrode 113

6.2 SEM images of the HCL-prepared nanostructured Pt/GC model electrodes 116

6.3 BCVs recorded on a polycrystalline Pt electrode and on nanostructured Pt/GC model electrodes 117

6.4 ORR activity and the corresponding hydrogen peroxide yields simultaneously monitored in the double-disk thin-layer flow-cell over a polycrystalline Pt electrode, on nanostructured Pt/GC model electrodes with different Pt surface coverages and on a blank GC substrate at different electrolyte flow rates 118

6.5 Linear dependence of the mass transport limited ORR current vs. the cube root of the electrolyte flow rate 119

6.6 Tafel plots for (a) geometric and (b) active surface area normalized kinetic oxygen reduction current over polycrystalline Pt electrode and nanostructured Pt/GC model electrodes 121
6.7 Hierarchy of model studies and simulations on transport effects in electrocatalytic reactions on structurally well-defined nanostructured model electrodes (arrays of ultramicroelectrodes) under defined transport conditions in a realistic cell geometry. 126

7.1 SEM images of the nanostructured Pt/GC model electrodes fabricated by HCL 136
7.2 BCVs recorded on a polycrystalline Pt electrode and nanostructured Pt/GC electrodes 136
7.3 Potentiodynamic electro-oxidation of methanol over a polycrystalline Pt electrode and nanostructured Pt/GC model electrodes at different flow rates 139
7.4 Potentiostatic electro-oxidation of methanol at 0.66 V over a polycrystalline Pt electrode and nanostructured Pt/GC model electrodes at different flow rates 142
7.5 Potentiostatic electro-oxidation of methanol at 0.76 V over a polycrystalline Pt electrode and nanostructured Pt/GC model electrodes at different flow rates 145
7.6 CO_2 current efficiencies during continuous potentiostatic electro-oxidation of methanol over a polycrystalline Pt electrode and nanostructured Pt/GC model electrodes at different potentials and different flow rates 146
7.7 Turnover frequencies (TOF) for methanol molecule oxidation to CO_2 on a polycrystalline Pt electrode and nanostructured Pt/GC electrodes at different potentials and flow rates 148

List of Tables

3.1 Atomic ratio of the surface element found in the XPS survey spectra on the GC substrates after different pretreatments 57
3.2 Atomic ratio of the carbon surface species found in the C(1s) detail spectra after different pretreatments on the GC substrates 57
3.3 H_{upd}-charges and resulting active surface areas on samples with different pretreatments and Pt deposition methods 66

4.1 Geometrical data of the different nanostructured Pt/GC electrodes as determined by SEM 75
4.2 Atomic ratio of the elements determined from the EDX spectra on CL- and HCL-fabricated Pt/GC electrodes 79
4.3 Compilation of the active Pt surface areas determined by H_{upd}-charge and the geometric Pt surface areas resulting from the SEM-based nanodisk/nanoparticle densities and sizes on nanostructured Pt/GC electrodes prepared via CL and HCL 83
4.4 Peak positions and peak intensity ratios determined by deconvolution of the m/z = 44 mass spectrometric current densities, and the geometric Pt surface areas related to Pt nanodisks/nanoparticles on the different nanostructured Pt/GC electrodes prepared either by CL or by HCL as described in Table 4.1 87

7.1 SEM and electrochemical characterization of the polycrystalline Pt electrode and the nanostructured Pt/GC electrodes prepared by HCL 137
7.2 Comparison of CO_2 current efficiencies on polycrystalline Pt bulk electrodes from literature [5] 151

Abbreviations

AFM	Atomic Force Microscopy
BCV	Base Cyclic Voltammetry
BSE	Backscattered Electrons
CL	Colloidal Lithography
DEMS	Differential Electrochemical Mass Spectrometry
DMFC	Direct Methanol Fuel Cell
EDX	Energy Dispersive X-Ray Analysis
GC	Glassy Carbon
HCL	Hole-mask Colloidal Lithography
MOR	Methanol Oxidation Reaction
MS	Mass Spectrometry
ORR	Oxygen Reduction Reaction
pc Pt	polycrystalline Platinum (electrode)
PE	Primary Electrons
PEMFC	Polymer-Electrolyte-Membrane Fuel Cell
SE	Secondary Electrons
SEM	Scanning Electron Microscopy
TEM	Transmission Electron Microscopy
TLFC	Thin-Layer Flow Cell
TOF	Turnover Frequency
XPS	X-ray Photoelectron Spectroscopy

1 Introduction

1.1 Departure to a new „Energy Age“

„Das Wasser ist die Kohle der Zukunft.
Die Energie von morgen ist Wasser, das durch elektrischen Strom zerlegt worden ist.
Die so zerlegten Elemente des Wassers, Wasserstoff und Sauerstoff, werden auf
unabsehbare Zeit hinaus die Energieversorgung der Erde sichern.“
Jules Verne aus *Die geheimnisvolle Insel* (1870)

Nowadays, there are two conflicting trends regarding the energy supply for the mankind: Whereas the world energy consumption increases continuously, the main energy providers are fossil fuels such as petroleum, coal and natural gas.

The supply of fossil fuels is finite [6–8]. For the nearest future there is a urgent need to rethink about energy supplies. Special focus lies on the transition from fossil fuels to so-called renewable energy sources like solar, wind or biomass [9, 10].

As mentioned by *Jules Verne* in 1870, the idea of using hydrogen as a primary form of energy is beginning to move from the pages of science fiction into the speeches of industry executives and politicans [9] („Greenery, innovation, and market forces are shaping the future of our industry and propelling us inexorably toward hydrogen energy.“ [11]). Later, Crabtree et al. [12] proposed the so-called „hydrogen society“: Hydrogen will be generated from the renewable energy sources and be used as energy carrier. An ideal system for gaining the stored chemical energy from hydrogen are fuel cells [12], which allow to directly convert chemical to electrical energy and heat at a high efficiency and without formation of harmful or poluting species.

The principle of fuel cells is simple and known already for more than one century. The technical demands on fuel cells however are high: the overall conversion of fuel and oxidant should be fast and efficient even at low temperatures, the catalyst and membrane materials should be stable under most caustic conditions and everything at a customer-friendly, economically, reasonable price.

The major task for academic and applied research today is to strengthen the activities to meet these challenges in moving towards commercialization of fuel cell technology to allow the vision of *Jules Verne* to become true some day! For instance, one *ansatz* may be the improvement of fuel cell catalysts/electrodes with respect to their activity, selectivity and stability.

In this thesis, the stability and electrocatalytic properties of model electrodes as simplified and well-defined 2D model versions of realistic fuel cell electrodes, which are rather complex networks, were systematically investigated. The outcome of this work leads to a deeper understanding of transport processes influencing the activity and selectivity of electrocatalytic reactions, which is important for the rational further development of (direct oxidation) fuel cell technology.

1.2 Fuel Cells – Alternative Energy Sources

Fuel cells are by definition galvanic cells, which directly convert chemical energy from continuously fed fuels and oxidants into electrical energy. The cell operates as long as fuel is supplied. It is not possible to store energy in fuel cells, the system operates as an energy converter.

In general, fuel cells are comprised of two electrodes (anode and cathode), separated by a semi-permeable membrane, which is conductive for ions such as H^+, OH^-, CO_3^{-2}, O^{2-} etc. depending on the type of fuel cell . The electrodes are interconnected via an external circuit with an interposed consumer load. A principle sketch of a so-called polymer-electrolyte-membrane fuel cell (PEMFC) is given in Fig. 1.1.

The predecessor of the todays PEMFC (fuel: H_2, oxidant: O_2) was already introduced in the 19^{th} century by Sir William Grove (1839), based on the ideas of Christian Friedrich Schönbein (1838). Both are considered as the „fathers“ of the fuel cell today. Their experiments consisted of little Pt-rod pairs dowsed into sulfuric acid, which were flowed with hydrogen and oxygen gas, respectively. However, since current and voltage were too low, the fuel cell prototype could not compete against the inventation of the electrical generator/dynamo by Werner von Siemens at that time. Nearly 100 years later, in 1955, Willard Thomas Grubb, a chemist working for General Electric (GE), improved the previous fuel cell design by introducing a sulfonated polystyrene ion-exchange membrane as electrolyte. Leonard Niedrach, also chemist at GE, developed a procedure for depositing platinum onto the ion-exchange membrane, which is required to catalyze the hydrogen oxidation at the anode and the oxygen reduction at the cathode. This fuel cell set-up became known as the so-called „Grubb-Niedrach fuel cell“ [13]. At this step of development, GE went on to develop this technology together with NASA and McDonnell Aircraft. This resulted in the first commercial use of a fuel cell within the *Gemini Project*. About 20 to 30 years ago, during the 1980s and 1990s, the membrane was exchanged by sulfonated tetrafluoroethylene based on a fluoropolymer-copolymer and Nafion containing PEMFCs were introduced [14]. The fuel cell power density and the lifetime were significantly increased due to the new membranes. Furthermore, nanoparticles supported on porous carbon material were introduced as catalysts.

Other possible fuels for a low-temperature PEM fuel cell type are short-chain alcohols. Using liquid fuels such as diluted methanol (Direct Methanol Fuel Cell – DMFC) or ethanol solutions instead of high-purity hydrogen gas offers practical advantages such as size, weight and reduction of costs for the purification of hydrogen gas. Furthermore, a liquid fuel has a higher energy density and is easier to handle

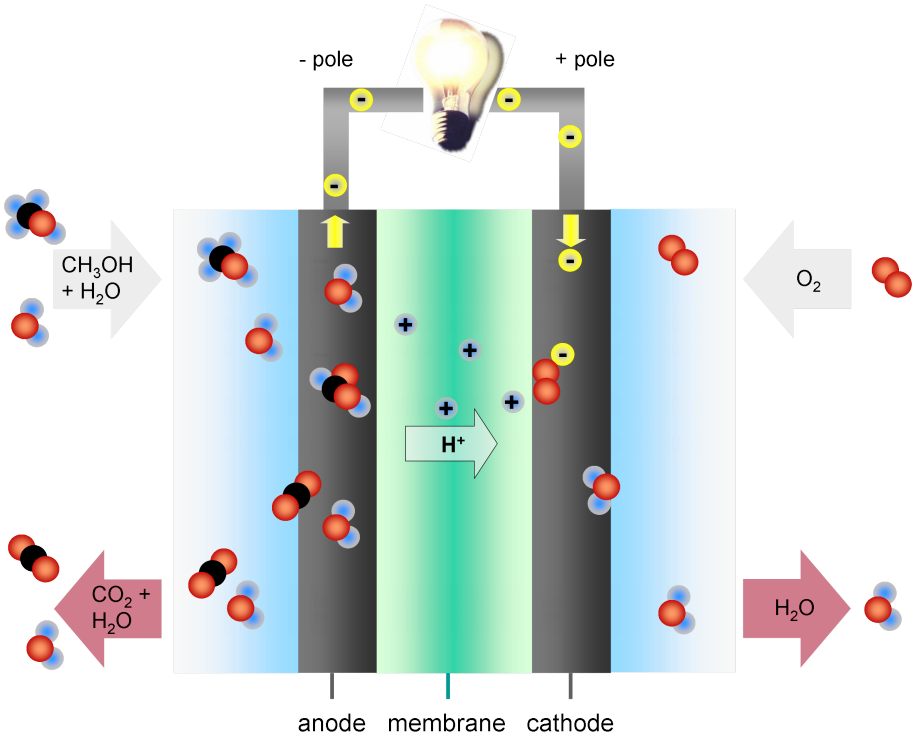

Figure 1.1: Schematic representation of a direct methanol fuel cell, representing the PEM fuel cell type. At the anode, a diluted methanol (CH_3OH) solution reaches the catalyst layer at the electrode surface. The catalyst facilitates the dissociation and oxidation of methanol and water (H_2O) to CO_2. (Six electrons and protons (H^+) are formed by the complete conversion of one methanol molecule to CO_2). While the generated electrons pass from the anode through an external circuit, where a device is interconnected to the cathode, the protons formed during several reaction steps are passed via the membrane to the cathode, where oxygen (O_2) is reduced to water.

for transport and storage.

Figure 1.1 schematically illustrates how a DMFC is working: The fuel, e.g., diluted methanol solution, reaches the catalyst layer of the anode. Methanol and water are adsorbed on the catalyst nanoparticles which are supported on high surface area carbon material (see also Fig. 1.2 a and b). Due to the (electro-)chemical reaction at the catalyst, protons and electrons are released until the CH_3OH molecule is converted and completely oxidised to the final product CO_2. Protons are transported across the membrane to the cathode, where oxygen (O_2) is reduced to water. Electrons are transported through an external circuit from the electron source (anode) to the electron sink (cathode), providing power to connected devices. Whereas water is consumed at the anode, it is produced at the cathode side (see Fig. 1.1).

The half-cell and total reactions are:

Anode:	$2\ CH_3OH + 2\ H_2O$	$\rightarrow$	$2\ CO_2 + 12\ H^+ + 12\ e^-$
Cathode:	$3\ O_2 + 12\ H^+ + 12\ e^-$	$\rightarrow$	$6\ H_2O$
Total:	$\mathbf{2\ CH_3OH + 3\ O_2}$	$\rightarrow$	$\mathbf{2\ CO_2 + 4\ H_2O}$

Regarding the number of released electrons per CH_3OH molecule, it is essential to note, that the overall efficiency and the power output of a DMFC depends sensitively on the complete conversion of methanol to CO_2. The methanol oxidation reaction (MOR) has been studied extensively since almost 30 years, both due to its application in DMFCs and from fundamental aspects. Excellent reviews are given, e.g., in refs. [15–20]. Therefore, it is well known that the MOR results in three different products, the complete oxidation product CO_2 and the incomplete oxidation products HCHO and HCOOH (see, e.g., refs. [20–24] and references therein), and that the reaction proceeds via a complex reaction network involving a number of adsorbed or desorbable reaction intermediates, as described first by Bagotzky et al. [2]. It was shown for Pt and Pt catalyst electrodes, that the MOR product yields depend strongly on experimental conditions, e.g., the catalyst loading [25].

At present, standard DMFCs contain relatively high amounts of catalyst leading to complete oxidation of methanol to CO_2 [26–28], in particular at elevated temperatures [29, 30]. However, this may be different in future applications. With the further reduction of the amount of anode catalyst for lower costs for costumers, one may reach a level where this is limited by increasing emission of incomplete (and toxic) oxidation products at the exhaust of the fuel cell. As it was shown by Jusys et al. [25] for the methanol oxidation on thin-film carbon-supported Pt (Pt/C) catalyst electrodes under enforced electrolyte flow, the product distribution changes significantly upon varying the catalyst loading at otherwise constant reaction conditions, from predominantly formaldehyde production at low catalyst loadings to increasingly higher yields of CO_2 (and hence lower formaldehyde yields) at higher catalyst loadings [25]. This will become even more relevant in the development of micro-DMFCs for portable applications, with their low absolute amount of catalyst and low methanol consumption.

Similar results were obtained for the oxygen reduction reaction (ORR, reaction at the PEMFCs cathodes). Earlier studies demonstrated that this leads also to H_2O_2 formation [31–34] in addition to the desired product, namely H_2O. This reaction product, H_2O_2, maybe further reduced to water [35–38]. On massive Pt and on

carbon-supported Pt/C catalyst electrodes, the ORR showed essentially no difference in the selectivity in terms of the resulting product distribution (ratio of H_2O and H_2O_2) [4, 39–42]. The particle separation in Pt/C catalysts was made responsible for changes in the catalyst activity [43], but selectivity effects were not discussed. Recently, Inaba et al. reported an increasing hydrogen peroxide production with decreasing Pt/C catalyst loading (below $10\,\mu g\,cm^{-2}$) in ORR measurements on thin-film catalyst electrodes on a glassy carbon support [44]. It is of high relevance to note that these observations also have consequences for practical applications of a PEMFC cathode. They clearly point out that with decreasing catalyst loading, which is strived for from economical reasons, there is an increasing risk of H_2O_2 production on the cathode catalyst even under typical cathode reaction conditions, which may have disastrous consequences on the lifetime of electrode or membrane due to corrosion effects [45, 46].

1.3 From Real Catalysts to Model Electrodes

Realistic fuel cell electrodes are considered as three dimensional (3D) networks of Pt nanoparticles which are deposited on high surface area carbon supports as schematically presented in Fig. 1.2 a. By providing a high surface area material effects, such as particle agglomeration or sintering, can be diminished. Furthermore, high surface area materials offer the possibility to reach a high conversion on a realitvely small projected geometric area. A magnified schematic representation of the crucial phase boundary, where the electrochemical reaction occurs is shown in Fig. 1.2 b.

To study electrocatalytic reactions such as the MOR or ORR, which involve several reaction steps, in more detail, including mass transport effects on the activity and selectivity, elementary mechanism and kinetics of electrocatalytic reactions, model electrodes are required. Model electrodes with a simplified and well-defined surface morphology sufficiently replace these rather complex 3D realistic catalysts, where additional vertical mass transport within the catalyst bed has to be included and particle separations can only be approximated. The new information obtained can help to understand and also to improve existing real systems.

A principle sketch of a model electrode used in this work is shown in Fig. 1.2 c. The presented nanostructured Pt/glassy carbon (GC) electrode consists of electrochemically active Pt nanostructures deposited on a planar, inert glassy carbon substrate. It can be described as taking a thin slice of a real 3D electrode to form a planar model electrode in two dimensions (2D) [47] and hence creates new possibilities to study mass transport effects in electrocatalytic reactions systematically. Because of their well-defined and rather regular arrangement, these electrodes are ideally

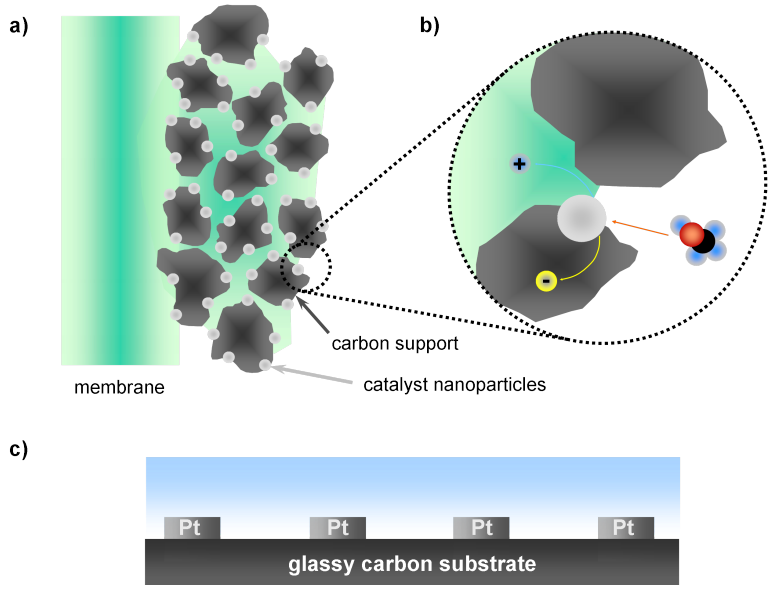

Figure 1.2: Schematic illustration of a real catalyst and a Pt/glassy carbon model electrode. (a) The catalyst layer of a PEM fuel cell is formed by a layer of carbon-supported catalyst nanoparticles (1–5 nm) deposited on a (Nafion) polymer electrolyte membrane. (b) Magnification of the so-called *three phase boundary* (TPB), where the (electro-)chemical reaction takes place. (c) Nanostructured Pt/glassy carbon model electrode representing a vertical two-dimensional cross-section through a three-dimensional network of Pt nanoparticles in a real catalyst layer.

suited for model studies of lateral transport effects, e.g., by investigating the change in reaction characteristics upon varying the density and/or size of the nanodisks or the electrolyte flow rate. From the same structural reasons, they are particularly attractive as (experimental) model system for quantitative comparison with simulations of the contributing transport and reaction processes. The latter would be very close to the simulations of diffusion processes to arrays of ultra-microelectrodes in a flow cell situation reported previously (see, e.g., [48–51]), complemented by lateral transport processes between the microelectrodes and by the surface reactions.

Model studies of catalytic and electrocatalytic reactions, performed on structurally and chemically well-defined, but nevertheless more realistic systems than, e.g., polycrystalline or single-crystal (electrode) surfaces and under close-to-realistic reaction conditions (e.g., pressure, temperature, particle-support interactions), have attracted increasing interest in recent years [52–55].

The aim of my work was to gain a deeper insight into electrocatalytic reactions and transport processes, in particular in fuel cell relevant reactions. A special focus was the correlation between the electrode morphology and the reaction activity

and selectivity. These aimes were followed by making use of new developments in the area of surface nanostructuring [56–64], Colloidal Lithography (CL) [47, 60–63, 65], Hole-mask Colloidal Lithography (HCL) [64] and the approach of „micellar techniques“ [66, 67] (see section 2.1 in *chapter* 2), which were applied for the controlled preparation of planar nanostructured Pt/GC model electrodes with defined particle sizes and particle distances. In addition to the narrow size distribution, the nanodisks/nanoparticles are arranged in a rather regular array with a narrow distribution of interparticle separations, which uniformly covers the entire accessible electrode area. The fabricated nanostructured Pt/GC model electrodes used in this work were investigated by surface sensitive characterization techniques such as SEM, TEM and AFM for physical characterization of the surface morphology and EDX and XPS for identifying the chemical composition of the electrode (see section 2.2 in *chapter* 2). The physically characterized nanostructured Pt/GC model electrodes were electrochemically characterized additionally and used for studying fuel cell relevant electrocatalytic reactions (see section 2.3 in *chapter* 2).

1.4 Mass Transport and Re-Adsorption Effects in Electrocatalytic Reactions

Mass transport processes, including the transport of reactants to and of reaction intermediates or products away from the electrode, can play an important role in electrocatalytic reactions, in addition to the chemical and electrochemical properties of the respective catalyst or electrode material. For instance, it is well known that in many electrocatalytic reactions, the reaction rate is limited by the transport of reactants to the electrode, resulting in a „mass transport limited current“ [68–72] (see Fig. 1.4 1^{st} panel). Less well known is that transport effects may alter also the overall behavior of the reaction, in particular its selectivity and hence the product distribution in reactions leading to more than one product. In *Heterogeneous Catalysis*, it is established that for decreasing space velocity the product distribution moves towards that expected for thermodynamic equilibrium in such reactions [73], and similar trends are expected also in *Electrocatalysis*.

Catalytic processes in *Heterogeneous Catalysis* consist of several important steps, namely *(i)* transport of the reactant(s) to the surface, *(ii)* (dissociative) adsorption on the surface, *(iii)* reaction with neighbouring adsorbed species, *(iv)* desorption of the product(s) and *(v)* off-transport away from the surface (see also Fig. 1.4 1^{st} panel). However, the crucial difference between a heterogeneous reaction, e.g., at the solid-vacuum interface and an electrocatalytic reaction at the solid-liquid interface

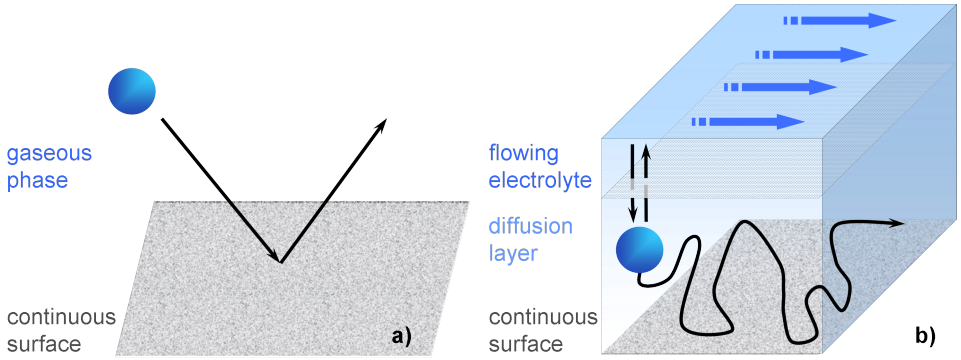

Figure 1.3: Schematic illustration of the motion of reactand molecules towards a surface: (a) *Surface Science*: reaction at the interface solid-vacuum (ultrahigh vacuum conditions) leads to a single-hit reaction and (b) *Electrocatalysis*: reaction at the interface electrode/electrolyte. The motion of a reactant is describable by Brownian motion. Several hits of the surface are possible as long as the reactant molecule remains in the diffusion layer above the electrode surface (the thickness of the diffusion layer depends on the electrolyte flow rate [74, 75]).

is that under high vacuum conditions mainly single-hit reactions occur (Fig. 1.3 a), whereas the motion of a reactant in the electrolyte (or respectively at high pressures in the gas phase at the solid-gas interface in *Heterogeneous Catalysis*) is describable by Brownian motion (Fig. 1.3 b). Several hits of the surface occur as long as the reactant molecule remains in the diffusion layer above the electrode surface. The thickness of the diffusion layer and hence the residence time of a reactant in the near surface reagion, will depend on the electrolyte flow rate [74, 75].

If one wants to study mass transport effects upon electrocatalytic reactions (liquid phase environment) by changing the electrode morphology in terms of varying particle sizes, inter-particles distances or the electrolyte flow rate on the reaction kinetics by means of the catalytic activity or the resulting product distribution (selectivity), one should at first consider how an (electro-)catalytic reaction proceeds in detail:

As schematically depicted in Fig. 1.4, an electrocatalytic reaction starts with the transport of a reactant to the electrode surface, where it is adsorbed; after the surface reaction, the product desorbs and is transported away from the electrode surface. In the *1st panel* of Fig. 1.4, an electrocatalytic reaction with only a single reaction product, e.g., the oxidation of H_2 to 2 H^+ in an electrolyte, is considered. Obviously, the kinetics of the total reaction can be affected by mass transport effects, by limiting the reactant supply or the off-transport of products, leading to purely „mass transport limited“ reaction.

In mixed kinetically and transport limited reactions such as the oxygen reduction reaction (ORR), the coverage of adsorbed reactants under steady-state conditions is

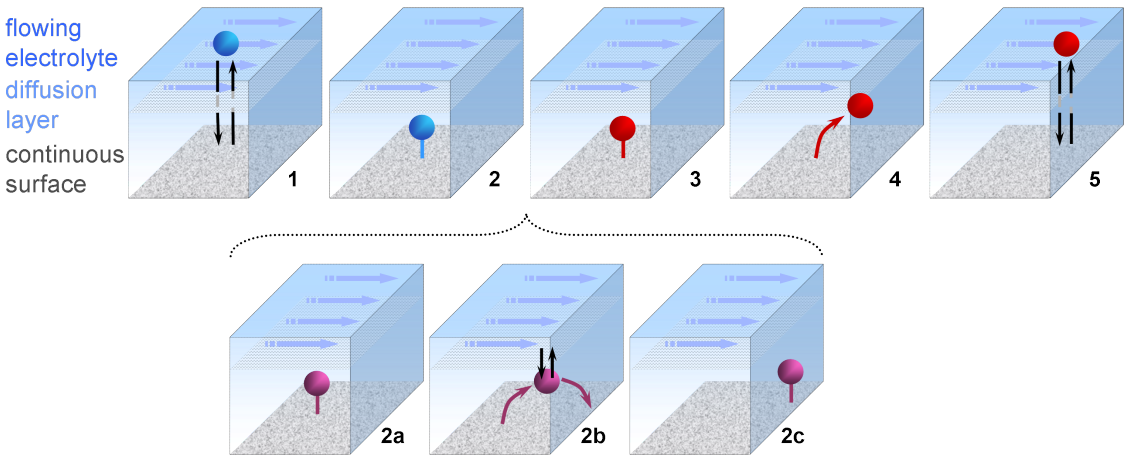

Figure 1.4: Schematic description of the proceeding elementary reaction steps involved in an (electro-)catalytic reaction. *1st panel*: Reaction with one possible product, e.g., oxidation of H_2 to 2 H^+ in an electrolyte. (1) Transport of the reactants (blue) from the flowing electrolyte via the diffusion layer to the electrode surface, (2) adsorption of the reactant at the electrode surface, (3) surface reaction of the reactant to the reaction product (red), (4) desoprtion of the reaction product into the stagnant diffusion layer and (5) transport of the reaction products away from the electrode, via the diffusion layer into the flowing electrolyte. *2nd panel*: Reaction with soluable, reactive reaction intermediate(s), e.g., reduction of oxygen to water and H_2O_2 as reaction intermediate. (1–5) as above, however after (2) adsorption of the reactant at the electrode surface, (2a) surface reaction of the reactant to a reaction intermediate (purple) occurs, (2b) desorption of the reaction intermediate, which remains in the diffusion layer above the electrode surface (or leaves the diffusion layer) and (2c) re-adsorbs at another active side. Subsequently, the sequences continues in the *1st* panel with step (3).

changed by the reduced supply of reactants to the surface. Furthermore, insufficient removal of products from the surface and/or near surface region, may also affect the kinetics of the surface reaction. The situation becomes more complicated if soluable, reactive reaction intermediates, for instance, in the case of the oxygen reduction reaction H_2O_2 is involved. As presented in the *2nd panel* of Fig. 1.4, the formed reaction intermediate (Fig. 1.4: 2a) not only remains adsorbed on the catalyst surface and reacts further, but desorbs into the stagnant diffusion layer above the electrode surface (Fig. 1.4: 2b). If so, the reaction intermediate has two options: *(i)* either leaving the diffusion layer into the flowing electrolyte and being off-transported or *(ii)* a possible re-adsorption and further reaction of the reaction intermediate to the final reaction product (Fig. 1.4: 2c) occurs.

In the general case discussed above, (electro-)catalytic reactions involve several elementary reaction steps, which may occur sequentially and/or in parallel and thus

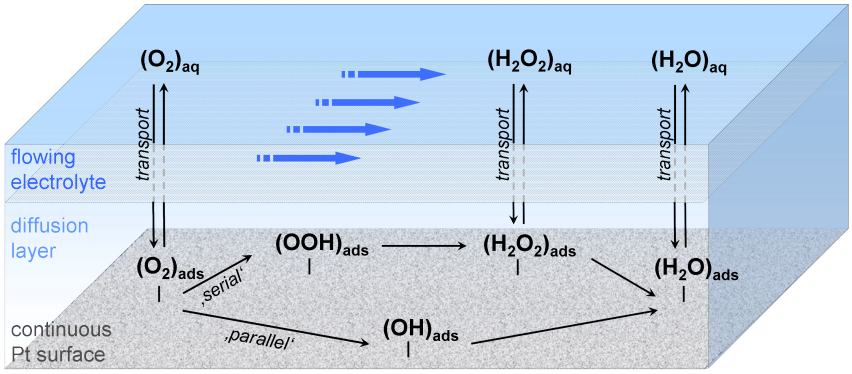

Figure 1.5: Simplified reaction scheme of the oxygen reduction reaction on a continuous Pt electrode as proposed by Damjanovic et al. [1] in a bird´s eye view representation. The flowing electrolyte and stagnant diffusion layer above the Pt surface are shown, demonstrating the vertical transport of an incoming reactant O_2 molecule and formed intermediate species, e.g., hydrogen peroxide (H_2O_2), to/away from the electrode surface. (Note: The arrows parallel to the Pt surface represent the possible reaction paths, they neither describe the motion nor reflect distances of/between the adsorbed species across the electrode surface.)

create complicated reaction networks. As examples for such complicated reaction networks, the reaction schemes of the already introduced half-cell reactions of a DMFC, the rather „simple“ oxygen reduction (two possible products: H_2O and H_2O_2) and the more „complex“ methanol oxidation (three possible products: HCHO, HCOOH and CO_2) will be described in more detail.

Oxygen Reduction Reaction – ORR

Mechanistic proposals about the oxygen reduction reaction is continuously discussed in literature starting from Frumkin [77] and Damjanovic [1] 50 years ago, coming to numerous publications in the end of the last century [31–34, 78, 79], ending up with very recent results of DFT-calculations [80–82]. A simplified, general reaction scheme for the ORR over a planar Pt electrode based on Damjanovic et al. [1] and Wroblowa et al. [78] proposals is given in Fig. 1.5 including arrows where transport may affect the reaction rate/selectivity. According to their incitations, oxygen is either reduced via a *parallel mechanism* [1] (Fig. 1.5 reaction branch in the foreground) or proceeds in a *serial process* [1] (Fig. 1.5 reaction branch in the background). The existence of one reaction branch does not rule out that of the other one. (Note: The arrows parallel to the Pt surface represent the possible reaction paths, they neither describe the motion nor reflect distances of/between the adsorbed species across the electrode surface.) Despite the apparent simplicity, the ORR represents an electrocatalytic network involving several elementary steps. Whereas the *direct mechanism* (parallel) is commonly described as „four-electron pathway“, the term

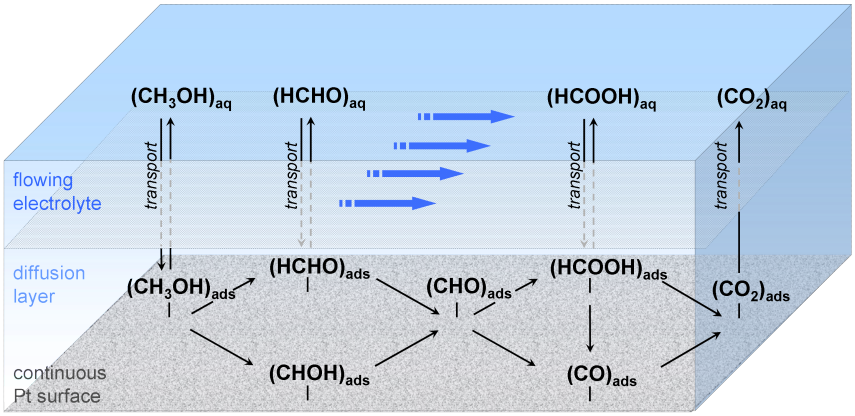

Figure 1.6: Reaction scheme describing the oxidation of methanol on a continuous Pt electrode after Bagotzky et al. [2] or recently Lamy et al. [76] in a bird´s eye view representation. The flowing electrolyte and stagnant diffusion layer above the Pt surface are shown, demonstrating the vertical transport of an incoming reactant CH_3OH molecule, of the resulting reaction side products, e.g., formaldehyde (HCHO), formic acid (HCOOH) and adsorbed CO to/away from the electrode surface. (Note: The arrows parallel to the Pt surface represent the possible reaction paths, they neither describe the motion nor reflect distances of/between the adsorbed species across the electrode surface.)

„two-electron pathway“ is used for the *two-step process* (serial) [31–34, 77, 79].

The H_2O_2 formation [31–34] and furthermore the H_2O_2 reduction to water [35–38] have been detected and quantified on various catalysts. However, there is only little information available about the ratio of the two possible reaction pathways in terms of the resulting product distribution (ratio of H_2O and H_2O_2) in the process of the ORR.

Methanol Oxidation Reaction – MOR

A more complex reaction scheme is given in Fig. 1.6, demonstrating schematically the possible (sequential and parallel) reaction pathways of the methanol oxidation to CO_2 based on the early work from Bagotzky et al. [2] and a recent review by Lamy et al. [76]. The scheme denotes where transport may affect the reaction rate/selectivity. (Note: The arrows parallel to the Pt surface represent the possible reaction paths, they neither describe the motion nor reflect distances of/between the adsorbed species across the electrode surface.) For more details about the contributing partial reactions the reader is referred to [20, 83, 84]. As already briefly mentioned above, the electro-oxidation of methanol results in three different products, namely CO_2 (complete oxidation) as well as HCOOH and HCHO (incomplete oxidation) products (see, e.g., [20–25, 85–88] and references therein).

It was found that the ratio of the different reaction products, or more precisely the MOR selectivity, strongly depend on the experimental conditions such as the concen-

tration of the methanol solution [5, 23, 89], the flow rate of the fuel [5] or the reaction temperature [29, 30] as well as on the type of electrode or catalyst, for instance the catalyst loading [25, 86, 89] or the composition of the catalyst [85, 87, 89–93], used. Among the many results it should be noted that increased formation of reaction side products on smooth Pt electrodes under enhanced mass transport conditions [5, 23, 89, 94] is observed, whereas complete conversion of methanol to CO_2 was reported on high-surface-area platinized Pt electrodes [85–87, 95, 96]. Therefore the question arises, whether the MOR selectivity is affected by the design of the electrode or enhanced mass transport conditions.

Mass Transport (Diffusion Fronts) over nanostructured Pt/GC Model Electrodes

It was already denoted, that transport of reactants to the electrode may affect the measured reaction rate by putting an upper limit on the rate, which results in the formation of a transport limited current (or „limiting current“) [68–72]. The transport of a reactant to the electrode surface is indicated by the vertical arrows in Fig. 1.4. The arrows represent the motion of an incoming reactant or a leaving reaction product from the stagnant diffusion layer into the flowing electrolyte and vice versa in Fig. 1.4 *1st* panel. Prominent examples of „mass transport limited“ reactions are the hydrogen oxidation or the continuous CO bulk oxidation (at higher potentials). For these rather „simple“ reactions with only one possible product like H^+/water or CO_2, respectively, the diffusion front of reactants to the electrode surface can be described as follows:

Identical mass transport limited currents for the continuous electro-oxidation of CO (at higher potentials) are obtained over a planar Pt film electrode and nanostructured Pt/GC electrodes with Pt coverages down to a critical value (samples with less than 20 % of the surface covered by Pt nanostructures) [97]. By this observation, it is indicated that for these electrodes the reactant transport to the array of Pt nanostructures can essentially be described by „planar diffusion“.

Similar to a continuous Pt surface (see Fig. 1.7 a) the transport of reactants proceeds by „vertical diffusion“ through the stagnant diffusion layer. This means that, if the density of the Pt nanostructures is high enough that all arriving molecules reaching the electrode surface are consumed (see Fig. 1.7 b). The diffusion of reactant molecules to the electrode surface can still be described by a one dimensional (1D) diffusion transport to a planar Pt surface, despite the distortion of the diffusion pattern close to the individual nanostructures (see Fig. 1.7 b). Decreasing Pt coverages, by means of increasing separation of the individual Pt nanostructures, result in increasing contributions of „hemispherical diffusion“ (see diffusion pattern

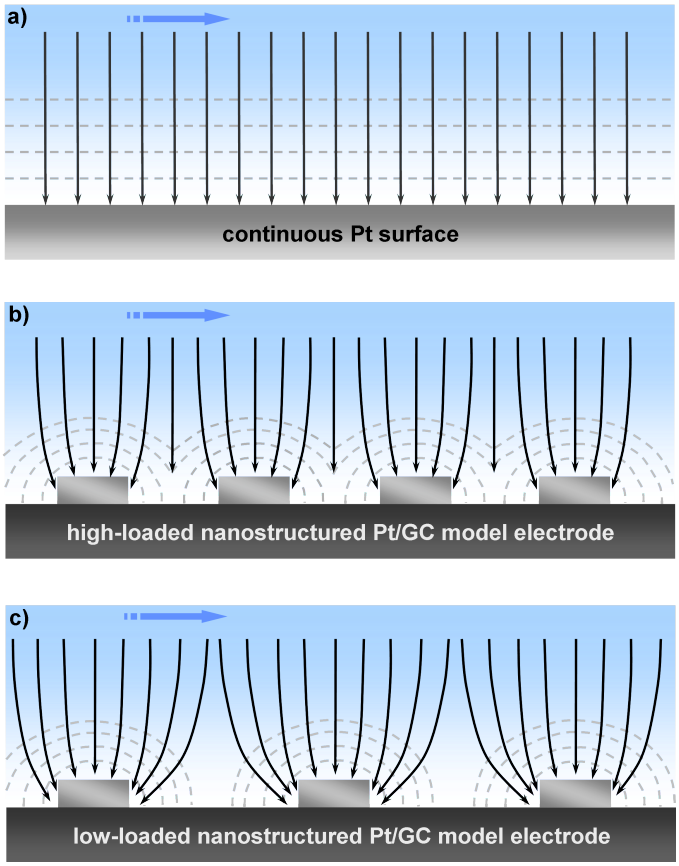

Figure 1.7: Schematic description of the diffusion front in a mass transport limited reaction (e.g., H_2 oxidation, continuous CO bulk oxidation at higher potentials) over (a) a planar continuous Pt electrode („planar diffusion“), (b) a nanostructured Pt/GC electrode with high Pt surface coverage, (contributions from „hemispherical diffusion“ close to the nanostructures and transformation at the periphery to almost „planar diffusion“), and (c) a nanostructured Pt/GC electrode with low Pt surface coverage, („hemispherical diffusion“). Dotted lines: lines of constant reactant concentration.

in Fig. 1.7 c). This was indicated by lower mass transport limited currents for electrodes with lower Pt coverage [97].

„DESORPTION – RE-ADSORPTION – REACTION“ CONCEPT

It was already noted above that mass transport effects not only influence the overall reaction rate, but also the selectivity:

As indicated by the arrows representing the motion of a formed reaction intermediate from the stagnant diffusion layer into the flowing electrolyte and vice versa (see Figs. 1.4 b, 1.5, 1.6), additional off-transport of incomplete reaction intermediates occurs and may change the resulting product distribution.

This latter off-transport is accounted in the recently introduced „desorption – re-

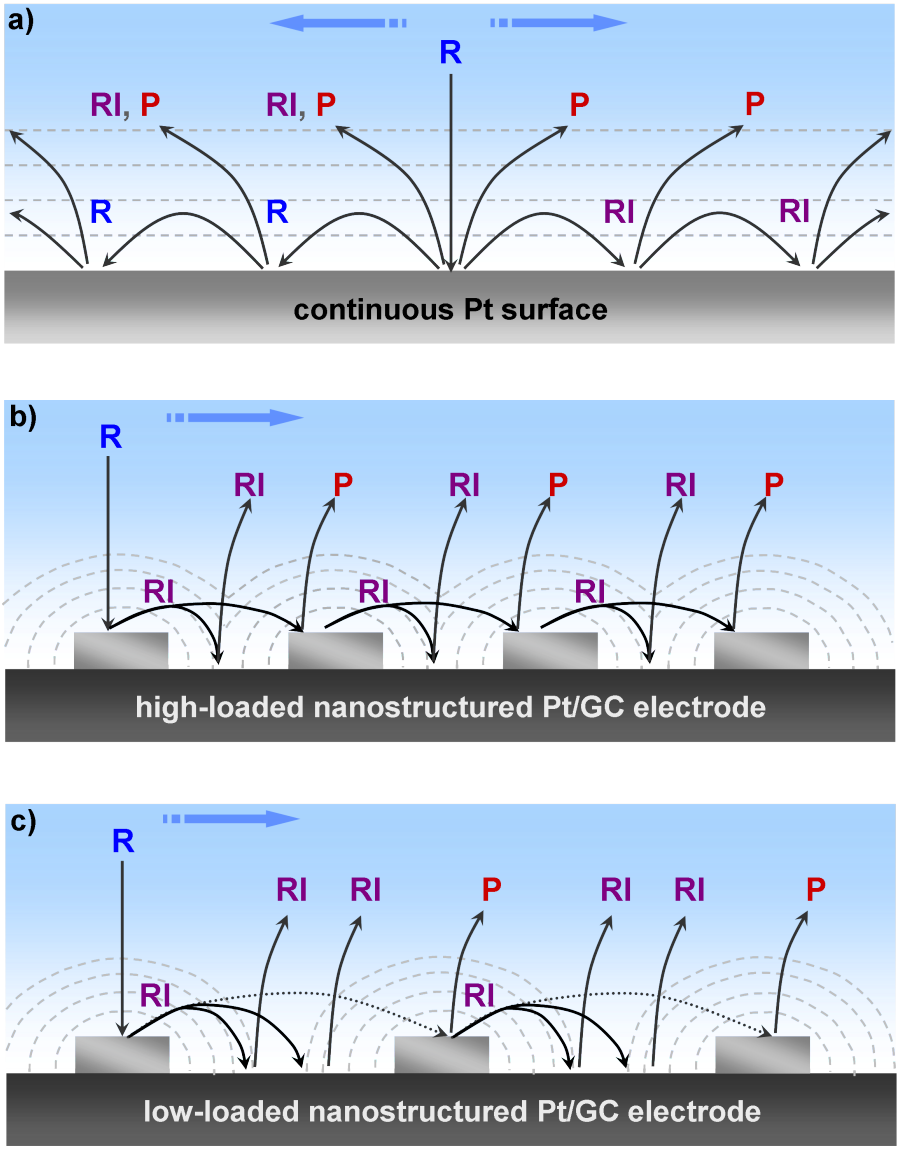

Figure 1.8: Schematic description of the desorption, diffusion, re-adsorption and reaction processes contributing to an electrocatalytic reaction which includes reaction pathways where volatile, reactive reaction intermediates are formed (desorption – re-adsorption – reaction process) on (a) a continuous Pt electrode („planar diffusion“) and on nanostructured Pt/GC model electrodes with (b) high Pt surface coverage (contributions from „hemispherical diffusion“ close to the nanostructures and transformation at the periphery to almost „planar diffusion“) and (c) low Pt surface coverage („hemispherical diffusion“). *Dotted lines:* lines of constant reactant concentration. **R**: reactant molecule arriving at the electrode surface, **RI**: reaction intermediate, **P**: product. The figure illustrates the multiple desorption, re-adsorption and further reaction of the reactant **R** or the reaction intermediate **RI** to reaction intermediate **RI** or product **P**, respectively, before the final off-transport of the respective species through the diffusion layer into the flowing electrolyte.

adsorption – reaction" concept (see *chapter* 6 and refs. [97–100]), which is schematically depicted in Fig. 1.8 a. According to this model, desorbable reaction intermediates formed on a catalytically active site can either further react on the surface to the final product (or another adsorbed reaction intermediate) or desorb into the stagnant diffusion layer. Subsequently, these desorbed species may either re-adsorb on the surface or eventually leave the diffusion layer into the flowing electrolyte and be removed from the reaction cell. If the reaction intermediate adsorbs again, it may again react or desorb, and this sequence may be repeated, until finally the reaction intermediate is either removed from the reaction cell or has reacted to another reaction intermediate or to the final product. In this picture, the chance for reacting to the final product will depend on the number of reaction attempts, and therefore on the number of re-adsorption events. The probability for re-adsorption and thus also for further reaction of the intermediates will depend not only on the number and distribution of active Pt sites, but also on the thickness of the diffusion layer and therefore on the electrolyte flow rate [74, 75].

Hence, the introduced nanostructured Pt/GC model electrodes offer an outstanding possibility for systematic studies of transport processes in electrolytic reactions. Because of their well-defined and rather regular structures, these electrodes are ideally suited for model studies on lateral transport effects, e.g., by investigating the change in reaction characteristics upon varying the density and/or size of the nanodisks or the electrolyte flow rate in electrocatalytic reactions such as the oxygen reduction reaction (reaction at a PEMFC cathode, *chapter* 6) or the methanol oxidation reaction (reaction at a DMFC anode, *chapter* 7).

1.5 Outline of the Thesis

In this thesis, nanostructured Pt/GC model electrodes were fabricated by Colloidal Lithography (CL), Hole-mask Colloidal Lithography (HCL) and „micellar techniques". Before the results of the stability and the electrocatalytic properties of these electrodes are presented and discussed, I will give a short overview about the different fabrication methods, the applied physical characterization techniques and the employed electrochemical instrumentation, evaluation methods and experimental details in *chapter* 2.

The stability of the nanostructured Pt/GC model electrodes prepared by CL (as representatives for the lithographic techniques) was investigated under enforced electrolyte flow and under continuous reaction conditions. For quantitative studies on the influence of transport and reaction parameters in electrocatalytic reactions, the electrodes have to be fully stable during the measurement. Therefore, a specific

plasma pre-treatment procedure was developed and sputter deposition rather than evaporation of Pt deposition method was employed. The results are presented in *chapter* 3.

In order to extend the parameter range in these model studies, the density of Pt nanodisks prepared by CL was reduced to very low values, with the Pt nanodisks covering about 1 % of the electrode surface. However, it was shown, that the electrochemical active Pt surface area (determined by H_{upd}-charge and CO_{ad} monolayer oxidation) is much higher than expected by comparison with higher coverage samples or than calculated from the density, size, and shape of the nanostructures derived from scanning electron microscopy images. In *chapter* 4, the origin of these deviations in the electrochemical behavior observed for nanostructured Pt/GC electrodes with very low densities of Pt nanodisks is elucidated, based on detailed electron microscopy studies and by comparing the electrochemical properties of the very low density Pt/GC electrodes with those of samples with higher densities of similar size Pt nanodisks prepared by CL. Furthermore, Hole-mask Colloidal Lithography (HCL) is introduced as the preferred method for the fabrication of nanostructured Pt/GC electrodes.

In *chapter* 5, an approach to prepare 2D model catalysts with smaller particles by the deposition of Pt-salt loaded reverse micelles on a glassy carbon substrate is introduced. The technique involves a sequential oxygen plasma and H_2 annealing treatment for removal of the polymer shell and reduction of the Pt-salt core. The potential of Pt-salt loaded micelles for synthesizing well-defined model electrodes for electrocatalytic studies was investigated by spectroscopic/microscopic and by electrochemical techniques. The data demonstrate the general viability of the micelle approach for electrocatalytic studies on these catalysts.

The following chapters present the results of detailed studies of mass transport processes in fuel cell relevant electrocatalytic reactions such as the ORR (reaction at a PEMFC cathode) and the MOR (reaction at a DMFC anode):

Chapter 6 illustrates and discusses mass transport effects in model studies of the ORR on nanostructured Pt/GC model electrodes, focusing on changes in the reaction characteristics (activity, selectivity) due to variations in the Pt nanodisk density and/or in the electrolyte flow rate. The nanostructured electrodes were prepared by HCL. Together with a polycrystalline Pt and a Pt-free GC electrode as reference, effects of varying the Pt nanodisk density and the electrolyte flow on the ORR reaction characteristics were investigated. Based on the presented findings, the „desorption – re-adsorption – reaction“ concept is introduced. This reaction model explains the observations (increasing amount of H_2O_2 as reaction intermediate with decreasing Pt coverage and increasing electrolyte flow rate) by the re-adsorption probability

of reactive, incomplete reaction products on neighboured active Pt sides after desorption into the electrolyte, which is determined by the chance of further reaction towards the stable final reaction products.

Chapter 7 reports about results of combined electrochemical and mass spectrometric measurements, following simultaneously the total reaction current and the CO_2 formation rate in potentiodynamic and potentiostatic methanol oxidation measurements on electrodes with various Pt coverages. The MOR was investigated on a set of nanostructured Pt/GC electrodes and, for comparison, identical experiments were performed also on a polycrystalline Pt electrode. The influence of varying the Pt coverage and the electrolyte flow rate on the MOR reaction characteristics in potentiodynamic and potentiostatic measurements were evaluated, and the resulting effects on the activity, CO_2 current efficiency and turnover frequency (TOF) for methanol oxidation to CO_2, are discussed.

Finally, the results from *chapters* 3 – 7 are summarized in English and additionally in German language in *chapter* 8.

2 Experimental

This chapter is divided in four sections: First, the techniques applied for nanostructured Pt/glassy carbon (GC) electrode fabrication employed by the collaborating groups of groups of Prof. Dr. B. Kasemo (Department of Applied Physics, Chalmers University, Gothenburg, Sweden) and Prof. Dr. P. Ziemann (Institute of Solid State Physics, Ulm University), respectively, are described in detail (see section 2.1). Second, surface analysis methods such as Scanning Electron Microscopy (SEM), Energy Dispersive X-Ray Spectroscopy (EDX), Transmission Electron Microscopy (TEM), X-Ray Photoelectron Spectroscopy (XPS) and Atomic Force Microscopy (AFM), which were applied for the physical characterization of the nanostructured Pt/GC model electrodes used in this work, are briefly depicted (see section 2.2). Third, electrochemical principles and the electrochemical instrumentation employed *viz.* DEMS and dual thin-layer flow cell configurations are presented (see section 2.3). Fourth and last, the detailed evaluation procedures for active surface area determination of the Pt/GC model electrodes, for calibration of the experimental set-ups and for evaluation of the activity and selectivity of the investigated electrocatalytic reactions are elucidated (see section 2.4).

2.1 Preparation Methods of Nanostructured Pt/Glassy Carbon Electrodes

Planar nanostructured Pt/GC model electrodes represent simplified and well-defined versions of real carbon-supported Pt/C catalysts. To fabricate such nanostructured Pt/GC model electrodes, *Nanotechnology* offers a number of preparation methods including lithographic techniques such as Electron Beam Lithography, Photolithography, Soft Lithography or Nanoimprint Lithography. (For a detailed overview the reader is referred to the chapter by Grant et al. in [101].) Furthermore, the formation of lithographic masks, based on self assemblys, are used in Nanosphere Lithography [102, 103], Colloidal Lithography [60–62, 104, 105] or more recently Hole-mask Colloidal Lithography [64]). Also, „direct“ deposition methods, in terms of the primary deposition of self assembling active material, such as block co-polymers [66], metal-colloids or micelles techniques [67, 106–108] and subsequent after-treatment procedures have to be mentioned.

In this work, nanostructured Pt/GC model electrodes were prepared by self assembled lithographic masks using Collodial Lithography and more recently Hole-mask Colloidal Lithography. These two methods enable the fabrication of well-defined nanostructures on large sample areas in (relatively) short times [47]. The interparticle distances can be varied in a controlled way [61]. A limitation of these techniques is

that at present the smallest preparable particle is about 20 nm in diameter, which is limited by the size of polystyrene (PS) beads available (smallest size of commercially PS particles are 20 nm). Additionally, as it will be shown in *chapter* 4, the CL procedure resulted in secondary Pt nanoparticles in between the Pt nanostructures. Furthermore, Pt/GC model electrodes were prepared by a micellar approach, where Pt nanoparticles in the range of 1–15 nm in diameter can be fabricated, which is comparable to the particle sizes between 3 and 6 nm used commonly in electrocatalysis. These three fabrication procedures are described in detail in the following subsections.

Pre-treatment of the glassy carbon substrates

Independent of the employed preparation procedure for the fabrication of well-defined planar nanostructured Pt/GC model catalysts, the GC substrate was polished and chemically pre-treated in the following way:

The GC disks (9 mm in diameter, Sigradur G from Hochtemperatur Werkstoffe GmbH) were polished with alumina slurry down to 0.3 μm grain size. Subsequently, the substrate was cleaned by immersion in 5 M KOH (1 min) and concentrated H_2SO_4 solution (1 min), followed by extensive rinsing with Millipore MilliQ water (resistivity ≥ 18 MΩ cm) after each step. Finally, the GC disk surfaces were dried in a N_2 stream.

2.1.1 Colloidal Lithography – *CL*

Prior to the lithographic process and the Pt deposition of the samples used in *chapter* 3, the polished and chemically cleaned GC surface was further pretreated in either (*i*) an Ar plasma (Pt evaporated samples: 50 W, 133 mbar, 30 s, PlasmaTherm Batchtop photoresist/reactive ion etching (PR/RIE), Pt sputter-deposited samples: 50 W, 13 mbar, 2 min, in situ Nordiko 2000 sputter system), (*ii*) an oxygen plasma (50 W, 333 mbar, 2 min, PlasmaTherm Batchtop PR/RIE), (*iii*) first in an oxygen (50 W, 333 mbar, 2 min, PlasmaTherm Batchtop RIE) and then in an Ar plasma (in situ Nordiko 2000 sputter system, same conditions as above), or (*iv*) the substrates were used without further pretreatment. The latter procedure was employed in ref. [65]. For the samples prepared via Pt sputter deposition, the preceding Ar-plasma treatment was done *in situ* in the same apparatus used for subsequent Pt sputter deposition and without exposing the GC surface to air before Pt deposition. This was expected to result in a significantly improved adhesion of the Pt film.

For the CL-prepared samples used in *chapter* 4 and 5, the GC substrate surface was first treated in oxygen plasma (50 W, 330 mbar, 2 min), followed by *in situ*

Argon-plasma (50 W, 13 mbar, 2 min) before a 20 nm thick Pt film was sputter-deposited.

Pt nanostructures were prepared on the planar glassy carbon substrate by Colloidal Lithography. The general preparation procedure of Pt nanostructures via CL was already described in detail in previous publications [47, 60–63, 65] and is schematically illustrated in Fig. 2.1. For the nanostructured Pt/GC samples used in *chapters* 3 and 4 a 20 nm thick Pt film was deposited either by electron-beam evaporation using an AVAC HVC 600 electron-beam evaporation system (10^{-6} mbar base pressure, $\sim$ 1 s^{-1}) or by sputter deposition, employing a Nordiko 2000 sputter system (50 W, 7 mbar, 1.7 s^{-1}). Thereafter, three layers of charged polymer solutions were adsorbed sequentially on the Pt film by pipetting a droplet of the respective solution (2 % poly(diallyldimethylammonium chloride), 2 % poly(sodium 4-styrenesulfonate) and 5 % aluminium chlorid hydroxide). This triple layer prevents the PS-beads from aggregation during the adsorption step by increasing the local hydrophobicity. The total thickness of the triple layer is around 1 nm [105].

Subsequently, a dilute layer of negatively charged polystyrene (PS) colloid particles (white sulfate latex, IDC, Portland, OR) with an approximate diameter of 110 nm was deposited on the resulting positively charged surface by dip-coating in an aqueous suspension [109] (Fig.2.1 c). Due to the electrostatic repulsion between the charged particles, a well-ordered PS-particle adlayer was formed. This adlayer was used as sputter-mask in a subsequent Ar-ion sputtering step (500 eV Ar ions, 105 s, 0.2 mA, Oxford Ionfab 300 ionbeam system), which removed the unprotected Pt film between the PS particles (Fig.2.1 d). Due to slight overetching by $\sim$10 nm, which was applied to secure complete removal of the Pt film, the resulting Pt nanostructures were supported on a GC neck of $\sim$10 nm height [63]. The Ar-ions mechanically remove the material between the adsorbed PS particles, whereas the material beneath the PS-beads is protected by them. The sputtering time depends on the material and the film thickness. Before the sputtering procedure, the colloid layer was warmed to 118 °C on a hot plate for 2 min (the time is PS-size dependent and the temperature substrate dependent) in order to relax the spherical PS particles into a hemispherical shape. This procedure was previously found to avoid the formation of cup-shaped Pt disks, which otherwise occured due to re-deposition of sputtered Pt material at the perimeter of the Pt nanostructures [65, 109]. This pre-melting step leads to even Pt nanostructures [109]. Next, the PS particles were removed by a UV/ozone treatment (75 min, 15 mW cm^{-2}, BHK, Clarmont, USA) (Fig.2.1 e). Finally, Pt nanostructures, whose geometrical shape resembles flat cylinders or disks, have been fabricated on the glassy carbon substrate.

The different Pt loadings (Pt surface coverage) on the samples prepared by Col-

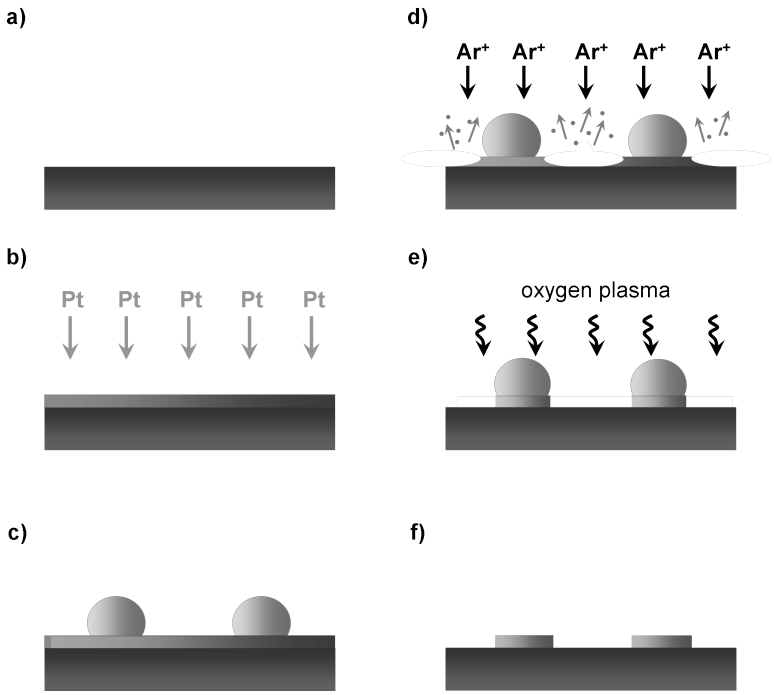

Figure 2.1: Schematic presentation of the Collodial Lithography procedure for the preparation of the nanostructured Pt/GC electrodes: CL starts with (a) a polished GC substrate, followed by (b) Pt film sputter deposition. On top of this, (c) an adlayer of PS particles is deposited by dip coating which is relaxed into hemispherical shape. In the next step, (d) the Pt film between the PS particles is removed by Ar^+ sputtering, before finally (e) the PS particles are removed by a UV/O_3 treatment, leaving (f) the Pt nanodisks.

lodial Lithography used in *chapter* 4 (or later on samples prepared by Hole-mask Colloidal Lithography used in *chapters* 6 and 7) were achieved by adjusting the salt concentration in the PS solution [61], which modifies the electrostatic repulsion between the particles and thus the interparticle distance during the adsorption step. The higher the salt concentration, the higher is the negative charge on the PS-beads, which leads to a decreasing separation of the particles [47]. The nonstructured „Pt-free“ sample (CL-00) used in *chapter* 4 was fabricated via the same sequence of substrate pretreatment, Pt deposition, and Ar^+ sputtering, however without the lithographic steps for the nanostructuring. In this case, the entire Pt film was removed (30 s overetch similar to the preparation of the nanostructured samples).

2.1.2 Hole-mask Colloidal Lithography – *HCL*

The nanostructured Pt/GC model electrodes used in *chapters* 4, 6 and 7 were fabricated by Hole-mask Colloidal Lithography, largely following the preparation procedure as specified by Fredriksson et al. [64].

HCL can be subsumed as a variation of Colloidal Lithography (see section 2.1.1 above) and is composed of fabrication steps which are commonly used in other nanofabrication techniques such as spin coating of polymer films, self assembly of colloidal nanospheres, thin film deposition or reactive ion etching [110].

The surfaces of the GC substrates were first polished and chemically cleaned before treatment by an oxygen plasma (50 W, 330 mbar, 2 min) and by an *in situ* Ar plasma (50 W, 13 mbar, 2 min). The Pt nanostructures were fabricated along the procedure schematically presented in Fig. 2.2.

A sacrificial polymethyl methacrylate (PMMA) resist layer and, on top of this, masking PS beads were deposited on the pre-treated GC substrate (Fig. 2.2 a). PMMA was deposited by spin coating, followed by subsequent treatment in an oxygen plasma (5 s) to increase the hydrophilicity of the surface. Next, a thin polyelectrolyte layer was pippeted on the PMMA surface. Finally, the charged PS beads were deposited. Afterward, a plasma-resistant, 20 nm thick Au film was evaporated on top (Fig. 2.2 b), which is referred to as the hole-mask. In the next step, the PS beads were removed by tape-stripping (Fig. 2.2 c), by simply attaching a piece of tape to the surface. As this tape is removed, the PS spheres are sticking more strongly to the tape than to the PMMA surface. Alternatively the nanospheres can be removed by cleaning the sample in an ultrasonic bath and iso-propanol [110].

This results in a masking Au film with well-defined holes (Au hole-mask) on the PMMA layer, where the PS beads were covering the surface during the film deposition process. As already mentioned above for the CL-procedure, the diameter and density of the adsorbed PS beads (or holes respectively) can easily be tuned by varying the salt concentration or the diameter of the PS beads [61]. A subsequent oxygen-plasma etching step (reactive ion etching step, RIE) removes the PMMA film in the holes of the hole-mask, while the Au covered area is protected (Fig. 2.2 d). One has to take care in setting the plasma conditions, since the RIE process etches the PMMA layer predominantely in forward direction. Therefore, etching will continue laterally creating an undercut into the polymer film, once the PMMA film is completely etched through vertically [110]. (On the other hand, a slight undercut is often beneficial for subsequent material deposition and mask-liftoff processing [110].) In the next step, Pt was deposited through the mask onto the GC surface (Fig. 2.2 e). This method also allows to fabricate, e.g., elongated struc-

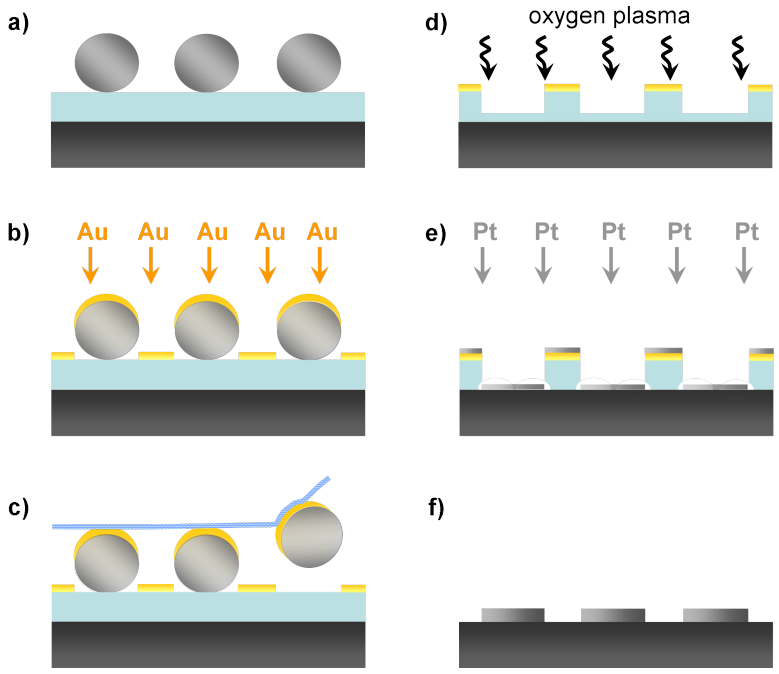

Figure 2.2: Schematic presentation of the Hole-mask Colloidal Lithography procedure for the preparation of nanostructured Pt/GC electrodes: HCL fabrication starts with a polished GC substrate. Thereon, (a) a sacrificial resist PMMA layer is deposited by spin-coating and masked with PS particles. In the next step, (b) a Au layer is evaporated on top. (c) The PS particles are removed by tape-stripping, resulting in the Au hole-mask. Afterward, (d) the PMMA layer is removed underneath the unprotected holes in the Au mask by an oxygen plasma treatment, followed by (e) Pt evaporation through the holes of the Au/PMMA mask. In the last step, (f) the Au/PMMA mask is lifted-off in acetone.

tures instead of disks, by simply tilting the sample, with respect to the evaporation source, during the hole-mask deposition step. For more details how to control size and shape of the holes (disk- or eliptical-shaped nanostructures, particle pairs or cones) the reader is referred to refs. [64, 110]. After removal of the PMMA/Au hole-mask by a lift-off step in acetone, the Pt nanodisks located in the former holes of the PMMA/Au hole-mask remain on the surface, while the remaining part of the Pt film is removed together with the PMMA/Au film. This results in an array of Pt nanodisks with well-defined size and lateral distribution (Fig. 2.2 f) similar to CL preparation, but without the crucial Ar^+ sputtering step for removal of the Pt film, which is characteristic of the latter approach.

2.1.3 Deposition of Pt-salt loaded Micelles and After-Treatment Procedure

Third, self-assembled arrays of platinum metal nanostructures were prepared using a reverse micelle preparation technique. This way the Pt/GC model electrodes used in *chapter* 5 were fabricated. The advantage of this technique is the possibility to prepare Pt nanoparticles of sizes (1–15 nm) fairly comparable to particle sizes of 3–6 nm in diameter in real carbon-supported Pt/C catalysts.

The general procedure was already described in detail in refs. [66, 67]. As schematically demonstrated in Fig. 2.3, polystyrene (PS)[1779] and poly(2–vinylpyridine) (P2VP)[695] diblock copolymers (Polymer Source Inc.) were dispersed in an apolar solvent such as dry toluene (Sigma-Aldrich) under continuous stirring for one week. This leads to the formation of spherical reverse micelles, within the hydrophobic PS-chains forming the outer shell, whereas the hydrophilic P2VP-parts are building the core (Fig. 2.3 a). (For more details of this procedure the reader is referred to ref. [66].) In the next step, a Pt-containing salt (Zeise salt: $K[PtCl_3(C_2H_4)] \cdot H_2O$, Sigma Aldrich) was introduced into the micellar solution and stirred under ambient conditions for an additional week (Fig. 2.3 b). The Pt-ions slowly migrate into the empty cores of the micelles, where they are ligated by complexation or protonization to the inner polymer block [66, 67]. At equlibrium, equal amounts of Pt-salt are present in all micelles.

For deposition of the Pt loaded reverse micelles on the GC substrates, these were dipped into the solution and then immersed at a constant velocity of $14\,\mathrm{mm\,min^{-1}}$. This led to an adlayer with homogeneously distributed Pt-salt loaded micelles on the GC substrate (Fig. 2.3 c). It turned out that, while the substrate is pulled out, the toluene evaporates more slowly than in the case of spin-coating. Thus, a monolayer of micelles is formed, which exhibits a high degree of hexagonal order (on SiO_2/Si wafers), reflecting the packing of the spherical micelles [67]. Since the core of the micelles is still filled with a metal precursor rather than with metal, additional steps are neccessary to produce regularly arranged, electrochemically active, „naked“ (polymer-chain-free), metallic Pt nanoparticles. Therefore, the specimens were exposed to a reactive oxygen plasma at 5 Pa for 90 s at room temperature, using a homebuilt plasma etching system at the Institute of Solid State Physics at Ulm University (Prof. Dr. P. Ziemann). This resulted in the removal of the PS outer shell of the reverse micelles, without significantly changing the morphology of the GC substrate surface [111]. Finally, the specimens were treated in a H_2 atmosphere (12 h, 600 °C, 5 Pa) to reduce the Pt compounds and create metallic Pt nanoparticles (Fig. 2.3 d).

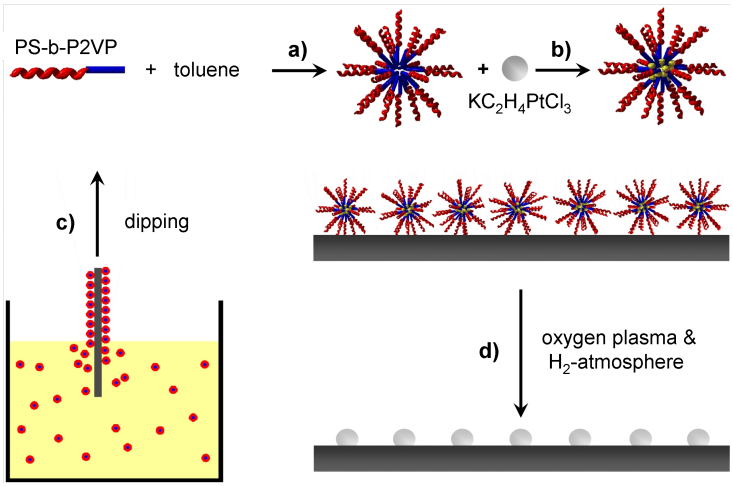

Figure 2.3: Schematic description of the preparation procedure of the model electrodes by deposition and post-processing of Pt-salt loaded micelles. (a) Preparation of the inverse micelles, (b) Pt salt loading, (c) deposition on the glassy carbon substrate by dip coating, and (d) removal of the polymer stabilizer shell and reduction of the Pt-salt core in an oxygen plasma and subsequent reduction in a H_2 atmosphere.

Most importantly, it was observed that despite such a chemically „agressive“ plasma process, the original ordered arrangement of the micellar self assembly is conserved and the polymer matrix was removed completely. Also, this method allows to control the particle size and to some extent, the separation [66, 67].

2.2 Physical Characterization Methods

To relate the (electro)catalytic properties of a (nanostructured electrode) surface to its composition and its morphology [112] (e.g., variation of particle size, separation and particle density), it is neccessary to characterize the electrode morphology and its chemical composition in detail.

The nanostructured Pt/GC model electrodes in this work were investigated by surface sensitive characterization techniques such as SEM, TEM and AFM for physical characterization of the surface morphology and EDX and XPS for identifying the chemical composition of the electrode. To gain a complete picture of the nanostructured Pt/GC surface morphology and chemical composition several of these techniques were used accordingly. Furthermore, the obtained results of the physical characterization were correlated to the results of the electrochemical characterization (see forthcoming section 2.4) permanently.

2.2.1 Scanning Electron Microscopy – *SEM*

Throughout this work, SEM was used for imaging the nanostructured Pt/GC electrode surfaces. Large-scale and high-resolution SEM micrographs of the samples under investigation are shown in the corresponding chapters (see *chapters* 3 – 7).

A principle sketch of the operation principle of a scanning electron microscope is given in Fig. 2.4 a. The primary electrons (PE) are accelerated by a voltage difference between cathode and anode. (10 kV accelerating voltage were applied for all SEM micrographs presented in this work.) A deflection coil system is used as scan generator in x-y directions. It is located in front of the final lens field and allows to scan the (primary) electron beam across the speciemen surface [112–114]. Due to the excitation by the PEs, secondary electrons (SE), backscattered electrons (BSE) and X-rays are produced (see Fig. 2.4 b). The yields of either SE or BSE or both of them are detected as a function of the position of the primary beam [112].

Because of distinct differences in their energy one can differentiate between secondary and backscattered electrons. SE are those electrons which are generated directly where the incident electron beam hits the surface and have a most probable energy of 2–5 eV ($E_{SE} \leq 50$ eV). Having only a very short mean free path in the material, they originate from surface near region of the specimen. In contrast, the BSE ($E_{BSE} > 50$ eV) result from elastical scattering of the incoming primary electrons and originate in depths down to 500 nm in the bulk material of the sample.

The intensity of the electrons leaving the sample surface (SE and BSE) is measured by a detector. The signal is amplified and swept („wobbled“) to trigger a reproduction of the electrode surface. In principle, such a micrograph is a locally resolved current density plot of the outgoing electrons of the electrode surface [47].

Contrast is caused by two effects: *(i)* heavy elements, e.g., Pt in comparison to carbon, are more efficient scatterers than lighter elements and thus, they appear brighter in the micrograph; *(ii)* parts of the surface facing the detector appear brighter than parts of the surface with their surface normal pointing away from the detector [112, 115].

For all micrographs shown in this work a LEO 1550 (Zeiss) instrument was used at 10 kV operating energy and with lateral resolution of ~ 1.5 nm. The measurements were performed in the Institute of Micro- and Nanomaterials, Ulm University (Prof. Dr. H. J. Fecht).
Latest SEM instruments achieve a lateral resolution down to 1 nm or even higher.

The SEM micrographs were evaluated with an image analysis software („*Q-PEP*“), which was developed and programmed by Dipl. Inf. S. Tiedemann and yielded the

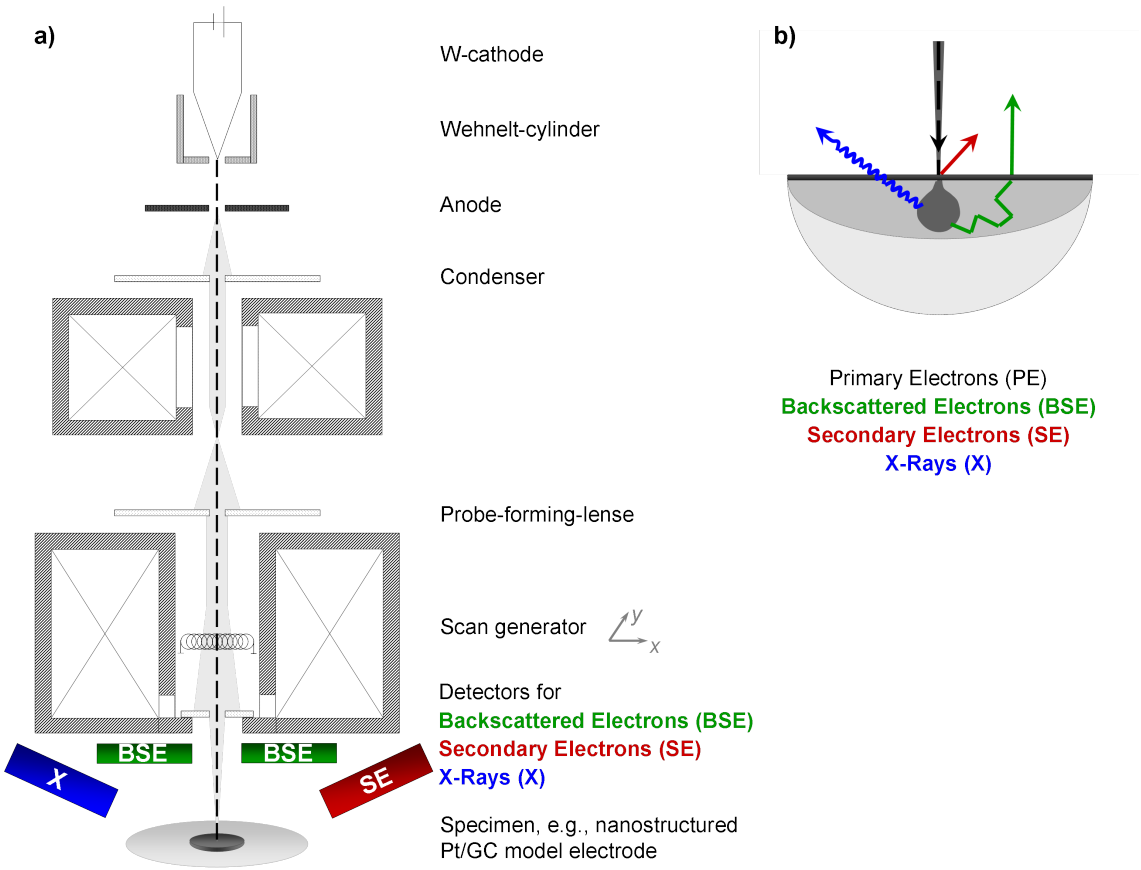

Figure 2.4: Schematic description of (a) a scanning electron microscope (SEM) set-up and (b) the origin of secondary electrons, backscattered electrons and X-ray quanta due to excitation by primary electrons presented as depth profile.

statistics on particle densities, particle separation / distances, Pt coverage and particle diameters. Only the images of nanostructured Pt/GC electrodes prepared by micellar techniques in *chapter* 5 were evaluated manually.

Furthermore, it is possible to combine SEM with energy dispersive X-ray analysis to investigate the chemical composition of the electrode surface [116–118]. This type of characterization method is described in the next subsection.

2.2.2 Energy Dispersive X-Ray Spectroscopy – *EDX*

Energy Dispersive X-Ray Spectroscopy (EDX) was specifically used for the verification of Pt nanoparticles on the glassy carbon substrate in-between Pt nanostructures prepared by Colloidal Lithography (see section 2.1.1). This topic is discussed in detail in *chapter* 4.

In Fig. 2.4 b and c, it was already indicated that secondary and backscattered electrons are not the only products from excitation by a primary electron beam.

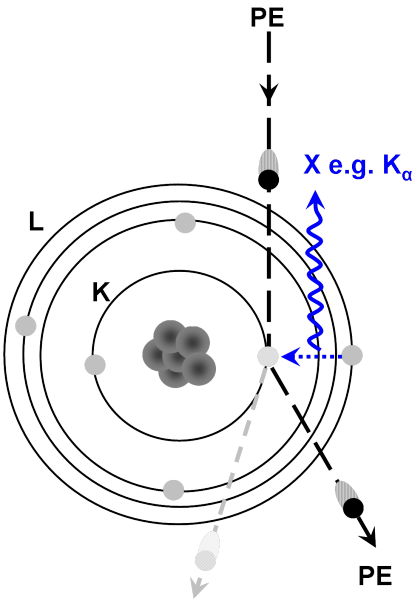

Figure 2.5: Principle scheme of Energy dispersive X-Ray (EDX) Analysis: A core hole is filled by an electron from a higher orbital, the gained energy allows to emit an X-ray photon.

Also X-rays are generated as products by scanning a sample surface in an electron microscope.

The interaction of an electron with an atom at the sample surface gives rise to characteristic emission lines. When a PE ejects a bound electron from an atomic shell, a photon with an element-characteristic energy is emitted from the respective surface atom. The resulting ion is highly unstable and photon emission occurs when the initial core-hole (see Fig. 2.5, in the K-shell) is filled with an electron from a higher orbital (see Fig. 2.5, from the L-shell). A K_α X-ray photon is emitted due to the energy (E_K-E_L) gained in the „filling process“, which is characteristic for the emitting atom. Thus, the elemental composition of a sample surface can be determined via X-ray emission in a SEM. The emitted X-rays are analysed with an energy dispersive X-ray detector. The combination of SEM and EDX offers the possibilty to obtain the local composition of the sample surface on a scale of about 5–10 nm [112]. However, because of the high penetration depth of the primary electrons ($\sim 0.3\,\mu$m at 6 kV operation energy) the EDX analysis averages over a relatively broad range below the sample surface and contains also contributions of the elemental composition of „bulk material“ [115].

EDX measurements were also performed in the LEO 1550 (Zeiss) instrument with locally resolved elemental analysis (EDX system Oxford Instruments GmbH, 6 kV

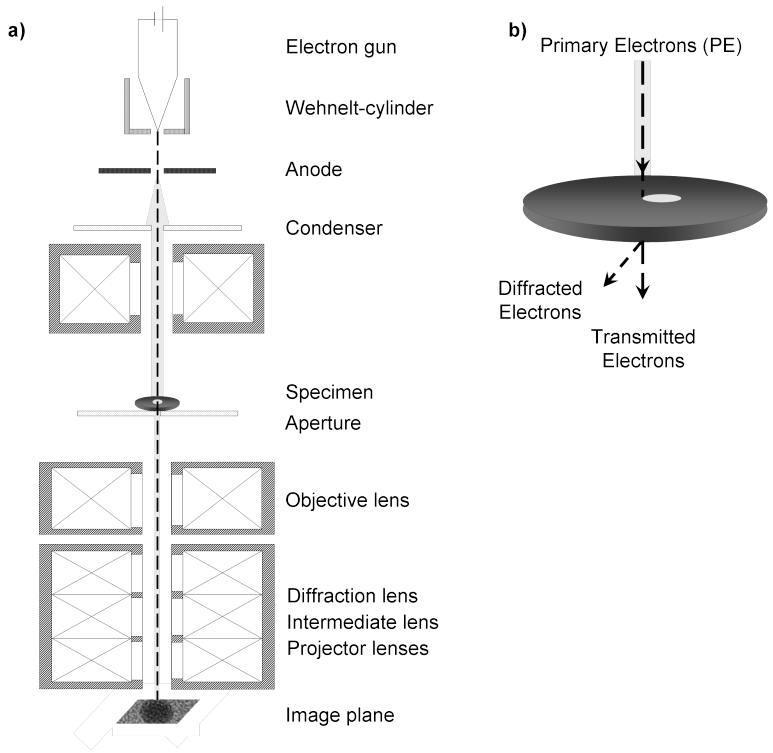

Figure 2.6: Schematic description of (a) a transmission electron microscope (TEM) set-up and (b) the origin of diffracted and transmitted electrons due to excitation by a primary electron beam.

operation energy) in the Institute of Micro- and Nanomaterials, Ulm University. The EDX spectra were analyzed using the INCA 400 Oxford Instruments software.

2.2.3 Transmission Electron Microscopy – *TEM*

Transmission Electron Microscopy (TEM) was used for structural analysis of the Pt/GC interface region on nanostructured samples which were prepared by Colloidal Lithography using different Pt deposition techniques (see *chapter* 3) and by Hole-mask Colloidal Lithography.

A schematic illustration of a transmission electron microscope is given in Fig. 2.6. In general, a TEM closely resembles an optical microscope, if one substitutes the optical by electromagnetic lenses. A high energy (100–400 kV) and high intensity primary electron beam is focused to parallel trajectories, which impinges on the specimen surface. The specimen thickness and density determine the attenuation of the primary electron beam while passing through the sample. In the bright-field imaging mode, which was utilized in this work, only non-diffracted electrons are collected and amplified by the electron optics. Contrast is generated by absorption of electrons in the specimen. Thus, heavier elements, e.g., Pt nanoparticles/nanostructures in

comparison to glassy carbon, or thicker regions appear dark, in contrast to elements with a low atomic number or thinner sample regions, which will appear bright. In contrast, „dark field imaging“ uses only the diffracted electron beams [116, 117]. Eventually, the displayed image is a two dimensional projection of the specimen along the optical axis. [112, 115]

Conventional TEMs obtain resolutions of about 0.2 nm. Recently, a resolution below 0.5 Å (50 pm) was achieved for a Transmission Electron Aberration-corrected Microscope (TEAM) [119].

Detailed structural information on the carbon-Pt interface in *chapters* 3 and 4 was obtained from cross-sectional HRTEM images using a CM 20 microscope (Philips, 0.21 nm point-to-point resolution), operated at 200 kV, and a Cs-corrected Titan 80-300 (FEI Company) operated at 300 kV. The measurements were performed in the Central Facility for Electron Microscopy, Ulm University (Prof. Dr. U. Kaiser). The cross-sectional samples were prepared by the standard preparation method, cutting small pieces of the nanostructured samples and glueing them together face to face. The resulting sandwich was sliced into thin vertical wafers, by mechanical grinding in a tripod. In a suebsequent step, the slices are continuously thinned by ion milling until the resulting wedge recieves electron transparency.

2.2.4 X-Ray Photoelectron Spectroscopy – *XPS*

The elemental composition of the nanostructured Pt/GC model electrode surfaces was determined by X-ray photoelectron spectroscopy (XPS), which is a commonly used ex-situ analytical characterization method for qualitative and quantitative surface analysis [120]. This technique was applied for analysing the glassy carbon support after different pre-treatments used in *chapter* 3, for evidencing the metallic character of the Pt nanoparticles prepared by micellar techniques in *chapter* 5, and additionally to the EDX analysis of the secondary Pt nanoparticles in *chapter* 4.

The XPS technique is based on the photoelectric effect, which is schematically described in Fig. 2.7 a. An incident X-ray photon with the energy hν is absorbed by an atom and a photoelectron (formerly a core or a valence electron with binding energy E_b) is ejected with the kinetik energy E_{kin}. The element specific core level binding energy/energies E_b of the sample surface can be calculated from the measured kinetic energy/energies of the emitted photoelectrons via the relation

$$E_b = h\,\nu \;-\; E_{kin} \;-\; \phi \tag{2.1}$$

where hν is the energy of the incoming photon (routinely used X-ray sources are Mg K_α with hν = 1253.6 eV and Al K_α with hν = 1286.3 eV) and ϕ is the work function

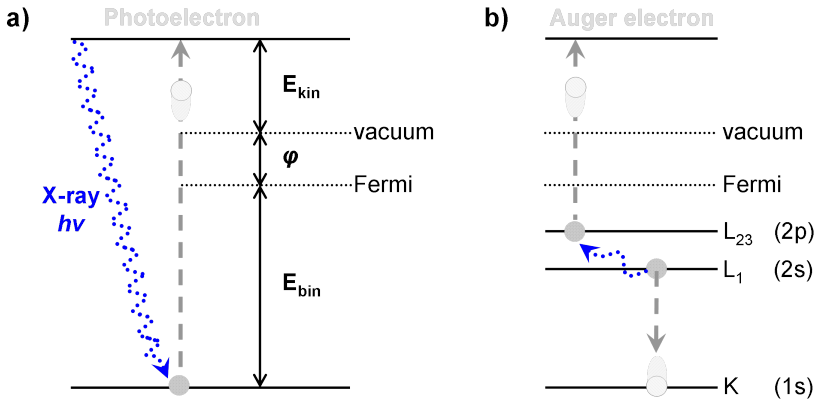

Figure 2.7: (a) Photoemission and (b) the Auger process.

(separation of the energy levels between the Fermi and vacuum niveau) of the sample [112, 121, 122]. Since the binding energy is element specific, it can be applied for determination of the qualitative and quantitative composition of the sample surface. Furthermore, the binding energy of an individual surface atom depends on its chemical environment, which causes chemical shifts in the binding energy of a respective core level electron in an individual surface atom. Thus, chemical information in terms of the oxidation state of the detected atom is obtained as well [112, 115]. (The binding energy decreases with decreasing oxidation state and vice versa [112, 115].)

After the emission of a photoelectron, an unstable ion with a hole in one of the core levels is left (see Fig. 2.7 b). By filling the vacancy at the core with an electron from a higher shell, the excited ion relaxes. During this transition process, energy releases which is absorbed by another electron. This electron, the so-called Auger electron, leaves the atom with an element specific kinetic energy. X-ray photoemission spectra are plots of the intensity of photoelectrons N(E) versus the calculated binding energy E_b (sometimes versus the measured kinetic energy E_{kin}) and contain Auger electron peaks as well. The latter ones have fixed kinetic energies, are independent of the X-ray source and are characteristic for the specific elements from which they are emitted [112, 115, 116]. XPS is highly surface specific (1–10 nm depending on the surface under investigation) because only photo- and Auger electrons generated close to the sample surface have a reasonable probability to emit from the sample and to be detected due to the short mean free path of the photoelectrons.

The chemical composition of the glassy carbon substrates in *chapter* 3 was characterized by XPS (PHI 5000C ESCA system) using monochromatized Mg K_α radiation and an emission angle of 45 ° (pass energy 5.85 eV for detail spectra) at Chalmers

University of Technology in Gothenburg, Sweden. (A binding energy of 284.3 eV for the C(1s) signal related to graphitic carbon in GC was used as internal standard [65, 123].)

The surface chemical composition of the resulting electrodes prepared by Pt-salt loaded micelles and respective after-treatments in *chapter* 5 were characterized by XPS (Physical Electronics PHI 5800 MultiESCA system, monochromatized Al K_α radiation) at the Institute of Surface Chemistry and Catalysis (Ulm University). All spectra were obtained at 45 ° electron emission and 187, 85, and 11.75 eV pass energy for overview (survey) and detail scans, respectively. The electron spectra were analyzed by PHI MultiPak software.

2.2.5 Atomic Force Microscopy – *AFM*

Atomic force microscopy was applied in *chapter* 3 to obtain topographic information about the glassy carbon surface roughness after different plasma pre-treatment procedures. Since this physcial characterization technique was used only once, it will be described just briefly.

Fig. 2.8 shows the experimental set-up for AFM. The specimen under investigation is mounted on a piezo electric scanner, which allows positioning of the sample along the x-, y- and z-axis. A on nm-scale sharp tip is connected to a flexible arm, the so-called cantilever. The tip at the cantilever is either attracted or repelled by the sample surface. A feedback control keeps the tip either at a constant interaction force or at a specific distance from the surface. The deflection of the tip/cantilever assembly is mostly measured in the following way: A laser beam is adjusted at the end of the cantilever, where it is reflected to quarter segment photodiode, e.g., two segments of the photodiode numbered by I and II for a simplified explanation are shown in Fig. 2.8. Segment II of the photodiode receives more light than I, if the tip/cantilever assembly bends towards the surface, and the other way around, if the tip/cantilever assembly bends away from the surface. The intensity difference between the segments I and II of the photodiode is a direct measure for the deflection grade of the cantilever and therefore for the interactive force between the tip and the specimen surface [112, 115]. The system is able to store the vertical position at each x-y position. The actual image is created by scanning the surface line by line. In turn, a topographic map of the specim surface is generated. The system can be operated in different modes, namely contact, tapping and non-contact mode [112, 115].

The morphology of the glassy carbon substrates after the different procedures for pretreatment, in particular the surface roughness, as well as the heights of the Pt

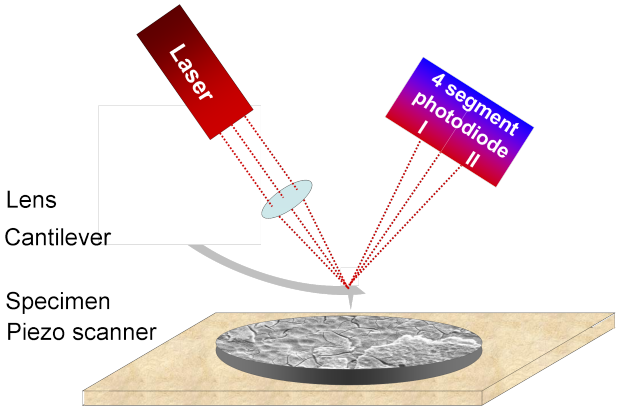

Figure 2.8: Schematic description of an atomic force microscope (AFM).

nanostructures were determined by a Digital Instrumentation Dimension 3000 Scanning Probe Microscope at Chalmers University of Technology in Gothenburg, Sweden.

2.3 Electrochemical Principles and Instrumentation

A short overview about the electrochemical background and instrumentation applied in this work, which allow studys of mass transport effects on the activity and selectivity of electrocatalytic reactions, is given in the following section. However, for a detailed description of electrochemical fundamentals such as electrode processes, potentials and thermodynamics of galvanic cells, kinetics of electrode reactions, potential sweep/step methods, mass transport, hydrodynamic methods, double-layer structures and adsorption isotherms, etc., the reader is referred to textbooks such as [74, 75, 124–127].

2.3.1 General Electrochemical Principles

> „*Electrochemistry is the study of structures and processes at the interface between an electronic conductor (the electrode) and an ionic conductor (the electrolyte) [...].*“
>
> *W. Schmickler* in *Interfacical Electrochemistry* [124]

For the better understanding of occuring processes in electrochemical systems, a detailed knowledge of the water and ion (electrolyte) structure in the near vicinity of an electrode is crucial. Generally, the electrode-electrolyte interface is charged since the electrode provides a charge which depends on the potential applied to the electrode. Hence, a charge distribution, consisting of two separated, however, narrow negative and positive charge carriers, is built up at the electrode-electrolyte interface. This is commonly known as *electric double-layer*. In the most simple

picture, this double-layer can be viewed as a capacitor with an extremely small effective plate separation [124]. A positively charged surface has a layer of basically negative charge carriers in the electrolyte solution close to the electrode surface and vice versa. (For details about double-layer models proposed by Helmholtz, Gouy and Chapman as well as Stern, the reader is referred to original articles such as [128–131].)

In contrast to *Heterogeneous Catalysis*, the driving force of an electrochemical reaction at an electrode surface is not only controlled by parameters like concentration, pressure and temperature, but also by electrical forces which affect the charge transfer through the interface [127] described above. These electric forces are characterized by the electrode potential which can be altered in an electrochemical cell by an external voltage [127].

Both scientific fields, *Electrocatalysis* and *Heterogeneous Catalysis*, have in common that adsorption is a mandatory step. Adsorption occurs at the phase boundary and leads to an increased concentration of the adsorbed species in the interfacial region in comparison to the concentration in the bulk electrolyte [75, 125, 127, 132] or the gas phase above the catalyst surface, respectively. For some molecules, the interaction with the surface is much stronger and the adsorption energies are in the same order of magnitude as the energy of a chemical bond. The term used to describe this kind of adsorption is *chemisorption*. Chemisorption involves strong overlap of molecular and substrate orbitals to form new bonding orbitals between them [127]. The influence of the bond formed with the surface on the rest of the molecule may lead to strong geometrical deformation of the molecule, which may evoke the dissociation of the adsorbate [127].

Basically, the reaction processes occuring at electrodes can be splitted into two types of process branches: *(i) Faradaic processes*, in which charges are transferred across the metal-solution interface. Electron transfer causes oxidation or reduction to occur: Electrons are either delivered from the electrode to an active species solvated in the electrolyte, which is then reduced (reaction at the cathode) or the electrode gains electrons from the active species, which is oxidised (reaction at the anode). Under some conditions, a given solid-liquid interface will show a potential range, in which no charge-transfer reactions occur because they are thermodynamically or kinetically unfavorable. However, *(ii) non-Faradaic processes* such as adsorption/desorption processes take place and the structure of the electrode-electrolyte interface can change. Applying a potential to the electrode, leads to changes in the charge of the electrode and in the distribution of ions at the electrode-electrolyte interface where the (electro-)chemical reaction occurs [74, 75]. (Details

about adsorption in an electrochemical environment and adsorption isotherms after Langmuir, Temkin and Frumkin can be found in textbooks like [75, 125, 127, 132].)

As already briefly mentioned above, electrochemical processes are not only affected by concentration or temperature, but in particular depend strongly on *(i)* the potential of the electrode, which mirrors the energy of the electrons within the electrode surface and *(ii)* the current, which reflects the rate of the electrochemical process at the electrode surface [75]. These two variables are connected via one of the central equations in electrochemistry, the *Butler-Volmer-equation* (for details see, e.g., [74, 75, 124]).

The most prominent technique employed to study reactions in electrochemical systems is *voltammetry* by means of measuring the current as a function of the varied potential. In particular in the area of preliminary mechanistic investigations, *sweep voltammetry-techniques* such as linear sweep (LSV) or cyclic voltammetry (CV) are probably most useful. Whereas for LSV, the linear potential scan starts from an initial value (E_1) to an end point (E_2), the scan direction is inverted at the selected reversal point (E_2) in the case of CV. An „electrochemical spectrum“ (I-E-plot) illustrates the current response of the working electrode upon a linear variation of the potential, which is obtained very fast. The current response indicates the potentials at which processes occur. While from the sweep rate dependence the involvement of coupled homogeneous reactions is readily identified, other complications such as adsorption can be recognised [125]. Generally, currents in the positive-going scan are denoted as anodic currents and currents measured in the negative-going scan as cathodic currents [74, 126]. To avoid any adsorbed (blocking) impurities, the potential range (E_1–E_2) applied in aqueous solution, lies between the gaseous H_2 and O_2 evolution. By this, surface site blocking species can be removed either by reduction or oxidation. In potential step voltammetry (I-t-transient), the applied potential is directly stepped from the starting point (E_1) to the end point (E_2) to induce the conversion of reactive species to the reaction product at the electrode surface, while charging/discharging the double-layer in front of the electrode [124]. The current is measured as a function of time. The immediate current response to the potential-step is a current-spike, induced by large contributions of the double-layer charging. A time-dependent decay follows the intial spike. (For detailed description about potential sweep techniques and in particular cyclic voltammetry the reader is referred to textbooks such as [74, 124–126].)

Being more quantitativ about size (and/or shape) of an I-E-plot, one should be able to determine the rate of the reaction at the electrode surface [75]. In „simple“ electrode reactions the rates of the corresponding chemical reactions (e.g., disso-

ciative adsorption) are much higher than those of mass transfer processes, which may affect the rate at which reactants, intermediates and products are delivered to/leaving the near surface region in electrochemical systems. Commonly, *mass transport* is meant to be the movement of material from one location in solution to another. The three modes of mass transport are:

- *Diffusion* refers to the random motion of a species along a concentration gradient, i.e., in average, species move from a higher concentrated region to lower concentrated regions. Assuming a planar electrode with infinite dimension, one dimensional diffusion is described by Fick´s laws (equations 2.2 and 2.3). Fick´s 1^{st} law is given by

$$flux_i = -D_i \frac{\partial c_i}{\partial x} \tag{2.2}$$

  it describes the flux of a species i through a plane parallel to and at the distance x to the electrode surface. D is the diffusion coefficient [length^2 time^{-1} : m^2 s^{-1}], and c_i is the concentration of species i at the distance x from the electrode surface.
  Fick´s 2^{nd} law is given by

$$\frac{\partial c_i}{\partial t} = D_i \frac{\partial^2 c_i}{\partial x^2} \tag{2.3}$$

  it describes the changes of the concentration of species i with time t due to diffusion.
- *Migration* refers to the random movement of charged species along a potential gradient under the influence of an electric field, which results from the electrical potential drop between the electrode/electrolyte interface [74, 125–127].
- *Convection* refers to the movement of species due to the flow of the solvent, which is, e.g., enforced by an external mechanical pump, gas bubbling or stirring of the electrolyte solution [75, 125–127].

Methods involving convective mass transport of reactants and products are sometimes called *hyrodynamic methods* [75]. They, for example, involve measurements of limiting currents or I-E-curves. Convection occurs within a thin-layer flow cell (see refs. [3, 4]) by forcing the electrolyte flow over the electrode surface. For the measurements in this study, the electrolyte flow rate was controlled via a syringe pump connected to the outlet of the thin-layer flow cell. The advantage of hydrodynamic methods is that a steady-state is attained rather quickly and that they remain constant in long-term measurements [75, 126]. For a simultaneous detection of reaction intermediates or products formed at the electrode surface, the thin-layer flow cell was combined with quantitative *Differential Electrochemical Mass Spectroscopy* or a so-called *Double Disk Dual Thin-Layer Flow Cell* was employed.

2.3.2 Differential Electrochemical Mass Spectroscopy – *DEMS*

Combining electrochemical measurements and on-line mass spectrometry (MS) for the analysis of electrochemical reaction products allows to study complex reaction networks like the electro-oxidation of small organic molecules in more detail. The electro-oxidation of a number of C_1- and C_2-molecules such as methanol, formaldehyde, formic acid, ethanol, acetaldehyde or ethylene glycol was studied on different types of electrodes, e.g., polycrystalline Pt bulk electrodes [5, 22, 89, 133–136], carbon-supported catalysts [137–140], single crystal electrode [141–143] or Pt film electrodes [144, 145].

Bruckenstein and Gadde introduced 1971 the idea of connecting an electrochemical cell to a mass spectrometer via a hydrophobic, gas permeable interface, to be able to detect volatile electrochemical reaction products [146]. However, the time delay from product formation at the porous Pt electrode used as working electrode in these studies to the product detection by MS was about 10 to 20 s [146]. In 1984, the set-up was improved by Wolter and Heitbaum, and named as electrochemical mass spectrometry (EMS). They introduced a porous Teflon membrane as connection between the elctrochemical cell and the MS and further extended the pumping system to a differentially pumped system, which includes two pumping stages [133, 147, 148]. The time delay between product formation and detection of volatile reaction products was significantly reduced to about 20 ms. Due to the differentially pumped vacuum system and furthermore due to the immediate variation in the measured product formation rate (differential values), when the Faradaic current is changed, this upgraded set-up was called „on-line Differential Electrochemical Mass Spectrometry“ (DEMS) [148, 149].

A schematic description of a DEMS set-up is given in Fig. 2.9. The electrochemical cell (liquid electrolyte phase) is connected to the DEMS (vacuum system) via a porous Teflon membrane (Scimat , 60 μm thick, 50 % porosity, 0.2 μm pore diameter) supported for mechanical stability on a porous stainless steel-frit. Because of the hydrophobicity of the Teflon material, the liquid phase is retarded in the electrochemical cell, whereas due to its porosity volatile and dissolved gaseous species are able to pass into the vacuum system. The critical pore size of the Teflon membrane for preventing the MS chamber of the liquid phase was calculated (by taking into account its dependence of the surface tension of water and the contact angle between water and the Teflon membrane as well) to be $r < 0.8\,\mu$m [133]. For DEMS application membranes with pore radii between 0.02–0.09 μm and thicknesses of about 50 to 150 μm are typically used [150].

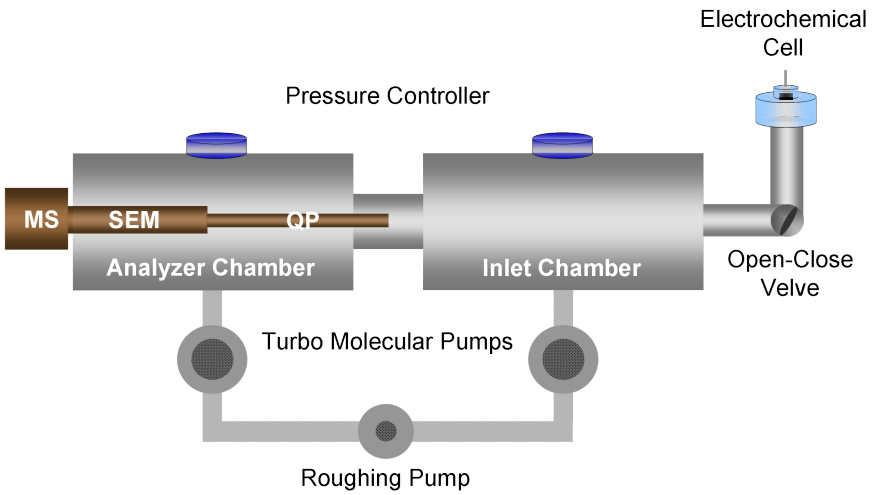

Figure 2.9: Schematic description of a standard differential electrochemical mass spectrometer (DEMS) set-up. The electrochemical cell can be separated from the vacuum system by an open/close valve.

After passing the Teflon membrane the volatile species evaporate into the vacuum system. It consists of two coupled, differently pumped (turbo-molecular pumps) vacuum chambers. The inlet chamber (pressure of 10^{-3} to 10^{-4} mbar) is connnected via a small aperture to the analyzer chamber (pressure about 10^{-6} mbar) in which a Balzers QMS 112 quadrupole mass spectrometer is located (see Fig. 2.9). The pressure of these two chambers is controlled by a Baratron and a cold cathode gauge, respectively. The gaseous molecules are ionized by electrons (electron beam ionization, electron energy $\sim 10\,\mathrm{eV}$). The formed ions, which are focused by electric optics are guided into the quadrupole analyzer, where they are separated by their respective mass-to-charge ratio (m/z). Finally, they are detected by an ion collector (electron multiplier and current measurement). A detailed review about the DEMS set-up was published by H. Baltruschat [148].

To attain instantaneous detection of volatile reaction products, the time delay between their electrocatalytical formation and their mass spectrometric detection has to be minimized. Therefore, the working electrode has to be positioned close to the Teflone membrane. This also helps to obtain a high collection efficiency (ratio of the number of molecules reaching the vacuum system and the overall amount of molecules produced at the electrode). Fast diffusion of gaseous species to the mass spectrometer was primarily achieved by sputter deposition of a metal film or varnishing a metallic lacquer directly onto the Teflon membrane, which led to a response of the detected reaction product signal within milliseconds after their formation. A number of electrode types and cell designs were introduced and described in detail

in order to obtain both a high collection efficiency and an instantaneous detection of reaction products (for details see [149]). However, these types of electrodes suffered from their non-defined mass transport conditions. The first cell design which offered on-line DEMS measurements with a low time constant (about 1 s), a high collection efficiency and in particular well-defined mass transport conditions, was introduced by Jusys et al. [3], employing a dual thin-layer compartment flow cell, which is described in the next section.

2.3.3 Thin-Layer Flow Cells

A thin-layer flow cell was used to investigate mass transport effects in electrocatalytic reactions studied on planar, glassy carbon supported model electrodes under well-defined mass transport conditions. This type of DEMS cell was developed by Jusys et al. [3] to simultaneously perform DEMS and electrochemical quartz microbalance (EQMB) measurements. The biggest advantage of this thin-layer flow cell type design is the defined mass transport. Furthermore, it allows a fast electrolyte exchange.

Dual Thin-Layer Flow Cell for DEMS Application

The dual thin-layer flow cell combines the compartment for electrochemistry with a second compartment for the detection of volatile reaction products by mass spectrometry. It was used for the measurements in *chapters* 3, 4, 5 and 7. A principle scheme of this cell is given in Fig. 2.10. The cell body itself consists of a Kel-F plate with capillaries for the electrolyte inlet and outlet, whose openings are centered on opposite sides of the body. The connection between the first and the second compartment is made by four connecting capillaries. The working electrode is pressed against a $\sim 50\,\mu$m thick gasket (exposed area of the working electrode $0.283\,\mathrm{cm}^2$) onto the first thin-layer compartment. The electrolyte enters the first thin-layer compartment in front of the working electrode.

The electrocatalytic reaction proceeds on the electrode, and the reaction product containing electrolyte flows through four connecting capillaries into the second thin-layer compartment. Here, the volatile reaction products can pass through the Teflon membrane and reach the inlet chamber of the vacuum system of the DEMS set-up. Depending on the electrocatalytic reaction investigated, the formed intermediates or products can be volatile or soluble, reactive molecules, which can be detected either by mass spectrometry or, in the case of electrochemically active intermediates, can be further oxidised or reduced at a second, *collector* electrode („Double Disk Dual Thin-Layer Flow Cell“ [4]).

Double Disk Dual Thin-Layer Flow Cell

To study mass transport effects on electrocatalytic reactions with non-volatile, but soluble, reactive intermediates the so-called „Double Disk Dual Thin-Layer Flow Cell“ was used in *chapter* 6 within this work. A schematic description of this specific cell design is given in Fig. 2.11.

Similar to the thin-layer flow cell for DEMS application described above (see Fig. 2.10), this cell combines a reasonable time resolution and a high collection efficiency under well-defined transport conditions. In the second compartment, a mirror-polished polycrystalline Pt disk (diameter 15 mm, exposed area 1.33 cm^2) is installed working as a *collector* electrode.

This Double Disk Dual Thin-Layer Flow Cell allows for further reaction of the electroactive reaction intermediates/products generated at the working electrode (*generator*) on the second electrode (*collector*), and thus to determine the amount of oxidizable (reducible) product species, similar to a rotating ring disk electrode (RRDE) set-up, but at a higher collection efficiency [4]. A detailed description of this type of dual thin-layer flow cell is given in ref. [4].

Recently this thin-layer flow cell type was employed for combining on-line DEMS and in-situ ATR-FT infrared spectroscopy by Heinen et al. [144].

The resulting electrolyte volume at the working electrode was about 5 μL. The electrolyte flow rate was controlled and driven by a syringe pump (World Precision Instruments AL-1000) connected to the outlet of the thin-layer flow cell. The time delay of this type of flow cells, in terms of the time passed between intermediate/product formation at the working electrode and detection via MS or *collector* electrode, respectively, was about 1–3 s, depending on the electrolyte flow rate. This time delay is corrected for in all graphs and calculations. Two Pt counter electrodes were connected to the thin-layer flow cell via separate ports at the inlet and outlet of the cell bodies. A saturated calomel electrode (SCE) was used as reference electrode (Schott Instruments, GmbH, Model, B2910+) and was connected to the flow cell via a Teflon capillary at the outlet. All potentials, however, are referred versus that of the reversible hydrogen electrode (RHE). All experiments were performed at room temperature.

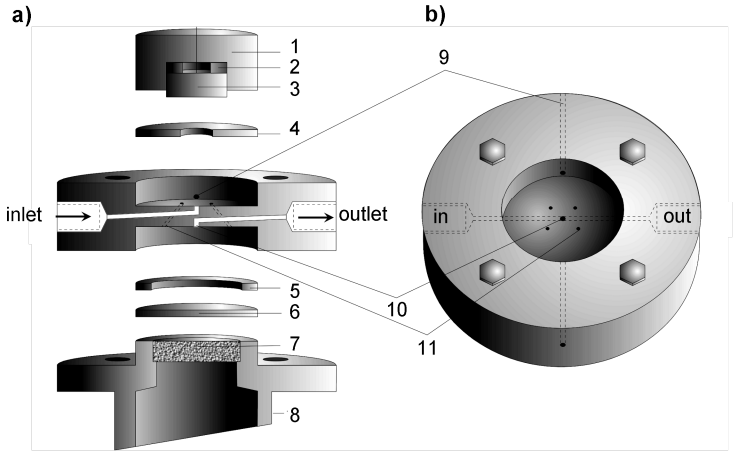

Figure 2.10: Schematic description of a dual thin-layer flow cell in (a) side view and (b) top view, developed by Jusys et al. [3], which was used for online DEMS measurements. (1) Kel-F support, (2) Kalrex gasket, (3) working electrode, (4,5) Teflon gaskets, (6) porous Teflon membrane, (7) stainless steel frit, (8) stainless steel connection to MS, (9) capillaries for contact wires, (10) inlet-outlet capillaries, (11) connection between first and second compartment.

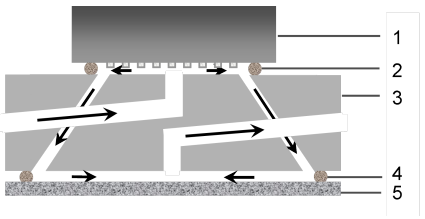

Figure 2.11: Schematic description of a double disk dual thin-layer flow cell developed by Jusys et al. [4] used for electrochemical measurements and simultaneously detection of soluble, reactive intermediates. (1) Working or „*generator*“ electrode, (2) Teflon gasket, (3) Kel-F body of the cell with the flow channels, (4) gasket, (5) polycrystalline Pt „*collector*“ electrode.

2.4 Electrochemical / Electrocatalytical Measurements and their Evaluation

ELECTROCHEMICAL PRE-TREATMENT

Prior to the electrochemical experiments, the nanostructured Pt/GC model electrodes were first pre-cleaned electrochemically by rapid potential cycling in Ar-saturated supporting electrolyte at a scan rate of $100\,\mathrm{mV\,s^{-1}}$ in the potential range of 0.04 V to 1.36 V to remove oxidizable contaminants, until a constant cyclic voltamogramm (CV) was achieved. The positive potential limit and the time spent at high potentials (above $\sim 1.1\,\mathrm{V}$ [21, 46]) are critical because the GC support can be oxidized at these potentials. This, in turn would lead to undermining the Pt nanostructures/nanoparticles, which were prepared by CL, HCL or deposition of Pt-salt loaded micelles, respectively. If the adherence of „undermined“ Pt nanostructures/nanoparticles to the GC substrate dramatically decreases, this results in a loss of Pt nanostrutures/nanoparticles and therefore in a decrease of the electrochemically active Pt surface area. On the other hand, insufficient cleaning of the sample likewise reduces the active Pt surface on the model electrode. The above potential window was found to represent the optimal compromise. The polycrystalline Pt electrode was pre-cleaned in the same way, however in the potential range from 0.04 V to a slightly higher potential of 1.56 V.

For potentiodynamic measurements, the scan rate and the potential window were lowered to $10\,\mathrm{mV\,s^{-1}}$ and 0.06 V – 1.16 V, respectively.

To ensure reproducibility, all experiments were repeated at least two times on two different specimens of the same sample type.

2.4.1 Active Surface Area Determination

The electrochemical properties and the corresponding active surface areas of the nanostructured Pt/GC model electrodes in this work were characterized by base cyclic voltammetry, by evaluating the hydrogen underpotential deposition (H_{upd}) on Pt, by Pt oxidation/Pt oxide reduction, and finally by pre-adsorbed CO_{ad} monolayer oxidation („CO_{ad} stripping“).

VIA HYDROGEN UNDER POTENTIAL DEPOSITION – H_{upd}

It is well known, that the electric charge of adsorbed hydrogen on Pt corresponds to the real active Pt surface area [151]. Therefore the H_{upd} adsorption charge derived from the integration of the current signal of the H_{upd} at potentials between 0.36 V and 0.06 V (negative-going scan), after subtracting the double-layer charg-

ing contribution, is generally used for determination of the active Pt surface area of an electrode or catalyst under investigation. The active Pt surface areas were determined by assuming a monolayer hydrogen charge on polycrystalline Pt equal to 210 μC cm^{-2} [2] and a H_{upd} coverage of 0.77 ML at the onset of H_2 bulk evolution at 0.06 V [152]. (For a detailed description of the integration procedure, including the determination of the onset potential, see ref. [152].) The active Pt surface area (S_{act}) was calculated via the relation

$$S_{act} = \frac{Q_{H_{upd}}}{0.77 \cdot 210} \tag{2.4}$$

where $Q_{H_{upd}}$ is the integrated charge from potentials between 0.36 V and 0.06 V (negative-going scan) for hydrogen underpotential deposition (see above). Since the amount of Pt on the electrode surface is directly reflected in the occuring current signal during potential cycling, the distinct Pt signals for hydrogen adsorption/desorption in the H_{upd} range and the signals for Pt oxidation/Pt oxide reduction become lower with decreasing Pt coverage. Therefore, the active surface areas of nanostructured Pt/GC model electrodes with very low Pt coverages (e.g., CL-00 and CL-01 samples in *chapter* 4 or the micelle-based sample in *chapter* 5) were determined via pre-adsorbed CO_{ad} monolayer oxidation, following the mass spectrometric signal for CO_2 formation via DEMS. The MS-signal is free of artefacts such as oxidation and reduction peaks at about 0.6 V on glassy carbon supported electrodes, which are generally attributed to the oxidative formation and reduction of quinones and which overlap with the Faradaic current signal for CO_{ad} oxidation [153]. Furthermore, they are free from contributions from double-layer charging, since up to 20 % of the total charge during CO_{ad} stripping in the Faradaic current signal are attributed to pseudocapacitive contributions [154].

VIA PRE-ADSORBED CO_{ad} MONOLAYER OXIDATION BY DEMS: „CO_{ad} STRIPPING“

The pre-adsorbed CO_{ad} monolayer oxidation was performed in a dual thin-layer flow cell connected to a DEMS set-up [3, 155], which allows for simultaneous electrochemical and mass spectrometric measurements, e.g., following the m / z = 44 signal for CO_2 formation, under controlled continuous-flow conditions, according to the procedure described by Jusys et al. [155]. The CO_2 production results from the two-electron oxidation reaction between CO_{ad} and neighboring OH_{ad} species, which are formed by dissociation of water.

For the CO_{ad} stripping experiments, CO was adsorbed on the electrochemically pre-cleaned (see electrochemcial pre-treatment procedure above) electrode surface at a constant electrode potential of 0.06 V for about 10 min, inserting 2 mL of CO-

saturated 0.5 M H_2SO_4 solution by an all-glass syringe through a separate port. Subsequently, the cell was carefully rinsed with CO-free, Ar-saturated supporting electrolyte (0.5 M H_2SO_4 solution) for at least 20 min at the same potential. Afterwards, the CO adlayer was oxidatively stripped in a positive potential scan from the adsorption potential of 60 mV up to 1.16 V (scan rate of 10 mV s^{-1}) recording both the Faradaic and the mass spectrometric signal for m/z = 44. The following base voltamogram of the CO_{ad}-free electrode surface was recorded for comparison.

The integrated CO_2 current signal ($Q_{CO_2^+,\,pcPt}$) (mass spectrometric ion current signal for m/z = 44) during CO_{ad} stripping on a polycrystalline Pt reference electrode was calibrated to the active surface area of the same polycrystalline Pt electrode ($S_{act,\,pcPt}$) derived from the H_{upd} charge (see section above). The active surface area of low loaded nanostructured Pt/GC model electrodes ($S_{act,\,Pt/GC}$) such as *CL-00* and *CL-01* samples in *chapter* 4 or the micelle-based sample in *chapter* 5 was calculated by

$$S_{act,\,Pt/GC} = S_{act,\,pcPt} \cdot \frac{Q_{CO_2^+,\,Pt/GC}}{Q_{CO_2^+,\,pcPt}} \tag{2.5}$$

where $Q_{CO_2^+,\,Pt/GC}$ is the charge of CO_2 formation during CO_{ad} stripping of a saturated monolayer of CO on the corresponding nanostructured Pt/GC sample.

Furthermore, the pre-adsorbed CO_{ad} monolayer oxidation experiment is commonly used for calibration of the mass spectrometric CO_2 current signal of the DEMS set-up via the constant K^*. The K^*-value is defined as the ratio between the mass spectrometric (Q_{MS}) and the Faradaic (Q_F) charge of the CO_{ad} stripping peak:

$$K^* = \frac{2 \cdot Q_{MS}}{Q_F} \tag{2.6}$$

where 2 corresponds to the number of electrons for the oxidation of an adsorbed CO_{ad} molecule to CO_2 (see also [25, 148, 155]). This procedure was applied for calibration of the DEMS set-up in *chapters* 3, 4 and 5.

2.4.2 Quantitative Evaluation of DEMS Measurements

DEMS is the method chosen for detection of volatile reaction products (e.g. CO_2) formed during electrocatalytic reactions [133, 148] such as formaldehyde [97], methanol [5, 5, 25], ethanol [156–159] or ethylene glycol [138, 160, 161] oxidation.

CALIBRATION OF THE EXPERIMENTAL SET-UP:
CALCULATION OF K^*

In *chapter* 7, the mass spectrometric m/z = 44 current signal was followed to quantify the formation rate of the reaction product CO_2 during the electro-oxidation of

methanol on nanostructured Pt/GC model electrodes and on a polycrystalline Pt reference electrode. As already mentioned above, the CO_2 signal of the DEMS set-up has to be calibrated (see eq. 2.6). It should be noted that the K^* value strongly depends on the electrolyte flow rate, due to the longer residence time of the electrolyte in the second compartment of the flow cell (see Fig. 2.10). The slower the flow, the more CO_2 is able to pass the membrane into the mass spectrometer. Since the methanol oxidation reaction in *chapter* 7 was studied at different electrolyte flow rates, ranging from 1 to 30 $\mu L\,s^{-1}$, the calibration constant K^* of the present DEMS set-up was determined in separate experiments by CO bulk oxidation in CO-saturated 0.5 M H_2SO_4 solution. The calibration experiments were performed on all electrodes at each electrolyte flow rate separately by following the Faradaic current and the CO_2 formation rate upon stepping the potential from $E_{init} = 60\,mV$ (the initial potential was held for $t_{init} = 30\,s$) to $E_{fin} = 1.06\,V$ (holding time $t_{fin} = 300\,s$). The respective K^* value was then calculated via the relation given in eq. 2.6, using, however, the corresponding mass spectrometric (I_{MS}) and the Faradaic (I_F) current instead of the charges.

CO_2 Current Efficiency – A_{CO_2}

A quantitative description of the contribution of volatile reaction products to the overall reaction is possible by calculating product distributions (yields) or current efficiencies (see, e.g., ref. [25]). For the present experiment, the current efficiency for CO_2 formation, A_{CO_2}, is an important value. In *chapter* 7, the CO_2 current efficiencies resulting during the oxidation of methanol on nanostructured Pt/GC model electrodes and on a polycrystalline Pt reference electrode at different electrolyte flow rates were calculated. They are obtained by conversion of the recorded $m/z = 44$ signal (I_{MS}) into a partial Faradaic current for CO_2 formation (I_{CO_2}) during methanol electro-oxidation, assuming 6 electrons per CO_2 molecule formed from one methanol molecule, and subsequent division of the partial current by the total (Faradaic) reaction current (I_F) via the relation

$$A_{CO_2} = \frac{6 \cdot I_{MS}}{K^* \cdot I_F} \tag{2.7}$$

corresponding to the procedure described in refs. [25, 133, 148].

Turnover Frequency – TOF

Additionally, the partial Faradaic current for CO_2 formation (I_{CO_2}) was used to determine the turnover frequency (TOF_{CO_2}) for methanol oxidation to CO_2 (*chapter* 7). The turnover frequency reflects the number of reactant molecules (methanol) converted per Pt surface site and per second to product molecules (CO_2). It was

calculated via

$$TOF_{CO_2} = \frac{I_{CO_2} \cdot N_A}{6 \cdot F \cdot \sum Ptsurfaceatoms} \tag{2.8}$$

where N_A is the Avogadro constant, 6 refers to the number of electrons per full conversion of a methanol molecule to CO_2, and F is the Faraday constant. (For further details see also ref. [25].)

2.4.3 Measurements with a Double Disk Dual Thin-Layer Flow Cell

A Double Disk Dual Thin-Layer Flow Cell configuration [4, 39] (see also Fig. 2.11), which is based on the flow cell design described in ref. [3], was applied for studying mass transport and re-adsorption effects in the oxygen reduction reaction (ORR) over nanostructured Pt/GC model electrodes and, for comparison over a polycrystalline Pt electrode and a bare GC substrate (*chapter* 6). It allows to further react electroactive reaction products generated at the working electrode (*generator*) on a second electrode (*collector*), and thus to determine the amount of oxidizable (reducible) product species (here: H_2O_2 during the reduction of O_2). The potentials of both generator and collector were controlled using a bi-potentiostat from Pine Instruments.

CALIBRATION OF THE EXPERIMENTAL SET-UP:
CALCULATION OF THE COLLECTION EFFICIENCY – N

Prior to the calibration experiment, the *generator* (polycrystalline Pt and nanostructured Pt/GC model electrodes) and the *collector* electrodes were pre-cleaned by rapid potential cycling in Ar-saturated supporting electrolyte in the potential range 0.04 to 1.36 V (scan rate 100 mV s^{-1}). The collection efficiency of the present set-up was determined by hydrogen evolution/oxidation experiments in Ar-saturated base electrolyte (0.5 M H_2SO_4 solution). In these measurements, the nanostructured Pt/GC samples and a polycrystalline Pt reference electrode were employed as *generator* electrodes, using different electrolyte flow rates. Upon stepping the *generator* potential from $E_{init} = 0.31$ V (the initial potential was held for $t_{init} = 30$ s) to a constant potential $E_{fin} = 30$ mV (holding time $t_{fin} = 180$ s), H_2 is formed, which is oxidized subsequently at the *collector* electrode at 0.3 V. The collection efficiency *N*, defined as

$$N = \frac{|I_{coll}|}{|I_{gen}|} \tag{2.9}$$

where I_{coll} and I_{gen} are the currents recorded at the corresponding electrodes (*collector* and *generator* electrode), was determined for each sample at the same, precisely

controlled electrolyte flow rate as used in the oxygen reduction reaction (ORR) experiments.

Determination of the H_2O_2 yield – $x_{H_2O_2}$

The hydrogen peroxide production at the generator electrode in O_2-saturated 0.5 M H_2SO_4 electrolyte was monitored using a polycrystalline Pt collector electrode biased at 1.2 V. Using the collection efficiency N determined previously (eq. 2.9), the fractional hydrogen peroxide yield, $x_{H_2O_2}$, during the ORR, which describes the fraction of H_2O_2 formed relative to the total amount of O_2 consumed, was calculated as

$$x_{H_2O_2} = \frac{2 \cdot \frac{I_{coll}}{N}}{I_{gen} + \frac{I_{coll}}{N}}. \tag{2.10}$$

where 2 corresponds to the number of electrons for the reduction of an O_2-molecule to H_2O_2 and I_{coll} and I_{gen} are the currents recorded at the corresponding electrodes (*collector* and *generator* electrode, respectively). This evaluation procedure follows that employed in rotating ring disk electrode (RRDE) measurements. For further details see, e.g., refs. [162–164].

Tafel Plots

In *chapter* 6, the mass transport-normalized kinetic ORR currents at the working (*generator*) electrode were determined as

$$I_k = \frac{I_{lim} \cdot I_{gen}}{I_{lim} - I_{gen}} \tag{2.11}$$

with I_{lim} denoting the ORR mass transport limited current at 0.2 V. They are presented in *chapter* 6 in Tafel plots as kinetic ORR current densities normalized to *(i)* the geometric electrode area and *(ii)* the active Pt surface area of the corresponding electrode. The latter was calculated via hydrogen underpotential deposition (H_{upd}) charge (see eq. 2.4).

Mass Transport Limited ORR Current

The advantages of the thin-layer flow cell configuration introduced and developed by Jusys et al. [3, 155], which was used in this work, were already mentioned in subsection 2.3.3 (see also Fig. 2.11). To summarize briefly: A high collection efficiency and reasonable time resolution under well-defined transport conditions are provided. In this flow cell configuration, a laminar flow regime is attained, which is proven by the equation describing the linear correlation between mass transport limited current

(I_{lim}) and the cubic root of the electrolyte flow rate (υ) [74, 165, 166]:

$$I_{lim} = k\ n\ F\ c\,\upsilon^{1/3}\,(DA/b)^{2/3}, \tag{2.12}$$

where k is the cell constant ($k = 1.467$ for a thin-layer channel-flow cell), n is the number of electrons, F is the Faraday constant, c is the concentration of the species involved in the reaction, υ is the electrolyte flow rate, D is the diffusion coefficient of the reacting species, A is the electrode surface area, and b is the thickness of the thinlayer gap, respectively.

Recently, a numerical calculation of the limiting current for the same cylindrical thin-layer flow cell as it was used in this study, based on the equation given above, was presented by Fuhrmann et al. [167].

A plot of the linear dependence of the mass transport limited ORR current (at 0.2 V) vs. the cube root of the electrolyte flow rate in the double disk dual thin-layer flow cell configuration over a polycrystalline Pt and nanostructured Pt/GC electrodes is presented in *chapter* 6.

2.5 Chemicals

Throughout this work, 0.5 M H_2SO_4 was used as base solution. The supporting electrolyte was prepared from Millipore MilliQ water (resistivity $\geq 18\,M\Omega\,cm$) and ultrapure sulphuric acid (Merck, suprapur), and was continuously de-aerated by high purity Ar gas (MTI Gases, N 6.0).

Chapters 3–5: For CO_{ad} stripping and continuous CO bulk oxidation experiments, CO-saturated (Messer-Griesheim, N 4.7) supporting electrolyte was employed.

Chapter 6: For continuous O_2 reduction experiments, the base solution was saturated with O_2 (MTI Gase, N 5.7).

Chapter 7: The methanol oxidation experiments were performed in 0.5 M H_2SO_4 solution containing 0.1 M of CH_3OH (Merck, purity = 99.5%).

3 Stability of Nanostructured Pt/Glassy Carbon Electrodes Prepared by Colloidal Lithography

Y. E. Seidel[1], R. W. Lindström[1], Z. Jusys[1], M. Gustavsson[2], P. Hanarp[2], B. Kasemo[2], A. Minkow[3], H. J. Fecht[3] and R. J. Behm[1]

[1] Institute of Surface Chemistry and Catalysis, Ulm University, D-89069 Ulm, Germany
[2] Dept. of Applied Physics, Chalmers University of Technology, S-41296 Gothenburg, Sweden
[3] Institute of Micro- and Nanomaterials, Ulm University, D-89069 Ulm, Germany

Published in

Journal of the Electrochemical Society 155 (3) (**2008**) K50–K58

Abstract

The stability of nanostructured Pt/glassy carbon (GC) model electrodes upon exposure to a realistic electrochemical/electrocatalytic reaction environment (continuous reaction, continuous electrolyte flow) was studied by microscopic techniques, X-ray photoelectron spectroscopy, and electrochemical measurements.

The model electrodes consist of Pt nanostructures with well-defined sizes and regular spacing on planar GC substrates, and were fabricated using colloidal lithography techniques. Additional plasma treatments of the GC substrates prior to Pt deposition were tested to improve the stability of the resulting Pt/GC model electrodes. Both evaporation and sputter deposition were used for Pt-film fabrication. The model catalysts prepared by Pt evaporation were found to be rather unstable. The stability was significantly improved for sputter-deposited Pt films, and Pt sputter deposition on a GC substrate, pretreated first in oxygen plasma and then in Ar plasma, resulted in stable model electrodes with a fully intact layer of Pt nanostructures after the electrocatalytic experiments.

3.1 Introduction

Model catalysts consisting of catalytically active nanoparticles deposited on a planar support material have been employed extensively for fundamental studies of catalytic reactions at the solid-gas interface [52–55, 101, 168]. Due to their well-defined structural properties and their accessibility to electron spectroscopies and structural characterization, these model systems have provided detailed insight into the molecular-scale processes contributing to the overall reactions. We recently developed similar model systems for studies of electrocatalytic reactions [65, 109], using Colloidal Lithography (2.1.1 CL) [59–63] as a tool for the controlled preparation of planar, nanostructured model electrodes with catalytically active noble-metal nanostructures of well-defined size and interparticle distances. Because of the narrow size distribution and the regular arrangement of the noble-metal nanostructures, as well as the possibility of independently varying these two parameters over a significant range, while also benefiting from the ability of CL to affordably produce large areas, these systems are particularly well suited for studies of transport effects. Such effects, which could significantly affect the reaction process, e.g., via creation of gradients and/or re-adsorption and further reaction of volatile reaction intermediates [25], can be studied by investigating the changes in reaction characteristics upon controlled variation of parameters such as electrolyte flow, density, or size of the active nanostructures [97, 111]. The first results on the morphology and electrochemical/electrocatalytic properties of a Pt/glassy carbon (GC) model system consisting of a uniform array of Pt nanostructures (120 ± 10 nm in diameter) on a planar GC substrate, using the oxidation of a preadsorbed CO_{ad} monolayer as test reaction, have been reported previously [65, 97, 109].

The application of these model systems for studying transport effects in electrocatalytic processes requires measurements under enforced electrolyte flow and under continuous reaction conditions, which in turn may lead to extensive gas evolution. In contrast to reaction studies at the gas-solid interface, these reaction conditions are highly demanding on the mechanical stability of the model catalysts. In fact, the first measurements on Pt/GC model catalysts under continuous reaction/transport conditions showed that the model catalysts appeared to lose activity with time, which could indicate a loss of Pt nanostructures from the substrate. For quantitative studies on the influence of transport and reaction parameters in electrocatalytic reactions, the electrodes have to be fully stable during the reaction. Therefore, with activity losses below a few percent over longer times, we have investigated in detail the stability of these nanostructured electrodes under continuous electrocatalytic reaction and electrolyte flow conditions. Results of this study and systematic attempts

to improve the stability are reported here.

The stability of the model electrodes was dominated by the adhesion between the Pt nanostructures and GC substrate and hence by the interaction between Pt and GC. Therefore, in the first step, we modified the surface chemistry and morphology/roughness of the GC substrate prior to Pt deposition by an additional processing step („pretreatment“) after mechanical polishing and chemical cleaning of the GC substrate and before Pt deposition. The polished and cleaned GC substrate was subjected to an Ar plasma or sequentially to an oxygen- and an Ar-plasma treatment [169]. The influence of varying the Pt deposition procedure was also investigated using not only Pt evaporation, as done previously [65], but also Pt sputter deposition. The plasma pretreatment of the GC surface was applied to remove adsorbed contaminants such as quinone-type adsorbed species [123], which via saturation of dangling bonds of the GC substrate may affect the interaction between GC and Pt. Furthermore, the plasma treatment is also expected to increase the surface roughness, which in turn could also help to improve the adhesion properties [169]. For similar reasons, sputter deposition of the Pt film was employed as an alternative to Pt evaporation to fabricate better adhering Pt films, because the higher kinetic energy and momentum of the Pt atoms/ions in the case of sputtering may cause penetration of Pt into the carbon substrate and thus a stronger mechanical binding of the Pt film on the carbon substrate and/or other adhesion-promoting effects. Finally, the initial electrochemical cleaning of the Pt deposit, which is typically performed by potential cycling [24, 65, 170], has to be optimized for each preparation procedure with respect to Pt cleaning and electrode stability to keep the oxidation of the GC support at a tolerable level and to remove organic adsorbates on the resulting Pt nanostructures [65, 171].

These topics were investigated using CL-prepared Pt/GC model electrodes with Pt nanostructures $\sim 145\,\text{nm}$ in diameter as an example. The morphology of the pretreated GC substrate and of the resulting nanostructured Pt/GC surfaces was characterized by atomic force microscopy (2.2.5 AFM) and scanning electron microscopy (2.2.1 SEM). Transmission electron microscopy (2.2.3 TEM) measurements yielded structural information on the interface between GC substrate and the Pt nanostructures, and the surface composition was evaluated by X-ray photoelectron spectroscopy (2.2.4 XPS). The stability of the Pt/GC model systems under electrocatalytic reaction conditions was evaluated by electrochemical measurements, comparing the cyclic voltammograms (CVs) in base electrolyte (base CVs) and the uptake of underpotential deposited hydrogen (H_{upd}) before and after the electrochemical experiments (2.4.1 Active Surface Area Determination via H_{upd}), and by SEM imaging before and after these experiments. The electrochemical/electrocatalytic measure-

ments were performed in a dual thin-layer flow cell (see section 2.3.3) connected to a differential electrochemical mass spectrometry (2.3.2 DEMS) set-up and included initial electrochemical cleaning by rapid potential cycling, base CVs, and subsequent CO_{ad} monolayer oxidation (2.4.1 „CO_{ad} stripping“) as well as CO bulk oxidation (via CO_{ad}) measurements. The latter reaction is expected to be particularly demanding for the structural integrity of the model electrodes because of considerable gas evolution during the reaction.

3.2 Results and Discussion

3.2.1 Characterization of the GC Substrate Surface and of the Pt/GC Model Catalysts

The Pt nanostructures produced in this study have a diameter of $\sim 145\,\text{nm}$ and an average distance between their centers of 210 nm (density $\sim 2 \times 10^9\,\text{cm}^{-2}$), which means that about 30 % of the geometric surface area of the GC substrate is covered by Pt nanostructures. Figure 3.1 shows SEM images of the resulting nanostructured Pt/GC model catalysts. The light grey area in the large-scale image in Fig. 3.1a represents the Pt-covered electrode surface (6 mm in diameter) on the GC support. The higher-resolution images in Fig. 3.1b, c demonstrate the regular spacing of the Pt nanostructures. Similar images were obtained for the different types of GC substrate pretreatment and for both types of Pt deposition, indicating that prior to the electrochemical measurements the Pt/GC model catalysts are fully covered by an adlayer of regularly spaced Pt nanostructures.

The chemical composition of the GC substrate before metal deposition and after polishing and chemical cleaning by base/acid treatment and subsequent Ar or oxygen plasma treatment was examined by XPS. The elemental surface compositions of a GC sample directly after chemical cleaning and those of samples treated subsequently in an oxygen or Ar plasma, as derived from XPS survey spectra, are listed in Table 3.1.

After chemical cleaning, the sample was contaminated by small amounts of Si, N, F, and Al. The fluorine most likely originated from the Teflon holders in which the samples were transported between the laboratories, while Si and Al traces could result from the base/acid cleaning of the surface after polishing and the base plate of the plasma system, respectively. Most of the contaminations were removed by the plasma treatment; only the nitrogen content was slightly increased. Surprisingly, the oxygen content was increased on both plasma treated surfaces compared to the polished sample, with a slightly higher value for the oxygen-plasma-treated sample

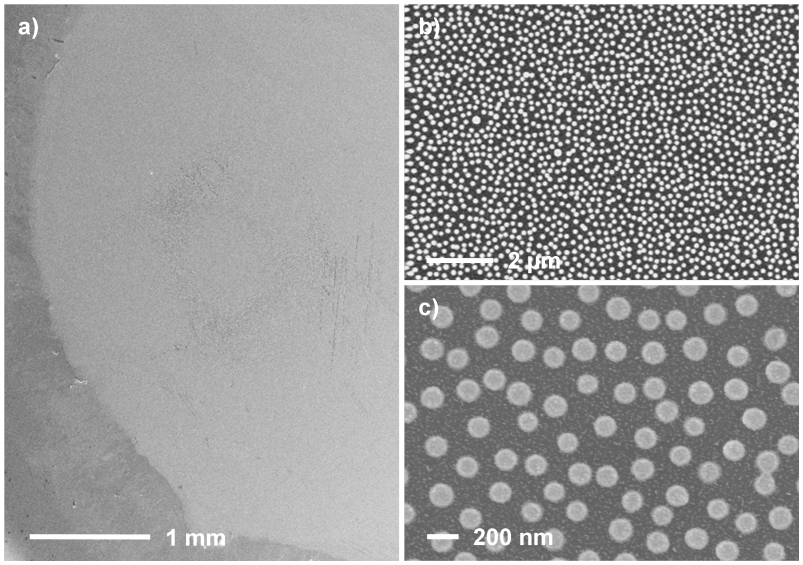

Figure 3.1: Representative SEM images of a nanostructured Pt/GC electrode surface prepared by Colloidal Lithography before electrochemical experiments (Pt evaporation, no further pretreatment of the GC substrate). (a) Overview (4.1 mm × 5.6 mm), light grey: Pt covered area, dark grey: GC substrate, (b) Large-scale (13.6 μm × 10.2 μm) and (c) high-resolution (2.8 μm × 2.1 μm) SEM images.

compared to the Ar-treated sample. Apparently, the dangling bonds created upon sputtering and removal of the other contaminants are saturated by oxygen, either during plasma treatment (O_2 trace impurities in the Ar gas in the low ppm range may be sufficient for this) or during subsequent exposure to air.

Detail spectra of the C(1s) region and the fits by different components are shown in Fig. 3.2, and the corresponding data are listed in Table 3.2. For all three samples, the spectra are dominated by the GC-related C(1s) peak at 284.3 eV. A second peak at ∼ 286.1 eV contributes to all samples by about 20 %, which is most likely related to oxygenated carbon species on the surface such as quinones, carbonyls, or phenolic species (see ref. [123] and references therein). Finally, a peak at ∼ 288.5 eV, which is more pronounced on the plasma pretreated samples than on the untreated sample, is attributed to surface carbonates.

From the similarity in carbonate intensity for the two plasma pretreated samples we conclude that carbonate formation occurs during subsequent exposure to air rather than during plasma treatment. A small peak at ∼ 291.7 eV on the untreated sample is related to contamination by fluorinated hydrocarbons. In conclusion, there are no significant differences between the different GC surface compositions. Nevertheless, the existing difference in surface termination may still have some effect on the interaction between the GC substrate and Pt film.

Table 3.1: Atomic ratio of the surface element found in the XPS survey spectra after different pretreatments.

surface element	**only base & acid cleaning** / atom %	**oxygen plasma** / atom %	**argon plasma** / atom %
C(1s)	86.9	83.5	83.5
O(1s)	9.8	15.5	14.7
F(1s)	2.1	-	-
N(1s)	0.6	1.0	1.1
Si(2p)	0.4	-	-
Al(2p)	-	-	0.7

Table 3.2: Atomic ratio of the carbon surface species found in the C(1s) detail spectra after different pretreatments.

GC sample processing	**binding energy** / eV	**FWHM** / eV	**area** / %
only base & acid cleaning	284.3	1.4	73.8
	286.1	1.9	20.1
	288.5	1.8	6.1
with additional oxygen-plasma treatment	284.3	1.3	63.6
	286.1	2.6	26.2
	288.5	2.0	10.2
with additional argon-plasma treatment	284.3	1.4	70.1
	286.1	2.0	19.7
	288.5	1.9	10.2

X-ray photoelectron spectra of the model catalysts after electrochemical treatment were published earlier [65].

They showed a broad Pt(4f) peak with a maximum at 71.2 eV and a high-energy component at 72.3 eV. These features were related to metallic Pt and oxidized Pt species, where the latter may result from transport to air. Similar results are also expected for the present model catalysts.

A second important factor for the contact between deposited film and substrate is the surface roughness. Based on the AFM images and AFM cross-sections shown in Fig. 3.3 and other similar data, the surface roughness does not differ significantly for the different GC surface treatments (Fig. 3.3a: no further treatment, Fig. 3.3b:

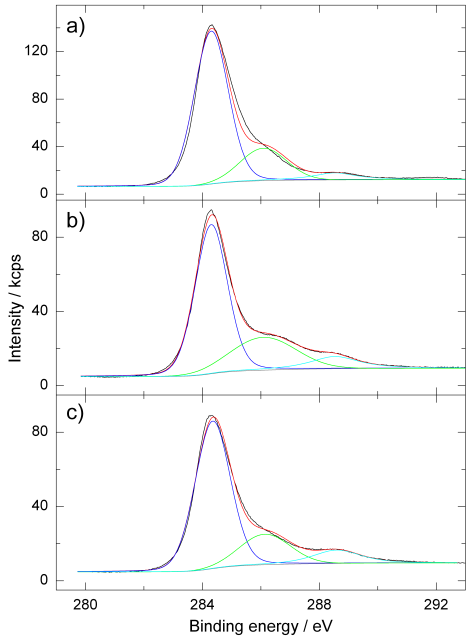

Figure 3.2: C(1s) detail spectra of the GC substrates after different pretreatment procedures on (a) a polished and chemically cleaned GC-substrate, (b) with additional oxygen-plasma pretreatment and (c) with additional Ar-plasma pretreatment.

oxygen plasma pretreatment, Fig. 3.3c: Ar plasma pretreatment). The surfaces were about equally rough on a nanoscopic scale, with peak-to-valley height variations of about 8.0 nm for a 1 μm^2 area (see also the line cuts in the middle row in Fig. 3.3). The corresponding root-meansquare values were $\sim$2 nm. The roughness values are average values from three section analyses not including deep scratches. Hence, the nanometer roughness detected by these measurements is apparently dominated by the polishing process preceding the further treatment before Pt deposition rather than by the subsequent plasma treatment.

3.2.2 Electrochemical Properties of the Nanostructured Pt/GC Model Electrodes

The electrochemical/electrocatalytic properties of the model catalysts were investigated by base CVs, oxidation of a preadsorbed CO_{ad} monolayer (2.4.1 „CO_{ad} stripping“), and CO bulk oxidation. The latter measurements were performed under continuous electrolyte flow in order to test the stability of the model systems under conditions relevant for electrocatalytic studies.

Representative results of the electrochemical/electrocatalytic measurements of the

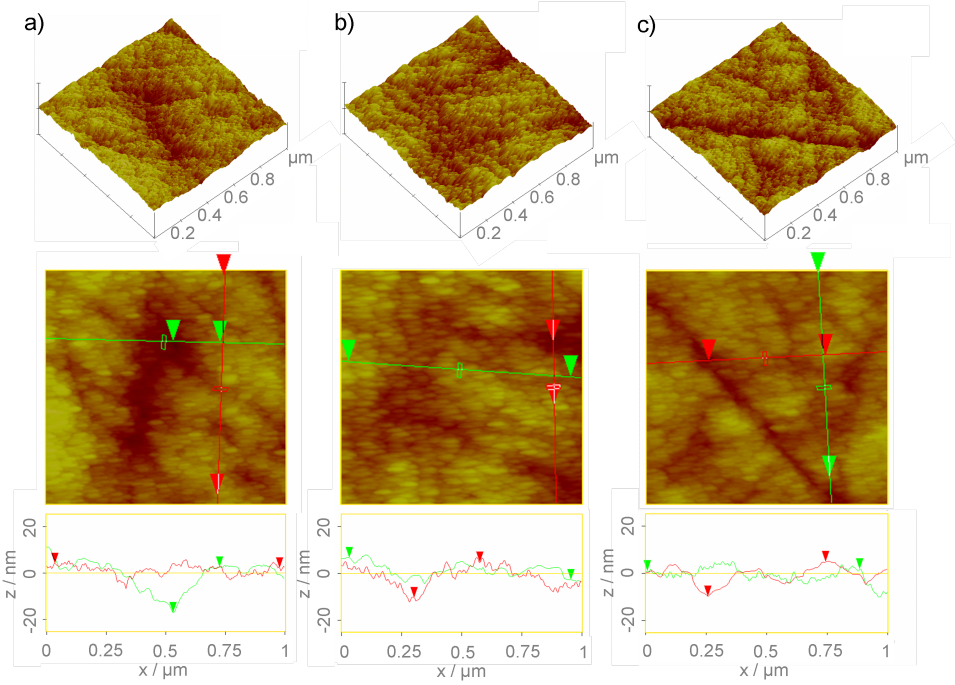

Figure 3.3: Representative AFM images and line scans of the GC substrate surface prior to Pt deposition on (a) a polished and chemically cleaned GC, (b) with additional oxygen-plasma pretreatment and (c) with additional Ar-plasma pretreatment. (Top row) AFM images in a bird´s eye view representation, (middle row) topview color scale representation, with brighter colors representing higher areas, and (bottom row) line cuts along the directions indicated in the AFM images.

nanostructured Pt/GC model catalysts are shown in Fig. 3.4 for samples prepared via either Pt evaporation (black lines) or sputter deposition (red lines) on Ar-plasma pretreated GC substrates and subsequently Colloidal Lithography. The resulting, stable Faradaic CV (upper graphs) and mass spectrometric current densities (lower graphs), recorded at a scan rate of $10\,\mathrm{mV\,s^{-1}}$ (second scan) after the CO_{ad} stripping scan (first scan), are normalized versus the electrochemically active surface area of the respective model systems (see Fig. 3.4a). The CVs of the nanostructured Pt/GC model electrodes (Fig. 3.4a, upper graph) show H_{upd} features characteristic for polycrystalline Pt [170, 172]. Except for the small difference in signal heights, with a slightly higher charge for the sample prepared via Pt sputter deposition, there is virtually no difference in the CVs of the two samples. The larger pseudo-capacitive currents in the double-layer region compared to pure polycrystalline Pt result from contributions from the GC support (Fig. 3.4a, upper graph) and are typical for Pt nanoparticle modified GC electrodes [65, 173–175] and carbon-supported catalysts [21, 155, 176–178]. The charge in the H_{upd} adsorption/desorption peaks was used to determine the electrochemically active surface area of the respective model electrode,

assuming a H_{upd} monolayer adsorption charge on polycrystalline Pt of $0.21\,mC\,cm^{-2}$ [2] and a hydrogen coverage at the onset of H_2 bulk evolution of 0.77 monolayers [152]. These values were determined before the electrochemical measurement, after the initial electrochemical cleaning procedure, and after the electrochemical measurements. The resulting values are collected in Table 3.3. The decrease in active surface areas is a straightforward, simple measure of the stability of the model electrode, although it does not contain any information about the origin or nature of the reaction-induced loss in active surface area (section 3.2.3).

The CO_{ad} stripping scans exhibit the characteristic double-peak structure, which was also reported previously for these nanostructured model electrodes [65], with peaks at ~ 0.70 and $\sim 0.765\,V$. Different from the H_{upd} signals, these traces reveal distinct differences between the two sample types (Pt evaporation and Pt sputter deposition). Similar to previous findings [65], the first oxidation peak is somewhat higher than the high-potential peak for the evaporated Pt-film-based electrodes, while samples prepared via Pt sputter deposition are characterized by a dominant low-potential peak and a much smaller high-potential component. These characteristics are fully reproduced in the mass-spectrometric scans, following the $m/z = 44$ signal of CO_2. The tenfold magnified mass-spectrometric traces (Fig. 3.4 a, lower graph, dotted lines) illustrate the existence of the characteristic CO_{ad} oxidation prewave which is commonly observed on Pt electrodes [133, 179, 180] and catalysts [155]. The exact ratio of the two peak heights was also found to depend on the Pt coverage, with the second peak increasing when going to lower Pt coverages (equivalent to smaller densities or sizes of the Pt nanoparticles) [97, 181]. The general trend of a more pronounced first peak on the Pt sputter-deposited samples compared to the Pt evaporated samples, however, was observed reproducibly for otherwise similar Pt/GC samples.

The formation of different CO_{ad} oxidation peaks on Pt electrodes was attributed to differently oriented facets on the polycrystalline Pt nanostructures [182–184], and accordingly the different appearance of the CO_{ad} stripping peaks on the two different sample types could be explained by structural differences of the film surfaces, such as differences in the preferential orientation or different contents of specific facets, different defect densities, etc. However, we have recently shown that for a nonstructured Pt/GC electrode, which was prepared in the same way except for the structuring step and which is structurally identical to the Pt nanostructures, CO_{ad} oxidation occurs only in a single low-potential peak at 0.70 V [97]. Furthermore, similar high-potential peaks have been reported for carbon-supported Pt/C catalysts [155, 176–178] and were explained in terms of a pronounced particle-size sensitivity of the CO_{ad} oxidation reaction [177, 178]. Therefore, we suggest that the

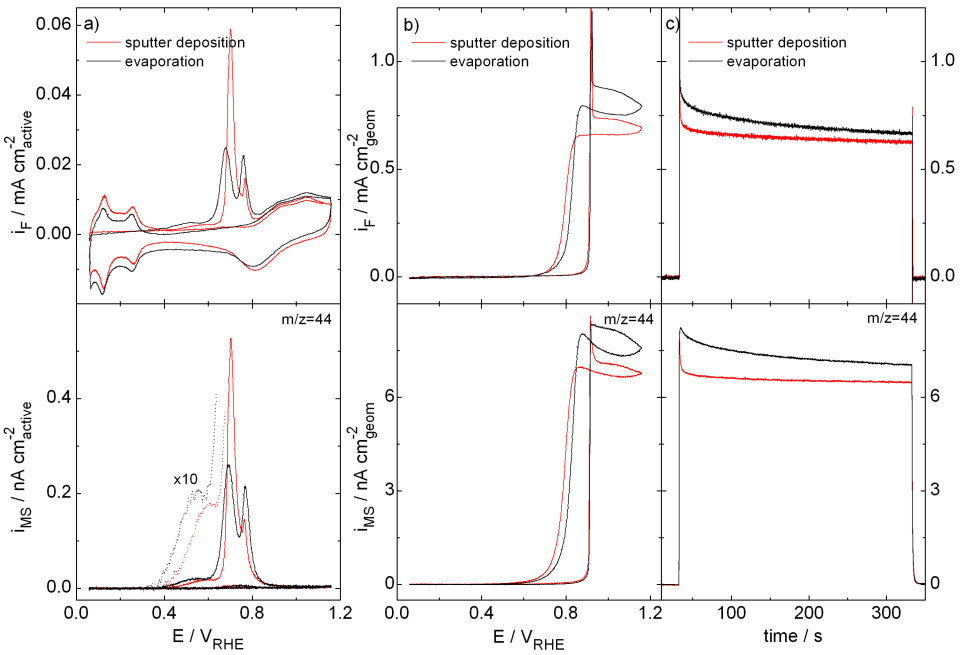

Figure 3.4: CO electro-oxidation on nanostructured Pt/GC electrodes pretreated in an Ar plasma (black line: vapor deposited Pt film, red line: sputter deposited Pt film), showing the Faradaic current densities (top) and the m/z = 44 mass spectrometric current densities (bottom) corresponding to CO_2 production. The CO_{ad} stripping current was normalized vs. the electrochemically active Pt surface area, and the currents of continuous CO oxidation were normalized vs. the geometric electrode surface area. (a) CO_{ad} stripping of preadsorbed CO ($E_{ad} = 0.06$ V), (b) continuous potentiodynamic CO oxidation, and (c) CO oxidation transients upon stepping the potential from 0.06 to 1.06 V (room temperature, CO-saturated 0.5 M H_2SO_4, 10 mV s^{-1}, 10 μL s^{-1} electrolyte flow).

low-potential peak results from CO_{ad} oxidation on the Pt nanostructures, while the high-potential peak is caused by CO_{ad} oxidation on small Pt nanoparticles. Direct experimental proof for the existence of such nanoparticles on the GC areas is presented in the following section; a more detailed study on the electrocatalytic role of these nanoparticles is presented in *chapter* 4.

The currents for continuous bulk oxidation of CO, presented both as a potentiodynamic measurement (Fig. 3.4b) and potentiostatic potential-step transients at 1.06 V (Fig. 3.4c), were normalized vs. the geometric electrode surface area. They closely resemble previous results obtained on massive, polycrystalline Pt electrodes [183, 185], Pt film electrodes [144], or Pt nanoparticles [155]. During potentiodynamic CO oxidation (Fig. 3.4b) the reaction is fully inhibited at lower potentials due to complete blocking by CO_{ad}, followed by a steep increase of the Faradaic current and the mass-spectrometric CO_2 signal at the onset of CO_{ad} oxidation. The

reaction starts at higher potentials than CO_{ad} stripping (Fig. 3.4a) because of the continuous supply of CO to the surface, which maintains a saturated adlayer to higher potentials and therefore hinders adsorption of OH species and subsequent CO oxidation. At further increasing potential the current is mass transport limited and then decreases due to Pt oxide formation. In the reverse, negative-going scan, the current approaches the mass transport limited value and then decays suddenly when the CO_{ad} oxidation rate becomes too small to avoid saturation of the surface by CO_{ad} (for more details see ref. [97]). The onset potential during CO bulk oxidation is virtually identical for both samples, similar to onset potentials observed during CO_{ad} stripping.

Also, the CO oxidation transients generally resemble previous data obtained on Pt electrodes and supported (model) catalysts [97, 111, 185]. In contrast to similar experiments on polycrystalline Pt [111] or polycrystalline Pt films [97], the transients of the nanostructured samples show a slight decay of both the Faradaic current and the mass spectrometric CO_2 signal with time, which is considerable for the sample prepared by Pt evaporation and rather small on the sample prepared by sputter deposition. In both cases the decay is larger than that observed on samples prepared by Pt sputter deposition on GC substrates pretreated in oxygen and Ar plasma [97]. Because samples prepared via Pt sputter deposition were significantly more stable than those fabricated via Pt evaporation, and sputter-deposited samples pretreated in oxygen and Ar plasma were the most stable (see the next section 3.2.3), we attribute the slight decay of the activity with time mainly to a decrease in active surface area due to a loss of Pt nanostructures rather than to a decay of the inherent Pt surface area normalized activity.

3.2.3 Stability of the Pt/GC Model Electrodes

The stability of the Pt/GC model electrodes in electrochemical and electrocatalytic measurements was evaluated by comparing the H_{upd} charge before and after these measurements and by SEM images recorded before and after the treatment. Because the morphology of the initial electrode was highly reproducible and independent of the GC treatment or Pt-deposition procedure, we present only SEM images recorded after the electrochemical measurements.

Typical SEM images of model electrodes prepared by Pt evaporation and different GC pretreatments are shown in Fig. 3.5a, b: chemical cleaning only and Fig. 3.5d e: additional Ar-plasma treatment. The corresponding base CVs before and after electrochemical treatment are shown in Fig. 3.5c, f. The images in the upper row indicate that after electrochemical measurements both surfaces still exhibit a rather

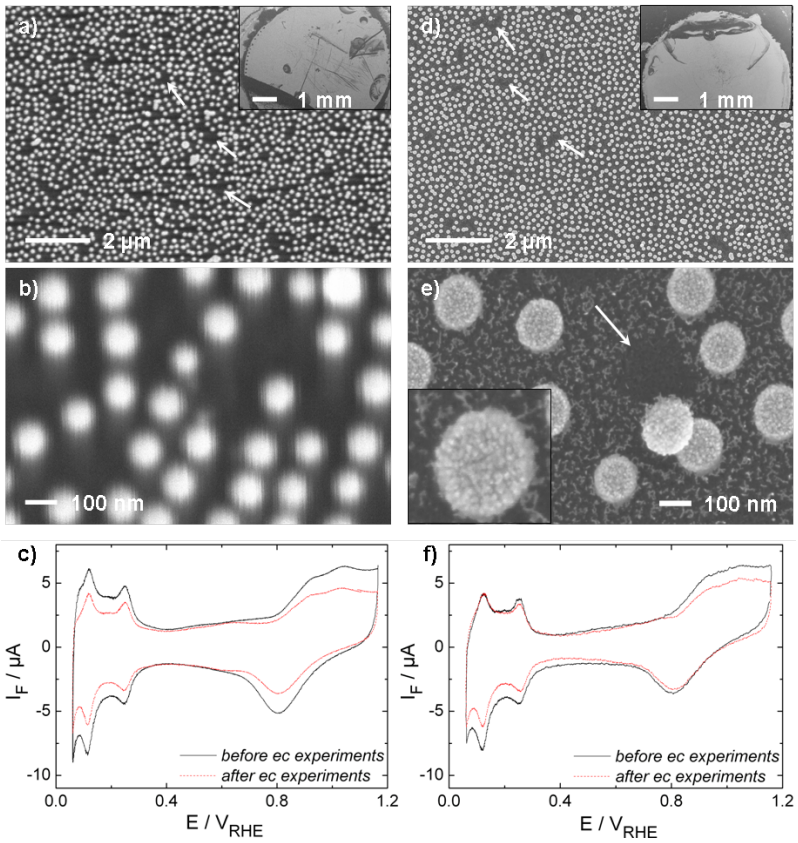

Figure 3.5: Representative SEM images of nanostructured Pt/GC model catalysts prepared by Pt evaporation on a GC substrate (a and b) without further treatment and (d and e) with Ar-plasma pretreatment, recorded after electrochemical cleaning (repetitive potential cycling to 1.36 V) and CO bulk oxidation in CO saturated 0.5 M H_2SO_4. (c and f) Base CVs recorded before and after the electrochemical measurements described above (0.5 M H_2SO_4, 10 mV s^{-1}).

homogeneous adlayer of Pt nanostructures. Apparently, on this scale the electrochemical treatment did not affect the Pt nanostructures. Going to a larger scale, however, the overview images in the insets reveal that on some areas („black areas“) of the GC surface the Pt adlayer is completely removed. We speculate that the removal of the Pt nanostructures on these areas is related to the formation of CO_2 bubbles formed at the electrode upon CO oxidation. As seen in the high-resolution SEM images (Fig. 3.5b, d), individual Pt nanostructures can also be removed from or displaced laterally on the surface during the CO oxidation experiments. This is evident, e.g., by the dark areas, which we expect to reflect the former locations of two Pt nanostructures (see white arrows).

In comparing the two samples (not pretreated or plasma pretreated), the Ar pretreatment improves the stability of the Pt nanostructures to some extent, as evidenced by the H_{upd} charge (38 % loss of active surface area on the untreated

sample and 23 % loss on the Ar- plasma pretreated sample; see Table 3.3) and by the SEM images. Nevertheless, after plasma pretreatment, the model electrodes are not fully stable against electrochemical/electrocatalytic measurements under realistic reaction conditions (continuous electrolyte flow and evolution of gaseous products).

Representative SEM images of the second type of nanostructured Pt/GC electrodes, which were prepared via Pt sputter deposition and subsequent Colloidal Lithography, are shown in Fig. 3.6 (top and middle row). Also, for these samples the GC substrate was pretreated in Ar and/or oxygen plasma. (Pt deposition on nontreated GC substrates was not investigated because it was known already that plasma pretreatment improves the stability of the Pt nanostructures on the substrate.) Similar to the experiments shown in Fig. 3.5, SEM images and base CVs were recorded before (CVs) and after (SEM images, CVs) CO_{ad} stripping and continuous CO oxidation experiments. High-resolution and medium-resolution SEM images after electrochemical treatment are shown in the top and middle row in Fig. 3.6, respectively, and the related base CVs recorded are presented in the bottom row (left column: Ar-plasma pretreatment, right column: oxygen and Ar-plasma pretreatment).

For the Ar-plasma pretreated model electrode, we find only a few small areas where the Pt nanostructures were removed completely, e.g., due to CO_2 bubble formation (see inset of Fig. 3.6a). The removal/displacement of individual Pt nanostructures in an otherwise intact adlayer area was not detected in high-resolution SEM images (Fig. 3.6b) and is insignificant. Accordingly, the CVs recorded in base solution before and after the CO oxidation experiments revealed a rather small Pt loss ($\sim$10 %) after the CO oxidation experiment, significantly less than the $\sim$23 % decrease of the active surface on the samples prepared by Pt evaporation on the Ar-pretreated substrate (Fig. 3.5f).

Furthermore, we tried a sequential oxygen- and Ar-plasma treatment, with a short-term (30 s) oxygen-plasma treatment followed by an Ar-plasma treatment (2 min). This procedure indeed resulted in further improvement of the stability of the Pt/GC model catalyst, as evidenced by the SEM images of these samples after CO oxidation experiments (Fig. 3.6 d and e) and the H_{upd} charges in Table 3.3. Evaluating a number of high-resolution SEM images, we found no evidence for detachment of individual Pt disks. Also, the complete loss of Pt disks on a larger area (bubble imprints) was not observed on these surfaces (see inset of Fig. 3.6d).

From the high-resolution SEM images (particularly Fig. 3.6b, e), it is evident that the internal structure of the Pt nanostructures depends sensitively on the deposition method. The size of the Pt grains in the nanostructures produced via sputter

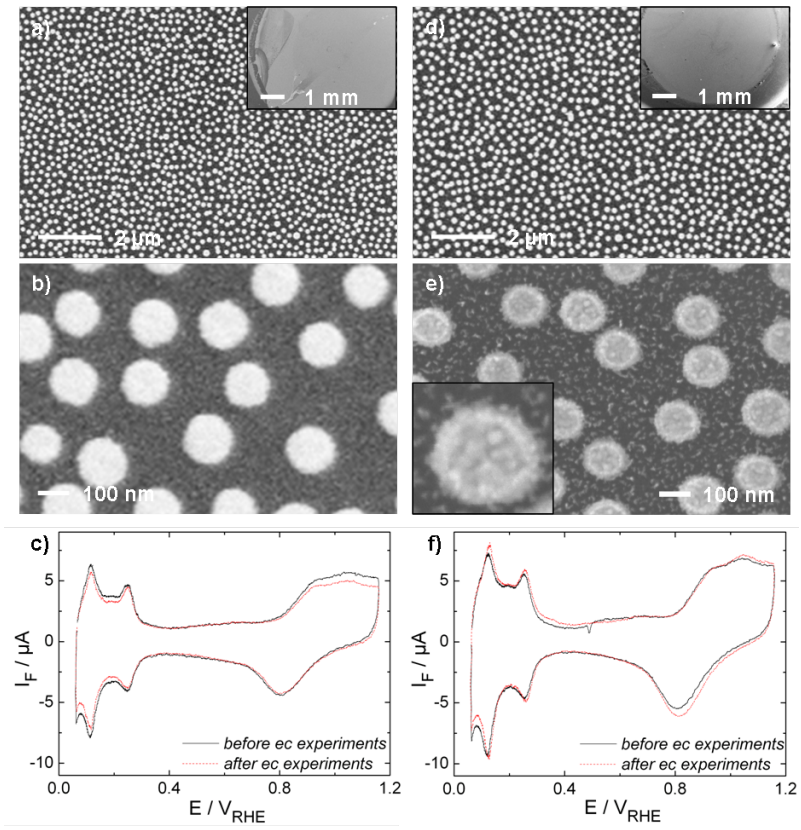

Figure 3.6: Representative SEM images of nanostructured Pt/GC model catalysts prepared by Pt sputter deposition on a GC substrate pretreated in (a and b) Ar-plasma pretreatment and (d and e) oxygen-plasma pretreatment followed by Ar-plasma pretreatment recorded after electrochemical cleaning (repetitive potential cycling to 1.36 V) and CO bulk oxidation in CO-saturated 0.5 M H_2SO_4. (c and f) Base CVs recorded before and after the electrochemical measurements described above (0.5 M H_2SO_4, 10 mV s^{-1}).

deposition (up to 15 nm in diameter) is about double that of the grains on the evaporated sample. A possible reason for this is the higher kinetic energy of the incident Pt atoms/clusters, which before they are thermalized „scan“ a larger area, i.e., that the kinetic energy provides an annealing effect, causing larger grains in the polycrystalline nanoparticles.

The generally better adhesion of the Pt nanostructures produced via sputter deposition on GC substrates compared to Pt evaporation based nanostructures agrees well with recent findings for the adhesion of Al films on GC substrates [169]. Based on the results of „tape peel-off“ tests, Kuhnke et al. determined a better adhesion of sputter-deposited metal (Al) films on GC substrates compared to evaporated metal films [169]. We believe that the improved adhesion of sputter-deposited films is a combination of several effects: the cleaning action related to higher energy and momentum of incident Pt atoms, the just-mentioned annealing effect causing larger

Table 3.3: H_{upd} and resulting active surface areas before and after cycling to higher potentials and electro-oxidation of CO on samples with different pretreatments and Pt deposition methods.

sample	GC sample processing	BEFORE H_{upd} / μC	BEFORE act. surf. area / cm^2	AFTER H_{upd} / μC	AFTER act. surf. area / cm^2	Pt loss / %
Pt evaporation	only base & acid cleaning	76	0.47	47	0.29	38.4
	with additional Ar-plasma	83	0.51	64	0.39	23.2
Pt sputtering	with additional Ar-plasma	74	0.46	66	0.41	10.8
	with additional oxygen- & Ar-plasma	94	0.58	93	0.58	~ 1

grains and better adhesion via more high-binding-energy sites, and the roughening, producing more binding sites per projected (unit) area.

In addition to GC pretreatment and Pt deposition, we also studied the influence of the positive potential limit during electrochemical cycling on the stability of the model electrodes (Fig. 3.7). For a sample prepared by Pt sputter deposition on a GC substrate pretreated in oxygen and Ar plasma, H_{upd} measurements indicate that there is no loss of active surface area upon cycling to 1.61 V, i.e., into the onset of O_2 evolution (Fig. 3.7a). Even after subsequent CO oxidation measurements (same conditions as for Fig. 3.5 and 3.6), subsequent H_{upd} measurements and SEM images show no indications for a loss of Pt particles (Fig. 3.7a–c). Comparable results were obtained for a model electrode prepared by Pt evaporation on an Ar-plasma pretreated sample. In this case, cycling to slightly lower potentials (positive potential limit 1.56 V), which are nevertheless 200 mV higher than the standard cleaning procedure (positive potential limit 1.36 V), shows negligible losses in surface area. The sensitivity of the adlayer toward flowing electrolyte is demonstrated by a subsequent experiment, where the electrolyte flow was enhanced by applying a slight overpressure to the electrolyte supply bottle. Base CVs and SEM images recorded subsequently reveal a considerable loss of active surface area (≥ 20 %) and Pt nanostructures on the sample (Fig. 3.7d–f).

Similar to observations after CO oxidation measurements (Fig. 3.5b), the Pt nanostructures are completely removed from entire areas. The effect of the electrolyte flow and reaction-induced gas evolution was illustrated in a third experiment per-

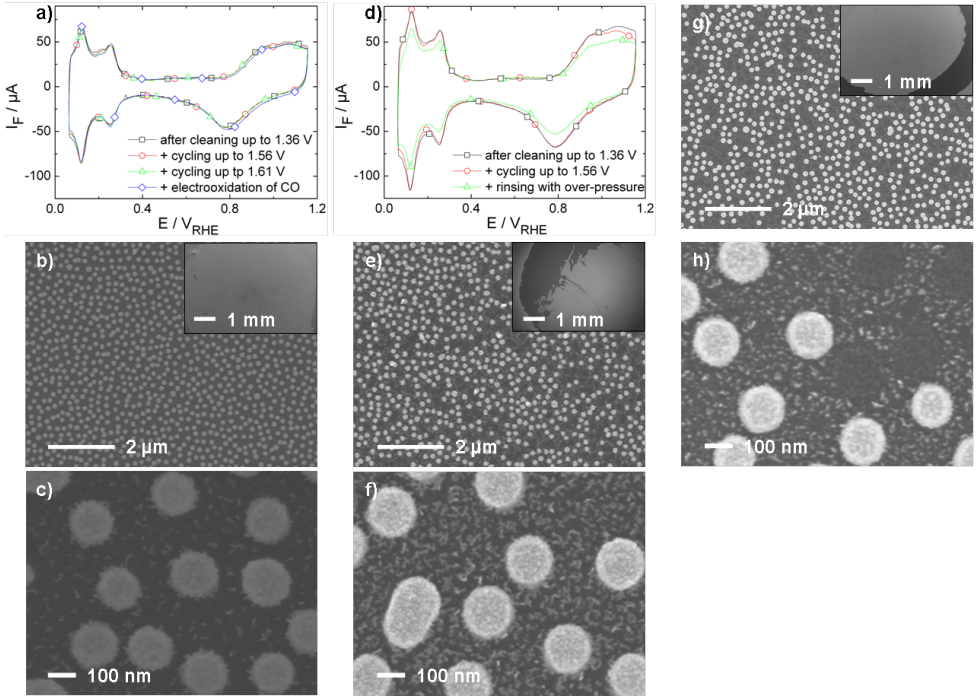

Figure 3.7: Representative SEM images and CVs of nanostructured Pt/GC model catalysts illustrating the effects: (a) Base CVs after electrochemical cleaning by repetitive cycling ($100\,\mathrm{mV\,s^{-1}}$) up to 1.36, 1.56 and 1.61 V on a Pt/GC model catalyst prepared by Pt sputter deposition on an oxygen and Ar plasma-treated GC substrate and after subsequent CO electro-oxidation measurements; (b and c) SEM images recorded on the sample in (a) after CO electro-oxidation treatment; (d) base CVs after electrochemical cleaning by repetitive cycling ($100\,\mathrm{mV\,s^{-1}}$) up to 1.36 and 1.56 V on a Pt/GC model catalyst prepared by Pt evaporation on an Ar-plasma-treated GC substrate and after subsequent exposure to pressure-enhanced electrolyte flow; (e and f) SEM images recorded on the sample in (d) after exposure to pressure-enhanced electrolyte flow; (g and h) SEM images recorded on a Pt/GC model catalyst prepared by Pt evaporation on an Ar-plasma pretreated GC substrate after standard electrochemical cleaning by repetitive cycling up to 1.36 V.

formed on a Pt/GC sample prepared by Pt evaporation on a Ar pretreated GC substrate and subsequent standard cleaning (cycling up to 1.36 V).

SEM images recorded after cycling (Fig. 3.5g, h) show areas where statistically distribute individual Pt nanostructures are missing ($\sim 10\,\%$ in these areas) but no areas with completely removed Pt nanostructures. Hence, the complete removal of Pt nanostructures on these samples is apparently associated with continuous CO oxidation, while electrochemical cleaning and base CVs in flowing electrolyte lead to the loss of individual Pt nanostructures only. Platinum dissolution and subsequent re-deposition, which was reported after keeping the potential at high values for extended times (up to 24 h [186]) [187, 188], is not significant under present conditions (several cycles to a positive potential limit of 1.36 V at a potential scan rate of $100\,\mathrm{mV\,s^{-1}}$) because of the short time spent at such high potentials. Platinum re-deposition is even further reduced by the continuous electrolyte flow in our experiments.

Finally, additional information on the Pt-GC interface and also on the surface of the Pt/GC model catalysts is obtained from cross-sectional TEM micrographs as shown in Fig. 3.8. The figure shows images of different magnifications (see scale bars on the images) of the sandwiched samples (for sample preparation see section 2.2.3 TEM), measured on a sample fabricated by Pt evaporation (left column) and on another sample produced by Pt sputter deposition (right column). Both samples were pretreated by Ar-plasma etching, where Ar sputtering is done in situ before sputter deposition but ex situ before evaporation. These representative TEM images provide further support for a lower stability of the Pt/GC electrodes produced by Pt evaporation. Figure 3.8a shows two Pt nanostructures, one on top of the other (see arrow), where the upper one was detached from the substrate, most likely the upper GC substrate, during sample preparation. Also, the neighboring nanostructure (at the left side) appears to consist of two layered nanoparticles based on its height, although in this case the two particles cannot be resolved. Such preparation-induced detachment of particles was not observed on samples prepared by sputter deposition (see, e.g., Fig. 3.8c). Figures 3.8b, d show magnified details with a single Pt nanostructure. Also, in this case the shape of the nanostructure in Fig. 3.8 b indicates that this was detached from the upper GC substrate surface and moved toward the lower substrate surface, together with the glue layer. The nanostructure in Fig. 3.8d, in contrast, is still on the correct substrate side. These images also illustrate the rather rough interface between Pt nanostructure and GC substrate, which is attributed to the initial roughness of the GC substrate (see AFM images in Fig. 3.3).

There are no distinct differences in interface roughness between evaporated and

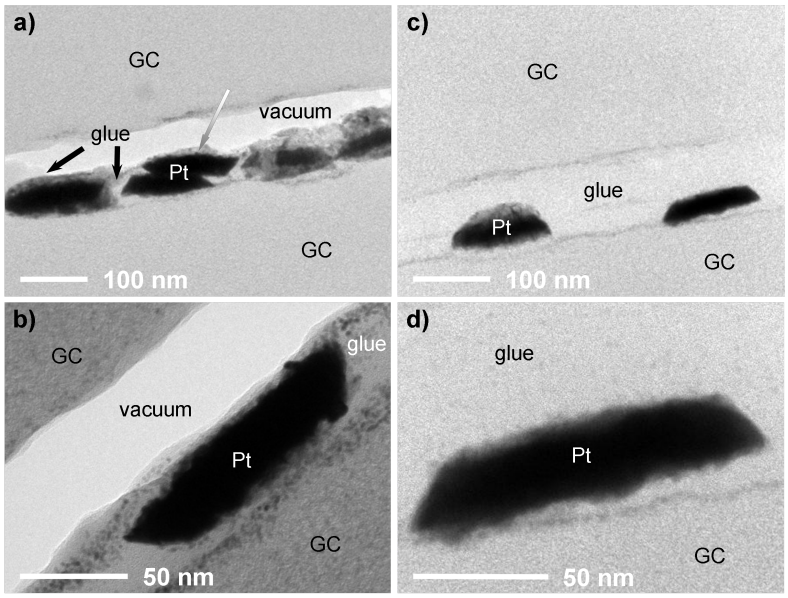

Figure 3.8: TEM cross-sections of the Pt/GC interface region in nanostructured Pt/GC model electrodes prepared via (a and b) Pt vapor deposition and (c and d) Pt sputter deposition on GC substrates pretreated in Ar plasma and subsequent Colloidal Lithography. Scale bars and the assignment of the different areas are given in the images (for sample preparation see section 2.2.3 TEM).

sputter-deposited Pt nanostructures.

Furthermore, we find a thin layer of high-contrast nanoparticles close to or at the surface, between the Pt nanostructure, which are attributed to Pt nanoparticles. As discussed in more detail in *chapter* 4, we suggest that these high-contrast nanoparticles represent Pt nanoparticles, with an average size of $\sim 5\,\mathrm{nm}$. These particles are also held responsible for the small white structures on the high-resolution SEM images, which are observed on the GC areas between the Pt nanostructures (see Fig. 3.5 and 3.6).

3.3 Conclusion

We have shown that, depending on the preparation procedure, the activity of nanostructured Pt/GC model electrodes prepared by Colloidal Lithography can deteriorate significantly during electrochemical/electrocatalytic measurements under realistic reaction and electrolyte flow conditions and upon formation of volatile gaseous products. Both base CVs and SEM images recorded before and after electrochemical cleaning (repetitive potential cycling) and reaction (CO_{ad} stripping and CO bulk oxidation) show a decrease in the electrochemically active surface area and a complete

loss of Pt nanostructure particles on larger areas. Furthermore, a loss or displacement of individual Pt nanostructures on otherwise intact adlayer areas is observed. Under present reaction conditions the stability is lowest for model electrodes prepared by Pt-film evaporation on a mechanically polished and chemically cleaned GC substrate and subsequent Colloidal Lithography ($\sim 40\,\%$ loss in active surface area). It is slightly improved if the GC substrate is treated in an Ar or oxygen plasma prior to Pt deposition (loss in active surface area $\sim 25\,\%$). Markedly higher stability is achieved by changing the Pt deposition method, using sputter deposition rather than evaporation. Samples pretreated in Ar plasma showed a strongly reduced tendency for removing the Pt adlayer in complete areas and no loss of individual Pt nanostructures (loss in active surface area $\sim 10\,\%$). Finally, GC pretreatment in first oxygen and then Ar plasma leads to model electrodes which are fully stable under present reaction conditions. These samples are also stable after electrochemical cleaning at more drastic conditions, upon potential cycling up to the onset of O_2 evolution (1.61 V). The measurements further indicate that the sample damage is mainly induced by the flowing electrolyte and product gas formation rather than by electrochemical cleaning.

Acknowledgement

This work was supported by the Landesstiftung Baden-Württemberg via the Kompetenznetz Funktionelle Nanostrukturen (project B9), the MISTRA fuel cell program, and the Swedish Energy Agency (grant no. P12554-1). The authors gratefully acknowledge Dr. A. Karpenko (Institute of Surface Chemistry and Catalysis, Ulm University) for the XPS evaluation and discussion and Dr. U. Hörmann (Electron Microscopy Institute, Ulm University) for the cross-sectional TEM analysis.

4 Nanostructured, Glassy Carbon Supported Pt/GC Electrodes: The Presence of Secondary Pt Nanostructures and How to Avoid Them

Y. E. Seidel[1], M. Müller[1], Z. Jusys[1], B. Wickman[2], P. Hanarp[2], B. Kasemo[2], U. Hörmann[3], U. Kaiser[3] and R. J. Behm[1]

[1] Institute of Surface Chemistry and Catalysis, Ulm University, D-89069 Ulm, Germany
[2] Dept. of Applied Physics, Chalmers University of Technology, S-41296 Gothenburg, Sweden
[3] Central Facility for Electron Microscopy, Ulm University, D-89069 Ulm, Germany

Published in

Journal of the Electrochemical Society 155 (10) (**2008**) K171–K179

Abstract

Nanostructured, glassy carbon (GC) supported Pt/GC electrodes, with Pt nanostructures (nanodisks) of controlled size (100–140 nm in diameter) and separation homogeneously distributed on a planar GC substrate, were recently shown to be interesting model systems for electrocatalytic reaction studies [M. Gustavsson, H. Fredriksson, B. Kasemo, Z. Jusys, C. Jun, and R. J. Behm, *J. Electroanal. Chem.*, **568**, 371 (2004)].

We present here electron microscopy and electrochemical measurements which reveal that the fabrication of these nanostructured electrodes via Colloidal Lithography, in addition to the intended nanodisks, results in a dilute layer of much smaller Pt nanoparticles (diameter ~ 5 nm) on the GC surface in the areas between the Pt nanodisks. We further demonstrate that by using the developed, related method of Hole-mask Colloidal Lithography (HCL) [H. Fredriksson, Y. Alaverdyan, A. Dmitriev, C. Langhammer, D. S. Sutherland, M. Zäch, and B. Kasemo, *Adv. Mater.* (*Weinheim, Ger.*), **19**, 4297 (2007)], similar electrodes can be prepared which are free from these Pt nanoparticles.

The effect of the additional small Pt nanoparticles on the electrochemical and electrocatalytic properties of these nanostructured electrodes, which is significant and can become dominant at low densities of the Pt nanodisks, is illustrated and discussed. These results leave HCL the preferred method for the fabrication of nanostructured Pt/GC electrodes, in particular, of low-density Pt/GC electrodes.

4.1 Introduction

Model studies of catalytic and electrocatalytic reactions, performed on structurally and chemically well-defined, but nevertheless more realistic systems than, e.g., polycrystalline or single-crystal (electrode) surfaces and under close-to-realistic reaction conditions (e.g., pressure, temperature, particle-support interactions), have attracted increasing interest in recent years [52–55]. Making use of new developments in the area of surface nanostructuring [56–64], we recently introduced Colloidal Lithography (2.1.1 CL) as a tool for the controlled preparation of planar nanostructured electrodes with defined particle sizes and particle distances [63, 65]. In this way, we could prepare nanostructured electrodes consisting of a planar glassy carbon (GC) substrate with electrochemically active Pt nanostructures (nanodisks) of adjustable, similar size (⌀ 80–140 nm) deposited on top. In addition to the narrow size distribution, the nanodisks are arranged in a rather regular array with a narrow distribution of interparticle separations, which uniformly covers the entire accessible electrode area. Both the size of the Pt nanodisks and their separation can be varied independently and in a controlled way. Hence, this method extends the possibilities of earlier lithographic approaches (compare ref. [56–58, 189] and [190]) for the preparation of such array structures, allowing the fabrication of arrays of ultra-microelectrodes with electrode sizes in the 100 nm range. Due to the well-defined arrangement of the nanodisks, which is much more regular than the statistical distribution of nanoparticles obtained, e.g., by physical vapor deposition or electrodeposition of metals, these model systems are ideally suited for studying transport and diffusion processes. Furthermore, they provide ideal test systems for simulations of these processes on arrays of microelectrodes [48–51, 191, 192].

These nanostructured planar electrodes were used as model systems for studies of the role of transport effects in electrocatalytic reactions, investigating the effect of the nanodisk density on their electrochemical and electrocatalytic properties [97, 99]. The influence of the preparation process on the stability of the active nanodisks during electrochemical/electrocatalytic measurements was investigated in detail and optimized to an extent that the resulting nanodisks are fully stable also during continuous electrolyte flow and continuous reaction conditions [193]. In addition to these electrocatalytic model studies, CL was also applied for preparing membrane electrode assemblies for fuel cell studies [109].

In order to extend the parameter range in these studies, we reduced this density of Pt nanodisks to very low values, with the Pt nanodisks (⌀ $\sim$140 nm) covering about 1% of the electrode surface (Pt surface coverage $\sim$1 %). Previous measurements on these samples had shown, however, that the electrochemical active Pt surface area

(2.4.1 Active Surface Area Determination) determined by hydrogen underpotential deposition (H_{upd}) and CO_{ad} monolayer oxidation („CO_{ad} stripping“) is much higher than expected by comparison with higher coverage samples or than calculated from the density, size, and shape of the nanostructures derived from scanning electron microscopy (2.2.1 SEM) images.

In the present *chapter* the origin of this deviating electrochemical behavior observed for nanostructured Pt/GC electrodes with very low densities of Pt nanodisks by detailed electron microscopy studies and by comparing the electrochemical properties of the very-low-density Pt/GC electrodes with those of samples with higher densities of similar size Pt nanodisks (Pt coverage ~ 20 and $\sim 40\,\%$), which were prepared in the same way, is elucidated. Electron microscopy measurements include high-resolution SEM and locally resolved elemental analysis by energy-dispersive X-ray analysis (2.2.2 EDX), as well as conventional and high-resolution transmission electron microscopy (2.2.3 CTEM and HRTEM) on cross-sectional samples. Furthermore, we introduce the newly developed, related method of Hole-mask Colloidal Lithography (2.1.2 HCL) [64] for the preparation of similar type nanostructured electrodes and characterize their structural and electrochemical properties. Measurements of the electrocatalytic properties of CL- and HCL-prepared nanostructured electrodes (CO bulk oxidation and formaldehyde oxidation) will be published elsewhere [97].

First the morphology and surface composition of the nanostructured electrodes is characterized by high-resolution SEM, CTEM, and HRTEM on cross-sectional samples and by locally resolved elemental analysis by EDX. In the second part, we concentrate on the electrochemical characterization of the Pt/GC model systems, by cyclic voltammetry (CV) and preadsorbed CO_{ad} monolayer oxidation (2.4.1 CO_{ad} stripping) performed in a dual thin-layer flow cell (see section 2.3.3) connected to a differential electrochemical mass spectrometry (2.3.2 DEMS) set-up. The results are discussed with special attention on identifying and understanding the origin of the substantial difference between the expected and experimentally observed electrochemical behavior of the low-Pt-coverage, CL-prepared Pt/GC electrodes.

4.2 Results and Discussion

We investigated five different types of nanostructured Pt/GC electrodes with Pt nanodisks of 100–140 nm in diameter and different separations and, correspondingly, different Pt coverages. These include *(i)* high-loading samples (CL-40) with $\sim$ 40 % Pt coverage ($\varnothing$ ~ 140 nm), *(ii)* medium-loading samples (CL-20) with $\sim 22\,\%$ Pt coverage ($\varnothing$ ~ 134 nm), and *(iii)* ultralow-loading samples (CL-01) with $\sim 1\,\%$ Pt

Table 4.1: Geometrical data of the different nanostructured Pt/GC electrodes, as determined by SEM, assuming cylindrical Pt nanodisks and spherical Pt nanoparticles (see Table 4.2). The Pt coverage is defined as the fraction of the GC surface covered by the projection of the Pt nanodisks and nanoparticles.

sample	Pt ∼	diameter / nm	density / μm^{-2}	Pt surface coverage / %	geom. Pt surface area / cm^2
CL-40	nanodisks	140 ± 24	26	40	0.18
	nanoparticles	3.9 ± 2.6	2510	3	0.034
	total	–	–	**43**	**0.21**
CL-20	nanodisks	134 ± 19	16	22	0.10
	nanoparticles	4.3 ± 3.2	2760	4	0.045
	total	–	–	**26**	**0.14**
CL-01	nanodisks	147 ± 6	0.5	0.8	0.003
	nanoparticles	6.5 ± 4	1810	6	0.068
	total	–	–	**6.8**	**0.071**
CL-00	nanoparticles	7.3 ± 4	1670	7	0.079
HCL-20	nanodisks	118 ± 12	20	22	0.1
HCL-10	nanodisks	94 ± 9	14	10	0.052

coverage (⌀ ∼147 nm), all of which were prepared by CL. Furthermore, we included *(iv)* medium-loading (HCL-20) and *(v)* low-loading (HCL-10) samples with ∼22 % Pt and 10 % Pt coverage, respectively (⌀ ∼118 and ∼94 nm), both prepared by HCL. All experiments were performed on three different samples of each type to ensure reproducibility. As references, we *(vi)* also included nonstructured samples, where the initial Pt film was completely removed by Ar^+ sputtering (CL-00), and a bare GC. The structural characteristics of the nanostructured electrodes used in the present study are summarized in Table 4.1.

4.2.1 Surface Characterization

Representative large-scale and high-resolution SEM images of the nanostructured Pt/GC electrodes with different geometric Pt coverage and of the reference sample (completely removed Pt film) are shown in Fig. 4.1. The large-scale images

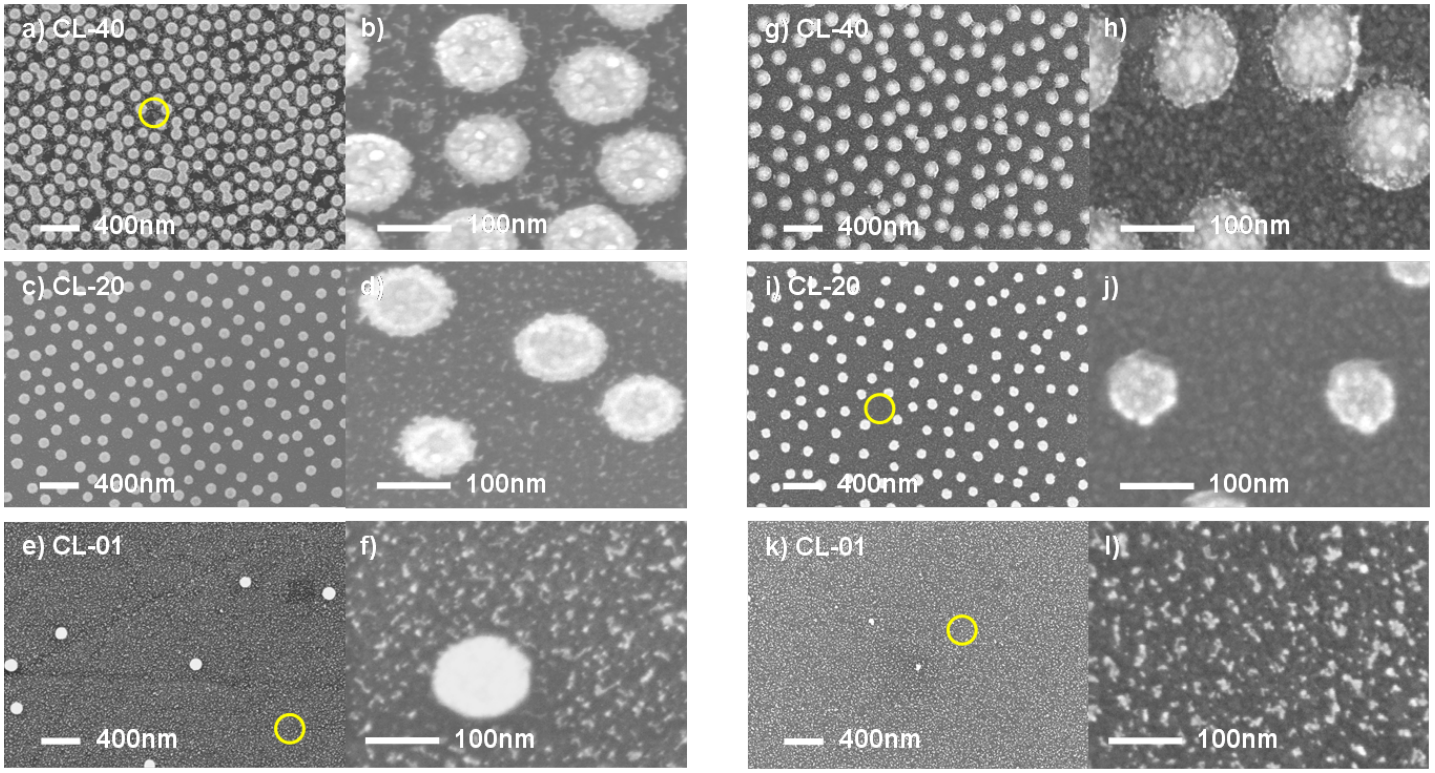

Figure 4.1: Representative large-scale (a, c, e, g, i, k) and high-resolution (b, d, f, h, j, l) SEM images of the nanostructured Pt/GC electrodes. (a, b) High Pt coverage ($\sim 43\,\%$) CL-prepared electrode (CL-40), (c, d) medium Pt coverage ($\sim 26\,\%$) CL-prepared electrode (CL-20), (e, f) ultralow Pt coverage ($\sim 7\,\%$) CL-prepared electrode (CL-01), (g, h) medium Pt coverage ($\sim 22\,\%$) HCL-fabricated electrode (HCL-20), (i, j) low Pt coverage ($\sim 10\,\%$) HCL-fabricated electrodes (HCL-10), and (k, l) a nonstructured Ar^+ sputtered electrode (CL-00) as reference. Large-scale images $2.5\,\mu\text{m} \times 3.4\,\mu\text{m}$; high-resolution images $330\,\text{nm} \times 460\,\text{nm}$. The bright circles in (a, e, i and k) denote the areas where the EDX analysis was performed.

of the higher Pt coverage samples (Fig. 4.1a, c, g and i) confirm the homogeneous distribution and narrow size distribution of the circular nanodisks expected from previous studies, both for the CL-prepared samples [60–63] (Fig. 4.1a, c) and for the HCL-fabricated samples [64] (Fig. 4.1g i). For these samples, two-dimensional Fourier transforms yield distinct rings, reflecting the short-range order in the layer of nanodisks. In agreement with the real-space SEM images, there is no evidence for long-range order. The situation is different for the ultralow-loading sample (CL-01, Fig. 4.1e), where the nanodisks are irregularly distributed on the surface. Apparently, during CL-fabrication the separation between the PS particles is so large that the electrostatic interactions between them are no longer strong enough to warrant a locally ordered distribution of them. Instead, it is dominated by the (random) spatial distribution of adsorbing PS particles. The images of the nonstructured „Pt-free“ CL-00 sample (Fig. 4.1k l) show a surface similar to the carbon surface between the Pt nanodisks of the CL-01 sample. The densities and sizes of the nanodisks evaluated from these images and the resulting Pt coverages are collected in Table 4.1.

In the high-resolution SEM images, features between the Pt nanodisks are visible on the three nanostructured electrodes prepared via CL (Fig. 4.1b, d and f). They are present also on the nonstructured sample (Fig. 4.1 l), in a similar density. In contrast, no such features were observed in high-resolution images on the HCL-prepared samples (see Fig. 4.1h and j).

At this point, we tentatively associate these features with Pt nanoparticles which originate from Pt clusters formed during the Ar^+ sputtering process (see Fig. 2.1d), which is applied to remove the unprotected Pt film between the adsorbed PS colloids. This assignment agrees with their presence on the CL-prepared nanostructured electrodes, where the lithographic process includes an Ar^+ sputtering step for removal of Pt film, and their absence on the HCL-prepared samples, where Ar^+ sputtering is not employed.

In order to confirm the presence of Pt nanoparticles on the CL-prepared samples in between the Pt nanodisks, these areas were analyzed by EDX. In Fig. 4.2 we show representative overview EDX spectra recorded on a CL-40 (black, full line), CL-01 (blue, dashed line), CL-00 (olive, dotted line), and HCL-10 (lavender, dashed and dotted line) electrode in areas between the Pt nanodisks. Carbon and oxygen are the predominant elements in the near-surface region (penetration depth of the primary electrons 0.3 μm), which is clearly demonstrated by the C K_α and O K_α peaks at 0.27 and 0.52 keV, respectively. In addition, Pt was also identified on the CL-40 sample in these areas (see, e.g., bright circle in Fig. 4.1a), despite the absence of Pt nanodisks, by the Pt M-peak at 2.05 keV (see also the inset in Fig. 4.2).

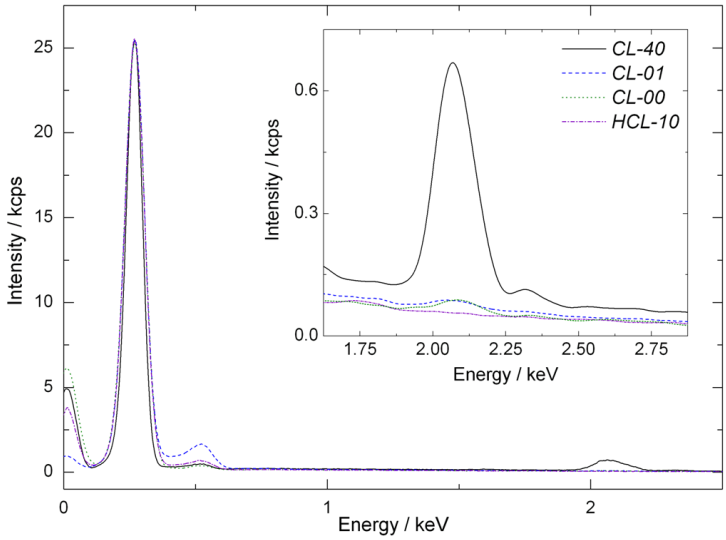

Figure 4.2: EDX spectra of the CL- and HCL-prepared nanostructured Pt/GC electrodes showing overview spectra of CL-40 (∼43 % Pt coverage; solid, black), CL-01 (∼7 % Pt coverage; dashed, blue), nonstructured CL-00 (completely sputtered; dotted, olive) and HCL-10 (∼10 % Pt coverage short-dashed, violet) electrode surfaces recorded in the areas marked in the SEM images in Fig. 4.1 a, e, i, and k, respectively. The inset shows magnified details of the Pt region.

Because of the close distance to the surrounding Pt nanodisks, however, this signal may well arise from scattered electrons which reached these nanodisks. Going to an ultralow-density CL-01 sample or to the CL-00 reference sample, the EDX-analyzed area (see bright circle in Fig. 4.1e and k, respectively) can be much further away from a Pt nanodisk. In these measurements, the Pt signal is considerably lower but still clearly detectable (0.08 and 0.06 atom %, respectively). In contrast to the CL-prepared samples, the amount of Pt detected between the Pt nanodisks on the HCL-10 electrode is at the detection limit of EDX analysis (∼0.01 atom %, see bright circle in Fig. 4.1i).

The atomic ratios of the elements found in the EDX spectra, averaged over different areas between the Pt nanodisks, are given in Table 4.2. An X-ray photoelectron spectroscopy analysis of the CL-00 sample, which is more surface sensitive than EDX, confirmed the EDX results and revealed a substantial amount of Pt on the surface of this sample.

Further information on the Pt nanoparticles is obtained from HRTEM images. The HRTEM image on the cross-sectional sample in Fig. 4.3a shows the trapezoidally shaped cross section of an individual Pt nanodisk. Furthermore, it reveals the presence of a thin layer of high-contrast nanoparticles close to or at the interface between GC and glue, in between the Pt nanodisks. The HRTEM images in Fig. 4.3b, c

Table 4.2: Atomic ratio of the elements determined from the EDX spectra (6 kV) in areas between the Pt nanodisks denoted by bright circles in Fig. 4.1 a, e, i, and k on the CL-prepared model electrodes CL-40 and CL-01, the HCL-fabricated HCL-10, and on the nonstructured CL-00 sample, respectively.

sample	**C** / atom %	**O** / atom %	**Pt** atom %
CL-40	97.5	1.4	1.1
CL-01	98.5	1.4	0.08
CL-00	98.2	1.7	0.06
HCL-10	97.0	3.0	0.01

show details of the interface between Pt nanodisk and GC substrate. These images (Fig. 4.3b and c) further resolve that the features, which were already observed by SEM, are spherically shaped and ~ 5 nm in diameter. Information on their structure can be derived from Fig. 4.3c, which resolves a face-centered cubic (fcc) structure of these spherical nanoparticles. This result further supports the EDX-based assignment of the features as Pt nanoparticles. They are also responsible for the numerous small white spots appearing on the GC substrate in the high-resolution SEM images (see Fig. 4.1b, d, f and l). Similar type Pt nanoparticles were also seen on CL-prepared electrodes where the Pt layer was deposited by evaporation rather than by sputter deposition [193], indicating that the nanoparticles are not formed during the deposition process, but rather during the final sputter-removal process. The nanoparticles spread over a layer of 5–10 nm thickness (Fig. 4.3a and b).

The vertical distribution of the Pt nanoparticles may result both from the final sputter process (see above) and from the preparation of the TEM sample („Ar^+ thinning“).

A similar kind of HRTEM image of the cross section of a HCL-fabricated sample is shown in Fig. 4.3d. It displays a Pt nanodisk and a few surrounding nanoparticles, which are also located in the glue (Fig. 4.3e). The characteristic layer of nanoparticles observed on the CL-prepared samples is clearly absent on the HCL-fabricated sample. A few nanoparticles are still resolved both at the surface and also distributed in the glue layer, where the latter seem to be related to the preparation of the TEM cross-section samples. Their density, however, is distinctly lower than on the CL-prepared nanostructured Pt/GC electrodes, where they form a homogeneous layer on the GC surface. This finding of essentially no Pt nanoparticles on the HCL-prepared nanostructured Pt/GC electrodes agrees also with the absence of

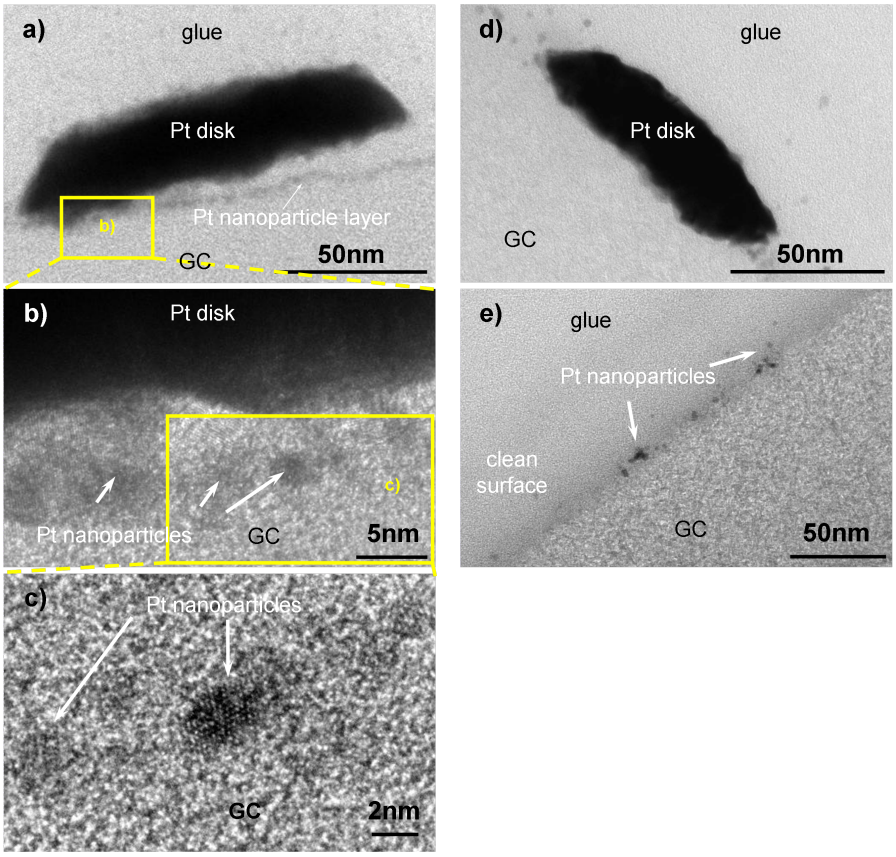

Figure 4.3: TEM micrographs of the Pt/GC interface region. (a–c) Nanostructured Pt/GC electrodes prepared via CL (CL-20) and (d, e) via HCL (HCL-10). Scale bars and the assignment of the different areas are given in the images. Large-scale images (a, d) 95×140 nm, (e) 148×225 nm; high-resolution images (b) 20×30 nm and (c) 12×18 nm. (For sample preparation see section 2.2.3 TEM.)

Pt nanoparticles in the high-resolution SEM images of these samples (see Fig. 4.1j).

For determining the Pt coverage, i.e., the fraction of the GC area covered by Pt nanodisks and nanoparticles, we describe both of them by circular features. Considering only the Pt nanodisks, this results in Pt coverages of $\sim 40\,\%$ (CL-40), $\sim 22\,\%$ (CL-20 and HCL-20), $\sim 10\,\%$ (HCL-10), and less than $1\,\%$ (CL-01) for the different samples. Including also the Pt nanoparticles between the Pt nanodisks, the amount of the Pt-covered surface is slightly increased, by $\sim 4\,\%$, for the CL-40 and CL-20 electrodes. For the CL-01 samples, the difference is, on a relative scale, much bigger, leading to a Pt coverage of $\sim 7\,\%$ (see Table 4.1). The influence of the shape of the Pt nanodisks and nanoparticles on the accessible geometric Pt surface is discussed in the following section, together the roughness factor of these features.

In total, the electron microscopy analysis provided clear proof for the presence of small Pt nanoparticles on the CL-prepared nanostructured electrodes in the areas

between the Pt nanodisks. These nanoparticles are about 5 nm in diameter and consist of high-contrast, fcc-structured material, which from the EDX results was identified as Pt. From the fact that they are present on the CL-prepared surfaces but negligible on the HCL-prepared electrodes, we conclude that their formation is related to the Ar^+ sputtering step for Pt film removal, which is part of the CL processing but does not appear in HCL-fabrication.

4.2.2 Electrochemical Characteristics

The electrochemical characteristics of the nanostructured Pt/GC electrodes were characterized by CV in base electrolyte and by the electrochemical (potentiodynamic) oxidation of a preadsorbed CO monolayer („CO_{ad} stripping“). The latter was used also for determining the active surface area (see section 2.4.1) of the electrode, which gave results similar to the H_{upd} determined surface areas, and area of the electrode, which gave results similar to the H_{upd} determined surface areas, and for calibrating the DEMS setup [155] (see section 2.3.2). Electrocatalytic measurements on these and other nanostructured samples, focusing on the effects of density and size of the Pt nanodisks on the reaction mechanism, will be reported in *chapters* 6 and 7 or separately in refs. [97–99].

Electrochemical Characterization

Figure 4.4 shows the resulting stable Faradaic signals recorded during cyclic base voltammograms at a sweep rate of $100\,mV\,s^{-1}$ on the different electrodes. The characteristic H_{upd} features observed for the nanostructured CL- or HCL-prepared electrodes and that for the CL-00 sample clearly indicate that the surfaces contain different amounts of polycrystalline metallic Pt [170, 172].

Due to contributions of the GC support, these samples generate higher pseudocapacitive features in the double-layer region compared to a polycrystalline Pt electrode [65, 173, 175]. For completeness, we also include a cyclic voltammogram recorded on a bare, unprocessed GC substrate (here the current signal is multiplied by a factor of 10). As expected, the characteristic H_{upd} features are missing on this sample, and the CV is dominated by oxidation and reduction peaks at about 0.6 V, which are generally attributed to the oxidative formation and reduction of quinones [153]. Comparing this CV with that recorded on the nonstructured CL-00 sample allows us to identify the contribution of the polished and acid/base-treated GC substrate to the CV of the latter sample.

The total active Pt surface area on the CL- or HCL-prepared samples and on the nonstructured CL-00 samples was calculated by assuming a H_{upd} monolayer charge

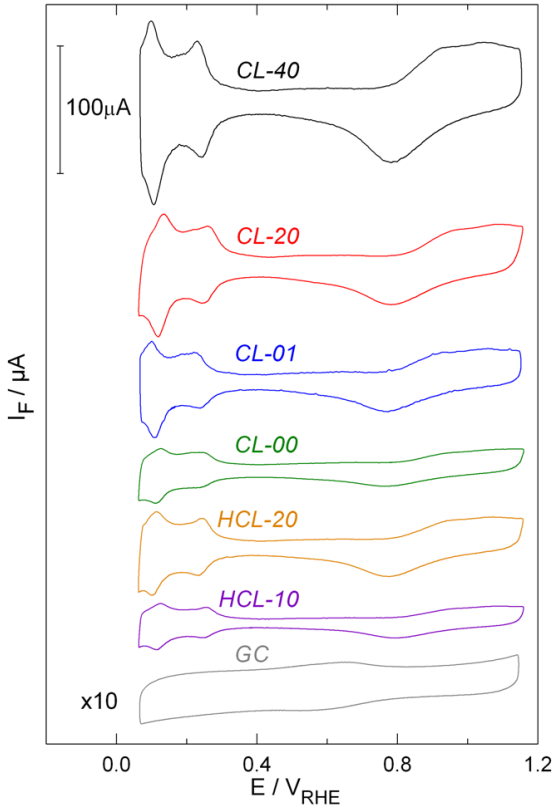

Figure 4.4: Base voltammograms (scan rate $100\,\mathrm{mV\,s^{-1}}$) which were recorded on the different samples prepared via CL or HCL, respectively: CL-40 ($\sim$ 43 % total Pt coverage, black), CL-20 ($\sim$ 26 % total Pt coverage, red), CL-01 ($\sim$ 7 % total Pt coverage, blue), nonstructured, Ar^+ sputtered sample CL-00 (olive), HCL-20 ($\sim$ 22 % Pt surface coverage, orange), and HCL-10 ($\sim$ 10 % Pt coverage, lavender). A blank GC substrate (grey) is included as reference. Note that the signal for the GC sample is multiplied by a factor of 10.

on polycrystalline Pt of $210\,\mu\mathrm{C\,cm^{-2}}$ [2] and a hydrogen coverage at the onset of bulk evolution of 0.77 monolayer. (For a detailed description of the integration procedure, including the determination of the onset potential, see ref. [152].) Integrating the H_{upd} current in the cathodic-going scan and subtracting the double-layer contribution yields the active Pt surface areas given in Table 4.3.

Relating the active Pt surface area to the exposed geometric Pt area of the electrode, the formal roughness factor (RF) for Pt was obtained. Gustavsson et al. reported an RF value of 2.6 for nanostructured electrodes prepared by CL [65]. (Note that in that study Pt was deposited by evaporation rather than by sputter deposition, as in the present study [193].) In the present study similar values are obtained for the CL-40 and CL-20 samples (compare Table 4.3, 3^{rd} column), considering only the Pt nanodisks on the electrode surface.

Table 4.3: Compilation of the active Pt surface areas determined by H_{upd}, the geometric Pt surface areas resulting from the SEM-based densities and sizes of the respective features (Pt nanodisks and Pt nanoparticles) and assuming different shapes of the Pt nanoparticles, and the resulting roughness factors of the different Pt/GC nanostructured electrodes. For the electrodes prepared by CL the Pt nanoparticles are included.

sample	**Pt ∼**	**act. Pt surf. area** / cm^2	**geom. Pt surf. area** / cm^2		
			disks	hemispheres	spheres
	nanodisks			0.178	
	nanoparticles		0.008	0.017	0.034
CL-40	**total**	**0.52**	**0.19**	**0.20**	**0.21**
	R-factor	*2.9*	*2.8*	*2.7*	*2.4*
	nanodisks			0.099	
	nanoparticles		0.011	0.023	0.045
CL-20	**total**	**0.34**	**0.11**	**0.12**	**0.14**
	R-factor	*3.4*	*3.1*	*2.8*	*2.4*
	nanodisks			0.003	
	nanoparticles		0.017	0.034	0.068
CL-01	**total**	**0.20**	**0.020**	**0.037**	**0.071**
	R-factor	*56*	*9.6*	*5.2*	*2.7*
CL-00	**total**	**0.17**	**0.020**	**0.040**	**0.079**
	R-factor		*8.5*	*4.3*	*2.1*
HCL-20	**total**	**0.23**		**0.104**	
	R-factor	*2.2*			
HCL-10	**total**	**0.11**		**0.052**	
	R-factor	*2.1*			

Using the same approach for the CL-01 sample, however, results in an estimated roughness factor of 56. In a second calculation, we also considered the Pt nanoparticles on the electrode surface. Their geometrical shape was described by *(i)* circular flat disks, *(ii)* hemispheres, and *(iii)* spheres. For the calculations, we used the diameters and the densities derived from high-resolution SEM images (see Table 4.1). The corresponding values for the geometric Pt surface area of the Pt nanoparticles are given in Table 4.3.

Relating the sum of the geometric Pt surface areas of the Pt nanodisks and the

Pt nanoparticles to the electrochemically measured active Pt surface area leads to a decrease of the RF values of the CL-prepared electrodes. This decrease is a clear effect for the CL-40 and CL-20 samples and is dramatic for the CL-01 electrode. Assuming spherical Pt nanoparticles, the RF values of the CL-40 (2.4) and CL-20 (2.4) electrodes closely resemble those of the HCL-fabricated samples (2.2) and that of a pristine Pt film (2.5) electrode. For the CL-01 sample, the resulting RF value of 2.7 is still slightly higher than on the other nanostructured electrodes but in the same range of values. This is particularly true when considering that uncertainties in the approximation of the Pt nanoparticles size and shape will have the highest impact on this sample.

In total, the H_{upd} measurements fully support our previous conclusion of the presence of approximately spherical Pt nanoparticles on the GC surface in the areas between the Pt nanodisks of the CL-prepared nanostructured electrodes, while on the HCL-prepared electrodes they are essentially absent. In addition, they clearly demonstrate that the surface of these nanoparticles is electrochemically accessible and that they are not covered by a carbon layer as expected, e.g., if they were embedded in the GC surface near region rather than being deposited on the GC surface.

Pre-adsorbed CO_{ad} Monolayer Oxidation

Representative CO_{ad} stripping traces are shown in Fig. 4.5. The $m/z = 44$ mass spectrometric signals are normalized to the respective K^* value for direct comparison of the different samples. As shown in Fig. 4.5a, the characteristic H_{upd} features are suppressed on the CO_{ad}-blocked Pt surface of the Pt/GC electrodes. The characteristic feature of the CL-prepared nanostructured electrodes, the formation of a double peak for CO_{ad} stripping with two maxima at ~ 0.70 and at $\sim 0.75\,V$, respectively [65, 97], is also observed in the present study on the high loading (CL-40) and the medium-loading (CL-20) electrodes. In contrast, on the ultralow-loading CL-01 and the nonstructured sputtered CL-00 samples, we only find a single CO_{ad} stripping peak at the high-potential position ($\sim 0.76\,V$). The active Pt surface areas calculated from the CO_{ad} charge and assuming a CO_{ad} saturation coverage of 0.75 monolayer [154] are almost identical to those determined from the H_{upd} charge.

The time-delay-corrected $m/z = 44$ ion current signals (see Fig. 4.5b) directly reflect the rate of CO_{ad} oxidation to CO_2. In the prewave region (0.4–0.6 V), the increasing mass spectrometric signal at $m/z = 44$ (see $\times 10$ magnified spectrometric traces) for CL-40, CL-20, HCL-20, and HCL-10 electrodes indicates the formation of small amounts of CO_2 by CO_{ad} oxidation in this potential range [97, 155]. In contrast, we find no such prewave signal on the CL-01 or on the CL-00 electrode. Similar findings (no measurable prewave CO_2 formation) were reported also for a

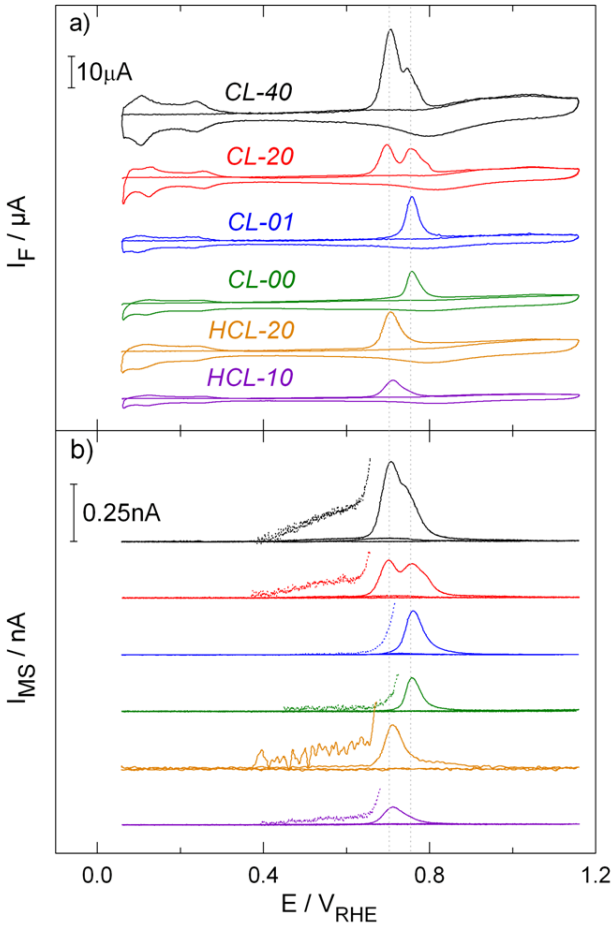

Figure 4.5: Potentiodynamic CO_{ad} stripping and subsequent CV images in 0.5 M sulfuric acid (scan rate scan rate 10 mV s^{-1}, flow rate 5 μL s^{-1}) recorded on nanostructured Pt/GC model electrodes prepared via CL or HCL: CL-40 ($\sim$ 43 % total Pt coverage, black), CL-20 ($\sim$ 26 % total Pt coverage, red), CL-01 ($\sim$ 7 % total Pt coverage, blue), a nonstructured Ar^+ sputtered CL-00 sample (olive), HCL-20 ($\sim$ 22 % Pt coverage, orange), and HCL-10 ($\sim$ 10 % Pt coverage, lavender). Prior to CO_{ad} monolayer oxidation, the model electrodes were saturated with CO at 0.06 V for 5 min and afterward rinsed with CO-free base solution for around 20 min. (a) Faradaic currents as measured and (b) mass spectrometric currents at m/z = 44 normalized to the respective K* values.

micelle-based Pt/GC nanostructured electrode [111], indicating that the prewave is associated with results from CO_{ad} stripping from the polycrystalline Pt nanodisks. This agrees well with previous observations of prewave CO_{ad} oxidation on polycrystalline Pt [133, 179].

Double-peak features were repeatedly reported for CO_{ad} stripping, e.g., on sputter-cleaned polycrystalline Pt surfaces [194], on preferentially oriented Pt nanoparticles [184, 195], or on single-crystal surfaces, including different facets of low-index planes [182, 184, 194]. They were generally attributed to the presence of differently ori-

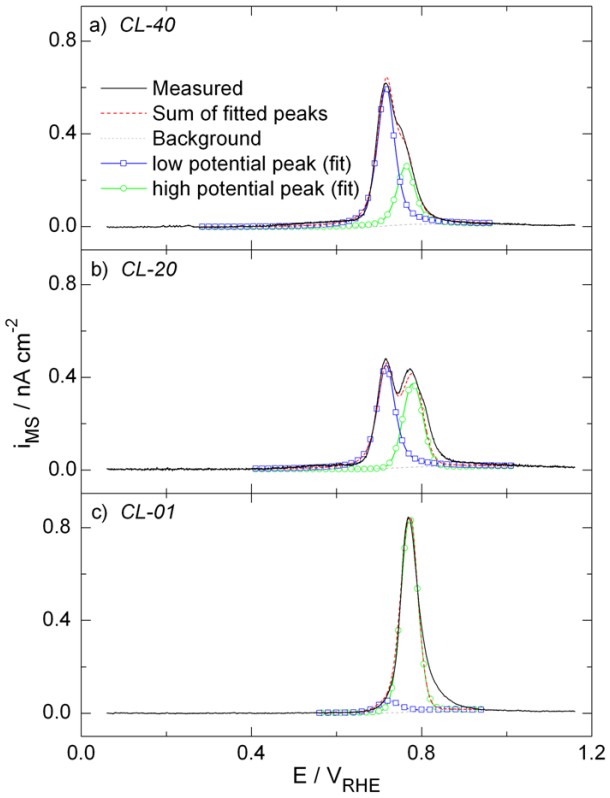

Figure 4.6: Deconvolution of the m/z = 44 mass spectrometric current signals recorded on CL-prepared, nanostructured Pt/GC electrodes during CO_{ad} monolayer oxidation into two peaks related to CO_{ad} oxidation on Pt nanostructures low-potential peak, 0.70 V and Pt nanoparticles (high-potential peak, 0.76 V): (a) CL-40, (b) CL-20, and (c) CL-01. The signals are normalized to the active Pt surface area of the respective electrodes for comparison. Solid, black - mass spectrometric current density; dotted, light grey - background; dashed, red - intensity of the fit of the two peaks; squares, blue - low potential peak (related to the Pt nanodisks), and circles, green - high potential peak (related to the Pt nanoparticles).

ented surface facets with differing CO_{ad} oxidation characteristics. For the present situation, this explanation appears unlikely. Instead, we favor an explanation which is based on reports of a shift of the CO_{ad} oxidation peak to higher potentials on smaller Pt nanoparticles [153, 155, 178] and of the formation of doublets due to agglomerate formation [153, 178], which the authors of the latter studies attributed to a particle size effect for CO_{ad} oxidation on Pt nanoparticles. Making use of this assignment, we propose that the low-potential CO_{ad} stripping peak is related to CO_{ad} oxidation on the polycrystalline Pt nanodisks, while the high-potential peak reflects CO_{ad} oxidation on the Pt nanoparticles.

The contributions of the respective peaks to the total CO_{ad} stripping signal of the

Table 4.4: Peak positions and peak intensity ratios determined by deconvolution of the m/z = 44 mass spectrometric current densities, and the geometric Pt surface areas related to Pt nanodisks and Pt nanoparticles on the different nanostructured Pt/GC electrodes described in Table 4.1.

sample	**peak position** / V	**Pt ∼**	**fraction of the geom. Pt surf. area** / %	**fraction of respective peak of the total CO_{ad} stripping signal** / %
CL-40	0.70	nanodisks	84	70 ± 2
	0.75	nanoparticles	16	30 ∓ 2
CL-20	0.70	nanodisks	69	55 ± 5
	0.76	nanoparticles	31	45 ∓ 5
CL-01	–	nanodisks	5	5 ± 3
	0.76	nanoparticles	95	95 ∓ 3
CL-01	0.76	nanoparticles	100	
HCL-20	0.71	nanodisks	100	
HCL-10	0.72	nanodisks	100	

different CL-prepared nanostructured electrodes was determined by deconvolution of the mass spectrometric current signals of these samples, as illustrated in Fig. 4.6a–c. The resulting contributions from the two peaks are given in Table 4.4.

The numbers given in Table 4.4 are mean values averaged over fits with slightly different parameters. For the CL-40 sample (Fig. 4.6a), the low-potential peak at 0.70 V contains ∼ 70 % of the total CO_{ad} charge, indicating that the Pt surface of this nanostructured electrode is dominated by the Pt nanodisks. This result fits well to the determination of the respective geometric surface areas based on the SEM images, which yielded ∼ 84 % on Pt nanodisks and about 16 % on Pt nanoparticles. For the CL-20 structure (Fig. 4.6b), the corresponding values are 55 ± 5% for the Pt nanodisks and 45 ± 5% for the Pt nanoparticle surface. In this case, the possible error is larger because of the worse separation of the two CO_{ad} stripping peaks. For comparison, the SEM-based geometrical surface area evaluation resulted in a contribution of ∼ 31 % of the surface area from the Pt nanoparticles, assuming

spherical nanoparticles. The low-potential peak is narrow and high, whereas the high-potential peak is broader and lower. Finally, for the CL-01 sample, there is only one dominant CO_{ad} oxidation peak at 0.75 V. The Pt nanodisks on this electrode are reflected by a small increase of the signal in the range from 0.66 to 0.72 V, which includes $\sim 5\,\%$ of the total CO_{ad} charge, while the remaining 95 % come from the Pt nanoparticles. Also, this result agrees well with the results from the SEM-based evaluation, where the Pt nanodisks contributed $\sim 5\,\%$ to the total geometric Pt surface area. For the HCL-fabricated HCL-20 and HCL-10 samples, which only showed a single CO_{ad} stripping peak, the contribution of this peak was 100 %.

In total, the clear correlation between the absence/presence of Pt nanoparticles on the nanostructured Pt/GC electrodes and the appearance of the high-potential CO_{ad} stripping peak, together with the qualitative agreement between the SEM-based Pt surface area and the charge in this peak, provide convincing proof that this peak arises from CO_{ad} oxidation on the Pt nanoparticles, in agreement with previous proposals of a particle-size-related upshift in CO_{ad} stripping peak [153, 178, 196]. Hence, this peak can be used for the unambiguous detection of Pt nanoparticles on these surfaces and for the quantitative evaluation of their surface area. CO_{ad} stripping demonstrated that nanostructuring via HCL does not cause Pt nanoparticle formation, whereas for CL fabrication Pt nanoparticles are abundant on the areas between the Pt nanodisks. On the ultralow-loading CL-prepared samples, the contribution from the Pt nanoparticles is dominant, but even on the medium-loading CL-prepared nanostructured electrodes it cannot be neglected.

4.3 Conclusion

In order to clarify the discrepancy between the experimentally determined electrochemical properties of nanostructured Pt/GC electrodes with very low densities of Pt nanostructures 100–140 nm and those expected on the basis of their structural characterization, we have investigated these electrodes by electron microscopy, including high-resolution SEM imaging, HRTEM imaging, and locally resolved EDX analysis, and by electrochemical measurements, including base voltammetry and CO_{ad} stripping. The results clearly demonstrate that on nanostructured electrodes prepared by colloidal lithography, the areas between the Pt nanodisks are covered by a dilute layer of Pt nanoparticles of 5 nm diameter. These were resolved in high-resolution SEM images and in HRTEM images, and were chemically identified by local EDX analysis. Using the particle sizes and densities determined by TEM and SEM, respectively, the contribution of the Pt nanoparticles to the geometric

Pt surface area was calculated. It was found to result in a measurable increase of the Pt coverage on medium- and high-loading nanostructured electrodes, and in a dramatic increase on Pt/GC electrodes with very low densities of the Pt nanodisks, e.g., on a surface with 1% Pt coverage. Comparison with the active Pt surface areas determined by H_{upd} and the geometrical surface calculated for cylindrical Pt nanodisks and spherical Pt nanoparticles reveals a close correlation between these two parameters, which is reflected by an almost constant roughness factor of 2.2–2.8. In contrast, without considering the Pt nanoparticles, the roughness factors would vary between 2 and 50.

Furthermore, we found that the Pt nanoparticles can be identified electrochemically by their characteristic CO_{ad} stripping signal, which is upshifted from 0.70 to 0.76 V compared to CO_{ad} oxidation on the polycrystalline Pt nanodisks. The ratio between the charges in the two peaks agrees well with the trends expected from electron microscopy imaging, with a dominant high-potential peak for the ultralow loading CL-01 sample, comparable intensities for the higher Pt loading CL-prepared samples, and a dominant low-potential peak for the HCL-prepared samples. This assignment for the two CO_{ad} stripping peaks agrees well with previous proposals of a particle-size-induced upshift of the CO_{ad} stripping peak on Pt nanoparticles.

Finally, a developed lithographic technique, HCL, was introduced as an alternative method for preparing similar type nanostructured Pt/GC electrodes, and we could clearly demonstrate that the electrodes prepared via this method are essentially free from Pt nanoparticles. HCL is proposed as the preferred method for the fabrication of nanostructured Pt/GC electrodes, and in particular, of electrodes with a low density of nanodisks.

Acknowledgement

This work was supported by the Landesstiftung Baden-Württemberg via the Kompetenznetz Funktionelle Nanostrukturen project B9, MISTRA contract no. 95014, and the Swedish Energy Agency grant no. P12554-1. We gratefully acknowledge A. Minkow Institute of Micro- and Nanomaterials, Ulm University for SEM and EDX imaging, and S. Tiedemann and A. Schneider both from the Institute of Surface Chemistry and Catalysis, Ulm University for developing a program for the evaluation of SEM images.

5 Nanostructured Pt/GC Model Electrodes Prepared by the Deposition of Metal-Salt Loaded Micelles

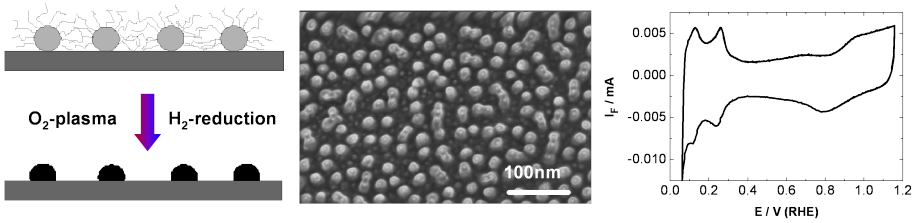

Y. E. Seidel[1], R. W. Lindström[1], Z. Jusys[1], J. Cai[1], U. Wiedwald[2], P. Ziemann[2] and R. J. Behm[1]

[1] Institute of Surface Chemistry and Catalysis, Ulm University, D-89069 Ulm, Germany
[2] Institute of Solid State Physics, Ulm University, D-89069 Ulm, Germany

Published in

Langmuir 23 (10) (**2007**) 5795–5801

Abstract

Novel, nanostructured, carbon-supported Pt model electrodes with homogeneously distributed Pt nanoparticles of uniform size were fabricated and analyzed with respect to their electrochemical properties. For this purpose, Pt-salt-loaded micelles were deposited on a glassy carbon substrate and subsequently exposed to an oxygen plasma and a H_2 atmosphere for removal of the polymer carriers and reduction of the Pt salt. The morphology of the resulting nanoparticles and their electrochemical/electrocatalytic properties were characterized by high-resolution scanning electron microscopy, X-ray photoelectron spectroscopy, cyclic voltammetry, and differential electrochemical mass spectrometry for CO electro-oxidation. The data demonstrate that this method is generally suited to the production of nanostructured model electrodes with well-defined and independently adjustable particle size and interparticle distance distributions, which are specifically suited for quantitative studies of transport processes in electrocatalytic reactions.

5.1 Introduction

In recent years, planar model catalysts have been increasingly employed for detailed mechanistic studies of catalytic and electrocatalytic processes, exploiting the well-defined structure and electronic and chemical properties of these model systems [52, 54, 55]. In most previous studies, the planar model catalysts were prepared either by the evaporation or electrochemical deposition of the catalytically active metal on the respective supporting substrates [52, 54, 55]. These methods result in a distribution of particle sizes and particle separations. Recent developments in nanotechnology have provided new opportunities for the fabrication of well-defined nanostructured planar model catalysts with essentially monodisperse particle sizes and/or regular particle separations. Lithographic techniques (e.g., E-beam Lithography [56–58] or, more recently, Colloidal Lithography [60, 61, 65, 109, 197]) have been employed to produce regular arrays of metal nanostructures with sizes in the 50 to 150 nm range. Planar model systems with smaller particles were prepared by the deposition of pre-formed metal particles on planar substrates, where the particle were synthesized using a water-in-oil method (see refs. [184, 198, 199] and references therein), ligand-stabilized colloid particles [106–108], or metal-salt-containing micelles on planar substrates [66, 67, 200, 201].

These model catalysts have mainly been employed in studies of heterogeneously catalyzed reactions at the solid-gas interface, whereas studies of electrocatalytic reactions are sparse [65, 184]. In recent investigations, we have utilized such nanostructured model catalysts prepared by Colloidal Lithography (see forgoing *chapters* 3 and 4) for the study of electrochemical and electrocatalytic processes [65, 97], and similar measurements were also reported for electrocatalytic studies on metal-decorated electrode membrane assemblies [109, 197]. In these studies, we were particularly interested in learning more about the influence of transport processes on the overall reaction process, which can, via desorption and re-adsorption of volatile reaction intermediates [25], affect the product distribution in more complex reaction processes with different main and side products and can be studied by evaluating the influence of the particle separation on the product distribution [25, 202].

In this *chapter* an approach to prepare quasi-2 D model catalysts with smaller particles by the deposition of Pt-salt loaded reverse micelles on a glassy carbon substrate and subsequent removal of the polymer/Pt reduction by a sequential oxygen plasma and H_2 annealing treatment is reported. Furthermore, the fabrication of self-assembled metal nanoparticle arrays by micellar techniques has the advantage of fast, inexpensive preparation [66, 201]. It is possible to synthesize a large number of samples with controlled particle size, composition, and separation. This scheme

had been utilized previously for the preparation of oxide-supported dispersed [203] and model catalysts [200], including a very recent study on the electrocatalytic O_2 reduction on indium tin oxide-supported model catalysts [201]. For electrochemical applications, however, substrates with higher conductivity would be favorable to prominent electrochemical artifacts related to the low conductivity of oxide substrates. In this case, specifically for carbon substrates, the selective removal of the polymer and the reduction of the Pt salt, without attacking the carbon substrate surface to an extent that the adhesion of the nanoparticle is severely reduced, pose a major problem.

The potential of metal-salt loaded micelles for synthesizing well-defined model electrodes for electrocatalytic studies was investigated by spectroscopic/microscopic and by electrochemical techniques. The resulting particle size and distribution on the model catalysts were characterized by scanning electron microscopy (2.2.1 SEM), and X-ray photoelectron spectroscopy (2.2.4 XPS) provided detailed information on the surface chemical composition. The electrochemical and electrocatalytic properties were characterized by cyclic voltammetry, pre-adsorbed CO_{ad} monolayer oxidation (2.4.1 CO_{ad} stripping), and bulk CO oxidation, employing electrochemical and on-line mass spectrometry measurements (2.3.2 DEMS) by use of a dual thin-layer flow cell (see section 2.3.3). The data demonstrate the general viability of the micelle approach for electrocatalytic studies on well-defined model catalysts.

5.2 Results and Discussion

5.2.1 Surface Characterization

Two types of samples were prepared from the same micelle solution. For *type 1*, the sample processing was conducted as described in section 2.1.3, whereas for *type 2* samples, the post-treatment was stopped after oxygen plasma processing. The SEM images (Fig. 5.1) of the nanostructured model electrodes indicate a homogeneous distribution of more or less circular nanostructures with an average separation of $40 \mp 10\,\text{nm}$. Their density is around 610 nanostructures μm^{-2}, which corresponds to a coverage of $\sim 30\,\%$. The average diameter of these objects is about $25 \mp 5\,\text{nm}$. The large-scale SEM images (Fig. 5.1a, c) show that the size, shape, and distribution of the nanostructures do not differ for the two post-treatment procedures, whereas after the electrochemical measurements there is a clear difference between *type 1* and *type 2* samples (Fig. 5.1b, d). In the latter case, for the oxygen plasma pre-treated sample, the nanostructures seem to be removed after the electrochemical measurements (Fig. 5.1b). In combination with the absence of stable Pt features in

the electrochemical characterization, we conclude that the Pt compound is largely dissolved in the electrochemical environment. For the reduced samples, the electrochemical treatment causes slight changes in the appearance of the nanostructures in the SEM images, but they clearly survived the electrochemical treatment (Fig. 5.1d). Furthermore, from the high-resolution images (Fig. 5.1g, h), it is obvious that the H_2-annealed particles (*type 1*) exhibit small, bright dots mostly in the central region of the nanostructures, whereas for *type 2* samples these bright dots are absent. These bright dots show up even more clearly after the electrochemical treatment (i.e., they are stable against electrochemical treatment, Fig. 5.1h), whereas part of the surrounding material appears to be removed by the electrolyte. Because heavy elements produce brighter contrasts in SEM images, it is tempting to conclude that the dots are Pt-rich and that the Pt content in the other regions of the nanostructures is significantly lower. Most likely, these parts still contain partially decomposed polymer material as a result of incomplete polymer removal.

Associating the bright dots with Pt nanoparticles is also supported by the electrochemical measurements (see below). To obtain more detailed information on the (metallic) Pt distribution in the nanoparticles, their shape, and the interface with the GC substrate, high-resolution transmission electron microscopy measurements are planned.

XP spectra were recorded from both sample types before and after the electrochemical measurements. The overview spectrum (Fig. 5.2a), which was largely identical (see below) for the two samples and also before and after the electrochemical measurements, is characterized by dominant C(1s), O(1s), and Pt(4f) peaks resulting from the glassy carbon support, oxygen (containing) adsorbates, and Pt nanoparticles, respectively. The high O(1s) intensity, which is lower after H_2 annealing than after oxygen plasma treatment and significantly higher after the electrochemical measurements, is mostly attributed to oxygen uptake during oxygen plasma treatment, ex-situ sample transport, and the electrochemical experiments. Weak signals of Si (Si(2s) and Si(2p)) and S (S(2s) and S(2p)) are also present for all samples. The Si contamination is due to the polishing procedure of the GC substrates, and the S contamination, which appears only after the electrochemical measurements, results from the sulfuric acid electrolyte (Fig. 5.2a).

A detailed scan of the Pt(4f) region resolves characteristic differences between the two sample types. After oxygen plasma treatment (*type 2* sample, Fig. 5.2b), the Pt(4f) peaks show a characteristic shift to higher binding energies (BEs), to about 72.5 and 75.8 eV, respectively, indicating that the surface of the Pt nanoparticles is completely transformed into an oxidized state, which is most likely $Pt(OH)_2$, and that no metallic Pt (characteristic BEs of 71.2 and 74.5 eV for the $4f_{7/2}$ and $4f_{5/2}$

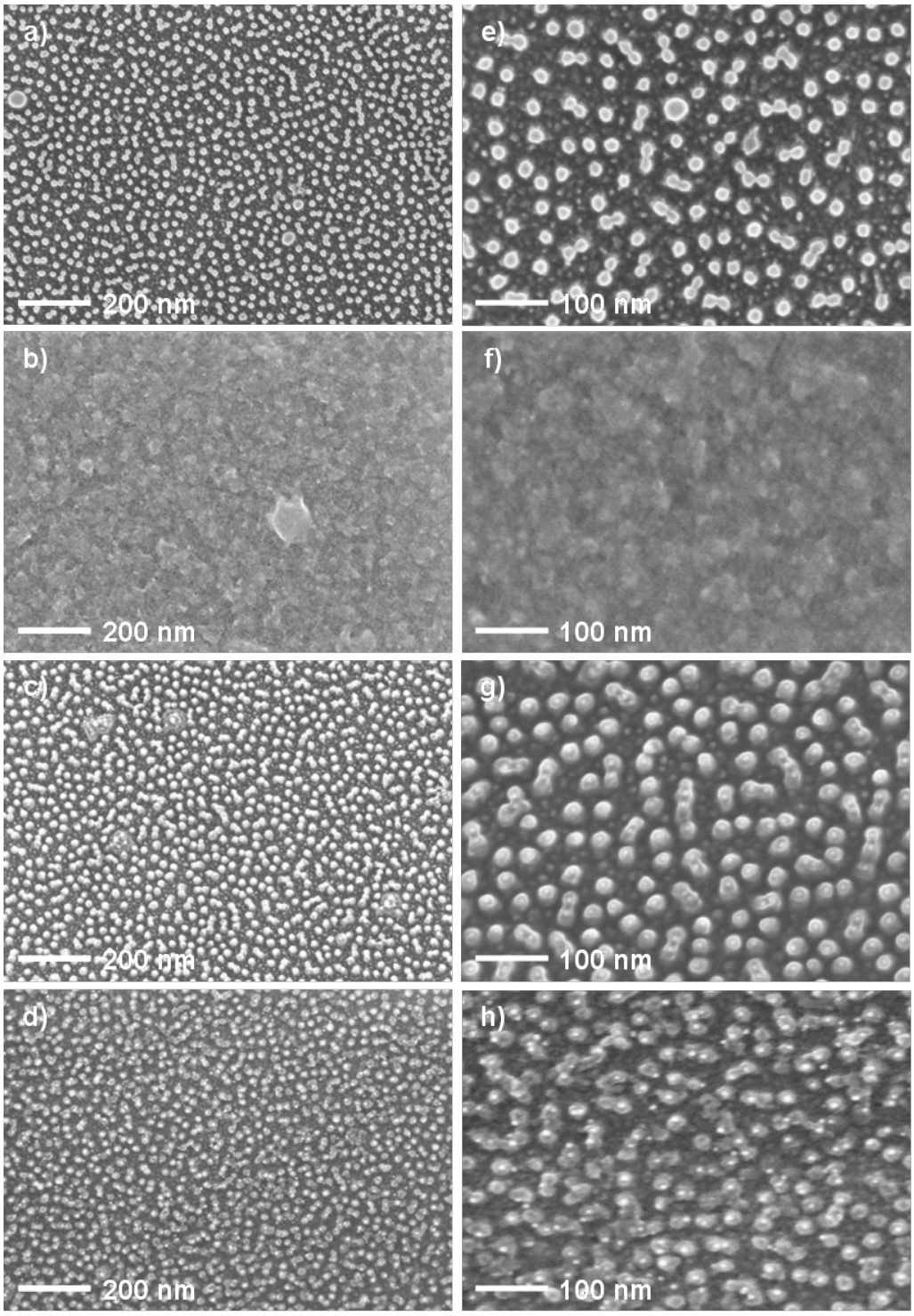

Figure 5.1: (a–d) Large-scale and (e–h) high-resolution SEM images of the micelle-based nanostructured Pt/GC model electrodes after different treatments: (a, e) after oxygen plasma treatment; (b, f) after electrochemical measurements of the oxygen plasma-treated sample; (c, g) after oxygen plasma and H_2 atmosphere treatment, and (d, h) after electrochemical treatment of the H_2-processed sample. Large-scale images $1.8\,\mu\text{m} \times 1.2\,\mu\text{m}$; high-resolution images $760\,\text{nm} \times 500\,\text{nm}$.

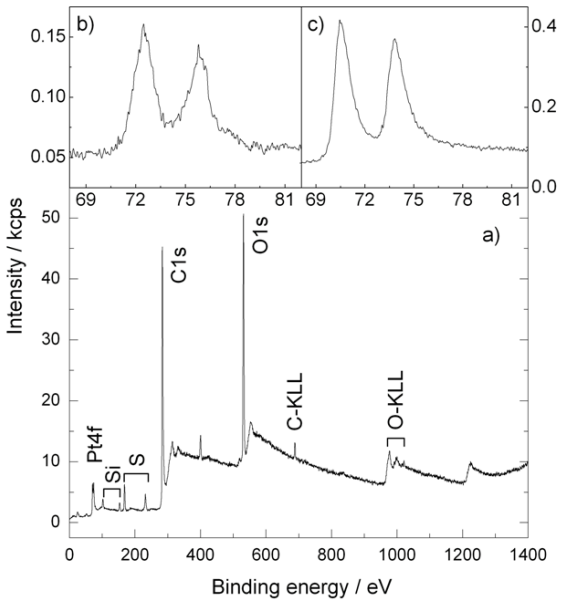

Figure 5.2: XP spectra of the Pt/GC electrodes showing (a) an overview spectrum of both sample types and (b, c) detailed spectra of the Pt(4f) signal of the oxygen plasma-treated sample (*type 2*) (b) and of the oxygen plasma- and hydrogen-treated sample (*type 1*) (c).

peaks, respectively [204]) is present on the surface. The asymmetric shape of the Pt(4f) peak points to a small contribution of Pt oxide, appearing as a small shoulder at 77.7 eV [204]. After subsequent H_2 treatment and electrochemical measurements, the Pt(4f) spectrum reveals a significant amount of metallic Pt (Fig. 5.2c). The main Pt(4f) intensities are down-shifted to the metallic Pt positions [204], and integration of the entire Pt(4f) peak shows that 70 % of the Pt surface species are metallic (BEs of 70.5 and 73.8 eV). The low BEs point to a particle size effect (i.e., very small Pt particles [205]). By comparison with the high-resolution SEM images discussed above, these small Pt particles are associated with the bright dots in the 25 nm nanoparticle, supporting our previous proposal that the larger composite nanostructures include very small Pt nanoparticles. The asymmetric shape of the peaks can be fitted with a second set of peaks at 71.6 and 75 eV, which comprise about 30 % of the total Pt intensity and reflect the presence of slightly positively charged Pt species. We expect these positively charged Pt species to result from the electrochemical experiments and, to some extent, from the exposure to air during storage. Therefore, these measurements give no indication of the presence of ionic Pt compounds at the surface of the nanoparticles during the electrochemical measurements.

5.2.2 Electrochemical Characterization

For the characterization of the electrochemical and electrocatalytic properties of the Pt/GC model electrodes, we performed the following types of experiments: *(i)* cyclic voltammetry in basic solution, *(ii)* electrochemical oxidation of a pre-adsorbed CO_{ad} monolayer (CO_{ad} stripping) during a potential sweep, and *(iii)* potentiodynamic and potentiostatic continuous electrochemical CO bulk oxidation.

Following previous reports [24, 65], the Pt/GC electrodes were cleaned by repetitive rapid cycling ($100\,mV\,s^{-1}$) within a preset potential window (between 0.06 and 1.16 V) in order to remove organic contamination that had either survived the oxygen plasma treatment or was picked up during sample transfer after that treatment and to reduce oxide surface species on the nanoparticles. This treatment was continued until reaching a stable CV trace. To avoid „electrochemical annealing“ [171] and oxidative corrosion of the GC substrate, the positive potential limit was set to 1.16 V, which turned out to be a reasonable compromise between the improved electro-oxidation of contaminants and the increasing loss of particles. (See also ref. [65].)

Figure 5.3 shows cyclic base voltammograms recorded for the two sample types. The resulting stable Faradaic signals before (solid line) and after (dotted line) a series of electrochemical CO oxidation experiments (ii and iii) were recorded at a sweep rate of $100\,mV\,s^{-1}$. The characteristic H_{upd} features observed for the *type 1* sample (Fig. 5.3a) indicates that the surface largely consist of polycrystalline metallic Pt [170, 172]. However, this sample exhibits higher pseudocapacitive features in the double-layer region compared to pure polycrystalline Pt (pc Pt), and these are due to contributions of the glassy carbon support [65, 175, 206]. The cyclic voltamogramms also clearly demonstrate the stability of the Pt nanostructures/particles against the electrochemical treatment, in good agreement with the SEM observations (as mentioned above). The situation is completely different for the *type 2* sample. Here the CV is dominated by oxidation and reduction peaks at about 0.6 V, which are generally attributed to the oxidative formation and reduction of quinones adsorbed on the glassy carbon surfaces [153]. The absence of the characteristic H_{upd} features reflects the absence of metallic Pt surface species, in good agreement with the XPS results and the SEM observations on the unreduced samples (Fig. 5.1a, b, e and f). Note that the voltammogram shows 10 times higher currents, in particular, much higher double-layer charging currents, than obtained on the *type 1* sample because of the high roughness of the *type 2* samples. Nevertheless, the characteristic H_{upd} features should also be clearly visible on this scale for a similarly sized Pt surface as in the *type 1* sample.

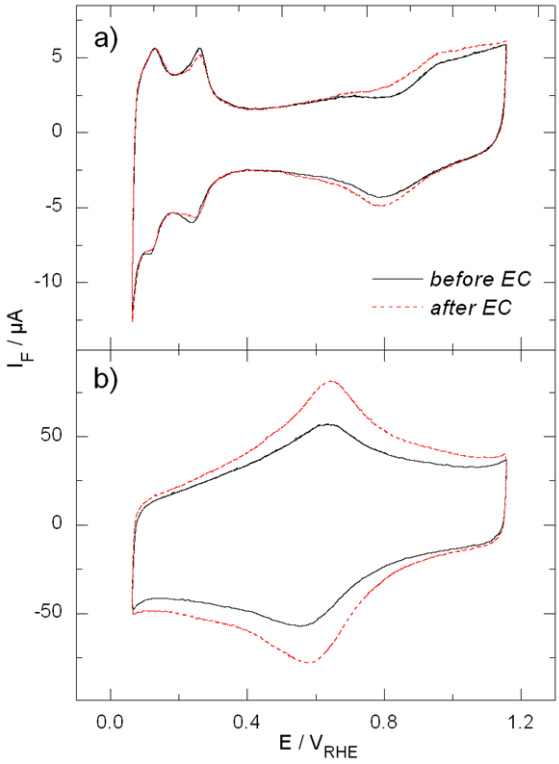

Figure 5.3: Base cyclic voltammograms ($100\,\mathrm{mV\,s^{-1}}$) before (solid line) and after (dashed line) the electrochemical oxidation experiments on (a) sample *type 1* and (b) sample *type 2*. Before these voltammograms were recorded, the surfaces were cleaned electrochemically by several potential sweeps to 1.16 V to remove oxidizable contamination.

Because of the lack of metallic Pt species on *type 2* samples, we did not investigate these samples further.

In the next step, we compared the active surface area of the Pt nanoparticles determined from SEM imaging with that derived from the electrochemical measurements. The real, active surface area of the nanostructures was calculated from the H_{upd} charge, assuming a H_{upd} monolayer charge on polycrystalline Pt of $210\,\mu\mathrm{C\,cm^{-2}}$ [2], and a hydrogen coverage at the onset of bulk evolution of 0.77 monolayer (ML) [152]. Integrating the H_{upd} current in the negative-going potential scan and subtracting the double-layer contribution lead to a H_{upd} charge of 0.013 mC, equivalent to an active surface area of $S_{real} = 0.080\,\mathrm{cm^2}$. Dividing this by the number of nanostructures on the GC substrate area accessible to the electrolyte ($G = 0.385\,\mathrm{cm^2}$), which is obtained from the density of 610 nanostructures per $\mu\mathrm{m^{-2}}$, we calculate an active surface area of around $342\,\mathrm{nm^2}$ per nanostructure for the Pt nanoparticles within a single nanostructure.

The „theoretical“ surface area of the nanostructures determined from SEM imaging is calculated from the geometric area, a nanostructure density of $6.1 \times 10^{10}\,\mathrm{cm^{-2}}$,

and the surface area per nanostructure. Using the mean diameter of 25 nm (see above), one obtains surface areas of $A_{sphere} = 1964\,nm^2$ and $A_{hemisphere} = 982\,nm^2$ per nanostructure for an ideal sphere or hemisphere, respectively, which results in total exposed surface areas of $A_{spheres\ on\ G} = 0.462\,cm^2$ and $A_{hemispheres\ on\ G} = 0.231\,cm^2$. Comparison with the active surface area leads to formal roughness factors of the nanostructures of $RF_{sphere} = 0.17$ and $RF_{hemisphere} = 0.35$.

The fact that the formal roughness factors of the nanostructures are less than 1 means that only parts of their surfaces are electrochemically active. This is caused by the presence of either nonreduced precursor species or surface contaminants that were not fully removed, or it could be explained by smaller Pt nanoparticles in the nanostructures. In a first-order approximation and neglecting the effect of surface contaminants, one can use the active surface area to determine the size of the Pt nanoparticles, assuming that these particles have a smooth outer surface and are not porous. For (fully accessible) spherical particles and a single particle per nanostructure, this leads to a diameter of $d_{sphere} = 10\,nm$. Taking hemispherical particles, where only the upper spherical part is accessible, one would obtain a particle diameter of about $d_{hemisphere} = 14\,nm$. This is significantly lower than the value of 25 nm derived from the SEM measurements for the nanostructure in total. Although we cannot rule out significant contributions of surface blocking by contaminants, the latter result would fit well with the interpretation of the SEM images that the platinum is concentrated in the bright dots in the high-resolution images. For several Pt particles per larger particle, equivalent to the bright dots in the particles, this would yield even smaller Pt particles, reaching a size of a few nanometers where final state effects are beginning to become effective.

In parallel studies of the same particles deposited on SiO_2 / Si substrates, detailed SEM and atomic force microscopy measurements revealed Pt nanoparticles with a diameter of $d_{real} = 8.5 \pm 1.4\,nm$ after 30 min of oxygen plasma treatment, followed by hydrogen reduction. These Pt nanoparticles represent the complete Pt content of the micelle cores, after full reduction of the Pt salt and complete removal of the polymer stabilizer. Accordingly, the larger Pt nanoparticles on the glassy carbon substrates still contain other materials. Most likely, this is polymer material, which has not been fully removed because of the much shorter oxygen plasma treatment required to avoid severe surface etching of the carbon substrate used in the present study.

The electrocatalytic behavior of Pt/GC model electrodes was characterized by potentiodynamic CO_{ad} stripping experiments (Fig. 5.4). For comparison, we also included data measured on a pc Pt electrode and on a nanostructured Pt/GC electrode prepared by Colloidal Lithography (CL). (For further details, see ref. [65].)

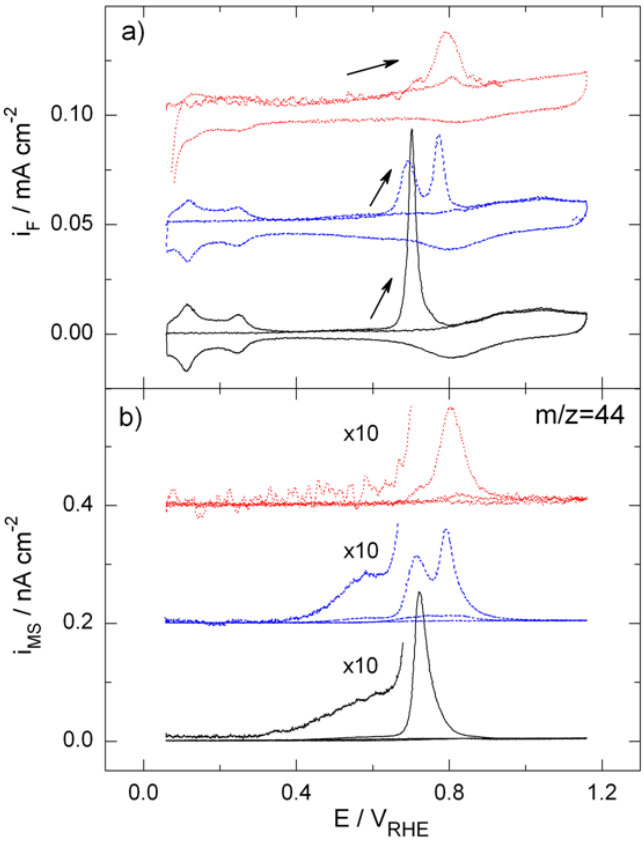

Figure 5.4: Potentiodynamic CO_{ad} stripping and subsequent base cyclic voltammograms in 0.5 M sulfuric acid (sweep rate 10 mV s^{-1}, flow rate 5 μL s^{-1}) on a micelle-based Pt/GC model catalyst (dotted line), a CL-prepared nanostructured Pt/GC model catalyst (dashed line) (ref. [65]), and a polycrystalline Pt electrode (solid line). Prior to CO_{ad} stripping, the samples were saturated with CO at 0.06 V for around 10 min and subsequently rinsed with CO-free base electrolyte for about 15 min. (a) Faradaic current densities and (b) mass spectrometric current densities at m/z = 44.

The experiments were performed in the following way: First, CO was adsorbed from a CO-saturated base electrolyte at 0.06 V for about 10 min, followed by rinsing with a CO-free basic solution. Finally, the adsorbed CO was oxidized in the positive-going potential scan. The recorded mass spectrometric currents were normalized versus the electrochemically active surface area of the respective electrodes. As shown in Fig. 5.4, the typical H_{upd} features are completely suppressed on the Pt electrodes in the first positive-going scan, which is attributed to CO_{ad} blocking. The characteristic feature of the three CO_{ad} stripping scans is the main CO_{ad} oxidation peak. For the micelle-based electrode, this peak is centered around 0.77 V (dotted line), whereas on the pc Pt electrode this appears at lower potentials, with a peak at 0.7 V (solid line). The appearance of a single CO_{ad} stripping peak and the re-

spective energies are typical for CO_{ad} stripping on pc Pt [185] and from small Pt nanoparticles [155, 184] (e.g., in carbon-supported Pt catalysts [155]). On the CL-prepared nanostructured Pt/GC electrode, we find a distinct double peak (dashed line), in good agreement with previous measurements on these samples [65]. Such kind of double peaks had been explained by CO oxidation on different facets [182], but other possibilities such as oxidation on differently sized grains/particles [184] or facets and grain boundaries [207] are possible as well. (For a detailed discussion about a shift in the peak potential due to particle size effects, see also the preceding *chapter* 4.) After the potential reverse, the following potential scan is similar to the cyclic voltammograms of the base. Assuming a CO_{ad} saturation coverage of 0.75–0.8 ML [154], one obtains values for the active Pt surface area that coincide rather closely with those calculated from the H_{upd} formation charge.

The rate of CO_{ad} oxidation to CO_2 is directly reflected by the $m/z = 44$ ion current signal (cf. Fig. 5.4b). For all three electrodes, the mass spectrometric traces closely follow the Faradaic current density with a shift of about 20 mV to higher potentials due to the time delay between CO_2 formation and detection [155]. In the pre-wave region, around 0.4–0.6 V, the $m/z = 44$ ion current density on the nanostructured electrodes increases (see $\times 10$ magnified mass spectrometric traces), which indicates the formation of small amounts of CO_2 by CO_{ad} oxidation in this potential range [133, 208] and is not observed on the micelle-based sample.

To examine the mass-transport-related current limitation on the Pt/GC model electrodes in more detail, continuous CO bulk electro-oxidation experiments were performed and compared to similar measurements on polycrystalline Pt electrodes. Potentiodynamic CO bulk oxidation DEMS measurements, performed by sweeping the potential within a defined potential window, here between 0.06 and 1.16 V, in CO-saturated basic solution, are shown in Fig. 5.5. Prior to the first positive-going scan, the electrodes were CO_{ad} saturated by CO pre-adsorption at 0.06 V for about 5 min. Similar to the CO_{ad} stripping experiments, the Faradaic currents show none of the characteristic H_{upd} features observed on the CO_{ad}-blocked Pt surfaces, indicative of a saturated CO adlayer (Fig. 5.5a). At more positive potentials, the Faradaic current signal starts at about 0.92 V and transforming into the steep main current increase at 1.02 V. On the micelle-based sample (dotted line), the current increases steeply at 0.95 V, passes through a maximum at 1.01 V, and then decays again up to the positive potential limit. In the reverse, negative-going scan it remains nearly constant down to ca. 0.94 V, where it rapidly decreases. The pronounced hysteresis is characteristic of CO bulk oxidation on Pt electrodes and is generally explained by CO_{ad} blocking of the surface during the positive-going scan, which is not present in the negative-going scan [209, 210].

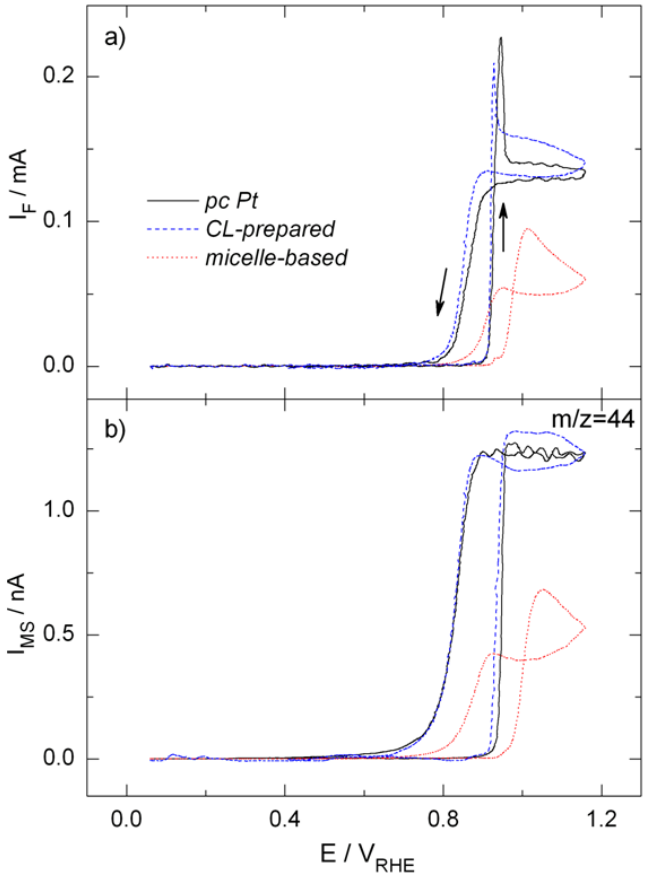

Figure 5.5: Potentiodynamic CO bulk oxidation (scan speed 10 mV s^{-1}, flow rate 5 μL s^{-1}) on a micelle-based Pt/GC model catalyst (dotted line), a CL-prepared nanostructured Pt/GC model catalyst (dashed line, see ref. [65]), and a polycrystalline Pt electrode (solid line). Prior to the experiments, CO had been adsorbed at 0.06 V for about 5 min, followed by multiple scans between 0.06 and 1.16 V in CO-saturated base electrolyte. (a) Faradaic currents and (b) mass spectrometric currents at m/z = 44.

The sharp spike in the positive-going scan is attributed to the oxidation of the pre-adsorbed CO adlayer, and the subsequent current results from the rate-limiting, slower provision of CO (transport limitation). These results also demonstrate that CO_{ad} oxidation is possible in the Pt oxide range (i.e., on a largely OH- and oxide-covered surface; reactive oxide [210]). On the polycrystalline Pt (solid line) and on the CL-prepared nanostructured Pt/GC electrode (dashed line), the entire signal is shifted to lower potentials, in good agreement with the CO_{ad} stripping results presented above. Furthermore, the maximum in the positive-going scan is much more pronounced, appearing now as a sharp spike in the Faradaic current signal with nearly no difference between pc Pt (0.94 V) and nanostructured CL-prepared Pt sample (0.93 V). After passing through this spike, the Faradaic current quickly

decays to almost constant values of 0.13–0.135 mA for pc Pt, whereas on the CL-prepared nanostructured Pt/GC sample the current first drops to 0.16 mA and then slowly decays to 0.12 mA up to the positive potential limit. Hence, for CO bulk oxidation the behavior of the CL-prepared nanostructured Pt/GC sample is largely identical to that of the pc Pt electrode, with some modification toward the behavior of micelle-based Pt/GC electrodes. The m/z = 44 ion current signal again largely follows the Faradaic current with a small shift of about 20 mV due to the time delay mentioned above (Fig. 5.4b).

Because this leads to opposite shifts in the positive- and negative-going scan, the hysteresis is more pronounced in the mass spectrometric current. In this case, the characteristic spike in the positive-going scan is basically absent, which is explained by the slow transport of CO_2 into the second compartment and then into the mass spectrometer as a result of the low flow rates. Also the mass spectrometric data clearly demonstrate that CO bulk oxidation is transport-limited for the pc Pt and the CL prepared nanostructured Pt/GC electrodes at about 1.24 nA, whereas on the micelle-based electrode a constant current is not achieved for CO bulk oxidation. Instead, the CO oxidation current decreases steadily from 0.7 nA at 1.04 V to about 0.54 nA at the positive potential limit of 1.16 V. The lower currents on the micelle-based electrode indicate that part of the CO arriving on the substrate surface is not accessible for oxidation, which is most likely due to the lower Pt coverage. The current decay at E > 1.0 V is explained by the surface oxidation of the Pt particles, which reduces their CO oxidation activity. This effect becomes apparent, however, only under conditions where the current is kinetically controlled.

In a second set of experiments, we followed the CO bulk oxidation on the same three electrodes in potentiostatic potential step transients in CO-saturated electrolyte to avoid effects related to the changing potential in the potentiodynamic measurements. These measurements were performed by stepping the potential from 0.06 to 1.06 V, the onset of mass transport limited currents in CO bulk oxidation on these electrodes, holding it there for 5 min, and then returning to 0.06 V (Fig. 5.6). Prior to the potential step, the electrodes were held at 0.06 V for 30 s to ensure CO_{ad} saturation. The general shape of the current transients of both Faradaic and mass spectrometric ion currents is about the same for the three different Pt specimens. In all three cases, the current increases at the potential step and then decays very slowly with time (see below). Also in this case, the initial spikes in the Faradaic current transients (Fig. 5.6a) are not equally reproduced in the mass spectrometric ion currents, which is partially due to the contribution from double-layer charging in Faradaic current spikes and partially results from the lower time resolution of the mass spectrometric measurements as discussed above.

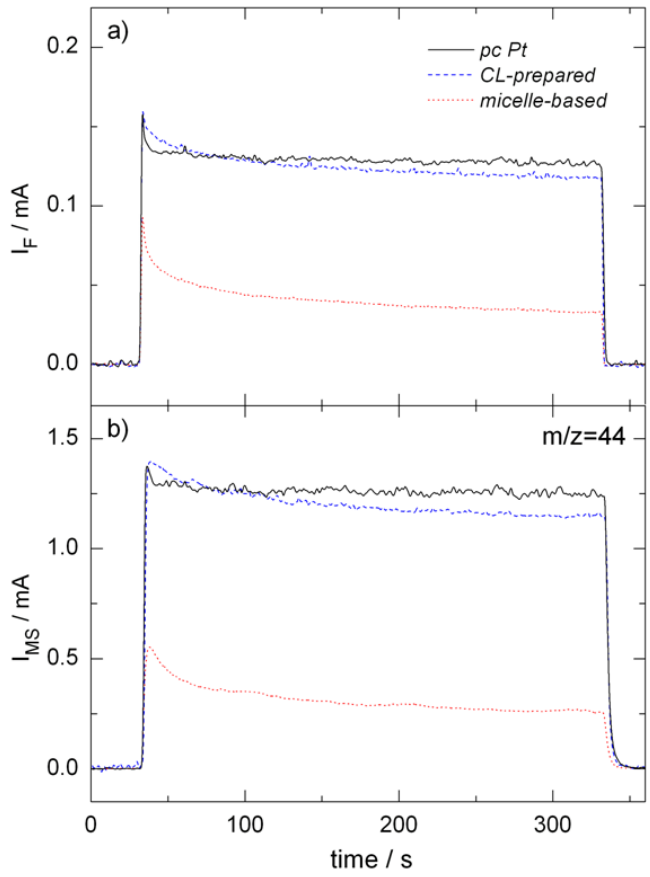

Figure 5.6: Potentiostatic electro-oxidation of CO (flow rate $5\,\mu L\,s^{-1}$, $E_{init} = 0.06\,V$, $t_{init} = 30\,s$, $E_{mid} = 1.06\,V$, $t_{mid} = 300\,s$) on a micelle-based Pt/GC model catalyst (dotted line), a CL-prepared nanostructured Pt/GC model catalyst (dashed line; ref. [65]), and a polycrystalline Pt electrode (solid line). Before the potential step to 1.06 V, CO had been pre-adsorbed at 0.06 V for 30 s. (a) Faradaic currents and (b) mass spectrometric currents at $m/z = 44$.

As expected from the potentiodynamic CO oxidation experiments, the resulting steady-state currents on the micelle-based Pt/GC electrode (dotted line) ($I_F = 0.03\,mA$, $I_{MS} = 0.25\,nA$) are significantly lower than those on the pc Pt (solid line) and CL-prepared nanostructured Pt electrodes (dashed line) ($I_F = 0.125\,mA$, $I_{MS} = 1.2\,nA$). However, both the micelle-based electrode and the CL-prepared nanostructured Pt/GC electrode exhibit a slow but continuous current decay with time (Faradaic current as well as mass spectrometric current), whereas on the pc Pt electrode the current signals are essentially constant. Additional experiments not shown here revealed that on the micelle-based sample the current decays for at least 500 s. Apparently, the nanostructured samples loose some activity with time. This may be related to insufficient CO_2 removal on the nanostructured samples, but again, other effects cannot be excluded.

Overall, the CO bulk oxidation experiments have shown that a mass transport limited current is not achieved on the micelle-based Pt catalysts because of the small amount of active metallic Pt. However, the CL-prepared nanostructured Pt/GC electrodes apparently completely consume the CO delivered to the substrate surface, although only about 23 % of the surface is covered with Pt nanoparticles. This is most likely related to the different CO transport on the two nanostructured model electrodes, with much larger structures on the CL-prepared electrodes than on the micelle-based electrode. Furthermore, diffusion to the Pt particle agglomerates (the bright dots in the SEM images) in the larger mixed nanoparticles resulting from micelle processing may effect the transport characteristics. Further work to improve the nucleation and accessibility of the active Pt particles is ongoing. Finally, the electrochemical/electrocatalytic data also underline the necessity of using highly conducting, inert substrates as well as continuous electrolyte flow to avoid artifacts introduced by ohmic drops in the substrate, by electrochemical activity introduced by the substrate [184, 199] or interaction with the substrate [201], or by diffusion limitations [201]. The last parameter requires the stable anchoring of particles on the substrate.

5.3 Conclusion

We have shown that the so-called micellar technique, involving the deposition of reverse micelles on a planar glassy carbon support and subsequent oxygen plasma/H_2 annealing treatment, is a viable method for producing nanostructured electrochemical model electrodes with similarly sized particles and defined particle separations. The model electrodes are stable in electrochemical measurements, as evidenced by subsequent SEM imaging, with no detectable particle losses during these measurements. Base CVs as well as potentiodynamic and potentiostatic CO electro-oxidation measurements indicate that the electrochemical and electrocatalytic properties of these model electrodes closely resemble those of Pt nanoparticles. These model electrodes with controlled particle sizes and/or particle separations give access to detailed studies on transport phenomena in electrocatalytic reactions.

Acknowledgement

We thank P. Walther (Central Facility for Electron Microscopy, Ulm University) and A. Minkow (Institute of Materials for Electro Technology) for high-resolution SEM measurements, B. Kern and L. Han for assistance with sample preparation,

H.-G. Boyen for many discussions, and M. Gustavsson, P. Hanarp, and B. Kasemo (Chalmers University of Technology, Gothenburg, Sweden) for the samples prepared by Colloidal Lithography. This work was supported by the Landesstiftung Baden-Württemberg within the Kompetenznetz Funktionale Nanostrukturen (projects B2 and B9) and by the Deutsche Forschungsgemeinschaft (SFB 569, project G2).

6 Mesoscopic Mass Transport Effects in Electrocatalytic Processes

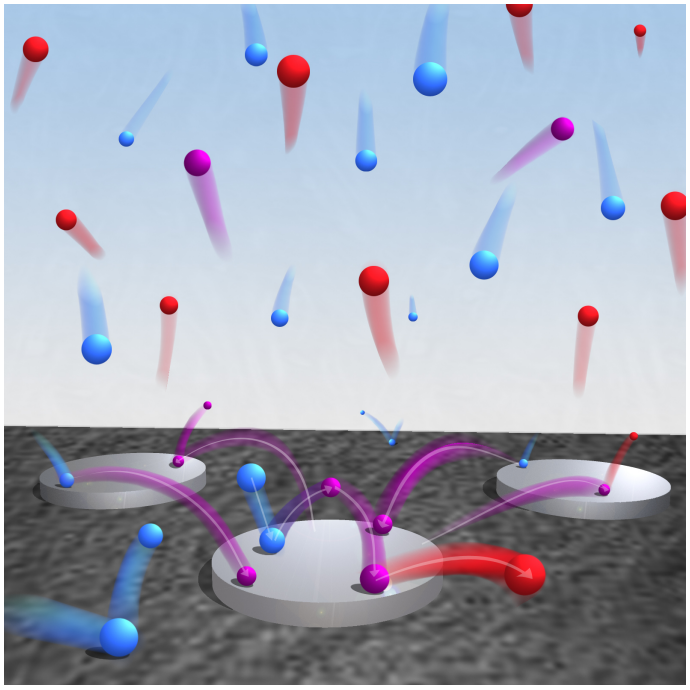

Cover of **Faraday Discussions** Volume 140, 2008
Electrocatalysis - Theory and Experiment at the Interface.

Y. E. Seidel[1], A. Schneider[1], Z. Jusys[1], B. Wickman[2], B. Kasemo[2] and R. J. Behm[1]

[1] Institute of Surface Chemistry and Catalysis, Ulm University, D-89069 Ulm, Germany
[2] Dept. of Applied Physics, Chalmers University of Technology, S-41296 Gothenborg, Sweden

Published in

Faraday Discussions 140 (**2008**) 167–184

Abstract

The role of mesoscopic mass transport and re-adsorption effects in electrocatalytic reactions was investigated using the oxygen reduction reaction (ORR) as an example. The electrochemical measurements were performed on structurally well-defined nanostructured model electrodes under controlled transport conditions in a thin-layer flow cell. The electrodes consist of arrays of Pt ultra-microelectrodes (nanodisks) of defined size (diameter ~ 100 nm) separated on a planar glassy carbon (GC) substrate, which were fabricated employing Hole-mask Colloidal Lithography (HCL). The measurements reveal a distinct variation in the ORR selectivity with Pt nanodisk density and with increasing electrolyte flow, showing a pronounced increase of the H_2O_2 yield, by up to 65 %, when increasing the flow rate from 1 to 30 $\mu L\,s^{-1}$. These results are compared with previous findings and discussed in terms of a reaction model proposed recently (A. Schneider *et al.*, *Phys. Chem. Chem. Phys.*, 2008, **10**, 1931), which includes *(i)* direct reduction to H_2O on the Pt surface and *(ii)* additional H_2O_2 formation and desorption on both Pt and carbon surfaces and subsequent partial re-adsorption and further reduction of the H_2O_2 molecules on the Pt surface. The potential of model studies on structurally defined catalyst surfaces and under well-defined mass transport conditions in combination with simulations for the description of electrocatalytic reactions is discussed.

The figure shows transport processes in an electrocatalytic reaction on an electrode surface with active metal structures (grey) on an inert substrate (black): with arriving reactants (blue), reactive intermediates (purple) desorbing into the diffusion layer, which can re-adsorb and react further, and final products (red) leaving into the bulk electrolyte.

6.1 Introduction

Electrocatalytic reactions have been investigated in much detail over many decades [211, 212]. In recent years, the interest in various electrocatalytic reactions has suddenly increased because of their potential applications in Fuel Cell Technology [15, 16, 18, 33, 127, 202, 213–218]. The kinetics and mechanism of these reaction were investigated by numerous techniques including purely electrochemical methods as well as combined electrochemical and in-situ spectroscopic techniques („hyphenated techniques“) such as various forms of in-situ IR spectroscopy [15, 144, 219–226], mass spectrometric techniques such as on-line differential electrochemical mass spectrometry (2.3.2 DEMS) [15, 84, 133, 140, 144, 148, 202, 222] or, most recently, X-ray absorption spectroscopy [227–232] and X-ray diffraction [180, 233–235]. These measurements, together with increasingly sophisticated theoretical studies [236–242], resulted in a wealth of mechanistic information on the individual reaction steps and in an increasingly better understanding of the molecular processes contributing to them [223].

Despite of this insight and the increasingly better agreement between theory and experiment, these model studies mostly miss one important point essential for a realistic description of the ongoing reaction, namely the transport steps required for transport of reactants to the electrodes, or of products away from the electrodes. In experimental model studies, electrolyte transport is enforced, e.g., in different types of flow cells, such as channel flow cells or other types of flow cells [70–72], which are employed for electrochemical measurements [4, 68, 243–249] or for in-situ spectroscopic studies (DEMS [3], IR [250]), or in measurements using other hydrodynamic methods. The latter include, e.g., measurements using the rotating (ring) disk electrode [33, 77, 176, 217] or wall-jet measurements [163, 251–254].

It is well accepted that transport of reactants to the electrode may affect the measured reaction rate by putting an upper limit on the rate, which results in the formation of a transport limited current (or „limiting current“) [68–72]. It is less realized, however, that transport effects may affect also the reaction pathways and their contributions to the total reaction, i.e., the selectivity of the reaction. First of all, a limited removal of reaction products may result in an accumulation of product species in front of the electrode surface and subsequently in back-reactions of the products or in blocking of the surface by adsorbed product species. Second, in reactions producing soluble, reactive reaction intermediates or reaction side products, the removal of these species from surface near regions may affect the reaction and in particular the product distribution by reducing the probability for re-adsorption and further reaction of these species (re-adsorption effects). Simple examples for such

cases are the oxidation of methanol or formaldehyde, which may result in the incomplete oxidation products formaldehyde and formic acid or in the complete oxidation product CO_2 for methanol oxidation, or in formic acid and CO_2 for formaldehyde oxidation (see ref. [140] and references therein). Recently, we have shown that for methanol oxidation on a thin-film carbon-supported Pt catalyst electrode and under enforced electrolyte flow, the product distribution changes significantly upon varying the catalyst loading, at otherwise constant reaction conditions, from predominantly formaldehyde production at low catalyst loadings to increasingly higher yields of CO_2 (and hence lower formaldehyde yields) at higher catalyst loadings [25]. The highest formaldehyde yield was obtained for a massive Pt electrode [5]. This was explained by a concept involving desorption of the incomplete oxidation products formaldehyde and formic acid and their subsequent re-adsorption and further oxidation to formic acid (formaldehyde) and CO_2 (formaldehyde and formic acid) („desorption–re-adsorption–reaction“ concept). With increasing surface roughness or with increasing thickness of the catalyst layer, the probability for re-adsorption and hence for further oxidation of these reactive intermediates increases, and therefore we expect also the fraction of complete oxidation products to increase, as observed experimentally. Similar trends were observed later also for formaldehyde oxidation [97, 140] for acetaldehyde oxidation [137], and for ethanol oxidation [156], where the yield of incomplete oxidation products formic acid or acetaldehyde/acetic acid was higher on massive Pt electrodes than on thin-film Pt/C catalyst electrodes under otherwise similar reaction conditions.

Following the above „desorption–re-adsorption–reaction“ concept, one would expect a decrease of the complete oxidation product yield also for an increasing electrolyte flow rate, because of the increasingly thinner diffusion layer, which makes it increasingly more probable that a desorbing reaction intermediate will leave the diffusion layer (or „boundary layer“) and is transported away rather than being re-adsorbed again. Such trend was indeed also observed experimentally for ethanol oxidation on a thin-film Pt/C electrode [156].

Furthermore, these studies revealed that also the reactant concentration may affect the product distribution [5, 156]. In this case, the explanation is less straightforward, since the probability for re-adsorption and further reaction of reaction intermediates is not altered. An increasing reactant concentration, however, will increase the reactant arrival rate at the electrode surface. If the reaction rate of adsorbed reactants or intermediates is not too high, an increasing adsorption rate will most simply result in an increasing steady-state coverage of these (re-)adsorbed reaction intermediates, which in turn may have consequences on the reaction characteristics and therefore also on the product distribution. For instance, the increasing

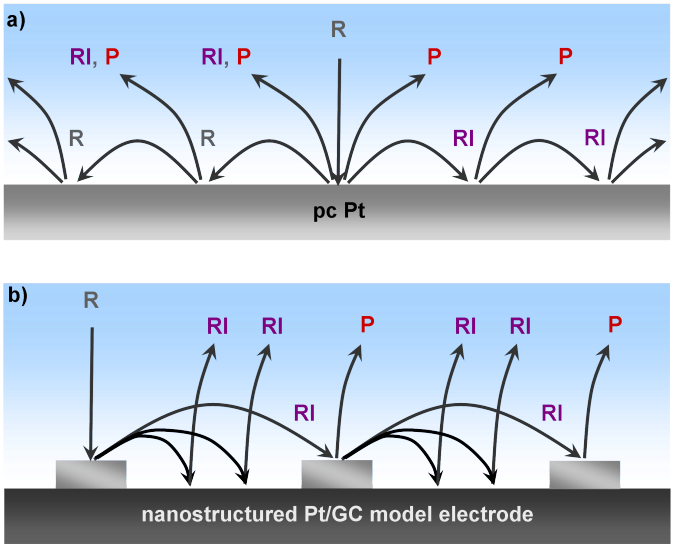

Figure 6.1: Schematic description of the desorption, diffusion, re-adsorption and reaction processes contributing to an electrocatalytic reaction which includes reaction pathways where volatile, reactive reaction intermediates are formed („desorption–re-adsorption–reaction“ process) (a) on a pc Pt electrode and (b) on a nanostructured Pt/GC model electrode. **R**: reactant molecule arriving at the electrode surface, right sequence: multiple desorption, re-adsorption and further reaction of the reaction intermediate **RI** to product **P** before its final off-transport through the diffusion layer into the flowing electrolyte; left sequence: desorption, multiple re-adsorption and further reaction of reactant **R** to reaction intermediate **RI** before its final off-transport through the diffusion layer into the flowing electrolyte.

CO_2 yield in potentiodynamic measurements of the ethanol oxidation reaction on a thin-film Pt/C electrode [156] was explained by an almost constant contribution of CO_2 formation via formation (at low potentials) and oxidation (at higher potentials) of CO_{ad}, while the formation of incomplete oxidation products acetaldehyde and acetic acid decreased significantly with decreasing ethanol concentration [156]. Effects induced by an adsorption induced change in steady-state adlayer composition and coverage have to be considered of course also when varying the electrolyte flow rate, which in addition to the modified re-adsorption probabilities will also change the reactant adsorption rate.

While we can understand these trends on a qualitative scale, a more quantitative understanding is still missing. It requires new experimental and theoretical approaches, which include not only the transport from the (flowing) bulk electrolyte to the electrode and vice versa, but also the desorption of incomplete oxidation/reduction products, their lateral diffusion in the diffusion layer, and the re-adsorption processes discussed above. This is illustrated schematically in Fig. 6.1a.

Recently, we have introduced nanostructured, glassy carbon (GC) supported Pt model electrodes (Pt/GC) [65, 97, 99, 193] for studies of transport processes in electrolytic reactions. These nanostructured electrodes, which consist of Pt nanodisks of fixed, defined diameter between 70 and 150 nm (height $\sim$20 nm) assembled in adlayers with a rather narrow distribution of separations between the Pt nanodisks, are produced via Colloidal Lithography (CL) [60–63, 65, 193] or, more recently, via Hole-mask Colloidal Lithography (HCL) [64, 181]. Because of their well-defined and rather regular structures, these electrodes are ideally suited for model studies on lateral transport effects, e.g., by investigating the change in reaction characteristics upon varying the density and/or size of the nanodisks (compare Fig. 6.1b) or the electrolyte flow rate. From the same structural reasons, they are particularly attractive as (experimental) model system for quantitative comparison with simulations of the contributing transport and reaction processes. The latter would be very close to the simulations of diffusion processes to arrays of ultra-microelectrodes in a flow cell situation reported previously (see e.g., [48–51]), complemented by lateral transport processes between the microelectrodes and by the surface reactions.

In the present *chapter*, mass transport effects in model studies of the oxygen reduction reaction (ORR) on nanostructured Pt/GC model electrodes, focusing on changes in the reaction characteristics (activity, selectivity) due to variations in the Pt nanodisk density and/or in the electrolyte flow rate are illustrated and discussed. The nanostructured electrodes were prepared by Hole-mask Colloid Lithography (2.1.2 HCL) rather than by Colloidal Lithography (2.1.1 CL) in order to avoid the formation and presence of additional undesired Pt nanoparticles of 3–5 nm diameter on the GC substrate in the areas between the Pt nanodisks, which were shown to be formed during CL processing and which may have significant impact on the reaction characteristics (see *chapter* 4) [181]. First measurements of the ORR performed on CL-prepared electrodes have shown that on these model electrodes significant amounts of H_2O_2 are formed at potentials where the carbon substrate is non-reactive, up to 0.8 V_{RHE}, and that the H_2O_2 yield is affected by the density of the nanodisks [99]. These findings were explained by the formation of H_2O_2 on the Pt nanodisks, its desorption, re-adsorption and further reduction of H_2O_2 on the other Pt nanodisks, which leads to a lower H_2O_2 yield with increasing density of Pt nanodisks [99]. Clear trends, however, were hard to evaluate, most likely due to effects introduced by the (undesired) Pt nanoparticles. In this *chapter*, the systematic expansion and continuation of these preliminary measurements, employing improved, HCL-prepared nanostructured electrodes, together with a polycrystalline Pt and a Pt-free GC electrode as reference, to investigate effects of varying the Pt nanodisk density and the electrolyte flow on the ORR reaction characteristics by

application of a double disk dual thin-layer flow cell (see sections 2.3.3 and 2.4.3) is reported. The results will be discussed in comparison with previous results of catalyst loading effects and the earlier results on the CL-prepared nanostructured Pt/GC electrodes. In a final outlook, the potential of these nanostructured electrodes for systematic, combined experimental and theoretical studies of mass transport effects in electrocatalytic reactions will be dicussed.

6.2 Results and Discussion

The nanostructured Pt/GC model electrodes with Pt nanostructures of $\sim 100\,\mathrm{nm}$ in diameter deposited on a planar glassy carbon (GC) substrate were prepared via Hole-mask Colloidal Lithography (2.1.2 HCL), following a recently developed procedure described in detail in ref. [64] and [181] (see Fig. 2.2). These include *(i)* a medium-loading sample (HCL-20) with $\sim 20\%$ Pt coverage ($\varnothing \sim 118\,\mathrm{nm}$), *(ii)* a low-loading sample (HCL-10) with $\sim 10\%$ Pt coverage ($\varnothing \sim 95\,\mathrm{nm}$), and *(iii)* an ultra-low loading sample (HCL-01) with $\sim 1\%$ Pt coverage ($\varnothing \sim 95\,\mathrm{nm}$). All experiments were performed on three different samples of each type to ensure reproducibility. As references, we also included a polycrystalline Pt sample (*pc Pt*) and a polished GC substrate.

The morphology of the resulting model electrodes is illustrated by the SEM images in Fig. 6.2. The large scale images (Fig. 6.2a, b) demonstrate the homogeneous distribution of the Pt nanodisks over the GC substrate surface for the model electrodes with higher surface coverage. Only for the ultra-low loaded sample depicted in Fig. 6.2c, the Pt nanodisks are essentially randomly distributed. High resolution images (Figs. 6.2d–f) show the morphology of the Pt nanodisks and the glassy carbon substrate. They clearly demonstrate the absence of Pt nanoparticles in between the Pt nanostructures.

The electrochemical properties of these electrodes were characterized by base voltammetry and by pre-adsorbed CO_{ad} oxidation („CO_{ad} stripping“). The cyclic voltammograms obtained in $0.5\,\mathrm{M}$ H_2SO_4 solution (Fig. 6.3) are characteristic for polycrystalline Pt, with distinct signals for hydrogen adsorption/desorption in the H_{upd} range between 0 and $0.35\,\mathrm{V}$, a double-layer region up to $\sim 0.8\,\mathrm{V}$, and the signals for Pt oxidation/Pt oxide reduction at potentials anodic of $0.8\,/\,0.6\,\mathrm{V}$. The H_{upd} and the Pt oxidation/reduction signals decrease with decreasing Pt coverage. These results closely resemble previous findings for similar type nanostructured electrodes [97, 181].

From the H_{upd} charges, the active Pt surface areas were determined to $0.45\,\mathrm{cm}^2$ (*pc*

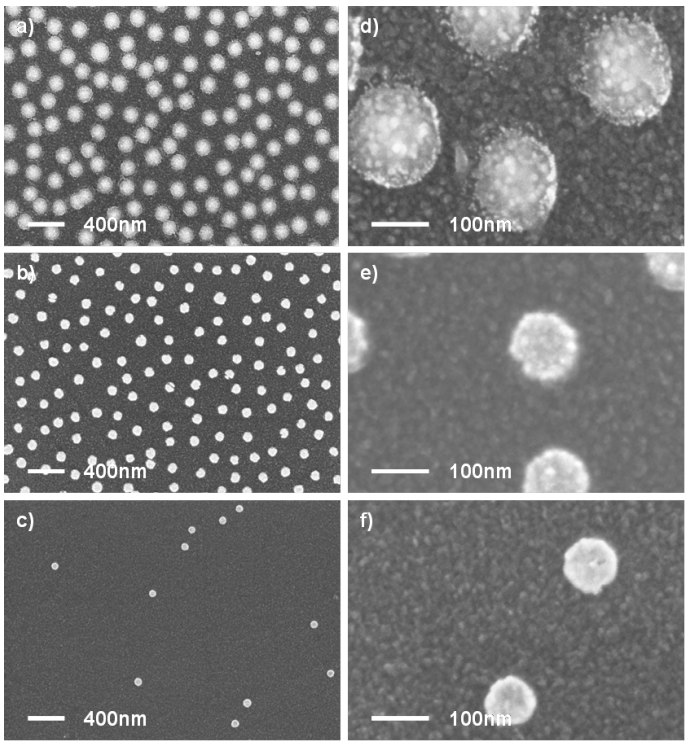

Figure 6.2: Representative large-scale (a–c) and high-resolution (d–f) SEM images of the HCL-prepared Pt/GC model-catalysts. (a, d) Medium Pt coverage ($\sim 22\,\%$ Pt, HCL-20), (b, e) low Pt coverage ($\sim 10\,\%$ Pt, HCL-10) and (c, f) ultra low Pt coverage ($\sim 1\,\%$ Pt, HCL-01). Large scale images $2.6\,\mu\text{m} \times 3.6\,\mu\text{m}$; high resolution images $420\,\text{nm} \times 580\,\text{nm}$.

Pt), $0.23\,\text{cm}^2$ (HCL-20), $0.11\,\text{cm}^2$ (HCL-10) and $0.006\,\text{cm}^2$ (HCL-01), respectively, assuming a monolayer hydrogen charge of $0.21\,\text{mC cm}^{-2}$ [2] and a H_{upd} coverage of $0.77\,\text{ML}$ at the onset of H_2 evolution [152]. The active surface areas follow exactly the SEM determined geometric surface area of the Pt nanodisks, underlining the identical morphology of the Pt nanodisks and the absence of additional, undesired Pt nanoparticles on the GC areas in between the Pt nanodisks. The latter would lead to a pronounced increase of the active Pt surface area compared to the Pt coverage at low Pt coverages, as was observed in an earlier study on CL-prepared nanostructured Pt/GC model electrodes [181].

These findings are qualitatively and quantitatively supported by previous CO_{ad} stripping measurements, which equally showed signals characteristic for polycrystalline Pt and yielded active Pt surface areas comparable to those determined by the H_{upd} uptake (see also ref. [181]). Furthermore, these data and also energy dispersive X-ray emission measurements confirmed that (undesired) Pt nanoparticles between the (desired) Pt nanodisks are essentially absent [181].

The ORR activity (a, d, g, k) and selectivity (b, e, h, l and c, f, i, m) of the polycrystalline Pt electrode (a–c), the nanostructured Pt/GC samples (d–m), and the

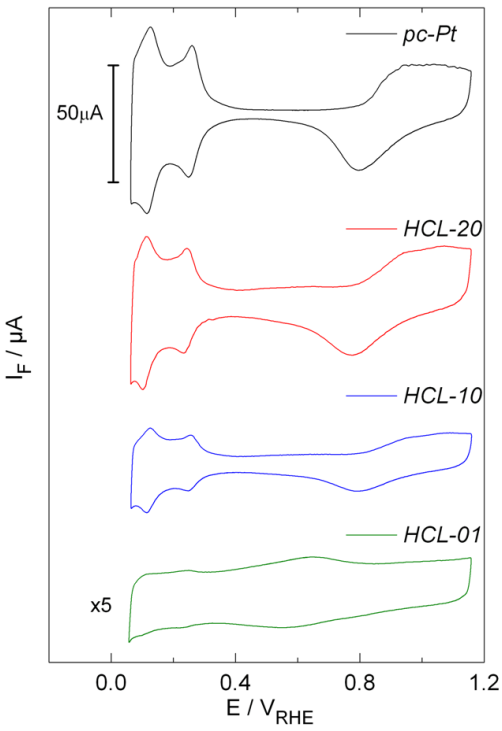

Figure 6.3: Base voltammograms (scan rate 100 mV s^{-1}) recorded on a pc Pt electrode (top line), on the nanostructured HCL-20 (∼ 22 % Pt surface coverage), HCL-10 (∼ 10 % Pt surface coverage) and the HCL-01 (∼ 1 % Pt coverage, bottom line; note, that the currents for that sample were multiplied by a factor of 5) sample.

Pt-free glassy carbon substrate (k–m) in the positive-going potential scan, measured as the Faradaic current for O_2 reduction (generator current) and as the H_2O_2 oxidation current on the collector (collector current), respectively by use of a double disk dual thin-layer flow cell (see section 2.3.3), are plotted in Fig. 6.4. To more specifically address mass transport effects, a wide range of electrolyte flow rates was employed, ranging to very low values (1 μL s^{-1}). The ORR Faradaic currents on the *pc Pt* and on the nanostructured Pt/GC electrodes (Fig. 6.4a, d, g and k) display the general features characteristic for the ORR on Pt under enforced mass transport, namely, a mass transport limited region at lower potential and a mixed mass transport/kinetically limited region at more anodic potentials, where the Faradaic current decays to zero on the PtO blocked surface at potentials positive of 0.9 V. These findings agree well with earlier data for the ORR on massive Pt electrodes [170], on carbon-supported Pt/C catalyst electrodes [162], and with the data obtained on the CL-prepared nanostructured Pt/GC electrodes [99]. Comparing the Faradaic currents on the different samples, two important trends can be distinguished. First, on the nanostructured Pt/GC electrodes the mass transport limited current gradually decreases with the decrease in Pt coverage, while those of the *pc*

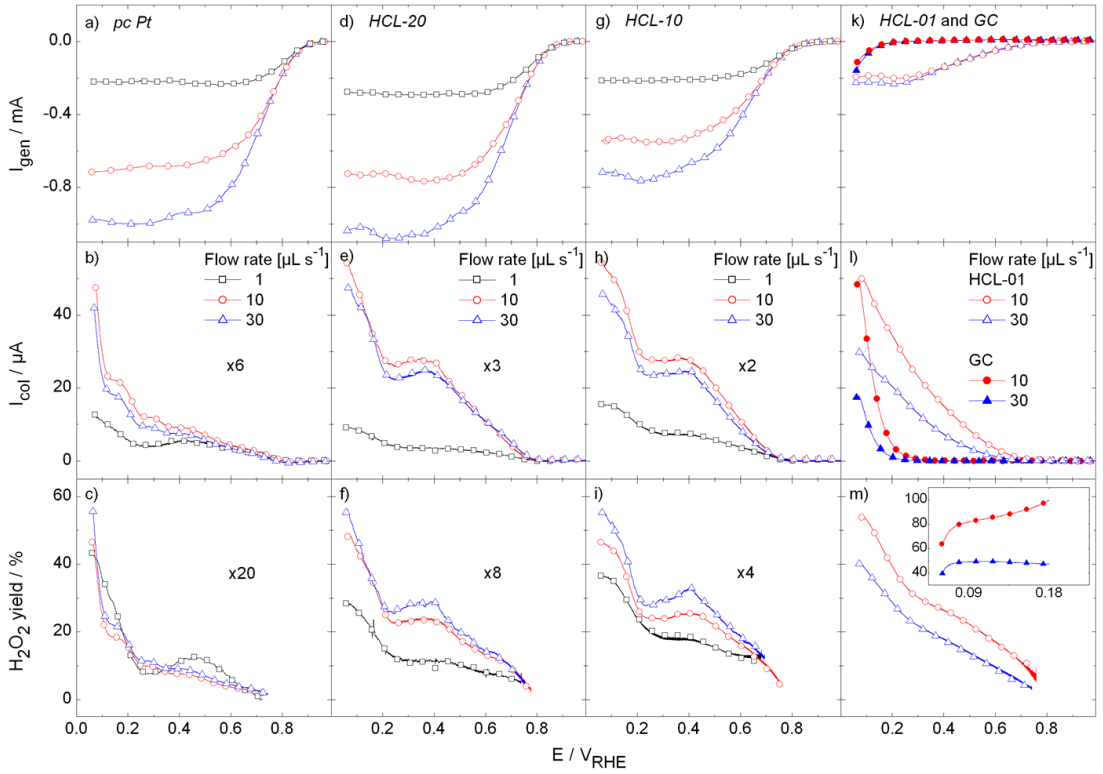

Figure 6.4: Oxygen reduction reaction activity (a, d, g, k), hydrogen peroxide oxidation at the smooth polycrystalline Pt collector electrode (geometric area 1.33 cm^2, biased at 1.2 V) (b, e, h, l), and the corresponding hydrogen peroxide yields (c, f, i, m) simultaneously monitored in the double-disk thin-layer flow-cell over a smooth polycrystalline Pt electrode (a–c), on nanostructured Pt/GC model electrodes: (HCL-20 (d–f); HCL-10 (g–i) and HCL-01), and on a blank GC substrate (k–m) at different electrolyte flow rates (1, 10, and 30 $\mu L\,s^{-1}$, for assignments see figure). Solution: 0.5 M H_2SO_4 (O_2-saturated), exposed electrode area 0.3 cm^2, potential scan rate 10 $mV\,s^{-1}$ (positive-going scan), room temperature.

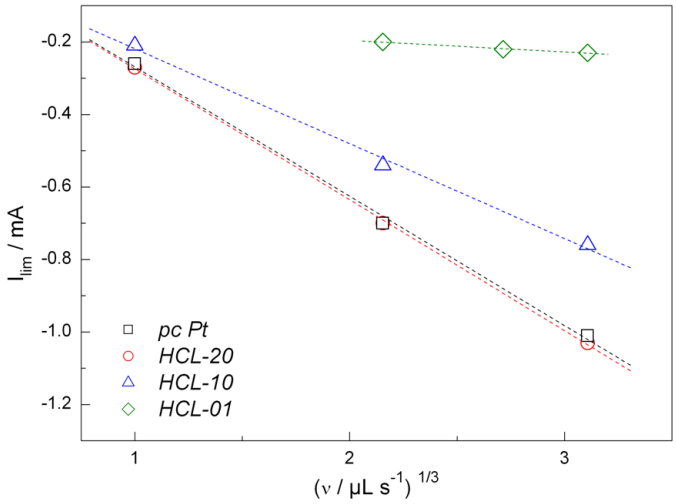

Figure 6.5: Dependence of the mass transport limited ORR current (at 0.2 V) vs. the cube root of the electrolyte flow rate in a dual thin-layer flow cell configuration over *pc Pt* electrode and over a nanostructured Pt catalysts supported on planar glassy carbon substrate (see figure). Solution: O_2-saturated 0.5 M H_2O_2, room temperature.

Pt sample and of the HCL-20 sample are approximately identical. Furthermore, the potential for transition from the purely mass transport limited regime to the mixed kinetically/mass transport limited regime depends sensitively on the Pt loading and on the electrolyte flow rate, shifting to lower potentials with decreasing Pt coverage and with increasing electrolyte flow.

The clear decrease of the mass transport limited ORR current with decreasing Pt coverage differs distinctly from the observation of a constant mass transport limited current on CL-prepared nanostructured Pt/GC electrodes [99]. The decay of the limiting ORR current can be understood by comparison with the results of previous simulations of the diffusion controlled current on arrays of ultra-microelectrodes on an inert substrate [48]. These simulations clearly identified two limiting situations, one where the individual microelectrodes are far apart and where the transport to each electrode can be described by hemispherical diffusion spheres, and a second one where the electrodes are close enough for an effective overlap of the diffusion spheres. In the first case, the total diffusion limited current is identical to the sum of the currents to separated individual microelectrodes, in the latter case it can be described by the diffusion limited current to a planar electrode [48]. Hence, the mass transport limited current starts to decrease only below a critical density of the microelectrodes. On the CL-prepared nanostructured Pt/GC electrodes, the additional Pt nanoparticles present on the GC surface between the Pt nanodisks were apparently sufficient to keep the Pt coverage/density above that critical value,

and the mass transport limited current remained constant despite a significant decrease in Pt nanodisk density [99]. On the present, HCL-fabricated nanostructured electrodes, where these Pt nanoparticles are absent, the critical density of Pt nanodisks is passed already for the HCL-10 sample at higher electrolyte flow rates. The decrease of the transport limited current at potentials cathodic of 0.2 V, which is particularly obvious at the higher flow rates on the nanostructured electrodes, is attributed to H_2O_2 under these conditions, which reduces the Faradaic current accordingly (2-electron pathway for H_2O_2 instead of the 4-electron pathway for H_2O) [99]. ORR measurements on a Pt-free glassy carbon substrate, which are included for comparison, show a small ORR activity at potentials negative of 0.2 V (Fig. 6.4k, blank symbols).

For flow cell measurements on a non-structured electrode, it is well known that the mass transport to the electrode, and thus the mass transport limited current (I_{lim}), decay with the cube root of the electrolyte flow rate υ ($I_{lim} \propto \sqrt[3]{\upsilon}$) [74, 165, 166]. Therefore, we plotted the mass transport limited current at 0.2 V, i.e., above the onset of the ORR current decrease due to H_2O_2 formation, as a function of the cube root of the electrolyte flow rate (Fig. 6.5, note that each data point is averaged over several measurements). The data clearly lie on straight lines, underlining that this relation is valid also for the nanostructured electrodes, and also for those with Pt densities below the critical density discussed above. The data for the *pc Pt* sample and the HCL-20 sample, where the Pt nanodisk density is above that limit under present transport conditions, are essentially identical. The slopes of the lines for the HCL-10 and the HCL-01 lines, however, are significantly lower than those of the *pc Pt* and the HCL-20 sample. This can be explained by inspecting the equation describing the correlation between mass transport limited current (I_{lim}) and electrolyte flow rate (υ) [74, 165, 166]:

$$I_{lim} = k\ n\ F\ c\, \upsilon^{1/3}\, (DA/b)^{2/3}, \tag{6.1}$$

where k is the cell constant ($k = 1.467$ for a channel-flow thin-layer cell), n is the number of electrons, F is the Faraday constant, c is the concentration of the species involved in the reaction, υ is the electrolyte flow rate, D is the diffusion coefficient of the reacting species, A is the electrode surface area, and b is the thickness of the thinlayer gap, respectively. Since the other factors are not changed in these measurements, it is obviously a change in the (effective) surface area A below the critical Pt nanodisk density which is responsible for the decreasing slope with lower Pt coverage.

The shift of the transition potential between the two reaction regimes and the related broadening of the mixed mass transport/kinetically limited region to lower

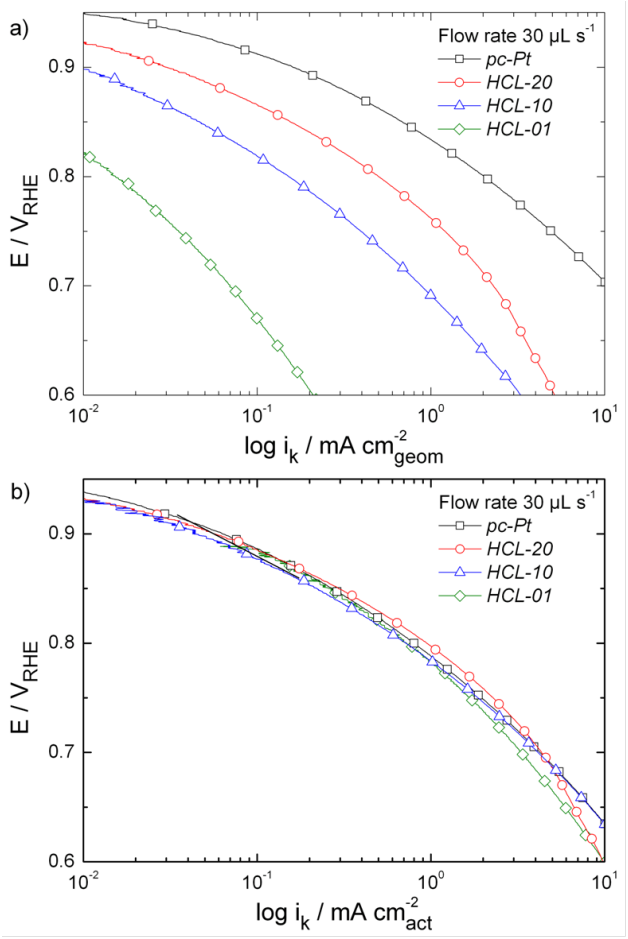

Figure 6.6: Tafel plots for geometric (a) and active (b) surface area normalized kinetic oxygen reduction current over smooth polycrystalline Pt (squares), and nanostructured Pt/GC model electrodes: HCL-20 (circles), HCL-10 (triangles) and HCL-01 (diamonds). The data are extracted from Fig. 5 a, d, g, k. The limiting currents were taken at 0.2 V.

potentials with decreasing Pt coverage can be explained by increasing kinetic limitations related to the lower Pt surface area available for the reaction. This can be simply demonstrated by removing mass transport effects and normalizing the resulting kinetic currents to the active Pt surface areas. Tafel plots (see section 2.4.3) of the kinetic current densities normalized to the geometric surface area, $i_{k,geom}$, which is identical for all samples (geometric surface area 0.283 cm^2), and the active Pt surface area normalized kinetic ORR currents densities, $i_{k,act}$, which decrease with Pt coverage, are presented in Fig. 6.6a, b, respectively, for an electrolyte flow rate of 30 $\mu L\, s^{-1}$. As expected, the slope of the lines is around 60 mV dec^{-1} in the high potential region (low overpotential, 0.9–0.86 V), while it is around 120 mV dec^{-1} in the lower potential region (0.8–0.7 V), in agreement with a one- or two-electron transfer in the rate limiting step, respectively [162, 255]. The almost identical Tafel curves

obtained for the active Pt surface area normalized kinetic ORR currents densities on the different samples clearly confirm that the wider range of the mixed transport limited/kinetically limited region is simply a consequence of the competition being kinetic control and mass transport control, where the former depends on the active Pt surface are, while the latter depends mainly on the geometric surface area and, at low Pt nanodisk densities, also on the active surface area A. Similar trends were observed for the lower flow rates.

The H_2O_2 peroxide production (see section 2.4.3) during the ORR over the *pc Pt* electrode decreases considerably with decreasing flow rate down to $1\,\mu L\,s^{-1}$ (Fig. 6.4b). Correcting, however, for the simultaneous decrease in Faradaic current, the resulting H_2O_2 yields do not change significantly with flow rate. The H_2O_2 production on *pc Pt* electrode was attributed to surface blocking effects, reducing the probability for finding neighboring empty Pt sites for O_2 dissociation. This favors the pathway for H_2O_2 formation, where only one adsorption site is assumed to be required [255]. Surface blocking starts by (bi)sulfate adsorption in the double-layer potential region, and increases rapidly at potentials $< 0.3\,V$ by H_{upd} adsorption. It is important to note that at potentials relevant for fuel cell cathode operation (0.7–0.8 V), H_2O_2 formation on the *pc Pt* electrode is negligible (Fig. 6.4c), and also in the double-layer range the H_2O_2 oxidation current and the H_2O_2 yields are very low on this electrode (see the expanded scales in Fig. 6.4b, c). For the nanostructured Pt/GC electrodes, the H_2O_2 production increases significantly with decreasing Pt coverage (Fig. 6.4e, h and i), resulting in a corresponding increase in H_2O_2 yields even at potentials relevant to cathode operation. A similar trend, though much less pronounced, was observed recently on CL-prepared nanostructured Pt/GC electrodes and explained by a reaction mechanism where *(i)* O_2 can be reduced to both H_2O and to H_2O_2 on the Pt surface, and where *(ii)* the resulting H_2O_2 intermediate can re-adsorb on other Pt sites and be further reduced to H_2O („desorption–re-adsorption–reaction“ concept) [99]. This is illustrated in Fig. 6.1, with H_2O_2 as reaction intermediate RI. At potentials below $0.2\,V$, H_2O_2 can be formed also on the carbon areas of the nanostructured Pt/GC electrodes, as evidenced by the onset of H_2O_2 formation on the Pt-free GC electrode (see Fig. 6.4l, m). Because of the low absolute currents, the contribution to the total H_2O_2 yield on the nanostructured Pt/GC electrodes, however, will be small. In the above reaction mechanism, the increase of the H_2O_2 yield with decreasing Pt coverage is simply due to the decreasing probability for desorbed (dissolved) H_2O_2 molecules to re-adsorb and further react on Pt sites. Correspondingly, the probability for H_2O_2 to escape into the bulk electrolyte and be removed from the reaction cell increases with decreasing probability for re-adsorption and hence lower Pt coverage.

Although the probability for H_2O_2 formation on Pt in a single reaction event can not be extracted from these data without extensive modeling (see section 6.3 Outlook), it must be quite high, as evidenced by the rather high H_2O_2 formation on the nanostructured Pt/GC samples with low Pt coverage (Fig. 6.4i, m). Correspondingly, the negligible amount of H_2O_2 formation on massive Pt electrodes [255] and on realistic carbon-supported Pt/C catalysts [162], in particular at potentials $> 0.3\,V$, points to a high probability for re-adsorption and further reduction of desorbable (dissolved) H_2O_2 intermediates on these electrodes/catalyst layers. Our results agree fully with previous findings of catalyst loading effects on thin-layer Pt/C catalyst electrodes by Inaba et al. [44]. Very recently, Bonakdarpour et al. reported a pronounced increase of H_2O_2 formation at low catalyst loadings for the ORR on RuSex/C catalyst electrodes and attributed this to the formation of H_2O_2 reaction intermediates [256]. While for the latter catalyst, significant H_2O_2 formation may appear as „expected“, considering the amount of H_2O_2 formation already on „normal loading“ thin-layer catalyst electrodes [163, 257], the observation of a high H_2O_2 yield in the ORR on Pt, even at potentials around 0.5–0.6 V, seems to be in complete contrast to the previous mechanistic understanding of the ORR on Pt [79, 258]. Furthermore, it is important to note that in a very different experiment, an increasing amount of H_2O_2 formation in the ORR on Pt with increasing electrolyte transport was reported and discussed also by S. Chen and A. Kucernak [259]. This clearly demonstrates the important role of re-adsorption effects (re-adsorption and further reaction of desorbable, reaction intermediates as described by the „ desorption–re-adsorption–reaction“ concept and illustrated in Fig. 6.1) for the mechanistic understanding of electrocatalytic reactions.

The much more pronounced effects on the HCL-prepared nanostructured Pt/GC electrodes compared to the CL-prepared ones can be simply explained by the presence of significant amounts of additional Pt nanoparticles on the GC surface, which are distributed in the surface areas between the Pt nanodisks on the latter samples. These nanoparticles, which are likely to be produced during sputtering step in the nanostructuring process [181], limit the decrease in re-adsorption probability when reducing the density of the Pt nanodisks.

This mechanism is fully supported by the trend for H_2O_2 formation upon varying the electrolyte flow rate. In contrast to the ORR on CL-prepared Pt/GC electrodes, not only the H_2O_2 formation but also the H_2O_2 yield increases clearly for the nanostructured HCL-20 and HCL-10 Pt/GC electrodes with increasing electrolyte flow (Fig. 6.4f, i). For the HCL-01 sample (Fig. 6.4m) we expect a similar general trend, but in this case the situation is more complicated because of the significant relative contributions from the (partly kinetically limited) ORR on the carbon substrate

areas at $E < 0.25\,V$ and the fact that, due to the very low Pt loading, the mixed transport and kinetically limited region ranges down to a potential of $\approx 0.25\,V$. Within the mechanism discussed above, that can be easily explained by the increasing probability for re-adsorption at lower electrolyte flow. Due to the increasing concentration gradient/thinner diffusion layer at higher electrolyte flow the probability for H_2O_2 formed at the electrode has a higher chance for escaping into the bulk electrolyte and be transported out of the reaction cell with increasing electrolyte flow. The probability for re-adsorption on Pt areas and further reduction to H_2O decreases accordingly. This effect is clearly visible on all nanostructured samples. At high Pt coverages, either due to high Pt loading (*pc Pt*, on realistic Pt/C catalysts or on nanostructured Pt/GC electrodes with additional Pt nanoparticles on the surface), where also the H_2O_2 yield is rather small, these electrolyte flow effects are essentially not detectable. On the present HCL-prepared Pt/GC electrodes, in contrast, they are clearly visible. Considering also that there is no H_2O_2 formation on the GC area at potentials > 0.2 V, these findings convincingly support the „desorption–re-adsorption–reaction“ concept introduced for the ORR on Pt recently [99]. On massive Pt electrodes and at commonly used electrolyte flow rates, the probability for re-adsorption of H_2O_2 and further reduction to H_2O is so high that H_2O_2 formation is hardly observed, despite the obviously rather high probability for H_2O_2 formation in a single adsorption/reaction step. Based on the data for the HCL-01 electrode, this probability must be higher than 30 % at 0.5 V!

Finally, it should be noted that although the measurements described in the present communication were performed on model surfaces to elucidate the effects of mass transport on the ORR activity and selectivity under defined reaction conditions, the results also have consequences for practical applications, e.g., in polymer electrolyte fuel cell (PEFC) cathodes. They clearly point out that with decreasing catalyst loading, which is strived for from economical reasons, there is an increasing risk of H_2O_2 production on the cathode catalyst even under typical cathode reaction conditions, which may have disastrous consequences on the lifetime of electrode or membrane due to corrosion effects [45, 46]. It is important to note that for a correct assessment of the H_2O_2 related corrosion effects, the macroscopic H_2O_2 yield measured at the exhaust of the catalyst is not decisive, but rather the local steady-state concentration in the electrode, which due to the re-adsorption effects may be much higher than the former.

6.3 Outlook

As mentioned in the Introduction, measurements on well-defined nanostructured samples under controlled transport conditions similar to those presented here provide an ideal basis for further simulations. Simulations of vertical transport to a non-structured sample in a similar flow cell geometry [260] or in a rectangular cell geometry [249] were published recently, further simulations coupling these transport/diffusion processes with a subsequent catalytic surface reaction (CO oxidation) are currently in progress [261]. On the other hand, (vertical) diffusion to arrays of regularly arranged ultra-microelectrodes of different shapes was calculated in a number of studies, starting from a fixed concentration at a defined plane above the electrode surface [48–51] (see Fig. 6.7a). This is identical to the situation in a flow cell, where above the diffusion layer the reactant concentration can be assumed to be constant and identical to the bulk concentration in the flowing electrolyte. A logical next step will be to combine these approaches and to include *(i)* lateral transport and re-adsorption processes according to Fig. 6.1 and 6.7b, and *(ii)* the specific geometry of the nanostructured model electrode surface in the simulation. Obviously, this requires a highly complex fully three-dimensional description of the ongoing transport processes. In order to avoid further complications, such calculations could first be applied to simulate the processes in a transport limited single-step reaction such as H_2 oxidation with negligible steady-state coverages of reactants and reaction intermediates, similar to the approach used in ref. [249]. These simulations should map out the macroscopic and mesoscopic (vertical) diffusion to a nanostructured surface in a realistic cell geometry and identify the influence of lateral transport processes and surface reaction of the reactants under conditions where effects related to changes in the composition and coverage of the adlayer can be neglected (see Fig. 6.7a). In a next step, one would include the formation, desorption, lateral transport and re-adsorption/further reaction of reaction intermediates (RI), as illustrated in Fig. 6.1 and 6.7b, but would still neglect possible changes in the composition/coverage of the adlayer under different steady-state conditions. For this level of simulation, where details of the surface processes can still be neglected, the ORR on nanostructured Pt/GC electrodes (in the transport-limited potential range), as described in the present contribution, would be a suitable experimental system.

Finally, in the last step, also details of the ongoing surface processes need to be included, at least to an extent that variations in the adlayer composition/coverage and the related changes in the catalytic properties of the active electrode areas can be accessed (see Fig. 6.7c). Suitable experimental examples would be the ORR in

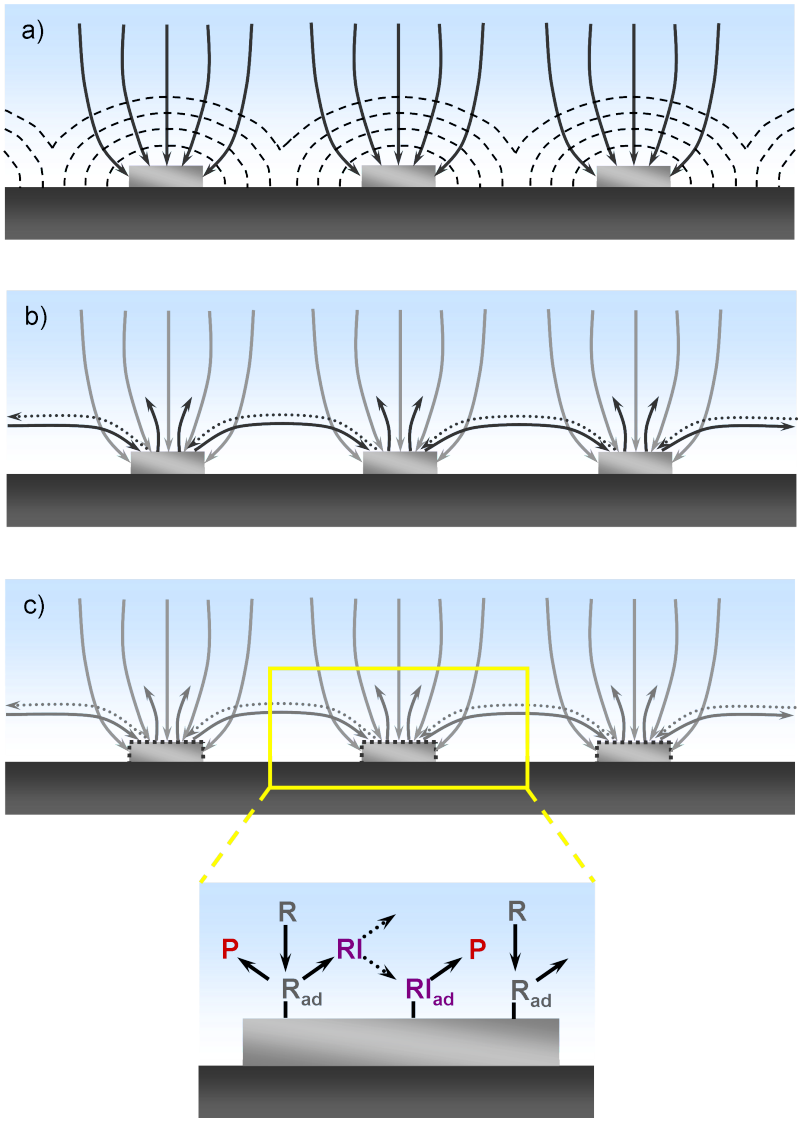

Figure 6.7: Hierarchy of model studies and simulations on transport effects in electrocatalytic reactions on structurally well-defined nanostructured model electrodes (arrays of ultramicroelectrodes) under defined transport conditions in a realistic cell geometry. (a) Vertical transport of reactants (**R**) to the model electrode without reaction intermediate formation or product re-adsorption and the surface (experimental example: H_2 oxidation); (b) as (a), but in addition also formation, desorption, lateral transport and re-adsorption/reaction of volatile reaction intermediates on the non-modified active surface of the model electrode (experimental example: O_2 reduction oxidation in the mass transport limited potential regime); (c) as (b) but in addition consideration of the surface processes, e.g., by density functional calculations, and the build-up of an adlayer formed by adsorbed reactants, reaction intermediates, and reaction side products (experimental examples with increasing complexity: CO oxidation (no **RI**), O_2 reduction in the mass transport limited potential regime (**RI**: H_2O_2), oxidation of methanol or formaldehyde (**RI**: formaldehyde (methanol oxidation only), formic acid).

the kinetically limited potential region on nanostructured Pt/GC samples or, even more complex, the oxidation of methanol or formaldehyde on the same electrodes. This requires a complex multi-scale approach for the combination of molecular scale surface processes and mesoscopic transport processes. The final goal of these kinds of combined experimental/theoretical approach would be a quantitative description of the experimental reaction characteristics (overall activity and product distribution under different reaction conditions) on these structurally simple and well-defined nanostructured model electrodes under controlled transport conditions, including a three dimensional (3D) description of the macroscopic and mesoscopic transport processes in the electrolyte above the electrode and of the molecular scale surface processes.

In total, this would be an enormous step towards a molecular understanding of electrocatalytic reactions, similar to the recent progress in heterogeneous catalysis reached by efforts to bridge the materials and pressure gap between surface science model studies under ultrahigh vacuum conditions on single-crystal model catalysts and catalytic studies on realistic supported catalysts and under realistic reaction conditions (see ref. [262] and subsequent articles in that special issue). One important difference between the two areas of heterogeneous catalysis and electrocatalysis highly relevant for the present considerations is that in the latter case even the proper description of electrocatalytic reactions under model conditions and on model electrodes requires inclusion of transport processes, which is not the case in surface science model studies performed under UHV conditions.

Finally, it should not be forgotten that despite the experimental and theoretical complexity of the tasks described above, we have so far obtained a proper description of an electrocatalytic reaction on a two dimensional (2D) electrode with regularly distributed active centers. The extension of this approach to the description of a 3D electrode with active centers, either in a regular structure or even in a disordered arrangement, as experienced experimentally in a thin film catalyst layer or in a porous fuel cell electrode, would again represent a major task.

6.4 Conclusion

We have investigated the role of mesoscopic transport effects in the oxygen reduction reaction on Pt by measuring the activity and selectivity (H_2O_2 formation) of the O_2 reduction reaction on nanostructured Pt/GC model electrodes in a dual thin-layer flow cell under controlled and varied electrolyte flow conditions and at different Pt coverages. The Pt/GC electrodes were fabricated by Hole-mask Colloidal Lithography and consist of Pt nanodisks of defined diameter supported on a glassy carbon

substrate, which are arranged in a rather regular array with a narrow distribution of separations.

In addition to the expected increase of the transport limited current with increasing Pt coverage in the low to medium Pt coverage regime and, for all Pt coverages, with increasing electrolyte flow rate υ, the data show a quantitative agreement with the $I_{lim} \propto \sqrt[3]{\upsilon}$ predicted for non-structured electrodes in a channel flow, with the slope depending on the Pt coverage on the nanostructured electrodes. This is explained by the geometric factor in the dependence of the limiting current on the electrolyte flow υ [165]. Furthermore, they show a clear trend to lower H_2O_2 yields with decreasing electrolyte flow. The same is observed for increasing Pt coverages, in agreement with previous findings. The results are explained in terms of a reaction model proposed recently, which includes *(i)* direct reduction to H_2O on the Pt surface, and *(ii)* significant formation and desorption of H_2O_2 on the Pt surface, at potentials $\leq 0.3\,\mathrm{V}$ also on the carbon surface, its subsequent partial re-adsorption and further reduction to H_2O on the Pt surface („desorption–re-adsorption–reaction“ concept). Because of the high probability for re-adsorption and further reduction of the volatile H_2O_2 reaction intermediates, the experimentally observed H_2O_2 formation is negligible on extended massive Pt electrodes or on carbon-supported Pt catalysts, although it is clearly formed on Pt at potentials $< 0.8\,\mathrm{V}$ Pt. These findings are compared to recent observations of an increased formation of complete oxidation products compared to incomplete oxidation products in the oxidation of different small organic molecules with increasing catalyst loading or decreasing electrolyte flow, which can be explained in similar terms, i.e., by an increasing probability for re-adsorption and further oxidation of volatile reaction intermediates to the complete oxidation product CO_2 with increasing catalyst loading or decreasing electrolyte flow.

In an outlook, the potential and further development of combined experimental and theoretical model studies on these nanostructured model electrodes for the understanding and description of electrocatalytic processes on model systems was mapped out. In the end, the description should, in a multi-scale approach, include *(i)* macroscopic and mesoscopic transport of the reactant in a realistic reaction cell and under defined electrolyte conditions, *(ii)* desorption, lateral transport, re-adsorption and further reaction of volatile reaction intermediates according to the „desorption–re-adsorption–reaction“ concept, and *(iii)* a molecular scale description of the ongoing surface processes and the adlayer resulting under reaction conditions.

Acknowledgement

This work was supported by the Landesstiftung Baden-Württemberg via the Kompetenznetz Funktionelle Nanostrukturen (project B9), MISTRA (Contract No. 95014) and the Swedish Energy Agency (Grant No. P12554-1). We gratefully acknowledge A. Minkow (Institute of Micro- and Nanomaterials, Ulm University) for the SEM images.

7 Transport Effects in the Electro-oxidation of Methanol Studied on Nanostructured Pt/Glassy Carbon Electrodes

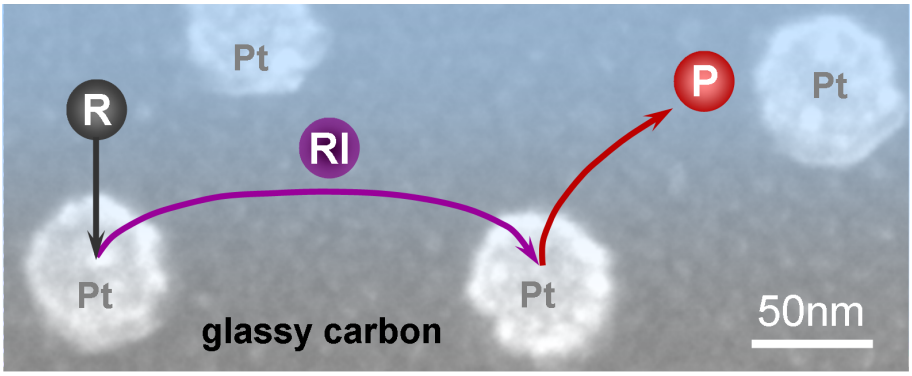

Y. E. Seidel[1], A. Schneider[1], Z. Jusys[1], B. Wickman[2], B. Kasemo[2] and R. J. Behm[1]

[1] Institute of Surface Chemistry and Catalysis, Ulm University, D-89069 Ulm, Germany
[2] Dept. of Applied Physics, Chalmers University of Technology, S-41296 Gothenborg, Sweden

Published in

Langmuir 26 (5) (**2010**) 3569–3578

Abstract

Transport effects in the methanol oxidation reaction (MOR) were investigated using nanostructured Pt/glassy carbon (GC) electrodes and, for comparison, a polycrystalline Pt electrode. The nanostructured Pt/GC electrodes, consisting of regular arrays of catalytically active cylindrical Pt nanostructures with 55 ± 10 nm in diameter and different densities supported on a planar glassy carbon (GC) substrate, were fabricated employing Hole-mask Colloidal Lithography (HCL). The MOR measurements were performed under controlled transport conditions in a thin-layer flow cell interfaced to a DEMS (differential electrochemical mass spectrometry) set-up.

The measurements reveal a distinct variation in the MOR activity and selectivity (product distribution) with Pt nanostructure density and with electrolyte flow rate, showing an increasing overall activity, reflected by a higher Faradaic reaction current, as well as a pronounced increase of the turnover frequency for CO_2 formation and of the CO_2 current efficiency with decreasing flow rate and increasing Pt coverage. These findings are discussed in terms of the „desorption–re-adsorption–reaction“ model introduced recently [Y.E. Seidel et al., *Faraday Discuss.* **140**, 167 (2008)].

Finally, consequences for applications in Direct Methanol Fuel Cells are outlined.

7.1 Introduction

Mass transport processes, including the transport of reactants to and of reaction intermediates or products away from the electrode, can play an important role in electrocatalytic reactions, in addition to the chemical and electrochemical properties of the respective catalyst or electrode material. For instance, it is well known that in many electrocatalytic reactions, the reaction rate is limited by the transport of reactants to the electrode, resulting in a „mass transport limited current“ [68–72]. Less known is that transport effects may alter also the overall behavior of the reaction, in particular its selectivity and hence the product distribution in reactions leading to more than one product. In Heterogeneous Catalysis, it is well known that in such reactions the product distribution moves towards that expected for thermodynamic equilibrium for decreasing space velocity [73], and similar trends are expected also in Electrocatalysis. Individual results fitting into that scheme can be found for a number of electrocatalytic reactions, e.g. oxygen reduction [259], or oxidation of methanol [5, 23, 25, 89], ethanol [156] or ethylene glycol [139], but more systematic studies of these aspects were missing.

A few years ago, we reported that for methanol oxidation on carbon-supported Pt catalyst electrodes the relative CO_2 yield increases systematically with increasing catalyst loading, and attributed that to increasing re-adsorption and subsequent further oxidation of the reactive intermediates formaldehyde and formic acid [25]. Comparable results were reported also in a number of other studies, involving, e.g., IR spectroscopy [29, 263] or UV-VIS spectroscopy [23, 93]. Following these results, we started a systematic study on mass transport effects in electrocatalytic reactions, using nanostructured Pt/GC electrodes and reactions under well-defined transport conditions [97–99]. These nanostructured electrodes, which are fabricated by Colloidal Lithography techniques [60–64], consist of regular arrays of electrochemically active Pt nanostructures, which are homogeneously distributed on a smooth inert glassy carbon electrode. The size and density of the nanostructures are well controlled and can be varied independently over a wide range [65]. Due to their well-defined and homogeneous geometry, these samples not only allow studies under well controlled reaction and transport conditions, but also represent ideal templates for the theoretical description, e.g., for combined modeling of reaction kinetics and transport aspects. Using these nanostructured electrodes, we studied a number of reactions which are either strongly mass transport limited, such as O_2 reduction [98, 99] or CO bulk oxidation [97, 264], or which result in two different products (O_2 reduction or formaldehyde oxidation) [97–99]. Based on these studies, recently the „desorption–re-adsorption–reaction“ model was introduced (see *chapter* 6) [98].

In addition to the direct formation of the reaction products, this includes indirect pathways, involving desorption of reactive intermediates, which can subsequently either adsorb again or leave the diffusion layer and be transported away with the flowing electrolyte. Upon re-adsorption on an electrocatalytically active material, the reaction intermediates may either react further or desorb again, which would start a new sequence. Re-adsorption on inert substrate material, in contrast, would result in immediate desorption. Hence, in that mechanism transport effects play a decisive role.

In this *chapter*, these model catalysts were used for a systematic investigation of transport effects in the electrocatalytic oxidation of methanol (methanol oxidation reaction – MOR). Both from fundamental aspects and due to its potential application in Direct Methanol Fuel Cells (DMFCs), this reaction has been studied extensively; excellent reviews are given, e.g., in refs. [15–20]. A better understanding of the methanol oxidation mechanism, including the transport effects investigated in this study, is therefore of considerable value not only from fundamental reasons, but also for further improvements in the DMFC technology.

The main previous results relevant for the present study can be summarized as follows: It is well known that the MOR results in three different products, the complete oxidation product CO_2 and the incomplete oxidation products HCHO and HCOOH (see, e.g., refs. [20–24] and references therein), and that the reaction proceeds via a complex reaction network involving a number of adsorbed or desorbable reaction intermediates, as described first by Bagotzky et al. [2]. It was shown for Pt and Pt catalyst electrodes, that the MOR product yields depend strongly on experimental conditions such as the concentration of methanol [5, 23, 89], Pt surface area / roughness [86, 89, 95], the electrolyte flow rate [5], the catalyst loading [25], the reaction temperature [29, 30], electrode potential [5, 30, 93, 263], structural effects (e.g., for single crystal electrode surfaces [5, 84], and nanoparticle size effects [265]). Furthermore, the composition of the catalyst is of importance as well [85, 87, 89–93].

In this *chapter*, results of combined electrochemical and mass spectrometric measurements (differential electrochemical mass spectrometry – 2.3.2 DEMS), following simultaneously the total reaction current (Faradaic current) and the CO_2 formation rate in potentiodynamic and potentiostatic measurements on electrodes with various Pt coverages are reported. The measurements were performed under well-defined transport conditions in a dual thin-layer flow cell (section 2.3.3). The resulting CO_2 current efficiency was evaluated. The MOR was investigated on a set of nanostructured Pt/GC electrodes with arrays of nanostructures of $\sim 55\,\mathrm{nm}$ in diameter and densities of ~ 20 and ~ 70 nanostructures per $\mu\mathrm{m}^2$. For comparison with the

nanostructured Pt/GC electrodes and with previous studies, identical experiments were performed also on a polycrystalline Pt electrode. First results on the structural characterization (size and density of the Pt nanostructures, Pt coverage) and electrochemical characterization (active surface area) of the different electrodes by hydrogen underpotential deposition (H_{upd}) are presented. Next, we evaluate the influence of varying the Pt coverage and the electrolyte flow rate on the MOR reaction characteristics in potentiodynamic and potentiostatic (at 0.66 and 0.76 V) measurements, and discuss the resulting effects on the activity, CO_2 current efficiency and turnover frequency (TOF) for methanol oxidation to CO_2 (see section 2.4.2). Finally, we will compare the present results with earlier findings on massive Pt electrodes or Pt/C catalyst film electrodes and briefly discuss the consequences for the MOR in Direct Methanol Fuel Cells.

7.2 Results and Discussion

7.2.1 Characterization of the Nanostructured Electrodes

Physical Characterization

Representative SEM images of the nanostructured electrodes with different Pt coverages are presented in Fig. 7.1. The large-scale images (Fig. 7.1a, c) demonstrate the homogeneous distribution and narrow size distribution of the circular nanodisks (bright circular spots) which agrees well with findings in previous studies using HCL-fabricated samples [64, 97, 98]. Two-dimensional Fourier transforms yield distinct rings, reflecting the short-range order in the layer of nanodisks [181]. The SEM images were used to determine the mean particle size and densities, as well as the Pt coverage. These structural characteristics are listed in Table 7.1. This way, we obtained Pt coverages of $\sim 17\,\%$ and $\sim 4\,\%$ (HCL-17 and HCL-04). The high-resolution images (Fig. 7.1b, d) clearly demonstrate the absence of Pt nanoparticles between the Pt nanodisks, which were recently observed for nanostructured Pt/GC electrodes prepared by Colloidal Lithography [181]. The images support the assumption of vertical, flat Pt nanodisks of cylindrical shape, which was used for the calculation of the geometric Pt surface area (values compare Table 7.1).

Electrochemical Characterization

The base cyclic voltammograms recorded on the corresponding sample types are shown in Fig. 7.2. For all samples, the CVs exhibit the H_{upd} features characteristic for polycrystalline Pt [170, 172], indicating that also on the nanostructured Pt/GC electrodes the Pt nanodisks are large enough to assume the electrochemical behavior

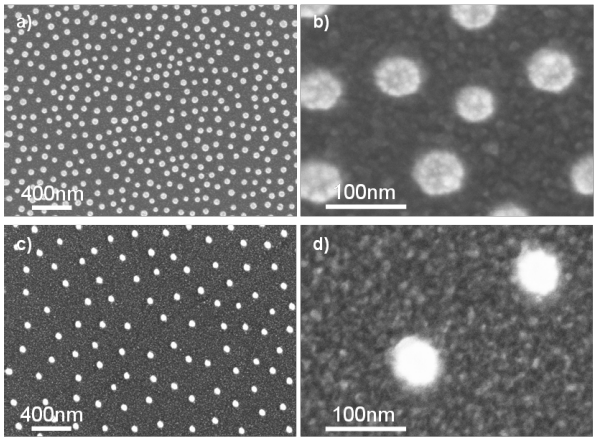

Figure 7.1: Large-scale (a, c) and high-resolution (b, d) SEM images of the nanostructured Pt/GC model electrodes fabricated by Hole-mask Colloidal Lithography. High-density nanostructured Pt/GC electrode HCL-17 (a, b) and low-density nanostructured Pt/GC electrode HCL-04 (c, d). Large-scale images 2.9 μm × 2.1 μm; high-resolution images 360 nm × 260 nm.

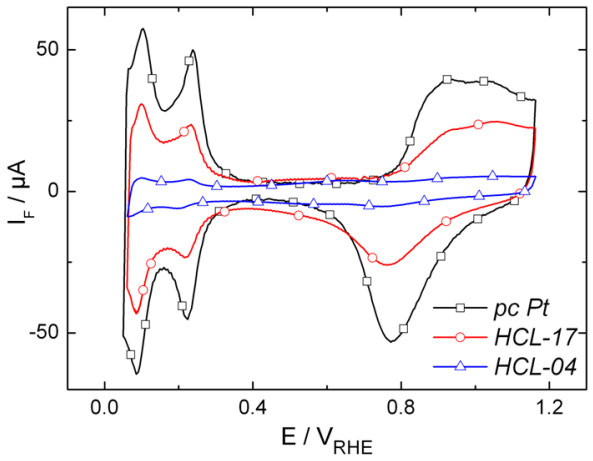

Figure 7.2: Stationary BCVs (scan rate 100 mV s^{-1}) recorded on polycrystalline Pt and on the two different nanostructured electrodes: pc Pt (100 % Pt coverage, black squares), HCL-17 ($\sim$ 17 % Pt coverage, red circles) and HCL-04 ($\sim$ 4 % Pt coverage, blue triangles).

of polycrystalline Pt (see Fig. 7.2 and assignments therein).

The active surface area of the polycrystalline Pt bulk electrode and the nanostructured Pt/GC electrodes was calculated from the H_{upd} charge in the cathodic scan, assuming a H_{upd} monolayer charge on polycrystalline Pt of 210 μC cm^{-2} [2] and a hydrogen coverage at the onset of bulk evolution of 0.77 monolayers (ML) [152]. The resulting values for the active surface areas of the different samples are given in Table 7.1. The last column of Table 7.1 shows the formal Pt roughness factor, obtained as the ratio of the active Pt surface and the geometric Pt surface area, which is usually around 2 for this kind of samples [97, 99, 181].

Table 7.1: SEM and electrochemical characterization of the pc Pt electrode and the nanostructured Pt/GC electrodes prepared by Hole-mask Colloidal Lithography (geometric surface area calculated assuming cylindrical shape for the Pt nanostructures).

sample	**coverage** / %	**particle diameter** / nm	**particle density** / μm^{-2}	**geom. Pt surf. area** / cm^2	**act. Pt surf. area** / cm^2	**Pt roughness factor**
pc Pt	100	- -	- -	0.283	0.501	1.8
HCL-17	17.3 ± 0.3	55 ± 9	72	0.118	0.272	2.3
HCL-04	4.0 ± 0.1	52 ± 8	17	0.029	0.045	1.6

7.2.2 Electrocatalytic Measurements

The reaction characteristics of methanol oxidation and possible transport effects were investigated first in potentiodynamic CH_3OH bulk oxidation (cyclic voltammetry) measurements and then in potentiostatic potential-step measurements, stepping the potential from $E_{init} = 0.06\,V$ to $E_{fin} = 0.66\,V$ and $0.76\,V$, respectively. The latter measurements allow us to better separate potential and time effects, and to characterize the reaction under (close to) steady-state conditions. During the experiments, both the electrochemical current and the CO_2 mass spectrometric current were recorded. All measurements were performed in flowing electrolyte, using three different flow rates of 1, 10 and 30 $\mu L\,s^{-1}$.

Potentiodynamic CH_3OH bulk oxidation

Representative oxidation current traces recorded on the different samples during continuous potentiodynamic methanol oxidation are plotted in Fig. 7.3. They largely reproduce the well-known bell-shaped CV traces known for the MOR on polycrystalline Pt electrodes [5, 15, 22, 89, 266] or on carbon-supported Pt/C catalysts [20, 25, 155, 266]. In the plots, the currents are magnified by a factor of 2 for the HCL-17 and by a factor of 10 for the HCL-04 sample. Independent of the electrolyte flow rate, we observed the following characteristics: The typical H_{upd} features ($E < 0.4\,V$) of Pt are suppressed in the positive-going scan in the Faradaic current trace. Hydrogen adsorption and methanol oxidation are inhibited by CO_{ad}, blocking the electrochemically active Pt surface at potentials lower than 0.4 V. Going to

higher potentials, the current starts to rise at about 0.5 V, leading to a distinct peak with its maximum located at 0.79 V on the polycrystalline Pt sample (Fig. 7.3, column a) and at around 0.78 V on the nanostructured Pt/GC samples (Fig. 7.3, column b and c). Following the current decline in that peak, the current starts to increase again at potentials positive of 1.08 V, up to the positive potential limit of 1.16 V. The currents in the peaks differ significantly for the different Pt coverages, with the highest maximum current for *pc Pt* and lower peak currents on the nanostructured Pt/GC electrodes: As expected for a kinetically limited reaction, the peak currents decrease with decreasing Pt coverage. The negative-going scan exhibits characteristics very similar to those of the positive-going scan, but the main peak is shifted to slightly lower potentials (for discussion see [20]). Its maximum is now located at 0.72 V on the *pc Pt* sample and at slightly lower potentials (0.70 V) on the nanostructured Pt/GC electrodes. The variation in the ratio of peak currents with Pt coverage, with higher peak current in the positive-going scan compared to that in the negative-going scan agrees with that reported in earlier studies. For polycrystalline Pt [5] or on Pt(553) [84], the peak height in the positive-going scan was found to be lower than in the negative going scan ($I_{positive-going\ scan} < I_{negative-going\ scan}$). (Note: We are referring to stationary CVs in these data.) About equal peak heights ($I_{positive-going\ scan} \approx I_{negative-going\ scan}$), similar to observations on the nanostructured electrodes were reported for Pt nanoparticles supported on SBA-15 [267], or on carbon (Vulcan XC72, for low Pt loadings) [25] or on a porous Pt electrode, in 1 M $HClO_4$ solution [22]. We attribute these differences to mass transport effects, which in turn influence the composition and coverage of the adlayer.

This tentative interpretation is supported also by the observation of distinct electrolyte flow rate effects. For both scan directions and for all samples investigated, the variation of the flow rate influenced the current peaks in the way that the peak current increased with decreasing flow rate. Similar effects of the mass transfer on the MOR rate were reported in RDE [268] or DEMS measurements [5] for methanol oxidation on smooth polycrystalline Pt electrode. In contrast, on a Pt/C catalyst electrode, enforced convection was reported to have no influence on the methanol oxidation rate [268] and comparable results were obtained also by Chojak et al. [30].

The Faradaic current densities, obtained by dividing the Faradaic currents (1^{st} row of panels in Fig. 7.3) by the corresponding active Pt surface area (Table 7.1), are plotted in the 2^{nd} row of panels in Fig. 7.3. The current densities for the high loaded samples *pc Pt* and *HCL-17* are almost identical for the same flow conditions, and also on the *HCL-04* sample the deviations are small. In total, this illustrates that kinetic limitations are dominant in the MOR under present reaction conditions. However, transport effects are still responsible for the subtle differences between the

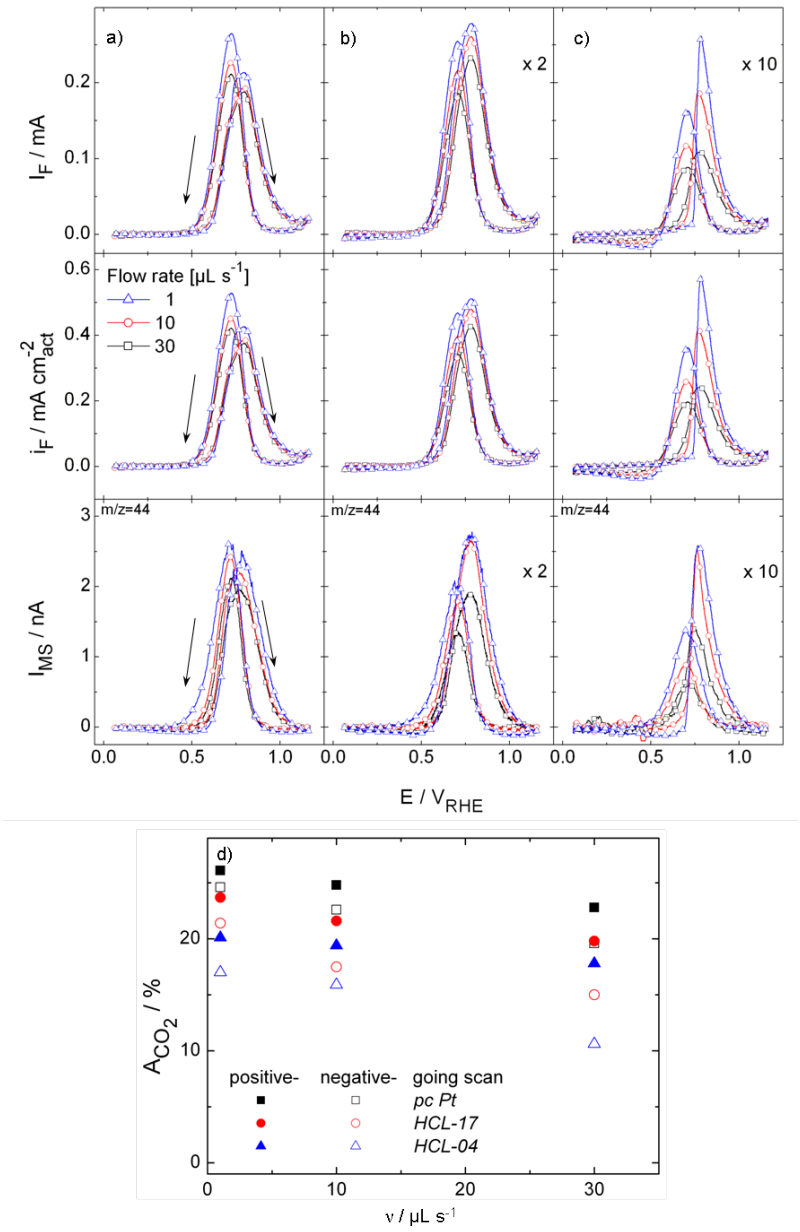

Figure 7.3: Potentiodynamic CH_3OH bulk oxidation (scan speed $100\,mV\,s^{-1}$) in 0.1 M CH_3OH containing 0.5 M H_2SO_4 at different flow rates ($1\,\mu L\,s^{-1}$ – blue, triangles; $10\,\mu L\,s^{-1}$ – red, circles; $30\,\mu L\,s^{-1}$ – black, squares) on a pc Pt electrode (column a) and on HCL-prepared nanostructured Pt/GC electrodes (HCL-17 column b, HCL-04 column c). 1^{st} row of panels: Faradaic currents; 2^{nd} row of panels: Faradaic currents (as presented in 1^{st} row) normalized to the respective active surface area (see Table 7.1) of the corresponding electrode, 3^{rd} row of panels: mass spectrometric currents at m/z = 44. (d) CO_2 current efficiencies calculated from the integrated Faradaic and mass spectrometric charges of the oxidation peaks (data from Figs. 7.3a–c) as a function of the electrolyte flow rate υ for the positive-going (filled symbols) and negative-going (blank symbols) potential scan.

three flow rates.

Both for the pc Pt electrode and the nanostructured Pt/GC electrodes, the signal shapes in the mass spectrometric CVs (MSCVs) at $m/z = 44$ (Fig. 7.3, 3^{rd} row of panels) deviate only slightly from the Faradaic current CVs, independent of the flow rate. After passing through the maximum, the signal decays continuously, to essentially zero, until reaching the reverse potential. This contrasts the behavior of the Faradaic CVs, where the current increased slightly at potentials higher than $\sim 1.08\,\mathrm{V}$ (see above). Hence, the increase in Faradaic current in the high potential range must be entirely due to formation of the incomplete oxidation products HCOOH and HCHO (see also ref. [20] and references therein). The $m/z = 60$ signal of methylformate, which results from reaction of formic acid with methanol and thus can be used to identify HCOOH formation [5, 20, 22, 25, 89, 155], was featureless for the nanostructured Pt/GC electrodes, indicating that the amounts of methylformate were below the detection limit.

The CO_2 formation rate decreases significantly from the *pc Pt* sample with 100% Pt coverage to the nanostructured *HCL-04* sample with $\sim 4\%$ Pt coverage, as it was already reported for carbon-supported Pt/C catalysts with decreasing loading [25]. Independent of the Pt coverage, we find an increasing CO_2 formation rate with decreasing flow rate. These trends, which were observed over a rather wide range of flow rates (1–30 $\mu\mathrm{L\,s^{-1}}$), resemble the findings by Wang et al. on *pc Pt* over a somewhat smaller range of flow rates (1–10 $\mu\mathrm{L\,s^{-1}}$) [5].

From the Faradaic currents and the partial currents for CO_2 formation, which can be calculated from the mass spectrometric currents, one can derive potential dependent current efficiencies for CO_2 formation during methanol oxidation. Because of the considerable effects arising from the fact that adsorption/decomposition of methanol and therefore the formation of adsorbed species may occur at different potentials than their oxidation to CO_2, which contradicts the assumption of a 6 electron process for CO_2 formation at the potential where CO_2 formation occurs, we will not focus on the potential dependent CO_2 current efficiencies. Instead, we will rather use the charge obtained by integration over the positive-going scan or the negative-going scan, respectively.

The integrated CO_2 current efficiencies obtained for the different electrodes and the various flow rates, as calculated from the integrated Faradaic and mass spectrometric currents in the positive- and negative-going scans, respectively, are summarized in Fig. 7.3d. The resulting CO_2 current efficiencies are below 30 % in all measurements. This underlines the prevailing formation of the incomplete oxidation products formaldehyde and formic acid during methanol oxidation under present reaction conditions and for all electrodes, making this the majority reaction pathway.

Furthermore, for all samples and electrolyte flow rates, the CO_2 current efficiency calculated for the positive-going scan (filled symbols) are higher than those calculated for the negative-going scan (blank symbols) under similar reaction conditions. Hence, the trend towards incomplete oxidation product formation is more pronounced in the negative-going than in the positive-going scan.

As a general trend, the CO_2 current efficiency decreases with decreasing Pt coverage and with increasing flow rate. This observation agrees well with results of previous studies on the MOR on carbon-supported Pt/C catalysts with different Pt loadings [25] or on Pt electrodes using different electrolyte transport characteristics. These were obtained either by varying the electrolyte flow rate or the methanol concentration [5]. (The latter also influences the transport of reactant molecules to the catalytically active surface.)

Continuous potentiostatic CH_3OH oxidation at 0.66 V

Potential step transients, recording the Faradaic and the mass spectrometric current (at m / z= 44) upon stepping the potential from 0.06 V to 0.66 V and back to the initial potential after 5 min reaction, are depicted in the 1^{st} and 3^{rd} row, respectively, in Fig. 7.4.

There are two clearly different time domains in these transients: The first domain is represented by the initial spike in the Faradaic current transients, which can arise from double-layer charging as well as from rapid oxidation of pre-adsorbed CO formed by interaction with CH_3OH prior to the potential step. This spike is not observed in the m / z= 44 ion currents, which can be explained in two ways: *(i)* by the actual absence of an initial current maximum in the CO_2 formation rate, or *(ii)* by a lower time resolution of the mass spectrometry (MS) measurement due to the smear out of the CO_2 concentration on the way from the working electrode to the membrane. From previous experiments following the oxidation of pre-adsorbed methanol adsorbate on Pt/C catalyst film electrode it is clear that stepping to 0.6 V will cause an initial spike also in the CO_2 formation rate [20, 25], and therefore we attribute the complete absence of such spike in the present measurements mainly to the smear out effects described above. (Note that double layer charging will nevertheless contribute significantly to the initial spike in the Faradaic current.)

The second time domain is given by the approximately exponential current decay. This current decay during the MOR is due to the build-up of the adsorbate layer during methanol adsorption and oxidation [269–272]. The decay is less pronounced on the *HCL-04* sample than on the other samples. (Note that the plotted current transients for the nanostructured Pt/GC samples are multiplied by a factor of 2 for the *HCL-17* and by a factor of 10 for the *HCL-04* electrode.) The

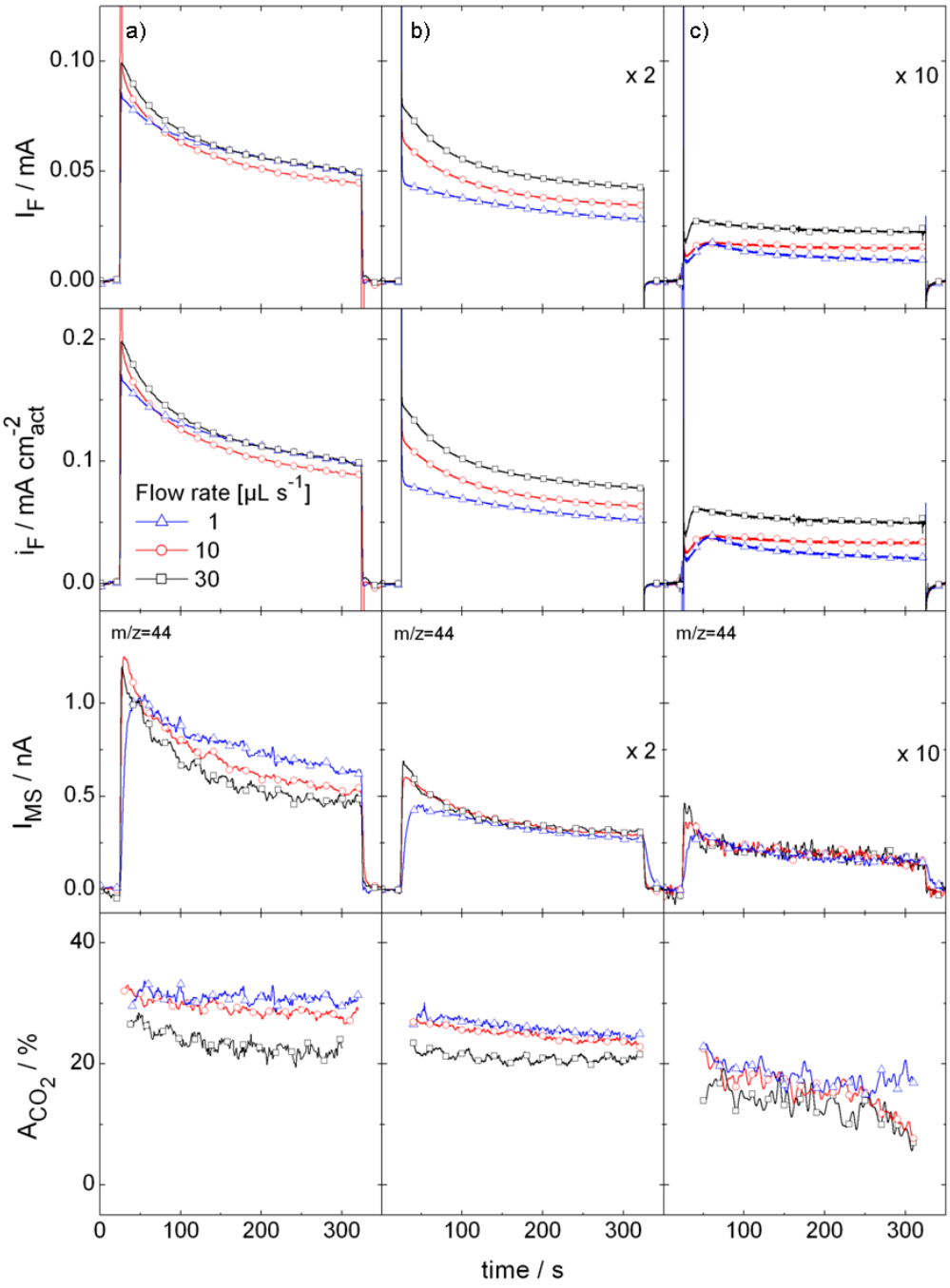

Figure 7.4: Continuous potentiostatic electro-oxidation of methanol in 0.1 M CH_3OH containing 0.5 M H_2SO_4 solution at different flow rates (1 μL s^{-1} – blue, triangles; 10 μL s^{-1} – red, circles; 30 μL s^{-1} – black, squares) on a pc Pt electrode (column a) and on HCL-prepared nanostructured Pt/GC electrodes (HCL-17 column b, HCL-04 column c). 1^{st} row of panels: Faradaic currents; 2^{nd} row of panels: Faradaic currents (as presented in 1^{st} row) normalized to the respective active surface area (see Table 7.1) of the corresponding electrode, 3^{rd} row of panels: mass spectrometric currents at m/z = 44 and 4^{th} row of panels: CO_2 current efficiencies. The potential was stepped from 0.06 V (t_{init} = 30 s) to 0.66 V (t_{fin} = 300 s).

Faradaic current transients closely follow those reported earlier for measurements in an analogous thin-layer flow-cell DEMS set-up on a *pc Pt* electrode under defined reactant transport conditions [5, 89], or in measurements on single-crystal Pt electrodes [269, 273–277], and on carbon-supported Pt/C catalysts [20, 25, 266, 268]. (The chronoamperometric measurements discussed in [266, 268] were performed in an RDE set-up, whereas in refs. [20, 25], the same dual thin-layer flow cell set-up was used. For the single-crystal measurements, standard two- [275] or three-compartment [276, 278, 279] hanging meniscus configurations were used.) Similar to the potentiodynamic current traces, the MOR current decreases with decreasing Pt coverage, in agreement with expectations for a largely kinetically rather than mass transport controlled reaction process. Similar conclusions may be drawn also from the little differences between the steady-state Faradaic currents at different flow rates on the *pc Pt* electrode. On the nanostructured electrodes, in contrast, the Faradaic currents increase with faster flow rates.

The Faradaic current densities (see above) are shown in the 2^{nd} row of panels in Fig. 7.4. Interestingly, the steady-state current densities decrease with decreasing Pt coverage, from about $0.1\,\mathrm{mA\,cm^{-2}}$ on *pc Pt* via below $0.08\,\mathrm{mA\,cm^{-2}}$ on *HCL-17* to $0.05\,\mathrm{mA\,cm^{-2}}$ on *HCL-04*. The latter two values refer to the highest flow rate; at lower flow rates the current densities are even smaller. These trends are even opposite to what would be expected for a reaction where transport of reactants is rate limiting. In that case the current density should increase with decreasing Pt coverage. This will be discussed further together with the CO_2 current efficiency.

The mass spectrometric signals of CO_2 formation are depicted in the 3^{rd} row of panels in Fig. 7.4. They largely reproduce the shape of the Faradaic current transients, except for the initial current spike (see above). The CO_2 formation rate decreases strongly with decreasing Pt coverage, analogous to the Faradaic current. The effect of the electrolyte flow rate depends on the Pt coverage. There is almost no effect on the nanostructured Pt/GC samples, although there are clear differences in the Faradaic currents and current densities on these electrodes. On the *pc-Pt* sample, the CO_2 formation rate increases with decreasing electrolyte flow, while the Faradaic currents are almost identical. Also this will be discussed further together with the CO_2 current efficiency.

The current efficiencies for CO_2 formation are displayed in the bottom row of panels in Fig. 7.4. For the nanostructured Pt/GC electrodes, especially for the low loading *HCL-04* sample, the quantitative evaluation of the current efficiency for CO_2 formation suffers from the very low MS signal and the resulting poor signal-to-noise ratio. The general trends of the CO_2 current efficiencies upon varying the Pt coverage or the electrolyte flow rate, however, are clearly resolved and follow those

obtained and discussed for the potentiodynamic MOR: The CO_2 current efficiency increases with increasing Pt coverage and decreasing electrolyte flow rate. For the present reaction and transport conditions, HCHO and HCOOH formation contribute by about 70 % on *pc Pt* to the Faradaic MOR current (1, 10 μL s^{-1}), slightly more for the *HCL-17* and significantly more ($>$ 80 %) for the *HCL-04* sample. Hence, the decreasing Pt coverage causes significant variations not only in the MOR activity, but also in the selectivity.

CONTINUOUS POTENTIOSTATIC CH_3OH OXIDATION AT 0.76 V

Analogous potentiostatic methanol oxidation experiments were performed on these electrodes upon stepping the potential from 0.06 V to a more anodic potential of 0.76 V for 5 min and then back to 0.06 V, where according to the potentiodynamic data in Fig. 7.3 the kinetic limitations should be less pronounced. Faradaic (top row of panels) currents and current densities as well as well as mass spectrometric currents (at m / z = 44) and CO_2 current efficiencies are presented in Fig. 7.5, analogous to the presentation in Fig. 7.4. Note that in the transients for the nanostructured Pt/GC samples the currents are multiplied by a factor of 5 for the *HCL-17* and by a factor of 20 for the *HCL-04* electrode.

The Faradaic current transients qualitatively resemble those obtained at 0.66 V in their characteristics. The absolute currents, however, are much higher than at 0.66 V. Furthermore, the decay with time is much more pronounced than at 0.66 V, in particular during the first 100 s of reaction. This is attributed to an increasing coverage of OH_{ad}/oxide species. Next, as already observed and discussed above, the Faradaic current decreases with Pt coverage, in the order *pc Pt* > *HCL-17* > *HCL-04*. There is, however, a subtle but nevertheless important difference. Opposite to the behavior at 0.66 V (see Fig. 7.4), for all samples the Faradaic current decreases with increasing flow rate (1^{st} row of panels in Fig. 7.5). A similar observation was reported for methanol oxidation on a *pc Pt* electrode under enforced mass transport in a RDE configuration [268]. The authors of that study tentatively explained the decrease in methanol oxidation current by an increasingly efficient removal of the incomplete oxidation products HCHO and HCOOH from the electrode, which in that case can not be oxidized further.

The Faradaic current densities also increase with increasing Pt coverage, similar to the trend at 0.66 V, but in this case the difference between the two nanostructured samples can hardly be resolved. As described for the Faradaic current, the effects caused by the electrolyte flow rate are opposite to those at 0.66 V on the nanostructured samples.

This tentative explanation can be checked and verified in the mass spectrometric

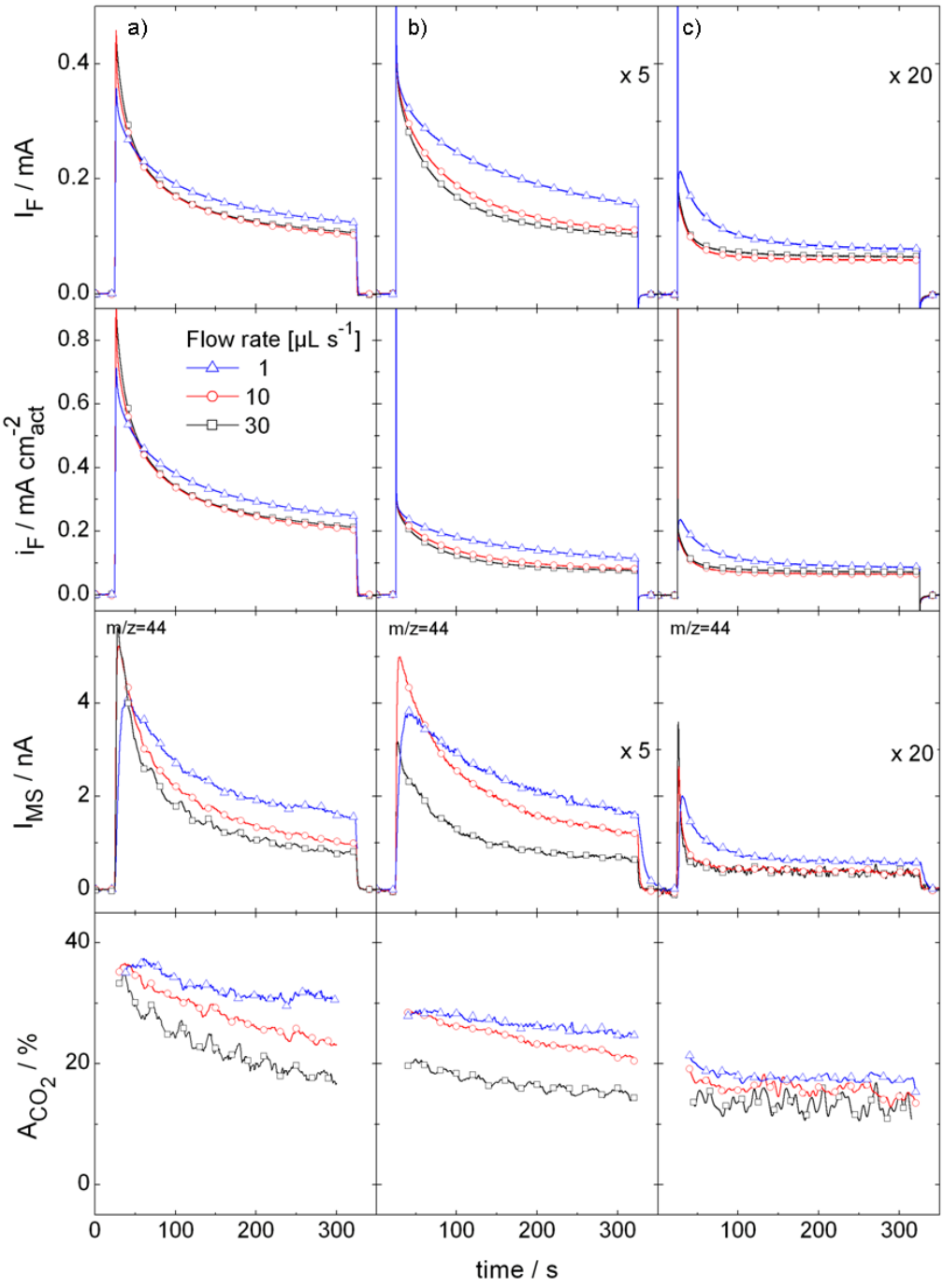

Figure 7.5: Continuous potentiostatic electro-oxidation of methanol in 0.1 M CH_3OH containing 0.5 M H_2SO_4 solution at different flow rates (1 μL s^{-1} – blue, triangles; 10 μL s^{-1} – red, circles; 30 μL s^{-1} – black, squares) on a pc Pt electrode (column a) and on HCL-prepared nanostructured Pt/GC electrodes (HCL-17 column b, HCL-04 column c). 1^{st} row of panels: Faradaic currents; 2^{nd} row of panels: Faradaic currents (as presented in 1^{st} row) normalized to the respective active surface area (see 7.1) of the corresponding electrode, 3^{rd} row of panels: mass spectrometric currents at m/z = 44 and 4^{th} row of panels: CO_2 current efficiencies. The potential was stepped from 0.06 V (t_{init} = 30 s) to 0.76 V (t_{fin} = 300 s).

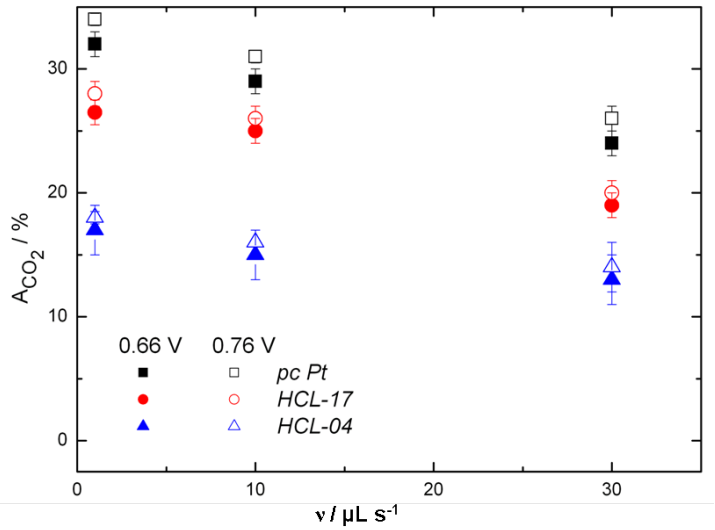

Figure 7.6: CO_2 current efficiencies after 180 s of continuous potentiostatic CH_3OH electro-oxidation at two different potentials (0.66 V – filled symbols and 0.76 V – blank symbols) on a pc Pt electrode (black squares) and on HCL-prepared nanostructured Pt/GC electrodes (HCL-17 red circles, HCL-04 blue triangles) as a function of the flow rate υ. The data are taken from Figs. 7.4 and 7.5.

measurements at m / z= 44 (Fig. 7.5, 3^{rd} row of panels). First of all, similar to the Faradaic currents the CO_2 signals are significantly higher for methanol oxidation at 0.76 V than at 0.66 V. Furthermore, the CO_2 formation rates directly follow the behavior of the Faradaic currents; with decreasing CO_2 formation for lower Pt coverage (*pc Pt* > *HCL-17* > *HCL-04*) and decreasing electrolyte flow. Similar to the Faradaic currents, the CO_2 formation currents decay much more rapidly during the initial 100 s after the potential step than during the reaction at 0.66 V.

The CO_2 current efficiencies show the same trends as already described for potentiodynamic measurements and for the potentiostatic measurements at 0.66 V. At least for the higher Pt coverages (*pc Pt* and *HCL-17*), the CO_2 current efficiency decreases with time, similar to observations at 0.66 V. Different from the lower potential reaction, however, this decrease continues even at the end of the measurement. (For the *HCL-04* electrode, a possible decay would be below the detection level given by the signal-to-noise ratio.) Furthermore, the decay increases with increasing Pt loading and decreasing electrolyte flow rate, in particular in the initial stage of the reaction.

The values for the CO_2 current efficiencies obtained in the potential step measurements (potential step to 0.66 V and 0.76 V) on the different electrodes and for the different electrolyte flow rates are summarized in Fig. 7.6. For direct comparison with previous data in ref. [5], we used the values obtained 180 s after the potential

step. These data lead to the following findings: First of all, at identical reaction conditions (on the same sample, at the same electrolyte flow rate), the CO_2 current efficiency is slightly higher at the higher reaction potential of 0.76 V than at 0.66 V. This „high potential effect“ is more pronounced on the higher coverage *pc Pt* and *HCL-17* samples than on the *HCL-04* sample. Most pronounced is the effect of the Pt coverage on the CO_2 current efficiency. At identical experimental conditions (e.g., $1\,\mu L\,s^{-1}$, 0.76 V), the CO_2 current efficiency decreases from 34 % on *pc Pt* down to almost half of that value, $\sim$18 %, on the HCL-04 electrode. The effect of the electrolyte flow rate on the CO_2 current efficiency is less pronounced, but still significant. On *pc Pt* and at 0.66 V, the CO_2 current efficiency decreases from 32 % for $1\,\mu L\,s^{-1}$ to 24 % at $30\,\mu L\,s^{-1}$. On the nanostructured electrodes, the changes are smaller, but still clearly obvious.

The higher turnover frequencies at the higher oxidation potential were already mentioned above. For a quantitative comparison, we calculated the TOF for methanol oxidation (number of methanol molecules converted per Pt surface site and per second) to CO_2. The resulting TOF values for potentiostatic oxidation at 0.66 V and 0.76 V measured 180 s after the potential-step are shown in Fig. 7.7 as a function of the active Pt surface area, and for different flow rates and potentials. For reaction at 0.66 V (methanol oxidation region; filled symbols), the TOF values are below 0.05 molecules $site^{-1}s^{-1}$ for the *pc Pt* sample and even below 0.025 molecules $site^{-1}s^{-1}$ for the nanostructured Pt/GC samples. They are significantly higher for the higher potential of 0.76 V, which corresponds approximately to the potential of the peak maximum in the potentiodynamic measurements. At 0.76 V, they range from 0.15 on *pc Pt* to 0.02 molecules $site^{-1}s^{-1}$ on *HCL-04* at $1\,\mu L\,s^{-1}$. (Note that the faster turnover rate at high potential is at least partly due to lower steady-state coverage of poisoning CO_{ad}, which is efficiently oxidized by OH_{ad}, and faster OH_{ad} formation [16, 20].) For the highest Pt coverage of 100 % (*pc Pt*), the TOF values are twice as high as at 0.66 V for 10 and $30\,\mu L\,s^{-1}$, and even three times higher for the lowest flow rate of $1\,\mu L\,s^{-1}$ ($\sim$0.15 molecules $site^{-1}s^{-1}$). The latter value agrees well with the data reported by Jusys et al. [25] for a carbon-supported Pt/C catalysts at low catalyst loadings (7–14 μg per cm^2). In that study, the measurements were performed at a somewhat higher flow rate ($5\,\mu L\,s^{-1}$). On the other hand, the number of Pt surface atoms on the low loaded Pt/C catalyst films used in that study is about 2 times higher than on the present *pc Pt* electrode [25].

Hence, the resulting space velocities, which are often decisive for the reaction behavior [73], are comparable in both cases. Similar to the previous observations [25], we also find a definite correlation between the TOF values for CO_2 formation and the

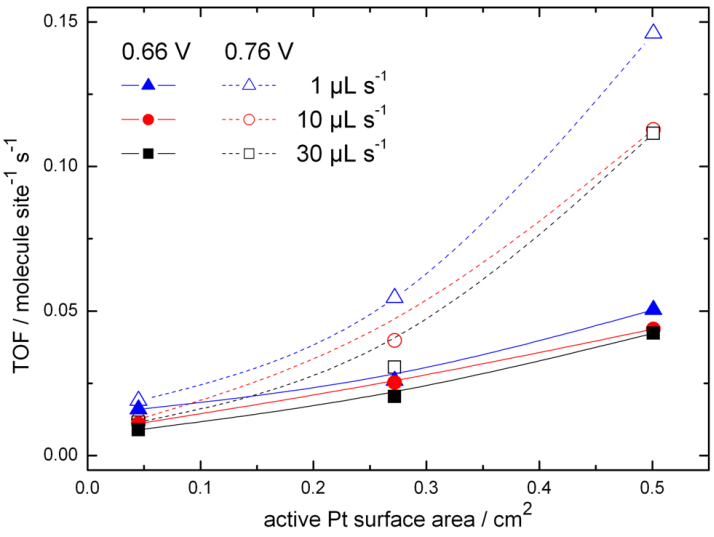

Figure 7.7: Turnover frequencies (TOF) for methanol molecule oxidation to CO_2 after 180 s of continuous potentiostatic CH_3OH electro-oxidation on a pc Pt electrode and on HCL-prepared nanostructured Pt/GC electrodes (HCL-17, HCL-04) at two different potentials (0.66 V – filled symbols and 0.76 V – blank symbols) and at various electrolyte flow rates ($1\,\mu L\,s^{-1}$ – blue, triangles; $10\,\mu L\,s^{-1}$ – red, circles; $30\,\mu L\,s^{-1}$ – black, squares) as a function of the active Pt surface area. The data are taken from Figs. 7.4 and 7.5, for reaction potential and electrolyte flow rate see figure.

Pt coverage, with the turnover frequency increasing from 0.025 molecules site^{-1}s^{-1} on the low Pt coverage electrode (*HCL-04*) to 0.15 molecules site^{-1}s^{-1} on *pc Pt*. Furthermore, for all samples the turnover frequency for CO_2 formation increases with decreasing electrolyte flow rate.

It is interesting to note that increasing the Pt coverage and hence the active surface area has a significant effect on the TOFs for CO_2 formation, which increase by factors of ~ 3 (at 0.66 V and an electrolyte flow rate of $1\,\mu L\,s^{-1}$) or ~ 10 (at 0.76 V and an electrolyte flow rate of $30\,\mu L\,s^{-1}$) (Fig. 7.7), is correlated with a somewhat lower, but nevertheless clearly visible increase in the CO_2 current efficiency, by a factor of ~ 1.9 (for 0.66 V and 0.76 V) (Fig. 7.6). The lower increase in CO_2 current efficiency compared to the increase in TOF for CO_2 formation results from the increase in Faradaic current density occurring at the same time.

First, an increase in Pt surface area normalized CO_2 formation rate (or in the total Faradaic current density) with increasing active Pt surface area (Pt coverage) seems to be in contrast with expectations based on the assumption of a kinetically limited reaction. We tentatively explain these trends by a change in surface coverage of reaction inhibiting adsorbates (CO_{ad}) with higher Pt surface area: With decreasing coverage of the Pt nanodisks (and thus with decreasing active Pt surface area),

the transport of methanol to the individual Pt nanodisks increases, due to the transition from planar to hemispherical diffusion. This in turn will increase the steady-state coverage of reaction inhibiting adsorbates at lower Pt surface areas, and thus lower the methanol oxidation rate. Second, a more pronounced increase of the TOF for CO_2 formation compared to that of the CO_2 current efficiency reflects a decreasing tendency for incomplete oxidation product formation, as expected from the „desorption–re-adsorption–reaction“ model (see below), in combination with a sizable increase in Faradaic current density and hence in the total reaction rate.

The differences in the MOR behavior between the nanostructured Pt/GC electrodes (*HCL-17* and *HCL-04* samples) and the *pc Pt* electrode, and the effects induced by varying the electrolyte flow agree very well with expectations based on the „desorption–re-adsorption–reaction“ model introduced recently [98]. In that model, indirect pathways, involving desorption of reactive intermediates, which can subsequently either adsorb again or leave the diffusion layer and be transported away with the flowing electrolyte, are included in addition to the direct formation of the reaction products. Upon re-adsorption on an electrocatalytically active material, the reaction intermediates may either react further or desorb again, which would start a new sequence. Re-adsorption on inert substrate material, in contrast, would result in immediate desorption.

Under slow-flow conditions, the chances for re-adsorption of HCHO and HCOOH and hence for further reaction CO_2 are higher than for faster flow conditions, since the chance of desorbing HCHO and HCOOH molecules (reactive incomplete oxidation products) to reach the Pt surface again for a further adsorption and reaction attempt increases the longer they remain in the diffusion layer. This again depends on the thickness of the diffusion layer, and hence on the electrolyte flow rate (decreasing thickness of the diffusion layer with higher flow rate [75]). A higher chance for re-adsorption and further reaction is expected also for the *pc Pt* sample, when comparing with the nanostructured samples. On *pc Pt*, re-adsorption will always occur on an active Pt surface, while on the nanostructured samples re-adsorption occurs with increasing probability on the inert GC substrate, which will not lead to further oxidation. This means, that it is more likely for incomplete oxidation products such as formic acid or formaldehyde to leave the diffusion layer without undergoing further reaction to the final (stable) product CO_2.

The above results closely follow a more general principle, which is known from Heterogeneous Catalysis [73] and which predicts that the product distribution in a catalytic reaction shifts towards its thermodynamic equilibrium with decreasing space velocity, i.e., with decreasing reactant flow or increasing amount of catalyst. This principle is likely to be valid also in Electrocatalysis. The results of the present

study on the structurally well-defined nanostructured electrodes, which were performed under well-defined mass transport and flow conditions, support this statement. In this case, the amount of catalyst is defined by the number of active Pt sites. Comparable results were reported recently also in studies of other electrocatalytic reactions allowing for different reaction pathways and reaction products, the reduction of oxygen [98, 99] (incomplete reduction product: H_2O_2, fully reduced product: H_2O) and the oxidation of formaldehyde [97] (incomplete oxidation product: HCOOH, complete oxidation product: CO_2), which were performed on similar type nanostructured Pt/GC electrodes (Pt nanostructures of about 100 nm in diameter). In all cases, the yield of the completely reacted product increases with increasing Pt coverage and with decreasing electrolyte flow.

Similar trends were recently reported by Jusys et al. [25], when studying the influence of the catalyst loading on the product distribution during methanol oxidation on Pt/C fuel cell catalysts, and in a DEMS study by Wang et al. [5] on the effect of the CH_3OH concentration and of the electrolyte flow rate on the MOR characteristics on pc Pt electrodes. In the first study [25], these authors revealed a pronounced influence of the Pt/C catalyst loading on the CO_2 current efficiency from a quantitative determination of the contributions from the different reaction pathways and products (formaldehyde, formic acid, CO_2) for different Pt/C catalyst loadings, with the CO_2 current efficiency increasing with higher catalyst loading. In the second DEMS study by Wang et al. [5], which was performed in a similar thin-layer flow cell and DEMS set-up as used here, these authors obtained lower values for the CO_2 current efficiency than obtained in the present study on *pc Pt*. The trend of a slight decrease with increasing electrolyte flow rate, however, agrees fully with our present findings, and also the lower absolute values can be fully explained by the slightly lower electrode potential in their study (see Table 7.2).

The trends agree also in the potential dependence, with an increase in the CO_2 current efficiency at higher applied constant potentials. Comparable mass transport effects were reported also in previous studies on O_2 reduction [259], ethanol oxidation [156] or ethylene glycol oxidation [139] on Pt particles or Pt/C catalyst electrodes under controlled electrolyte flow conditions, giving further credibility for the „desorption–re-adsorption–reaction“ model.

In total, the trends mapped out quantitatively in this study on nanostructured Pt/GC electrodes and indicated also in a number of previous studies using smooth Pt electrodes or Pt/C catalyst film electrodes [5, 25, 89, 266], make clear that the MOR, although commonly considered as kinetically controlled reaction, is in fact influenced also by transport effects, and that these transport effects play a considerable role, in particular for the product distribution, but also for the overall activity.

Table 7.2: CO_2 current efficiencies on polycrystalline Pt bulk electrodes (geom. surface area 0.283 cm^2) after one minute after the potential was stepped from E_{init} to E_{fin}. c concentration of CH_3OH in 0.5 M H_2SO_4; v electrolyte flow rate.

$\mathbf{E}_{init}$ / V	$\mathbf{E}_{fin}$ / V	$\boldsymbol{c}$ / mol L^{-1}	v / μL s^{-1}	$\mathbf{A}_{CO_2}$ / %
0.05	0.65	0.001	10	55*
0.05	0.75	0.01	1.1	49*
0.05	0.60	0.1	1.9	18*
0.05	0.60	0.1	8.3	16*
0.06	0.66	0.1	1	32
0.06	0.66	0.1	10	30
0.06	0.76	0.1	1	35
0.06	0.76	0.1	10	32

* These values are taken from H. Wang et al., *J. Appl. Electrochem.* **31**, 759 (2001).

The latter effects are mainly induced by the variations in the coverage and composition of the adlayer under steady-state conditions, which will result in more or less pronounced blocking of the active surface. Considering also the similar mass transport effects obtained for other electrocatalytic reaction, both on nanostructured Pt/GC electrodes [97–99] and on Pt nanoparticles or Pt/C catalyst electrodes [139, 156, 259], we propose that *(i)* the „desorption–re-adsorption–reaction“ model is of general validity for electrocatalytic reactions involving the formation of desorbable reaction intermediates and that *(ii)* the inclusion of transport effects and the use of well-defined transport conditions are essential for the mechanistic understanding of many electrocatalytic reactions even in model studies. Because of their simple and well-defined geometry, nanostructured Pt/GC electrodes represent ideal test systems for quantitative studies of mass transport effects in electrocatalytic reactions, and provide an excellent basis for modeling the underlying reaction and transport processes.

Finally we would like to mention that the transport effects in the MOR verified and discussed in the present paper are of relevance also for technical applications, for methanol oxidation in a DMFC. While in a standard fuel cell, the high amount of catalyst will lead to complete oxidation of methanol to CO_2 [26–28], in particular at elevated temperatures [29, 30], this may be different in future applications. With the further reduction of the amount of anode catalyst, one may reach a level where this is limited by increasing emission of incomplete (and toxic) oxidation

products at the exhaust of the fuel cell. This will become even more relevant in the development of micro-DMFCs for portable applications, with their low absolute amount of catalyst and low methanol consumption. Here particular care has to be taken to avoid transport induced emission of incomplete oxidation products such as formaldehyde. Similar aspects of course apply also for the Direct Ethanol Oxidation Fuel Cell (DEFC) (incomplete oxidation product: acetaldehyde) or other fuel cells based on organic molecule oxidation. Hence, the understanding and consideration of transport processes is also important for the directed further development of direct oxidation fuel cells, for optimizing the distribution of catalyst with respect to maximum activity and for avoiding emission of incomplete oxidation products under conditions of low catalyst loading.

7.3 Summary and Conclusions

The role of transport effects in the methanol oxidation characteristics and in particular their influence on the product distribution (HCHO, HCOOH, CO_2) during continuous methanol oxidation were investigated using nanostructured Pt/GC electrodes of different Pt coverage and, for comparison, a non-structured pc Pt electrode. The nanostructured Pt/GC electrodes, which were fabricated by Hole-mask Colloidal Lithography, consist of Pt nanostructures with defined diameter forming rather regular arrays with a narrow particle distribution supported on a planar, smooth glassy carbon substrate. The overall reaction kinetics and the product distribution, specifically the CO_2 formation rates, were determined by combined electrochemical and DEMS measurements, which were performed in a dual thin-layer flow cell connected to a DEMS set-up under well-defined, controlled electrolyte flow conditions and using different, widely varying electrolyte flow rates.

Bulk oxidation of methanol, performed in potentiodynamic and in potentiostatic potential-step measurements at potentials of 0.66 and 0.76 V, respectively, revealed reaction characteristics which are comparable to those of massive Pt electrodes. As expected for a kinetically controlled reaction, the Faradaic reaction current increased severely with increasing Pt coverage, whereas the current densities normalized versus active Pt surface area are of comparable order of magnitude, though not identical. On the other hand, distinct transport effects were observed as well, as evidenced by the increase of the Pt surface area normalized reactivity (overall reaction current density) with increasing Pt coverage.

Furthermore, both the CO_2 formation rate and the CO_2 product yield depend strongly on the Pt coverage and on the electrolyte flow rate and hence on the thickness of the diffusion layer above the electrode surface, with an increasing Pt coverage

and decreasing electrolyte flow rate resulting in an increasing CO_2 yield and methanol turnover to CO_2. This in turn results in an increased current efficiency for CO_2 formation.

These findings fully agree with expectations based on the „desorption–re-adsorption–reaction“ model introduced recently, according to which reactive incomplete reaction products can re-adsorb after desorption into the electrolyte and further react towards the stable final reaction products [98]. For the MOR, increasing re-adsorption and hence decreasing off-transport of the reactive intermediates HCHO and HCOOH out of the reaction cell leads to an increasing CO_2 current efficiency or decreasing contents of the incomplete oxidation products formaldehyde and formic acid, if i) the Pt coverage is increased and therefore the distance between the Pt nanostructures is decreased or if ii) the thickness of the diffusion layer is increased by slower electrolyte flow and therefore the residence time of partially oxidized dissolved molecules in the near surface region is extended.

Because of the good agreement of our data also with results of previous studies on electrocatalytic reactions, which were performed both on nanostructured Pt/GC electrodes as well as on smooth Pt or Pt/C catalyst film electrodes, we propose that *(i)* the „desorption–re-adsorption–reaction“ model is of general validity for electrocatalytic reactions involving the formation of desorbable reaction intermediates and that *(ii)* the inclusion of transport effects and the use of well-defined transport conditions are essential for the mechanistic understanding of many electrocatalytic reactions even in model studies. Because of their simple and well-defined geometry, nanostructured Pt/GC electrodes represent ideal test systems for quantitative studies of mass transport effects in electrocatalytic reactions, and provide an excellent basis for modeling the underlying reaction and transport processes.

Besides these fundamental aspects, the understanding and consideration of transport processes is also important for the directed further development of direct oxidation fuel cells, for optimizing the distribution of catalyst with respect to maximum activity and for avoiding emission of incomplete oxidation products under conditions of low catalyst loading.

Acknowledgement

This work was supported by the Ministry of Science, Research and the Arts Baden-Württemberg and the European Social Fund (ESF) within the Schlieben-Lange-Programm, the Landesstiftung Baden-Württemberg via the Kompetenznetz Funktionelle Nanostrukturen (project B9), MISTRA (Contract No. 95014) and the Swedish Energy Agency (Grant No. P12554-1). We gratefully acknowledge A. Minkow

(Institute of Micro- and Nanomaterials, Ulm University) for the SEM images. We also thank one of the referees for pointing out the correlations between the changes in CO_2 current efficiency and TOF upon reducing the Pt coverage.

8 Summary / Zusammenfassung

8.1 Summary

The aim of this work was to study the stability and the electrocatalytic properties of nanostructured Pt/glassy carbon surfaces, which represent simplified, well-defined and reliable two dimensional model systems of the commonly used real carbon-supported Pt/C catalysts. These model electrodes consist of well-defined arrays of electrocatalytically active Pt nanodisks/nanoparticles supported on a planar, inert glassy carbon (GC) substrate. It was demonstrated that these model systems are ideally suited for studying mass transport processes and their effect on the kinetics of electrocatalytic reactions.

First in *chapter* 3, the stability of nanostructured Pt/GC electrodes prepared by *Colloidal Lithography* (CL) was demonstrated comparing the active surface area via H_{upd} charge and SEM micrographs recorded before and after a defined experimental protocol, simulating realistic reaction conditions including continuous electrolyte flow and evolution of gaseous products. The highest stability with essentially no evidence for loss of Pt nanostructures was obtained for samples where the GC substrate was pre-treated first in oxygen and then in Ar plasma, and where sputter deposition rather than evaporation was used as Pt deposition method.

In order to clarify the discrepancy between the experimentally determined electrochemical properties of nanostructured Pt/GC electrodes with very low densities of Pt nanostructures, e.g., $\sim 1\,\%$ Pt coverage, and those expected on the basis of their structural characterization, these electrodes were investigated in more detail in *chapter* 4. Systematic electron microscopy measurements, including high-resolution SEM and TEM imaging, and locally resolved EDX analysis were correlated to the results of electrochemical measurements, including base cyclic voltammetry and CO_{ad} stripping. The results clearly demonstrated that on nanostructured Pt/GC electrodes prepared by CL, the areas between the Pt nanodisks are covered by a dilute layer of Pt nanoparticles of about 5 nm in diameter. An advanced lithographic technique, so-called *Hole-mask Colloidal Lithography* (HCL), was introduced as an alternative method for preparing similar type nanostructured Pt/GC electrodes. It was demonstrated that the electrodes prepared via this method are essentially free from the residual Pt nanoparticles.

Aiming for more realistic model systems with respect to the particle size (diameter of Pt nanostructures prepared by CL or HCL used in this work: 50–140 nm) a „micellar approach“ for the Pt/GC electrode preparation was employed in *chapter* 5. This technique involves the deposition of reverse, Pt salt filled micelles on a planar GC support and subsequent oxygen plasma/H_2 annealing treatment. It represents a

viable method for producing nanostructured Pt/GC electrodes with similarly sized particles (Pt nanoparticle diameter: 3–8 nm) and defined particle separations. The electrodes were stable during a defined experimental protocol, as revealed by H_{upd} charge determination and subsequent SEM imaging, with no detectable particle losses during these measurements. CO electro-oxidation measurements including pre-adsorbed CO_{ad} stripping and CO bulk oxidation indicate that the electrocatalytic properties of these model electrodes closely resemble those of Pt nanoparticles.

In the following chapters the focus turned to the detailed study of mass transport processes in electrocatalytic reactions, including the transport of reactants to and of reaction intermediates or products away from the electrode. Transport of reactants to the electrode not only affects the reaction rate, e.g., resulting in a „mass transport limited current“, but may also alter the overal behaviour of the reaction, in particular its selectivity and hence the product distribution in reactions leading to more than one product.

Therefore, the influence of mesoscopic transport effects on a rather „simple“ reaction, namely the oxygen reduction reaction (ORR, two possible reaction products: H_2O_2 and H_2O) was studied in *chapter* 6. The activity and selectivity (H_2O_2 formation) of the ORR was systematically investigated under controlled and varied electrolyte flow conditions on nanostructured Pt/GC electrodes (at different Pt coverages), a polycrystalline Pt (pc Pt) and a GC substrate as reference electrodes. Besides the expected increase of the mass transport limited current with increasing Pt coverage and with increasing electrolyte flow rate, the measurements revealed a clear trend to an increasing amount of the reactive intermediate H_2O_2 with *(i)* increasing separation of the Pt nanostructures and therefore active Pt sides and *(ii)* with increasing electrolyte flow rate. Based on these findings, the „desorption – re-adsorption – reaction“ concept was introduced. This reaction model explains the observations by the re-adsorption probability of reactive incomplete reaction products on neighbouring active Pt sites after desorption into the electrolyte and therefore the chance of further reaction towards the stable final reaction products. The re-adsorption probability strongly depends on *(i)* the separation of the Pt nanostructures and *(ii)* the electrolyte flow rate and hence the thickness of the stagnant diffusion layer above the electrode surface. Hence, the re-adsorption probability decreases with increasing interparticle distances or with increasing electrolyte flow rate resulting in a thinner diffusion layer.

Finally, the role of transport effects in a more „complex“ reaction network, the methanol oxidation reaction (MOR), and in particular their influence on the resulting product distribution (HCHO, HCOOH, CO_2) was systematically studied in

chapter 7. The measurements were performed on nanostructured Pt/GC electrodes with different Pt coverages and a pc Pt electrode under widely varied electrolyte flow rates. It was found that the CO_2 formation rate depends strongly on the Pt coverage and on the electrolyte flow rate, with an increasing Pt coverage and decreasing electrolyte flow rate resulting in an increasing current efficiency for CO_2 formation and methanol turnover to CO_2. These findings fully agree with expectations based on the „desorption – re-adsorption – reaction“ concept (see above). For the MOR, increasing re-adsorption and hence decreasing off-transport of the reactive intermediates HCHO and HCOOH out of the reaction cell leads to an increasing CO_2 current efficiency or decreasing contents of the incomplete oxidation products HCHO and HCOOH. This occurs if *(i)* the Pt coverage is increased and therefore the distance between the Pt nanostructures is decreased or if *(ii)* the thickness of the diffusion layer is increased by slower electrolyte flow and therefore the residence time of partially oxidized dissolved molecules in the near surface region is extended.

To conclude, the results presented in this work mediate mesoscopic transport effects induced by the electrode morphology and reaction characteristics such as activity and selectivity in electrocatalytic reactions. The application of the 2D nanostructured Pt/GC model electrodes offered the possibility to vary the transport conditions arbitrarily and to correlate the results, respectively. It is important to note that these results basically agree with results of previous studies on electrocatalytic reactions, which were performed on smooth Pt, Pt single crystales or Pt/C catalyst film electrodes, on which the correlation between electrode morphology and resulting product distribution was hardly possible.

It is therefore proposed that *(i)* the „desorption–re-adsorption–reaction“ model is of general validity for electrocatalytic reactions involving the formation of desorbable reaction intermediates and that *(ii)* the inclusion of transport effects and the use of well-defined transport conditions are essential for the mechanistic understanding of many electrocatalytic reactions even in model studies. Because of their simple and well-defined geometry, the introduced nanostructured Pt/GC electrodes represent ideal test systems for quantitative studies of mass transport effects in electrocatalytic reactions, and provide an excellent basis for further modeling the underlying reaction and transport processes.

In addition to this fundamental point of view, the understanding and consideration of transport processes is also of relevance for technical applications for, e.g., ORR or MOR in Direct Methanol Fuel Cells (DMFC). Considering the trends of further reduced amounts of catalyst, one may reach catalyst loadings where an increasing emission of incomplete reaction products due to the lack of active sites can occur.

This may have an impact on the long-term performance due to carbon support corrosion and damages of the membrane by increasing amounts of H_2O_2 (ORR), or generate toxic products such as HCHO at the exhaust of the DMFC in the MOR.

Hence, the understanding and consideration of transport processes is also important for the rational further development of (direct oxidation) fuel cells, for optimizing the distribution of catalyst at low catalyst loadings such that maximum activity is obtained, while the formation of reactive intermediates/side products, e.g., corrosive H_2O_2 (longer electrode lifetime) or toxic HCHO are kept at tolerable levels.

8.2 Zusammenfassung

Das Ziel der vorliegenden Arbeit war es, zum einen die Stabilität und zum anderen elektrokatalytische Eigenschaften, insbesondere Transportprozesse in Brennstoffzellen relevanten Reaktionen, auf nanostrukturierten Oberflächen zu untersuchen. Zu diesem Zweck wurden elektrokatalytisch aktive Pt-Nanostrukturen (Scheibchen oder Partikel) gleicher Größe, regelmäßig auf planaren, elektrochemisch inerten Glaskohlenstoffträgern (GC) angeordnet. Diese Elektroden stellen aufgrund ihrer wohl definierten Oberflächenmorphologie vereinfachte 2-dimensionale Modellsysteme, der herkömmlichen kohlenstoffgeträgerten Pt/C Realkatalysatoren dar. Im Rahmen dieser Dissertation wurde gezeigt, dass derartige nanostrukturierten Pt/GC Modellsysteme ideal geeignet sind, um durch Massentransport limitierte Prozesse, sowie deren Einfluss auf die Kinetik elektrokatalytischer Reaktionen, zu untersuchen.

In *Kapitel* 3 wurde zunächst systematisch die Stabilität von nanostrukturierten Pt/GC Modellelektroden, welche mittels *Colloidal Lithography* (*CL*, *dt.* Kolloid-Lithographie) hergestellt wurden, untersucht. Die „Stabilität“ der Proben wurde durch einen „vorher/nachher“ Vergleich der aktiven Platinoberfläche (H_{upd}) und elektronenmikroskopischer Aufnahmen, bestimmt. Die Modellelektroden durchliefen ein experimentelles Protokoll, welches reale, in einer Brennstoffzelle auftretende Reaktionsbedingungen, wie z.B. kontinuierlichen Elektrolytfluss und stetige Entwicklung von gasförmigen Reaktionsprodukten, simulierte. Maximale Stabilität, in Form von vernachlässigbar geringem Verlust an Pt-Nanoscheibchen auf der GC-Oberfläche, zeigten Proben *(i)* deren GC-Träger zunächst mit Sauerstoff- und anschließend mit Argon-Plasma behandelt wurde und *(ii)* deren Pt-Nanostrukturen durch Aufsputtern anstelle von Pt-Verdampfung hergestellt wurden.

Um die Diskrepanz zwischen den experimentell bestimmten Charakteristika nanostrukturierter Pt/GC Modellelektroden mit sehr geringem Oberflächenbedeckungsgrad durch Pt-Nanoscheibchen, z.B. nur 1 % Pt Bedeckung, und den Daten, welche aufgrund der physikalischen Charakterisierung zu erwarten waren, aufzuklären, wurden diese Proben in *Kapitel* 4 eingehend untersucht. Systematisch durchgeführte elektronenmikroskopische Untersuchungen, einschließlich hochauflösender REM- und TEM-Abbildungsverfahren, sowie lokal auflösende EDX-Analysen, wurden mit den Ergebnissen elektrochemischer Charakterisierungsmethoden wie Basiszyklovoltammetrie und *CO_{ad} stripping* (*dt.* Oxidation einer voradsorbierten CO_{ad}-Monolage) korreliert. Die Befunde bewiesen eindeutig die Präsenz feinverteilter Pt-Nanopartikel (~ 5 nm im Durchmesser), welche sich auf dem GC-Träger in den Bereichen zwischen den Pt-Inseln befanden, die durch *CL* hergestellt worden waren. Ein weiterentwick-

eltes lithographisches Verfahren, die so gennante *Hole-mask Colloidal Lithography* (*HCL*, *dt.* „Lochmasken“ Kolloid-Lithographie), wurde in diesem Zusammenhang als alternative Herstellungsmethode nanostrukturierter Pt/GC Modellelektroden vorgestellt. Die Ergebnisse der physikalischen und elektrochemischen Charakterisierung zeigten eindeutig, dass durch *HCL* hergestellte Proben keine „sekundären“ Pt-Nanopartikel aufweisen.

Um die vorliegenden Pt/GC Modellsysteme hinsichtlich ihrer Pt-Partikelgröße realistischer zu gestalten, wurde in *Kapitel* 5 ein auf Mizellen basierender Herstellungsansatz vorgestellt. Diese Methode beinhaltet die Abscheidung inverser, mit Pt-Salz gefüllten Mizellen auf einem planaren Glaskohlenstoffträger und anschließender Nachbehandlung mit Sauerstoffplasma und Tempern in einer H_2-Atmosphäre. Dieses Verfahren stellt eine geeignete Methode zur Herstellung nanostrukturierter Pt/GC Modellelektroden mit Pt-Nanopartikeln homogener Größe (3–8 nm) und definierten Partikelabständen dar. Die Stabilität der resultierenden Proben, während der Durchführung eines festgelegten experimentellen Protokolls, wurde anhand von einem „vorher/nachher“ Vergleich der H_{upd}-Ladungen und REM-Aufnahmen untersucht, mit dem Ergebnis, dass es keinerlei Anzeichen für einen signifikanten Partikelverlust gibt. Untersuchungen zur Elektrooxidation von CO, einschließlich CO_{ad} *stripping* und CO „bulk“ Oxidation zeigten, dass die elektrokatalytischen Eigenschaften dieser anhand des Mizellen-Verfahrens hergestellten Modellsysteme denen von „herkömmlichen“ Pt-Nanopartikeln entsprechen.

In den letzten Kapiteln dieser Arbeit wurden Massentransporteffekte, in Form von Antransport von Edukten zur Elektrode hin und Abtransport von Zwischen-/Endprodukten von der Elektrode weg, in elektrokatalytischen Reaktionen systematisch untersucht. Transport von Edukten an die Elektrodenoberfläche beeinflusst nicht nur die Reaktionsrate, z.B. in Form eines durch Massentransport limitierter Grenzstromes. Massentransporteffekte können auch das allgemeine Reaktionsverhalten, insbesondere die Selektivität und somit die Produktverteilung in Reaktionen mit mehr als einem Endprodukt, verändern.

Aus diesem Grund, wurde in *Kapitel* 6 der Einfluss von mesoskopischen Transporteffekten, auf die relativ „einfache“ Sauerstoffreduktionsreaktion (*engl.* Oxygen Reduction Reaction, *ORR*), bei der nur zwei Reaktionsprodukte, H_2O_2 und H_2O, auftreten, untersucht. Die Aktivität und Selektivität (Bildung von H_2O_2) der ORR wurde systematisch auf nanostrukturierten Pt/GC Modellelektroden bei verschiedenen Flussraten, sowie auf einer planaren, polykristallinen Pt-Elektrode und einem GC-Substrat als Referenzelektroden, untersucht. Die Messungen zeigten, dass neben dem zu erwartenden Anstieg des durch Massentransport limitierten Grenzstromes

mit zunehmender Pt-Bedeckung und schnellerer Elektrolytflussrate, auch eine vermehrte Bildung des reaktiven Zwischenproduktes H_2O_2 *(i)* mit zunehmender Separation der Pt-Nanostrukturen /der aktiven Plätze) und *(ii)* mit schnellerer Elektrolytflussrate, zu verzeichnen ist.

Aufgrund der präsentierten Ergebnisse wurde das „Desorption–Re-Adsorp-tion–Reaktion“ Konzept eingeführt. Dieses Reaktionsmodell ermöglicht die Erklärung der experimentellen Befunde durch die Re-Adsorptionswahrscheinlichkeit reaktiver Zwischenprodukte auf benachbarten aktiven Pt Plätzen nach der Desorption in den fließenden Elektrolyten und somit der Möglichkeit der Weiterreaktion zum stabilen Endprodukt. Die Re-Adsorptionswahrscheinlichkeit hängt insbesondere *(i)* von der Separation der Pt Nanostrukturen und *(ii)* von der Elektrolytflussrate, was gleichbedeutend mit der Dicke der stagnierenden Diffusionsschicht über der Elektrodenoberfläche ist, ab. Infolgedessen, sinkt die Re-Adsorptionswahrscheinlichkeit mit zunehmendem Abstand zwischen den Pt-Nanostrukturen (Separation) oder mit zunehmender Elektrolytflussrate, was in einer dünneren starren Diffusionsschicht resultiert.

Zuletzt wurde die Rolle von Transporteffekten in einem „komplexeren“ Reaktionsnetzwerk, der Elektrooxidation von Methanol (*engl.* Methanol Oxidation Reaction, *MOR*) in *Kapitel* 7 untersucht. Die Untersuchungen wurden auf nanostrukturierten Pt/GC Modellelektroden mit unterschiedlichem Pt-Bedeckungsgrad, sowie einer polykristalline Pt-Elektrode mit variierenden Elektrolytflussraten durchgeführt. Im Mittelpunkt der Studie stand der Einfluss der induzierten Transportbedingungen auf die resultierende Produktverteilung, also das Verhältnis von HCHO, HCOOH und CO_2. Es wurde gezeigt, dass die CO_2 Bildungsrate insbesondere von der Pt-Bedeckung (Partikeldichte) und der Elektrolytflussrate abhängt. Mit zunehmender Partikeldichte und langsamerer Elektrolytflussrate wurden eine höhere CO_2-Stromausbeute und ein höherer Umsatz von Methanol zu CO_2 verzeichnet. Diese Befunde stimmen sehr gut mit den Erwartungen gemäß des „Desorption–Re-Adsorption–Reaktion“ Konzeptes (siehe oben) überein. Für die MOR führt die häufigere Re-Adsorption und somit der seltenere Abtransport eines reaktiven Zwischenproduktes, wie HCHO und HCOOH, aus dem Reaktionsraum zu einer ansteigenden CO_2-Stromausbeute bzw. zu geringeren Anteilen der unvollständigen (teiloxidierten) Reaktionsprodukte HCHO und HCOOH, wenn *(i)* der Grad der Pt-Bedeckung hoch ist und somit die Abstände zwischen den Pt-Nanostrukturen entsprechend gering sind oder wenn *(ii)* die Dicke der Diffusionsschicht durch eine langsame Elektrolytflussrate erhöht und somit die Aufenthaltszeit der nicht vollständig oxidierten, gelösten Moleküle in der Nähe der Elektrodenoberfläche verlängert wird.

Zusammenfassend kann man sagen, dass im Rahmen dieser Arbeit zum ersten Mal der Einfluß mesoskopischer Transporteffekte, herbeigeführt durch entsprechende Elektrodenmorphologie, im Zusammenhang mit elektrokatalytischen Reaktionseigenschaften, wie Aktivität und Selektivität, auf molekularer Skala beschrieben und diskutiert wird.

Die präsentierten Ergebnisse stimmen im allgemeinen sehr gut mit Befunden vorangegangener Studien elektrokatalytischer Reaktionen (Oxidation von CO, ORR, MOR) auf polykristallinen Pt-Elektroden, Pt-Einkristallen oder kohlenstoffgeträgerten Pt/C Elektroden überein. Aus diesem Grund kann man annehmen, dass *(i)* das „Desorption–Re-Adsorption–Reaktion“ Konzept allgemein hin für elektrokatalytische Reaktionen, welche über die Bildung von reaktiven, löslichen Zwischenprodukten verlaufen, gültig ist und dass *(ii)* die Berücksichtigung von Transporteffekten, sowie festgelegte Transportbedingungen für das mechanistische Verständnis vieler elektrokatalytischer Reaktionen, sogar in Modellstudien, essentiell sind. Aufgrund ihrer einfachen und wohl definierten Geometrie, stellen die im Rahmen dieser Arbeit eingeführten nanostrukturierten Pt/GC Modellelektroden ideale Testsysteme für quantitative Studien von Massentransporteffekten in elektrokatalytischen Reaktionen dar und liefern eine exzellente Basis für weitere Arbeiten zur Modellierung und Simulation der zugrunde liegenden Reaktionen und Transportprozesse.

Zusätzlich zu diesen fundamentalen Gesichtspunkten, ist das Verständnis und die Berücksichtigung von Transportprozessen höchst relevant für technische Anwendungen, wie z.B. die Sauerstoffreduktions- und Methanoloxidationsreaktion in Direkt-Methanol-Brennstoffzellen (*engl.* Direct Methanol Fuel Cells, *DMFC*). In Anbetracht der auf Kostengründen basierenden Tendenz zur weiteren Reduktion der Katalysatormenge in Brennstoffzellen, könnten grenzwertige Katalysatorbeladungen unterschritten werden, bei denen eine zunehmende Produktion an unvollständigen Reaktionsprodukten, aufgrund des Mangels an aktiven Plätzen, auftreten könnte. Dieses Szenario könnte die Langzeitbelastung der DMFC aufgrund der Korrosion der Kohlenstoffträger und Membranschäden (zunehmende Bildung von H_2O_2) erheblich beeinflussen. Des Weiteren könnten toxische Produkte wie HCHO, gebildet während der MOR, am Auslass der DMFC entstehen.

Demzufolge, ist das Verständnis und die Berücksichtigung von Transportprozessen insbesondere wichtig für die rationale Entwicklung von (Direkt-Oxidations-) Brennstoffzellen, für die Optimierung der Katalysatorpartikelverteilung hinsichtlich einer maximalen Aktivität, die dennoch eine längere Lebenszeit garantiert und zusätzlich den Ausstoß unvollständiger Reaktionsprodukte, wie oxidativem H_2O_2 oder toxischem HCHO, bei geringen Katalysatorbeladungen vermeidet.

Bibliography

[1] Damjanovic, A., Genshaw, M. A., and Bockris, J. O. *J. Chem. Phys.* **45**, 4067 (1966).

[2] Bagotzky, V. S., Vassiliev, Y. B., and Khazova, O. A. *J. Electroanal. Chem.* **81**, 229–238 (1977).

[3] Jusys, Z., Massong, H., and Baltruschat, H. *J. Electrochem. Soc.* **146**, 1093–1098 (1999).

[4] Jusys, Z., Kaiser, J., and Behm, R. J. *Electrochim. Acta* **49**, 1297 (2004).

[5] Wang, H., Löffler, T., and Baltruschat, H. *J. Appl. Electrochem.* **31**, 759–765 (2001).

[6] Hallock, J. J. L., Tharakan, P. J., Hall, C. A. S., Jefferson, M., and Wu, W. *Energy* **29**, 1673 (2004).

[7] Green, D. L., Hopson, J. L., and Li, J. *Energy Policy* **34**, 515–531 (2006).

[8] Mason, J. *Energy Policy* **35**, 1315–1329 (2007).

[9] Dunn, S. *International Journal of Hydrogen Energy* **27**, 235–264 (2002).

[10] McDowall, W. and Eames, M. *Energy Policy* **34**, 1236–1250 (2006).

[11] Hoffmann, P. , Tomorrow´s fuel: hydrogen, fuel cells, and the prospect for a cleaner planet. Cambridge, MA: MIT Press, August 2001; Ingriselli, F., President, Texaco Technology Ventures. Powering future mobility with electric transportation technologies. Presentation to House Science Committee, US House of Representatives, 23 April 2001.

[12] Crabtree, G. W., Dresselhaus, M. S., and Buchanan, M. V. *Physics Today* **57** (December), 39–44 (2004).

[13] Gevorkian, P. *„Fuel Cell Technology“* in *Alternative Energy Systems in Building Desgin*, chapter 7, p. 245–266. Mcgraw-Hill Professional (2009).

[14] Larminie, J. and Dicks, A. *Fuel Cell Systems Explained.* John Wiley & Sons, West Sussex (2001).

[15] Iwasita-Vielstich, T. *„Progress in the Study of Methanol Oxidation by In Situ, Ex Situ and On-Line Methods“* in *Advances in Electrochemical Science and Engineering*, vol. 1, eds.: H. Gerischer, C. W. Tobias, chapter 3, p. 127–170. VCH Verlagsgesellschaft, Weinheim (1990).

[16] Jarvi, T. D. and Stuve, E. M. *„Fundamental Aspects of the Vacuum And Electrocatalytic Reactions of Methanol and Formic Acid on Platinum Surfaces“* in *Electrocatalysis*, series: Frontiers of Electrochemistry, eds.: J. Lipkowski, P. N. Ross, chapter 3, p. 75–153. Wiley-VCH, New York (1998).

[17] Chrzanowski, W. and Wieckowski, A. *„Methanol Oxidation Catalysis on Well Defined Platinum/Ruthenium Electrodes: Ultrahigh Vacuum Surface Science and Electrochemistry Approach“* in *Interfacial Electrochemistry: Theory, Experiment, and Applications*, ed.: A. Wieckowski, chapter 51, p. 937–954. Marcel Dekker Inc., New York (1999).

[18] Lamy, C., Léger, J.-M., and Srinivasan, S. *„Direct Methanol Fuel Cells: From a Twentieth Century Electrochemists Dream to a Twenty-First Century Emerging Technology“* in *Modern Aspects of Electrochemistry*, no. 34, eds.: J. O'M. Bockris, B. E. Conway, R. E. White, chapter 3, p. 53–118. Kluwer Academic/Plenum Publishers, New York (2001).

[19] Vielstich, W. *„CO, Formic Acid, and Methanol Oxidation in Acid Electrolytes - Mechanisms and Electrocatalysis“* in *Encyclopedia of Electrochemistry - Interfacial Kinetics and Mass Transport*, vol. 2, eds.: A. J. Bard, M. Stratmann, E. J. Calvo, chapter 5.2. Wiley-VCH, Weinheim (2003).

[20] Jusys, Z. and Behm, R. J. *„Methanol, Formaldehyde and Formic Acid Adsorption/Oxidation on Carbon-Supported Pt Nanoparticle Fuel Cell Catalyst: A Comparative Quantitative DEMS Study“* in *Fuel Cell Catalysis: A Surface Science Approach*, ed.: M. T. M. Koper, chapter 13, p. 411–464. John Wiley & Sons, New York (2009).

[21] Willsau, J., Wolter, O., and Heitbaum, J. *J. Electroanal. Chem.* **185**, 163–170 (1985).

[22] Iwasita, T. and Vielstich, W. *J. Electroanal. Chem.* **201**, 403–408 (1986).

[23] Childers, C. L., Huang, H., and Korzeniewski, C. *Langmuir* **15**, 786–789 (1999).

[24] Jusys, Z. and Behm, R. J. *J. Phys. Chem. B* **105**, 10874–10883 (2001).

[25] Jusys, Z., Kaiser, J., and Behm, R. J. *Langmuir* **19**, 6759–6769 (2003).

[26] Wasmus, S., Wang, J.-T., and Savinell, R. F. *J. Electrochem. Soc.* **142**, 3825–3833 (1995).

[27] Lin, W.-F., Wang, J.-T., and Savinell, R. F. *J. Electrochem. Soc.* **144**, 1917–1922 (1997).

[28] Sanicharane, S., Bo, A., Sompalli, B., Gurau, B., and Smotkin, E. S. *J. Electrochem. Soc.* **149**, A554 (2002).

[29] Kardash, D. and Korzeniewski, C. *Langmuir* **16**, 8419–8425 (2000).

[30] Chojak, M., Jusys, Z., and Behm, R. J. (2008). private communication.

[31] Tarasevich, M. R., Sadkowski, A., and Yeager, E. *„Oxygen Electrochemistry“* in *Comprehensive Treatise of Electrochemistry*, vol. 7, eds.: J. O'M. Bockris, B. E. Conway, E. Yeager, S. U. M. Khan and R. E. White, chapter 6, p. 301–398. Plenum Press, New York (1983).

[32] Kinoshita, K. *Electrochemical Oxygen Technology.* John Wiley & Sons, New York (1992).

[33] Adzic, R. R. *„Recent Advances in the Kinetics of Oxygen Reduction“* in *Electrocatalysis*, series: Frontiers of Electrochemistry, eds.: J. Lipkowski, P. N. Ross, chapter 5, p. 197–242. Wiley-VCH, New York (1998).

[34] Markovic, N. M. and Ross, P. N. *„Electrocatalysis at Well-Defined Surfaces: Kinetics of Oxygen Reduction and Hydrogen Oxidation/Evolution on Pt(hkl) Electrodes“* in *Interfacial Electrochemistry: Theory, Experiment, and Applications*, ed.: A. Wieckowski, chapter 46, p. 821–842. Marcel Dekker Inc., New York (1999).

[35] Hsieh, S. J. and Gewirth, A. A. *Surf. Sci.* **498**, 147–160 (2002).

[36] Li, X. and Gewirth, A. A. *J. Am. Chem. Soc.* **125**, 7086–7099 (2003).

[37] Balbuena, P. B., Calvo, S. R., Lamas, E. J., Salazar, P. F., and Seminario, J. M. *J. Phys. Chem. B* **110**, 17452–17459 (2006).

[38] Miah, M. R. and Ohsaka, T. *J. Electrochem. Soc.* **154**, F186–F190 (2007).

[39] Jusys, Z., Kaiser, J., and Behm, R. J. *J. Phys. Chem. B* **108**, 7893–7901 (2004).

[40] Paulus, U. A., Wokaun, A., Scherer, G. G., Schmidt, T. J., Stamenkovic, V., Markovic, N. M., and Ross, P. N. *Electrochim. Acta* **47**, 3787 (2002).

[41] Paulus, U. A., Wokaun, A., Scherer, G. G., Schmidt, T. J., Stamenkovic, V., Radmilovic, V., Markovic, N. M., and P. N. Ross, J. *J. Phys. Chem. B* **106**, 4181 (2002).

[42] Stamenkovic, V., Schmidt, T. J., Ross, P. N., and Markovic, N. M. *J. Phys. Chem. B* **106**, 11970 (2002).

[43] Watanabe, M., Sei, H., and Stonehart, P. *J. Electroanal. Chem.* **261**, 375 (1989).

[44] Inaba, M., Yamada, H., Tokunaga, J., and Tasaka, A. *Electrochem. Sol. Stat. Lett.* **7**, A474–A476 (2004).

[45] LaConti, A. B., Hamdan, M., and McDonald, R. C. *„Mechanism of Membrane Degradation for PEMFCs“* in *Handbook of Fuel Cells – Fundamentals, Technology and Applications*, vol. 3 – Fuel Cell Technology and Applications, eds.: W. Vielstich, A. Lamm and H. A. Gasteiger, chapter 49, p. 647–662. John Wiley & Sons, Ltd., Chichester (2003).

[46] Roen, L. M., Paik, C. H., and Jarvi, T. D. *Electrochem. Sol. Stat. Lett.* **7**, A19–A22 (2004).

[47] Gustavsson, M. *Nanostructured Fuel Cell Catalysts.* Chalmers University of Technology, PhD-Thesis, (2006).

[48] Morf, W. E. *Anal. Chim. Acta* **330**, 139–149 (1996).

[49] Dickinson, E. J. F., Streeter, I., and Compton, R. G. *J. Phys. Chem. B* **112**, 4059–4066 (2008).

[50] Morf, W. E. *Anal. Chim. Acta* **341**, 121–127 (1997).

[51] Morf, W. E., Koudelka-Hep, M., and de Rooij, N. F. *J. Electroanal. Chem.* **590**, 47–56 (2006).

[52] Rainer, D. R., Xu, C., and Goodman, D. W. *J. Mol. Catal. A* **119**, 307–325 (1997).

[53] Lambert, R. M. and Pacchioni, G. *Chemisorption and Reactivity on Supported Clusters and Thin Films,* NATO ASI series, Series E: Applied Science – vol. 331. Kluwer Academic Publisher, Dordrecht (1997).

[54] Henry, C. R. *Surf. Sci. Rept.* **31**, 231–325 (1998).

[55] Freund, H. J. *Surf. Sci.* **500**, 271–299 (2002).

[56] Jacobs, P. W., Ribeiro, F. H., Somorjai, G. A., and Wind, S. J. *Catal. Lett.* **37**, 131–136 (1996).

[57] Wong, K., Johansson, S., and Kasemo, B. *Faraday Discuss.* **105**, 237–246 (1996).

[58] Yang, M. X., Jacobs, P. W., Yoon, C., Muray, L., Anderson, E., Attwood, D., and Somorjai, G. A. *Catal. Lett.* **45**, 5–13 (1997).

[59] Burmeister, F., Schäfle, C., Mattes, T., Böhmisch, M., Boneberg, J., and Leiderer, P. *Langmuir* **13**, 2983–2987 (1997).

[60] Werdinius, C., Österlund, L., and Kasemo, B. *Langmuir* **19**, 458–468 (2003).

[61] Hanarp, P., Sutherland, D., Gold, J., and Kasemo, B. *Colloids Surf. A* **214**, 23–26 (2003).

[62] Österlund, L., Kielbassa, S., Werdinius, C., and Kasemo, B. *J. Catal.* **215**, 94 (2003).

[63] Österlund, L., Grant, A., and Kasemo, B. *„Lithographic Techniques in Nanocatalysis“* in *Nanocatalysis*, series: NanoSience and Technology, eds.: U. Heiz, U. Landman, chapter 4, p. 269–341. Springer, Berlin-Heidelberg-New York (2007).

[64] Fredriksson, H., Alaverdyan, Y., Dmitriev, A., Langhammer, C., Sutherland, D. S., Zäch, M., and Kasemo, B. *Adv. Mater.* **19**, 4297–4302 (2007).

[65] Gustavsson, M., Fredriksson, H., Kasemo, B., Jusys, Z., Jun, C., and Behm, R. J. *J. Electroanal. Chem.* **568**, 371–377 (2004).

[66] Spatz, J. P., Mößmer, S., Hartmann, C., Möller, M., Herzog, T., Krieger, M., Boyen, H.-G., Ziemann, P., and Kabius, B. *Langmuir* **16**, 407–415 (2000).

[67] Kästle, G., Boyen, H.-G., Weigl, F., Lengl, G., Herzog, T., Ziemann, P., Riethmüller, S., Meyer, O., Hartmann, C., Spatz, J., Möller, M. M., Ozawa, M., Banhart, F., Garnier, G., and Oelhafen, P. *Adv. Funct. Mater.* **13**, 853–861 (2003).

[68] Gerischer, H., Mattes, I., and Braun, R. *J. Electroanal. Chem.* **10**, 553–567 (1965).

[69] Levich, V. G. *Physicochemical Hydrodynamics.* Prentice Hall, Eaglewood Cliffs, New Jersey (1962).

[70] Albery, W. J., Jones, C. C., and Mount, A. R. *„New Hydrodynamic Methods“* in *New Techniques for the Study of Electrodes and their Reactions*, series: Comprehensive Chemical Kinetics, vol. 29, eds.: R. G. Compton, A. Hamnet, chapter 4, p. 129–148. Elsevier Science Publishers, Amsterdam (1989).

[71] Brett, C. M. A. and Oliveira-Brett, A. M. F. C. *„Hydrodynamic Electrodes“* in *Electrode Kinetics: Principles and Methodology*, series: Comprehensive Chemical Kinetics, vol. 26, eds.: C. H. Bamford, C. F. H. Tipper, R. G. Compton, chapter 5, p. 355–441. Elsevier Science Publishers, Amsterdam (1986).

[72] Cooper, J. A. and Compton, R. G. *Electroanal.* **10**, 141–155 (1998).

[73] Thomas, J. M. and Thomas, W. J. *Principles and Practice of Heterogeneous Catalysis.* VCH Verlagsgesellschaft, Weinheim (1997).

[74] Hamann, C. H., Hamnett, A., and Vielstich, W. *Electrochemistry.* Wiley-VCH, Weinheim (1998), 1. edition.

[75] Bard, A. J. and Faulkner, L. R. *Electrochemical Methods – Fundamentals and Applications.* John Wiley & Sons, New York (2001), 2. edition.

[76] Lamy, C., Lima, A., Rhun, V. L., Delime, F., Coutanceau, C., and Léger, J.-M. *J. Power Sources* **105**, 283–296 (2002).

[77] Frumkin, A. N., Nekrasov, L., Levich, V. G., and Ivanov, J. *J. Electroanal. Chem.* **1**, 84–90 (1959).

[78] Wroblowa, H. S., Pan, Y.-C., and Razumney, G. *J. Electroanal. Chem.* **69**, 195–201 (1976).

[79] Gattrell, M. and MacDougall, B. *„Reaction Mechanism of the O_2 Reduction/Evolution Reaction“* in *Handbook of Fuel Cells – Fundamentals, Technology and Applications*, vol. 2 – Fuel Cell Electrocatalysis, eds.: W. Vielstich,

A. Lamm and H. A. Gasteiger, chapter 30, p. 443–464. John Wiley & Sons, Ltd., Chichester (2003).

[80] Jacob, T. *Fuel Cells* **6**, 159–181 (2006).

[81] Rossmeisl, J. and Nørskov, J. K. *Surface Science* **602**, 2337–2338 (2008).

[82] Nilekar, A. and Mavrikakis, M. *Surface Science* **602**, L89–L94 (2008).

[83] de Lima, R. B., Paganin, V., Iwasita, T., and Vielstich, W. *Electrochim. Acta* **49**, 85–91 (2003).

[84] Housmans, T. H. M., Wonders, A. H., and Koper, M. T. M. *J. Phys. Chem. B* **110**, 10021–10031 (2006).

[85] Entina, V. S. and Petry, O. A. *Elektrokhimiya* **4**, 678–681 (1968).

[86] Ota, K.-I., Nakagawa, Y., and Takahashi, M. *J. Electroanal. Chem.* **179**, 179–186 (1984).

[87] Shibata, M. and Motoo, S. *J. Electroanal. Chem.* **209**, 151–158 (1986).

[88] Shibata, M., Furuya, N., and Watanabe, M. *J. Electroanal. Chem.* **229**, 385–394 (1987).

[89] Wang, H., Wingender, C., Baltruschat, H., Lopez, M., and Reetz, M. T. *J. Electroanal. Chem.* **509**, 163–169 (2001).

[90] Entina, V. S., Petrii, O. A., and Rysikova, V. T. *Elektrokhimiya* **3**, 758–761 (1967).

[91] Reddington, E., Sapienza, A., Gurau, B., Viswanathan, R., Sarangapani, S., Smotkin, E. S., and Mallouk, T. E. *Science* **280**, 1735–1737 (1998).

[92] Jusys, Z., Kaiser, J., and Behm, R. J. *Electrochim. Acta* **47**, 3693–3706 (2002).

[93] Islam, M., Basnayake, R., and Korzeniewski, C. *J. Electroanal. Chem.* **599**, 31–40 (2007).

[94] Korzeniewski, C. and Childers, C. L. *J. Phys. Chem. B* **102**, 489–492 (1998).

[95] Podlovchenko, B. I. and Petukhova, R. P. *Elektrokhimiya* **8**, 889–904 (1972).

[96] Gromyko, V. A., Khazova, O. A., and Vassiliev, Y. B. *Elektrokhimiya* **12**, 1352–1357 (1976).

[97] Lindström, R. W., Seidel, Y. E., Jusys, Z., Gustavsson, M., Kasemo, B., and Behm, R. J. *J. Electroanal. Chem.* , doi: 10.1016/j.jelechem.2009.04.034 (2009).

[98] Seidel, Y. E., Schneider, A., Jusys, Z., Wickman, B., Kasemo, B., and Behm, R. J. *Faraday Discuss.* **140**, 167–184 (2008).

[99] Schneider, A., Colmenares, L., Seidel, Y. E., Jusys, Z., Wickman, B., Kasemo, B., and Behm, R. J. *Phys. Chem. Chem. Phys.* **10**, 1931–1943 (2008).

[100] Seidel, Y. E., Schneider, A., Jusys, Z., Wickman, B., Kasemo, B., and Behm, R. J. *Langmuir* **26**, 3569–3578 (2010).

[101] Heiz, U. and Landman, U. *Nanocatalysis,* series: NanoSience and Technology. Springer, Berlin-Heidelberg-New York (2007).

[102] Hulteen, J., Treichel, D., Smith, M., Duval, M., Jensen, T., and van Duyne, R. *J. Phys. Chem. B* **103**, 3854–3863 (1999).

[103] Haynes, C. and van Duyne, R. *J. Phys. Chem. B* **105**, 5599–5611 (2001).

[104] Hanarp, P., Sutherland, D., Gold, J., and Kasemo, B. *J. Colloid Interface Sci.* **241**, 26–31 (2001).

[105] Hanarp, P. *Optical properties of nanometer disks, holes and rings prepared by Colloidal Lithography.* Chalmers University of Technology, PhD-Thesis, (2003).

[106] Schmidt, T. J., Noeske, M., Gasteiger, H. A., Behm, R. J., Britz, P., Brijoux, W., and Bönnemann, H. *J. Electrochem. Soc.* **145**, 925–931 (1998).

[107] Zhong, C.-J. and Maye, M. M. *Adv. Mater.* **13**, 1507–1511 (2001).

[108] Chusuei, C. C., Lai, K., Davis, K. A., Bowers, E. K., Fackler, J. P., and Goodman, D. W. *Langmuir* **17**, 4113–4117 (2001).

[109] Pettersson, D., Gustavsson, M., Lagergren, C., and Lindbergh, G. *Electrochim. Acta* **51**, 6584–6591 (2006).

[110] Fredriksson, H. *Nanostructures of Graphite and Amorphous Carbon - Fabrication and Properties.* Chalmers University of Technology, PhD-Thesis, (2009).

[111] Seidel, Y. E., Lindström, R., Jusys, Z., Cai, J., Wiedwald, U., Ziemann, P., and Behm, R. J. *Langmuir* **23**, 5795–5801 (2007).

[112] Niemantsverdriet, J. W. *Spectroscopy in Catalysis – An Introduction.* Wiley-VCH, Weinheim (1993).

[113] Goldstein, J., Newbury, D. E., Joy, D. C., Echlin, P., Lyman, C. E., Lifshin, E., Sawyer, L., and Healy, M. J. R. *Scanning Electron Microscopy and X-Ray Microanalysis.* Springer, New York (2002), 3. edition.

[114] Reimer, L. and Kohl, H. *Transmission Electron Microscopy: Physics of Image Formation,* series: Springer Series in Optical Science, vol. 36. Springer, New York (2008), 5. edition.

[115] Henzler, M. and Göpel, W. *Oberflächenphysik des Festkörpers.* Teubner Studienbücher – Physik, Stuttgart (1991).

[116] Niemantsverdriet, J. W. *„Catalyst characterization with spectroscopic techniques“* in *Catalysis: An Integrated Approach to Homogeneous, Heterogeneous and Industrial Catalysis*, series: Studies in Surface Science and Catalysis, vol. 79, eds.: J.A. Moulijn, P.W.N.M. van Leeuwen, R.A. van Santen, chapter 10, p. 363–400. Elsevier Science Publishers, Amsterdam (1993).

[117] Bergeret, G. and Gallezot, P. *„Particle Size and Dispersion Measurements“* in *Handbook of Heterogeneous Catalysis*, vol. 2, eds.: G. Ertl and H. Knözinger and J. Weitkamp, chapter 3.1.2, p. 439–464. Wiley-VCH, Weinheim (1997).

[118] Bergeret, G. *„Characterization of Metallic Catalysts by X-Ray and Electron Microscopy Techniques“* in *Catalysis by Metals*, vol. 2, eds.: A. J. Renouprez, H. Jobic, chapter 9, p. 167–180. Springer, Berlin (1997).

[119] Erni, R., Rossel, M. D., Kisielowski, C., and Dahmen, U. *Phys. Rev. Lett.* **102**, 096101–1 – 096101–4 (2009).

[120] Briggs, D. and Seah, M. P. *Practical Surface Analysis – Auger and X-Ray Photoelectron Spectroscopy,* vol. 1. John Wiley & Sons, Chichester (1990), 2. edition.

[121] Foger, K. *„Dispersed Metal Catalysts“* in *Catalysis – Science and Technology*, vol. 6, eds.: J.R. Anderson, M. Boudart, chapter 4, p. 227. Springer, Berlin (1984).

[122] Taglauer, E. *„Surface Chemical Composition“* in *Handbook of Heterogeneous Catalysis*, vol. 2, eds.: G. Ertl and H. Knözinger and J. Weitkamp, chapter 3.2.1.1, p. 614. Wiley-VCH, Weinheim (1997).

[123] Kamau, G. N., Willis, W. S., and Rusling, J. F. *Anal. Chem.* **57**, 545–551 (1985).

[124] Schmickler, W. *Interfacial Electrochemistry.* Oxford University Press, New York (1996).

[125] Pletcher, D. *Instrumental Methods in Electrochemistry.* Horwood Publishing Ltd., Chichester (2002).

[126] Fisher, A. C. *Electrode Dynamics (Oxford Chemistry Primers, No. 34).* Oxford University Press, Oxford (2003).

[127] Vielstich, W., Gasteiger, H. A., and Lamm, A., editors. *Handbook of Fuel Cells – Fundamentals, Technology and Applications,* vol. 2 – Fuel Cell Electrocatalysis. John Wiley & Sons, Ltd., Chichester (2003).

[128] von Helmholtz, H. *Ann. Physik* **89**, 211 (1853).

[129] Gouy, G. *Compt. Rend.* **149**, 654 (1910).

[130] Chapman, D. L. *Phil. Mag.* **25**, 475 (1913).

[131] Stern, O. *Z. Elektrochem.* **30**, 508 (1924).

[132] Brett, C. M. A. and Brett, A. M. O. *Electrochemistry – Principles, Methods, and Applications.* Oxford University Press, Oxford (1993).

[133] Wolter, O. and Heitbaum, J. *Ber. Bunsenges. Phys. Chem.* **88**, 2–6 (1984).

[134] Wasmus, S., Cattaneo, E., and Vielstich, W. *Electrochim. Acta* **35**, 771–775 (1990).

[135] Jusys, Z., Kaiser, J., and Behm, R. J. (2001). unpublished work.

[136] Wang, H. and Baltruschat, H. *J. Phys. Chem. C.* **111**, 7038–7048 (2007).

[137] Wang, H., Jusys, Z., and Behm, R. J. *J. Appl. Electrochem.* **36**, 1187–1198 (2006).

[138] Wang, H., Zhao, Z., Jusys, Z., and Behm, R. J. *J. Power Sources* **155**, 33–46 (2006).

[139] Wang, H., Jusys, Z., and Behm, R. J. *J. Electroanal. Chem.* **595**, 23–36 (2006).

[140] Jusys, Z. and Behm, R. J. *ECS Transactions* **16**, 1243–1251 (2008).

[141] Baltruschat, H. and Schmiemann, U. *Ber. Bunsenges. Phys. Chem.* **97**, 452 (1993).

[142] Hartung, T., Schmiemann, U., Kamphausen, I., and Baltruschat, H. *Anal. Chem.* **63**, 44–48 (1991).

[143] Schmiemann, U., Müller, U., and Baltruschat, H. *Electrochim. Acta* **40**, 99–107 (1994).

[144] Heinen, M., Chen, Y. X., Jusys, Z., and Behm, R. J. *Electrochim. Acta* **52**, 5634–5643 (2007).

[145] Heinen, M., Jusys, Z., and Behm, R. J. *„Reaction Pathways Analysis and Reaction Intermediate Detection Via Simultaneous DEMS and ATR-FTIRS“* in *Handbook of Fuel Cells – Fundamentals, Technology and Applications*, vol. 5 – Advances in Electrocatalysis, Materials, Diagnostics and Durability: Part I, eds.: W. Vielstich, H. Yokogawa and H. A. Gasteiger, chapter 12, p. 183–214. John Wiley & Sons, Ltd., Chichester (2008).

[146] Bruckenstein, S. and Gadde, R. R. *J. Am. Chem. Soc.* **93**, 793–794 (1971).

[147] Wolter, O. and Heitbaum, J. *Ber. Bunsenges. Phys. Chem.* **88**, 6–10 (1984).

[148] Baltruschat, H. *J. Amer. Soc. Mass Spectr.* **15**, 1693–1706 (2004).

[149] Baltruschat, H. *„Differential Electrochemical Mass Spectrometry As a Tool for Interfacial Studies“* in *Interfacial Electrochemistry: Theory, Experiment, and Applications*, ed.: A. Wieckowski, chapter 33, p. 577–597. Marcel Dekker Inc., New York (1999).

[150] Schmidt, T. J. *Electrocatalysis of low temperature fuel cell reactions*. University of Ulm, PhD-Thesis, (2000).

[151] Nart, F. and Vielstich, W. *„Normalization of Porous Active Surfaces“* in *Handbook of Fuel Cells – Fundamentals, Technology and Applications*, vol. 2 – Fuel Cell Electrocatalysis, eds.: W. Vielstich, A. Lamm and H. A. Gasteiger, chapter 21, p. 302–315. John Wiley & Sons, Ltd., Chichester (2003).

[152] Biegler, T., Rand, D. A. J., and Woods, R. *J. Electroanal. Chem.* **29**, 269–277 (1971).

[153] Maillard, F., Schreier, S., Hanzlik, M., Savinova, E. R., Weinkauf, S., and Stimming, U. *Phys. Chem. Chem. Phys.* **7**, 385–393 (2005).

[154] Weaver, M. J., Chang, S. C., Leung, L. W. H., Jiang, X., Rubel, M., Szklarczyk, M., Zurawski, D., and Wieckowski, A. *J. Electroanal. Chem.* **327**, 247–260 (1992).

[155] Jusys, Z., Kaiser, J., and Behm, R. J. *Phys. Chem. Chem. Phys.* **3**, 4650–4660 (2001).

[156] Wang, H., Jusys, Z., and Behm, R. J. *J. Phys. Chem. B* **108**, 19413–19424 (2004).

[157] Wang, H., Jusys, Z., and Behm, R. J. *Fuel Cells* **4**, 113–125 (2004).

[158] Colmenares, L., Wang, H., Jusys, Z., Jiang, L., Yan, S., Sun, G. Q., and Behm, R. J. *Electrochim. Acta* **52**, 221–233 (2006).

[159] Jiang, L., Colmenares, L., Jusys, Z., Sun, G. Q., and Behm, R. J. *Electrochim. Acta* **53**, 377–389 (2007).

[160] Wang, H., Jusys, Z., and Behm, R. J. (2008). in preparation.

[161] Schnaidt, J., Heinen, M., Jusys, Z., and Behm, R. J. (2008). in preparation.

[162] Paulus, U. A., Schmidt, T. J., Gasteiger, H. A., and Behm, R. J. *J. Electroanal. Chem.* **495**, 134–145 (2001).

[163] Colmenares, L., Jusys, Z., and Behm, R. J. *J. Phys. Chem. C* **111**, 1273–1283 (2007).

[164] Colmenares, L., Guerrini, E., Jusys, Z., Nagabhushana, K. S., Dinjus, E., Behrens, S., Habicht, W., Bönnemann, H., and Behm, R. J. *J. Appl. Electrochem.* **37**, 1413–1427 (2007).

[165] Weber, S. G. and Long, J. T. *Anal. Chem.* **60**, 903A–913A (1988).

[166] Bard, A. J. and Faulkner, L. R. *Electrochemical Methods – Fundamentals and Applications*. John Wiley & Sons, New York (1980), 1. edition.

[167] Fuhrmann, J., Linke, A., Langmach, H., and Baltruschat, H. *Electrochim. Acta* **55**, 430–438 (2009).

[168] Zhdanov, V. P. and Kasemo, B. *Surf. Sci. Rept.* **39**, 25–104 (2000).

[169] Kuhnke, M., Lippert, T., Ortellib, E., Scherer, G. G., and Wokaun, A. *Thin Solid Films* **453-454**, 36–41 (2004).

[170] Angerstein-Kozlowska, H., Conway, B. E., and Sharp, W. B. A. *J. Electroanal. Chem.* **43**, 9–36 (1973).

[171] Cervino, R. M., Triaca, W. E., and Arvia, A. J. *J. Electrochem. Soc.* **132**, 266–268 (1985).

[172] Conway, B. E., Barber, J., and Morin, S. *Electrochim. Acta* **44**, 1109–1125 (1998).

[173] Takasu, Y., Fujiwara, T., Murukami, Y., Sasaki, K., Oguri, M., Asaki, T., and Sugimoto, W. *J. Electrochem. Soc.* **147**, 4421–4427 (2000).

[174] Cherstiouk, O. V., Simonov, P. A., Chuvilin, A. L., and Savinova, E. R. *„Model nanostructured electrodes - An approach to study size structural effects in electrocatalysis“* in *The global climate change: A coordinated response by electrochemistry and solid-state science and technology*, ed.: A. Wieckowski, E. W. Brooman, E. J. Rudd, T. F. Fuller, J. Leddy, p. 56–71. The Electrochemical Society, Inc., Pennington, New Jersey (2001).

[175] Cherstiouk, O. V., Simonov, P. A., Zaikowskii, V. I., and Savinova, E. R. *J. Electroanal. Chem.* **554–555**, 241–251 (2003).

[176] Schmidt, T. J., Gasteiger, H. A., and Behm, R. J. *J. Electrochem. Soc.* **146**, 1296–1304 (1999).

[177] Maillard, F., Eikerling, M., Cherstiouk, O. V., Schreier, S., Savinova, E. R., and Stimming, U. *Faraday Discuss.* **125**, 357–377 (2004).

[178] Arenz, M., Mayrhofer, K. J., Stamenkovic, V., Blizanac, B. B., Tomoyuki, T., Ross, P. N., and Markovic, N. M. *J. Am. Chem. Soc.* **127**, 6819–6829 (2005).

[179] Santos, E., Leiva, E. P. M., Vielstich, W., and Linke, U. *J. Electroanal. Chem.* **227**, 199–211 (1987).

[180] Markovic, N. M., Grgur, B. N., Lucas, C. A., and Ross, P. N. *J. Phys. Chem. B* **103**, 487–495 (1999).

[181] Seidel, Y. E., Müller, M., Jusys, Z., Wickman, B., Hanarp, P., Kasemo, B., Hörmann, U., Kaiser, U., and Behm, R. J. *J. Electrochem. Soc.* **155**, K171–K179 (2008).

[182] Becdelièvre, A. M. D., de Becdelièvre, J. J., and Clavilier, J. *J. Electroanal. Chem.* **294**, 97–110 (1990).

[183] Gasteiger, H. A., Markovic, N. M., and Ross, P. N. *J. Phys. Chem.* **99**, 8290–8301 (1995).

[184] Solla-Gullon, J., Herrero, E., Vidal-Iglesias, F. J., Feliu, J., and Aldaz, A. *Electrochem. Comm.* **8**, 189–194 (2006).

[185] Gilman, S. *J. Phys. Chem.* **67**, 1989–1905 (1963).

[186] Dam, V. A. T. and de Bruijn, F. A. *J. Electrochem. Soc.* **154**, B494–B499 (2007).

[187] Darling, R. M. and Meyers, J. P. *J. Electrochem. Soc.* **150**, A1523–A1527 (2003).

[188] Komanicky, V., Chang, K. C., Menzel, A., Markovic, N. M., You, H., Wang, X., and Myers, D. *J. Electrochem. Soc.* **153**, B446–B451 (2006).

[189] Crommie, M. F., Lutz, C. P., and Eigler, D. M. *Science* **262**, 218–220 (1993).

[190] Piner, R. D., Zhu, J., Xu, F., Hong, S., and Mirkin, M. V. *Science* **283**, 661–663 (1999).

[191] Scharifker, B. R. *J. Electroanal. Chem.* **458**, 253–255 (1998).

[192] Morf, W. E. and de Rooij, N. F. *Sens. and Actuat. B* **44**, 538–541 (1997).

[193] Seidel, Y. E., Lindström, R., Jusys, Z., Gustavsson, M., Hanarp, P., Kasemo, B., Minkow, A., Fecht, H. J., and Behm, R. J. *J. Electrochem. Soc.* **155**, K50–K58 (2008).

[194] Gasteiger, H. A., Markovic, N. M., and Ross, P. N. *J. Phys. Chem.* **99**, 16757–16767 (1995).

[195] Zhdanov, V. P. and Kasemo, B. *Chem. Phys. Lett.* **376**, 220–225 (2002).

[196] Ye, H., Crooks, J. A., and Crooks, R. M. *Langmuir* **23**, 11901–11906 (2007).

[197] Ekström, H., Hanarp, P., Gustavsson, M., Fridell, E., Lundblad, A., and Lindbergh, G. *J. Electrochem. Soc.* **153**, A724–A730 (2006).

[198] Solla-Gullon, J., Montiel, V., Aldaz, A., and Clavilier, J. *J. Electroanal. Chem.* **491**, 69–77 (2000).

[199] Solla-Gullon, J., Rodes, A., Montiel, V., Aldaz, A., and Clavilier, J. *J. Electroanal. Chem.* **554-555**, 273–284 (2003).

[200] Kielbassa, S., Häbich, A., Schnaidt, J., Bansmann, J., Weigl, F., Boyen, H.-G., Ziemann, P., and Behm, R. J. *Langmuir* **22**, 7873–7880 (2006).

[201] Kumar, S. and Zou, S. *Electrochem. Comm.* **8**, 1151–1157 (2006).

[202] Behm, R. J. and Jusys, Z. *J. Power Sources* **154**, 327–342 (2006).

[203] Feldmeyer, G., Schubert, M. M., Hartmann, C. S., Plzak, V., Möller, M. M., and Behm, R. J. (2002). unpublished work.

[204] Moulder, J. F., Stickle, W. F., Sobol, P. E., and Bomben, K. D. *Handbook of X-Ray Photoelectron Spectroscopy,* ed.: J. Chastain. Perkin Elmer Cooperation, Eden Prairie, Minnesota, USA (1992).

[205] Wertheim, G. K., DiCenzo, S. B., and Youngquist, S. E. *Phys. Rev. Lett.* **51**, 2310–2313 (1983).

[206] Takasu, Y., Iwazaki, T., Sugimoto, W., and Murakami, Y. *Electrochem. Comm.* **2**, 671–674 (2000).

[207] Savinova, E. R., (2006). private communication.

[208] Gilman, S. *J. Phys. Chem.* **66**, 2657–2663 (1962).

[209] Breiter, M. and Hoffmann, K. *Z. Elektrochem.* **64**, 462–467 (1960).

[210] Stonehart, P. *J. Electroanal. Chem.* **15**, 239–244 (1967).

[211] Bockris, J. O. and Wroblowa, H. *J. Electroanal. Chem.* **7**, 428–451 (1964).

[212] Vielstich, W. *Fuel Cells.* Wiley-Interscience, Bristol (1965).

[213] Gottesfeld, S. and Zawodzinski, T. A. *„Polymer Electrolyte Fuel Cells“* in *Advances in Electrochemical Science and Engineering*, vol. 5, eds.: R. C. Alkire, H. Gerischer, D. M. Kolb, C. W. Tobias, p. 195–301. Wiley-VCH, Weinheim (1997).

[214] Vielstich, W. and Iwasita, T. *„Fuel Cells“* in *Handbook of Heterogeneous Catalysis*, vol. 4, eds.: G. Ertl and H. Knözinger and J. Weitkamp, p. 2090–2111. Wiley-VCH, Weinheim (1997).

[215] Lamy, C. and Léger, J.-M. *J. Chim. Phys.* **88**, 1649–1671 (1991).

[216] Weaver, M. J. *J. Phys. Chem.* **100**, 13079–13089 (1996).

[217] Markovic, N. M. and Jr., P. N. R. *Surf. Sci. Rept.* **45**, 117–229 (2002).

[218] Vielstich, W., Gasteiger, H. A., and Lamm, A., editors. *Handbook of Fuel Cells – Fundamentals, Technology and Applications,* vol. 1 – Fuel Cell Fundamentals and Survey of Systems. John Wiley & Sons, Ltd., Chichester (2003).

[219] Beden, B., Lamy, C., Bewick, A., and Kunimatsu, K. *J. Electroanal. Chem.* **121**, 343–347 (1981).

[220] Villegas, I., Kizhakevariam, N., and Weaver, M. J. *Surf. Sci.* **335**, 300–314 (1995).

[221] Hamnett, A. *„Mechanism of Methanol Electro-Oxidation“* in *Interfacial Electrochemistry: Theory, Experiment, and Applications*, ed.: A. Wieckowski, chapter 47, p. 843–884. Marcel Dekker Inc., New York (1999).

[222] Iwasita, T. and Nart, F. C. *In-Situ Fourier Transform Infrared Spectroscopy: A Tool to Characterize the Metal-Electrolyte Interface at a Molecular Level*, chapter in *Advances in Electrochemical Science and Engineering*, 123–216. VCH, Weinheim (1990).

[223] Sun, S.-G. *„Studying Electrocatalytic Oxidation of Small Organic Molecules With in-Situ Infrred Spectroscopy“* in *Electrocatalysis*, series: Frontiers of Electrochemistry, eds.: J. Lipkowski, P. N. Ross, chapter 6, p. 243–290. Wiley-VCH, New York (1998).

[224] Korzeniewski, C. *„Vibrational Coupling Effects on Infrared Spectra of Adsorbates on Electrodes“* in *Interfacial Electrochemistry: Theory, Experiment, and Applications*, ed.: A. Wieckowski, chapter 20, p. 345–352. Marcel Dekker Inc., New York (1999).

[225] Nart, F. C. and Iwasita, T. *„In-situ FTIR as a Tool for Mechanistic Studies – Fundamentals and Applications“* in *Encyclopedia of Electrochemistry - Interfacial Kinetics and Mass Transport*, vol. 2, eds.: A. J. Bard, M. Stratmann, E. J. Calvo, chapter 3.4, 243–289. Wiley-VCH, Weinheim (2003).

[226] Kunimatsu, K., Uchida, H., Osawa, M., and Watanabe, M. *J. Electroanal. Chem.* **587**, 299–307 (2006).

[227] Allen, P. G., Conradson, S. D., Wilson, M. S., Gottesfeld, S., Raistrick, I. D., Valerio, J., and Lovato, M. *Electrochim. Acta* **39**, 2415–2418 (1994).

[228] Couves, J. W. and Meehan, P. *Physica B* **208 & 209**, 665–667 (1995).

[229] Alonso-Vante, N., Fieber-Erdmann, M., Rossner, H., Holub-Krappe, E., Giorgetti, C., Tadjeddine, A., Dartyge, E., Fontaine, A., and Frahm, R. *J. Phys. IV France* **7**, C2. 887–889 (1997).

[230] O'Grady, W. E., Hagans, P. L., Pandya, K. I., and Mariche, D. L. *Langmuir* **17**, 3047–3050 (2001).

[231] Alonso-Vante, N., Malakhov, I. V., Nikitenko, S. G., Savinova, E. R., and Kochubey, D. I. *Electrochim. Acta* **47**, 3807–3814 (2002).

[232] Roth, C., Martz, N., Morlang, A., Theissmann, R., and Fuess, H. *Phys. Chem. Chem. Phys.* **6**, 3557–3562 (2004).

[233] Lucas, C. A., Markovic, N. M., and Ross, P. N. *Phys. Rev. Lett.* **77**, 4922–4925 (1996).

[234] Lucas, C. A., Markovic, N. M., Grgur, B. N., and Ross, P. N. *Surf. Sci.* **448**, 65–76 (2000).

[235] Wang, J. X., Robinson, I. K., Ocko, B. M., and Adzic, R. R. *J. Phys. Chem. B* **109**, 24–26 (2005).

[236] Koper, M. T. M. and Schmickler, W. *„A Unified Model of Electron and Ion Transfer Reactions at Metal Electrodes“* in *Electrocatalysis*, series: Frontiers of Electrochemistry, eds.: J. Lipkowski, P. N. Ross, chapter 7, p. 291–322. Wiley-VCH, New York (1998).

[237] Wasileski, S. A., Koper, M. T. M., and Weaver, M. J. *J. Phys. Chem. B* **105**, 3518–3530 (2001).

[238] Nørskov, J. K., Bligaard, T., Logadottir, A., Bahn, S., Hansen, L. B., Bollinger, M., Bengaard, H., Hammer, B., Sljivancanin, Z., Mavrikakis, M., Xu, Y., Dahl, S., and Jacobsen, C. J. H. *J. Catal.* **209**, 275–278 (2002).

[239] Greeley, J. and Mavrikakis, M. *Nature Materials* **3**, 810–815 (2004).

[240] Taylor, C. D. and Neurock, M. *Curr. Opinions Sol. Stat. Mater. Science* **9**, 49–65 (2005).

[241] Stamenkovic, V., Mun, B. S., Mayrhofer, K. J. J., Ross, P. N., Markovic, N. M., Rossmeisl, J., Greeley, J., and Nørskov, J. K. *Angew. Chem.* **45**, 2815–2818 (2006).

[242] Stamenkovic, V. R., Mun, B. S., Arenz, M., Mayrhofer, K. J. J., Lucas, C. A., Wang, G., Ross, P. N., and Markovic, N. M. *Nature Materials* **6**, 241–247 (2007).

[243] Aoki, K., Tokuda, K., and Matsuda, H. *J. Electroanal. Chem.* **79**, 49–78 (1977).

[244] Unwin, P. R. and Compton, R. G. *„he Use of Channel Electrodes in the Investigation of Interfacial Reactions Mechanisms“* in *New Techniques for the Study of Electrodes and their Reactions*, series: Comprehensive Chemical Kinetics, vol. 29, eds.: R. G. Compton, A. Hamnet, chapter 6, p. 173–296. Elsevier Science Publishers, Amsterdam (1989).

[245] Wakabayashi, N., Uchida, H., and Watanabe, M. *Electrochem. Sol. Let.* **5**, E62–E65 (2002).

[246] Madden, T. H., Arvindan, N., and Stuve, E. M. *J. Electrochem. Soc.* **150**, E1–E10 (2003).

[247] Madden, T. H. and Stuve, E. M. *J. Electrochem. Soc.* **150**, E571–E577 (2003).

[248] Wakabayashi, N., Takeichi, M., Uchida, H., and Watanabe, M. *J. Phys. Chem. B* **109**, 5836–5841 (2005).

[249] Fuhrmann, J., Zhao, H., Holzbecher, E., Langmach, H., Chojak, M., Halseid, R., Jusys, Z., and Behm, R. J. *Phys. Chem. Chem. Phys.* **10**, 3784–3795 (2008).

[250] Chen, Y.-X., Heinen, M., Jusys, Z., and Behm, R. J. *Angew. Chem. Int. Ed.* **45**, 981–985 (2006).

[251] Yamada, J. and Matsuda, H. *J. Electroanal. Chem.* **44**, 189–198 (1973).

[252] Bergelin, M., Feliu, J. M., and Wasberg, M. *Electrochim. Acta* **44**, 1069–1075 (1998).

[253] Koponen, U., Peltonen, T., Bergelin, M., Mennola, T., Valkiainen, M., Kaskimies, J., and Wasberg, M. *J. Power Sources* **86**, 261–268 (2000).

[254] Green, C. L. and Kucernak, A. *J. Phys. Chem. B* **106**, 11446–11456 (2002).

[255] Markovic, N. M., Gasteiger, H. A., and Ross, P. N. *J. Phys. Chem.* **99**, 3411–3415 (1995).

[256] Bonakdarpour, A., Delacote, C., Yang, R., Wieckowski, A., and Dahn, R. J. *Electrochem. Comm.* **10**, 611–615 (2008).

[257] Colmenares, L., Jusys, Z., and Behm, R. J. *Langmuir* **22**, 10437–10445 (2006).

[258] Damjanovic, A. *„Mechanistic Analysis of Oxygen Electrode Reactions“* in *Modern Aspects of Electrochemistry*, no. 5, eds.: J. O'M. Bockris, B. E. Conway, p. 369–483. Plenum Press, New York (1969).

[259] Chen, S. and Kucernak, A. *J. Phys. Chem. B* **108**, 3262–3276 (2004).

[260] Fuhrmann, J., Zhao, H., Holzbecher, E., and Langmach, H. *J. Fuel Cell Sci. & Technol.* **5**, 021008/1–021008/10 (2008).

[261] Zhang, D., Deutschmann, O., Seidel, Y. E., and Behm, R. J. (2008). in preparation.

[262] Imbihl, R., Behm, R. J., and Schloegl, R. *Phys. Chem. Chem. Phys.* **9**, 3459 (2007).

[263] Kardash, D., Korzeniewski, C., and Markovic, N. *J. Electroanal. Chem.* **500**, 518–523 (2001).

[264] Seidel, Y. E., Jusys, Z., Wickman, B., Kasemo, B., and Behm, R. J. *ECS Trans.* **25**, 91–102 (2010).

[265] Bergamaski, K., Pinheiro, A. L. N., Teixeira-Neto, E., and Nart, F. C. *J. Phys. Chem. B* **110**, 19271–19279 (2006).

[266] Gojkovic, S. L. *J. Electroanal. Chem.* **573**, 271–276 (2004).

[267] Cheng, D., Wang, W., and Huang, S. *J. Phys. Chem. C* **111**, 1631–1637 (2007).

[268] Gojkovic, S. L. and Vidakovic, T. R. *Electrochim. Acta* **47**, 633–642 (2001).

[269] Lu, G.-Q., Chrzanowski, W., and Wieckowski, A. *J. Phys. Chem. B* **104**, 5566–5572 (2000).

[270] Hoster, H. E., Iwasita, T., Baumgärtner, H., and Vielstich, W. *Phys. Chem. Chem. Phys.* **3**, 337–346 (2001).

[271] Hoster, H. E., Iwasita, T., Baumgärtner, H., and Vielstich, W. *J. Electrochem. Soc.* **148**, A496–A501 (2001).

[272] Housmans, T. H. M. and Koper, M. T. M. *J. Phys. Chem. B* **107**, 8557–8567 (2003).

[273] Gasteiger, H. A., Markovic, N. M., Ross, P. N., and Cairns, E. J. *J. Phys. Chem.* **97**, 12020–12029 (1993).

[274] Gasteiger, H. A., Markovic, N., Ross, P. N., and Cairns, E. J. *J. Electrochem. Soc.* **141**, 1795–1803 (1994).

[275] Herrero, E., Franaszczuk, K., and Wieckowski, A. *J. Phys. Chem.* **98**, 5074–5083 (1994).

[276] Tremiliosi-Filho, G., Kim, H., Chrzanowski, W., Wieckowski, A., Grzybowska, B., and Kulesza, P. *J. Electroanal. Chem.* **467**, 143–156 (1999).

[277] Iwasita, T., Hoster, H., John-Anacker, A., Lin, W.-F., and Vielstich, W. *Langmuir* **16**, 522–529 (2000).

[278] Gasteiger, H. A., Ross, P. N., and Cairns, E. J. *Surf. Sci.* **293**, 67–80 (1993).

[279] Gasteiger, H. A., Markovic, N. M., Ross, P. N., and Cairns, E. J. *Electrochim. Acta* **39**, 1825–1832 (1994).

Appendix

Publications

Comprehending Papers

- Y. E. Seidel, A. Schneider, Z. Jusys, B. Wickman, B. Kasemo and R. J. Behm; *Transport Effects in the Electro-Oxidation of Methanol Studied on Nanostructured Pt/Glassy Carbon Electrodes*; Langmuir, **26** (5), 3569–3578, (2010). [Chapter 7]

- Y. E. Seidel, A. Schneider, Z. Jusys, B. Wickman, B. Kasemo and R. J. Behm; *Mesoscopic Mass Transport Effects in Electrocatalytic Processes*; Faraday Discussions, **140**, 167–184, (2008). [Chapter 6]

- Y. E. Seidel, Z. Jusys, B. Wickman, P. Hanarp, B. Kasemo, U. Hörmann, U. Kaiser and R. J. Behm; *Nanostructured, Glassy Carbon Supported Pt/GC Electrodes: The Presence of Secondary Pt Nanostructures and how to avoid them*; J. of the Electrochem. Soc., **155** (10), K171–K179, (2008). [Chapter 4]

- Y. E. Seidel, R. W. Lindström, Z. Jusys, M. Gustavsson, P. Hanarp, B. Kasemo, A. Minkow, H. J. Fecht and R. J. Behm; *Stability of Nanostructured Pt/Glassy Carbon Electrodes Prepared by Colloidal Lithography*; J. of the Electrochem. Soc., **155** (3), K50–K58, (2008). [Chapter 3]

- Y. E. Seidel, R. W. Lindström, Z. Jusys, J. Cai, U. Wiedwald, P. Ziemann and R. J. Behm; *Nanostructured Pt/GC Model Electrodes Prepared by the Deposition of Metal-Salt-Loaded Micelles*; Langmuir, **23** (10), 5795–5801, (2007). [Chapter 5]

Papers not included in the Thesis

- H. Schwechten, M. Heinen, Y. E. Seidel, Z. Jusys, B. Wickman, B. Kasemo and R. J. Behm; *Kinetic DEMS Studies of CO Adsorption and continuous CO Oxidation on nanostructured Pt/Glassy Carbon Model Electrodes*; in preparation.

- B. Wickman, Y. E. Seidel, Z. Jusys, B. Kasemo and R. J. Behm; *Electrocatalytic Properties of Pt/Ru Nanoparticle Pair Arrays with controlled Separation*; submitted.

- D. Zhang, O. Deutschmann, Y. E. Seidel and R. J. Behm; *Interaction of Mass Transport and Reaction Kinetics during Electrocatalytic CO Oxidation in a Thin-Layer Flow Cell*; submitted.

- J. Fuhrmann, H. Zhao, H. Langmach, Y. E. Seidel, Z. Jusys and R. J. Behm; *The Role of reactive Reaction Intermediates in Two-Step Heterogeneous Electrocatalytic Reactions: A Model Study*; submitted.

- Y. E. Seidel, Z. Jusys, R. W. Lindström, M. Gustavsson, B. Kasemo and K. Krischer; *Oscillatory Behavior in Galvanostatic Formaldehyde Oxidation on nanostructured Pt/Glassy Carbon Model Electrodes*; Chem. Phys. Chem., **11** (7), 1405–1415, (2010).

- Y. E. Seidel, Z. Jusys, B. Wickman, B. Kasemo and R. J. Behm; *Mesoscopic Transport Effects in Electrocatalytic Reactions*; ECS Trans., **25**, 91–102, (2010).

- R. W. Lindström, Y. E. Seidel, Z. Jusys, M. Gustavsson, B. Wickman, B. Kasemo and R. J. Behm; *Electrocatalysis and Transport Effects on Nanostructured Pt/GC Electrodes*; J. Electroanal. Chem., doi:10.1016/j.jelechem.2009.04.034, (2009).

- A. Schneider, L. Colmenares, Y. E. Seidel, Z. Jusys, B. Wickman, B. Kasemo and R. J. Behm; *Transport Effects in the Oxygen Reduction Reaction on nanostructured, planar Glassy Carbon supported Pt/GC Model Electrodes*; Phys. Chem. Chem. Phys., **10**, 1931–1943, (2008).

Conference Contributions

Talks

- Wissenschaftsforum Gemeinschaft Deutscher Chemiker (GDCh), Frankfurt a. Main (2009):
  Y. E. Seidel, A. Schneider, Z. Jusys, B. Wickman, B. Kasemo and R. J. Behm; *Transport Effects on Fuel Cell relevant Electrocatalytic Reactions investigated by use of Nanostructured Pt/GC Model Electrodes*

- Statusworkshop des Kompetenznetzes Funktionale Nanostrukturen (KNFS), Bad Herrenalb (2008):
  Y. E. Seidel, A. Schneider, Z. Jusys, B. Wickman, B. Kasemo and R. J. Behm; *Transporteffekte an nanostrukturierter Oberflächen*

- Wissenschaftsforum Gemeinschaft Deutscher Chemiker (GDCh) - Electrochemistry: Crossing Boundaries, Giessen (2008):
  Y. E. Seidel, A. Schneider, Z. Jusys, B. Wickman, B. Kasemo and R. J. Behm; *Nanostructured Glassy Carbon Supported GC/Pt Electrodes for Model Studies of Fuel Cell relevant Electrocatalytic Reactions*

- Nanotech Northern Europe 2008, Copenhagen, Denmark (2008):
  Y. E. Seidel, A. Schneider, Z. Jusys, B. Wickman, B. Kasemo and R. J. Behm; *Nanostructured Glassy Carbon Supported GC/Pt Electrodes for Model Studies of Fuel Cell relevant Electrocatalytic Reactions*

- Statusworkshop des Kompetenznetzes Funktionale Nanostrukturen (KNFS), Bad Herrenalb (2007):
  Y. E. Seidel, R. W. Lindström, Z. Jusys, U. Wiedwald, P. Ziemann and R. J. Behm; *Elektrokatalytische Funktion nanostrukturierter Oberflächen*

- Statusworkshop des Kompetenznetzes Funktionale Nanostrukturen (KNFS), Bad Herrenalb (2006):
  Y. E. Seidel, R. W. Lindström, Z. Jusys, U. Wiedwald, P. Ziemann and R. J. Behm; *Elektrokatalytische Funktion nanostrukturierter Oberflächen*

- 57^{th} Annual Meeting of the International Society of Electrochemistry, Edinburgh, Scotland (2006):
  Y. E. Seidel, R. W. Lindström, Z. Jusys, U. Wiedwald, P. Ziemann and R. J. Behm; *Preparation and Electrochemical Characterization of Nanostructured Pt-Electrodes Produced by Metal-salt Loaded Micellar-Technique*

Invited Talks

- „Aktiv in Wissenschaft und Familie“– Netzwerkveranstaltung der Schlieben-Lange-Stipendiatinnen, Stuttgart (2009):
  Y. E. Seidel,Z. Jusys, B. Wickman, B. Kasemo and R. J. Behm; *Energie der Zukunft: Brennstoffzellen verstehen*

Poster

- Bunsen Colloquium, Günzburg – Reisensburg Castle (2009):
  B. Wickman, Y. E. Seidel, Z. Jusys, B. Kasemo and R. J. Behm; *Electrocatalytic properties of Pt/Ru nanoparticle pair arrays with controlled separation*

- Statusworkshop des Kompetenznetzes Funktionale Nanostrukturen (KNFS), Bad Herrenalb (2008):
  R. J. Behm, Y. E. Seidel, R. W. Lindström, D. Zhang, O. Deutschmann, P. Leiderer, J. Boneberg; *Elektrokatalytische Funktion nanostrukturierter Oberflächen – Reaktion und Massentransport*

- ESF-FWF Conference in Partnership with LFUI: Nanotechnology for Sustainable Energy, Obergurgl, Austria (2008):
  Y. E. Seidel, A. Schneider, Z. Jusys, B. Wickman, P. Hanarp, B. Kasemo and R. J. Behm; *Nanostructured, glassy carbon supported Pt/GC Model Electrodes: Problems of Nanostructuring*

- 11^{th} Ulm ElectroChemical Talks (UECT), Neu-Ulm (2008):
  A. Schneider, Y. E. Seidel, Z. Jusys, L. Colmenares, B. Wickman, B. Kasemo and R. J. Behm; *Mass Transport Effects in the ORR on Nanostructured Pt/GC Model Electrodes prepared by Hole-mask Colloidal Lithography*

- 41. Jahrestreffen Deutscher Katalytiker, Weimar (2008):
  Y. E. Seidel, A. Schneider, L. Colmenares, Z. Jusys, B. Wickman, B. Kasemo and R. J. Behm; *Elektrokatalytische Eigenschaften nanostrukturierter Modell-Katalysatoren*

- Statusworkshop des Kompetenznetzes Funktionale Nanostrukturen (KNFS), Bad Herrenalb (2007):
  R. J. Behm, Y. E. Seidel, R. W. Lindström, D. Zhang, O. Deutschmann, P. Leiderer, J. Boneberg; *Elektrokatalytische Funktion nanostrukturierter Oberflächen – Reaktion und Massentransport*

- Wissenschaftsforum Gemeinschaft Deutscher Chemiker (GDCh), Ulm (2007):
  Y. E. Seidel, A. Schneider, M. Müller, L. Colmenares, Z. Jusys, B. Wickman, B. Kasemo and R. J. Behm; *Electrocatalytic properties (anodic and cathodic reactions) of nanostructured model-catalysts prepared by Colloidal Lithography*

- Statusworkshop des Kompetenznetzes Funktionale Nanostrukturen (KNFS), Bad Herrenalb (2006):
  R. J. Behm, Y. E. Seidel, R. W. Lindström, D. Zhang, O. Deutschmann, P. Leiderer, J. Boneberg; *Elektrokatalytische Funktion nanostrukturierter Oberflächen – Reaktion und Massentransport*

- 57^{th} Annual Meeting of the International Society of Electrochemistry, Edinburgh, Scotland (2006):
  Y. E. Seidel, R. W. Lindström, Z. Jusys, M. Gustavsson, B. Kasemo and R. J. Behm; *Stability and Electrocatalytic Properties of Nanostructured Pt/GC Electrodes Prepared by Colloidal Lithography*

Acknowledgement

Diese Dissertation wurde am Institut für Oberflächenchemie und Katalyse (Universität Ulm) angefertigt. Finanziell unterstützt wurde sie von der Landesstiftung Baden-Württemberg durch das „Kompetenznetz Funktionelle Nanostrukturen“ im Rahmen des Projektes B9 (Förderperiode 2006–2008) und 2009 durch Ministerium für Wissenschaft, Forschung und Künste (Baden-Württemberg) im Rahmen des Schlieben-Lange-Programms.

Mein besonderer Dank gilt meinem Doktorvater, Prof. Dr. R. Jürgen Behm für die Möglichkeit diese interessante Arbeit zu einem spannenden Thema über „kleine Teilchen“ durchzuführen, für die große Unterstützung trotz der z.T. „erschwerten“ Bedingungen hervorgerufen durch meine „kleinen Teilchen“ und für die unendliche Geduld und Rücksicht bei Besprechungen und Seminaren, wenn Santina oder Rasmus sich auch einbringen wollten.

Special thanks go to Dr. Zenonas Jusys, my supervisor, who guided and taught me in the last years. He always encouraged me for critical thinking and waited with me in the lab until we got the „perfect CO_{ad} stripping“. Thanks a million, *Zenonas*, for sharing your knowledge, your support as well as your patience and regard!

A very special gratefulness to Prof. Dr. B. Kasemo and in particular to Björn Wickman and Dr. Marie Stenfeldt for providing me with model electrodes. Many thanks to *Björn*, who was not only a co-author, but become a good friend. Ein ebenso großer Dank gilt Prof. Dr. P. Ziemann and Dr. Ulf Wiedwald für die zahlreichen Mizell-Proben. Vielen lieben Dank Ulf, für die langen Telefongespräche, die zum Gelingen des Verfahrens beigetragen haben.

Vielen Dank an Prof. Dr. H. J. Fecht und an Alexander Minkow für die vielen spannenden Stunden am SEM und die aufschlussreichen EDX Analysen, an Prof. Dr. U. Kaiser und Dr. Ute Hörmann für die hochaufgelösten TEM-Bilder, sowie an Dr. Jun Cai und Dr. Alexander Karpenko für die XPS-Messungen, sowie Thomas Häring und Gerd Bräth für die vielen Kleinigkeiten, die zum Messerfolg beigetragen haben.

Ein dickes Dankeschön an meine Freunde und Kollegen aus der Elektrokatalyse-Gruppe, allen voran Martin und Luis, Johannes, Christian und Halina. Many thanks to our international (alumnae) team-members Shigou, Wei, Sylvain, Rakel, Rune, Malgorzata and Luhua for the diversified time (not only!) in the lab.

Mein besonderer Dank gilt Anja Schneider und Matthias Müller für die Unterstützung im Labor, sowie Dipl. Inf. Simon Tiedemann für „Q-PEP“.

Vielen lieben Dank an Denisia, Isabell, Börgi und Verena für die unzähligen Male, die ihr als Babysitter eingesprungen seid und an Sandra und Jen aus dem benach-

barten Büro für eure Nachsicht und Geduld, als Santina und Rasmus unsere Arbeitszeit „unterhaltsamer“ gestalteten!

An dieser Stelle möchte ich mich auch bei Dr. Anneliese Wilsch-Irrgang bedanken, die mich inspirierte und mir stets ein großes Vorbild ist. Vielen lieben Dank, *Liese*, für die schöne Zeit in Düsseldorf und die Einblicke, die ich gewinnen durfte.

Des Weiteren sei Dr. Harry E. Hoster gedankt, der mir bei einem kurzen Rundgang durch das Institut den Zugang zur Wissenschaft ebnete.

In diesem Zusammenhang sei auch Tina, meine beste Freundin dankend erwähnt, die nach Abschluss unseres gemeinsamen Lehramtstudiums, meinte, dass „ich nicht für die Schule geeignet sei und besser an der Uni bleiben solle“.

Mama und *Papa*, ich danke euch von ganzem Herzen dafür, dass ihr immer an mich geglaubt habt, dass ihr mich in meinen Entscheidungen bedingungslos unterstützt habt und dass ihr mir stets mit Rat und Tat zur Seite standet. Ohne euch hätte ich dies alles nicht erreicht. Vielen lieben Dank für eure mentale und tatkräftige Unterstützung, für die „geopferten“ Überstunden und Urlaubstage, für die erholsamen Wochenenden im „Hotel-Mama“, vielen lieben Dank für eure Liebe und Unterstützung und dafür, dass ihr immer für mich da seid!

Ein ebenso großer Dank gilt meinem Bruder Christian, meinen Schwiegereltern Heike und Jossi, sowie Felix und Sarah, die mich mit Worten und Taten, vor allem mit Babysitten unterstützten und mich nie im Stich gelassen haben! Vielen lieben Dank dafür!

Danke, *Santina* und *Rasmus*, dass ihr eure „kindliche“ Leichtigkeit und eure Naivität, die Neugier und euren Wissensdurst, Eigenschaften mit denen ihr das Leben entdeckt, auf mich übertragt. Ich danke euch von ganzem Herzen dafür, dass ihr mir jeden Tag aufs Neue zeigt, worauf es im Leben wirklich ankommt.

Meine unendliche Dankbarkeit gegenüber meinem Mann, lässt sich nicht so einfach in Worte fassen. Ein Versuch könnte lauten: Ich danke dir, *Philipp*, für den Tatendrang, die Kraft und die Zuversicht, die du immer wieder in mir hervorrufst, für dein Vertrauen, das Wissen dich an meiner Seite zu haben, was auch passiert und deine große Liebe, mit der du mir jeden Tag neu begegnest und die das Leben so lebenswert macht.

Ehrenwörtliche Versicherung:

Hiermit erkläre ich, *Yvonne Eva Seidel*, dass ich die vorliegende Dissertation selbständig verfasst, keine weiteren als die angegebenen Quellen und Hilfsmittel benutzt und wörtliche oder sinngemäße Zitate als solche gekennzeichnet habe.

Ulm, den 10. Mai 2010 *Yvonne E. Seidel*